Tsunami propagation in Cartesian space over rigid & elastic seabeds, plus propagation on the sphere with rigid seabed.

Author: Byron Williams

Supervisor: Dr. Usama Kadri

Submitted: February 2024

Submitted for the degree of Ph.D. in Mathematics

School of Mathematics
Cardiff University,
Senghennydd Road,
Cardiff,
CF24 4AG,
Wales, U.K.

Acknowledgements

I would like to thank and acknowledge the contributions - either directly or indirectly - of the following people/organisations.

- My supervisor Dr. Usama Kadri:- for giving me the opportunity to pursue this work in the first place, and then for all the helpful directions over the course of many years, including the occasional nudge when necessary to get me back on track.
- Dr Ali Abdolali:- NWS/NCEP/Environmental Modelling Centre, National Oceanic and Atmospheric Administration (NOAA), College Park, MD 20740, USA:- for his collaboration during the work presented in chapter three of this thesis. In particular, his contribution of numerical results obtained from 2D numerical solvers (mild slope equations and depth integrated models). His numerical results served as independent validation of the model derived in Chapter three.
- My wife Mrs. Alison S. Williams:- for her continued understanding and encouragement over the course of all my mathematical studies. Without her support finding the time and space to concentrate on mathematics over the extended periods required just would not have been possible.
- My daughter Miss Tegan L. Williams:- for support, encouragement and comedy interjections.
- Comprehensive nuclear-Test-Ban Treaty Organisation (CTBTO):- for the hydrophone data used in Chapter four.
- Incorporated Research Institutions for Seismology (IRIS):- for the seismic data used in Chapter four.
- United States Geological Survey (USGS) for the finite fault model data Chapter four.
- Finally I would like to thank all of the staff at the school of Mathematics in Cardiff along with the many PhD students I have met during my years as a PhD student. A special mention to Berna Gomez and Mohammed Alghazi (and family). They have been a source of inspiration and encouragement throughout my research journey.

Summary

This work discusses the generation and propagation of tsunamis and their associated acoustic–gravity waves. Many studies of tsunamis have been carried out in the past, dating back decades, but here we aim to extend the results of two - relatively recent - key papers. In the process new results were found, which it is hoped, may help in the future development of tsunami early warning systems.

The first extension takes the rigid seabed, purely acoustic, slender fault model as developed by Mei and Kadri and adds the restoring force of gravity. With this addition, it becomes possible to derive the equations governing the tsunami propagation as well as the acoustic-gravity waves. Since the underlying mathematical model is linear, we found more complex multi-fault clusters could be handled quite easily using superposition. Results were validated with numerical models.

The next step aimed to address the more realistic scenario whereby the seabed is now regarded as an elastic medium. The inclusion of elasticity has some interesting consequences. Firstly the acoustic–gravity waves are found to terminate after a finite time, with the decay time most affected by seabed rigidity. Secondly, elasticity enables coupling of the acoustic–gravity waves to the seabed and propagation with the shear wave velocity. We derive improved estimates for these frequencies. Next, elasticity enables the propagation of a second surface wave of negligible amplitude which travels at the speed of sound - this is not seen in the rigid model. The cut-off frequency for this wave is derived.

We also noted the acoustic-gravity wave signal carried information which depended on the time evolution and geometry of the rupture. We show that, with appropriate filtering, information on the fault's geometry and dynamics can be retrieved.

Finally we shift perspective from a local, Cartesian coordinate system to a global spherical coordinate system. By application of appropriate scales, the equations governing the defocusing and focusing of the tsunami amplitude due to the spherical geometry involved can be derived. The acoustic–gravity waves undergo a similar defocusing/focusing effect. A qualitative comparison is made with the Tonga eruption of 2022 which saw tsunami and acoustic–gravity wave propagation on a global scale.

CONTENTS

[1] [1]

[2] [2]

LIST OF FIGURES

LIST OF TABLES

Chapter 1

Introduction

1.1 Water waves

Surface water waves are a familiar sight to most people and can be observed in various situations. Their amplitudes can range from very small capillary waves - such as occur when an insect disturbs the surface of the water - to enormous tsunamis many meters high, capable of widespread destruction. Sitting somewhat in the middle of this range are the wind waves produced by meteorological processes (air pressure fluctuations and wind) interacting with the fluid surface - see Figure 1.1[1].

In addition to the surface waves there are also acoustic–gravity waves and internal waves. Acoustic–gravity waves are low frequency compression waves that travel at near the speed of sound in water ($\approx 1500\,\mathrm{ms}^{-1}$), and can occupy the entire depth of the water column. They can be generated by submarine earthquakes, landslides, impacting meteors, underwater explosions and even interactions between surface waves [6, 7]. Internal waves oscillate within the body of the liquid (as opposed to on its surface), and can arise when layers of density stratification exist. A useful classification of the various water waves possible based roughly on the restoring force that is in action (surface tension, gravity, compressibility) can be found in [8]. The classification suggests eight categories in all. This thesis will focus on two of those categories - namely the acoustic–gravity waves and the tsunamis.

Tsunamis are a form of surface wave usually generated by an underwater earthquake (rupture) or landslide. They are characterised by long wavelengths which can be in excess

[1] (`https://commons.wikimedia.org/wiki/File:Ripples_waves_bee.jpg`), Ripples waves bee, `https://creativecommons.org/licenses/by-sa/3.0/legalcode`

of 100 km. With the tsunamis having such long wavelengths they are classified as shallow-water waves due to their wavelength greatly exceeding the water depth - even in the deep ocean. Shallow-water waves incur very little dispersion, so that their speed of propagation is independent of their wavelength. The propagation speed of shallow-water waves is - to a good approximation - given by $\sqrt{gh}$, where $g = 9.81\,\mathrm{ms}^{-2}$ is the acceleration due to gravity, and h is the water depth. As a point of interest if a tsunami were to pass under a ship located far from shore in deep water its effect would be barely noticeable. It is only when the tsunami reaches shallower water that its speed decreases and amplitude increases in a process known as shoaling.

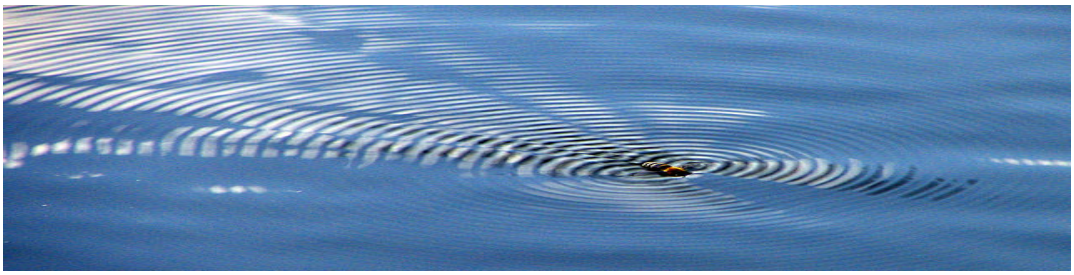

(a) Small ripples produced by insect in contact with the water surface. No machine-readable author provided. Bogdan assumed (based on copyright claims)

.

(b) Wind waves produced by air blowing over water surface.

(c) Tsunami over-topping wall, Miyako Japan 11^{th} March 2011. Image Mainichi Shimbun/Reuters

Figure 1.1: Various water waves.

1.2 Motivation

To understand the motivation for studying tsunamis and acoustic–gravity waves it is only necessary to look back at the many historical events involving tsunamis where loss of life and/or damage to property has occurred. The National Geophysical Data Centre[2]

[2] `https://www.ngdc.noaa.gov/`

places the first recorded tsunami in Syria over 4000 years ago. Moving forward in time to 1854 we find the Tokai and Nankai earthquakes which caused a tsunami up to 10 m high in Japan and represent the earliest tsunami to be recorded by instruments [9]. The tsunami waves were recorded on a tide gauge in San Francisco. A few years later we find the 1883 Krakatoa volcano eruption tsunami made famous in the 1968 film "Krakatoa East of Java". The eruption produced tsunamis with heights up to 15 m which claimed 36,000 lives along the Sunda Strait [9]. More recently there is the 2011 Tohoku Oki event, with epicentre off the northern coast of Honshu. This was the biggest earthquake to be recorded in Japan producing tsunamis with maximum run-up heights of around 40 m [9]. This earthquake and tsunami are regarded as the principal cause of the Fukushima nuclear disaster. Very recent examples include 2018 Sulawesi / Palu and Tonga 2022. However, the deadliest event so far recorded is that of December 26^{th} 2004 in Sumatra. More than 228,000 people from 14 countries lost their lives over the course of this single event [9]. Data on the deep water propagation of the tsunami was recorded on bottom pressure gauges [10] and - by chance - on satellite altimeters [11, 12].

1.3 Tsunami Early Warning Systems (TEWS)

Ideally one desires the ability to predict tsunamigenic events ahead of time, but this is not possible with current technology. So until technology advances sufficiently these events (and many others) demonstrate that a primary reason for the scale of the devastation suffered is the lack of a reliable early warning system. Current systems are heavily dependent on DART buoys (Deep ocean Assessment & Recording of Tsunamis), Figure 1.2[3] and seismic data. The DART buoys may be capable of accurate tsunami evaluation, but depending on particular circumstances there may not be much time for post-analysis warnings. The tsunami has to move past the DART buoy in order for its bottom pressure sensors to record an event. On the other hand seismic data arrives quickly, and provides information on earthquake size and location (moment magnitude M_w and epicentre). However, at the present time, analysis of the seismic data fails to assess which earthquake events will produce significant tsunamis, and so many false alarms are possible by this method. Work is currently being done to better categorise the data and isolate potential tsunamigenic events using Artificial Intelligence (AI) and machine learning [13].

It has been proposed that acoustic–gravity waves can act as suitable precursors to an

[3] `https://commons.wikimedia.org/wiki/File:DART_II_System_Diagram.jpg`, `https://commons.wikimedia.org/wiki/Template:PD-US`

on-coming tsunami due to their higher propagation speed allowing them to out-run the surface waves in the far-field [14, 3]. In this way they can "fill-the-gap" between the seismic and DART methods. It has also been shown that the acoustic–gravity waves carry information relating to the rupture geometry and timing [4, 15]. This information can be extracted via an inverse process [4, 16, 17, 2] to generate rupture parameters for use in forward tsunami modelling.

One recent development in the domain of TEWS is an international collaboration which aims to utilise thousands of kilometres of undersea fibre-optic cables as a giant sensor array. The idea is that sensors capable of measuring temperature, pressure and seismic acceleration will piggyback onto the undersea telecommunications network[4].

With advances in technology and theoretical understanding of tsunamigenic events it is hoped that many fatalities can be avoided in future. It is with this goal in mind that we are driven to better understand acoustic–gravity waves and, of course, the surface tsunamis themselves.

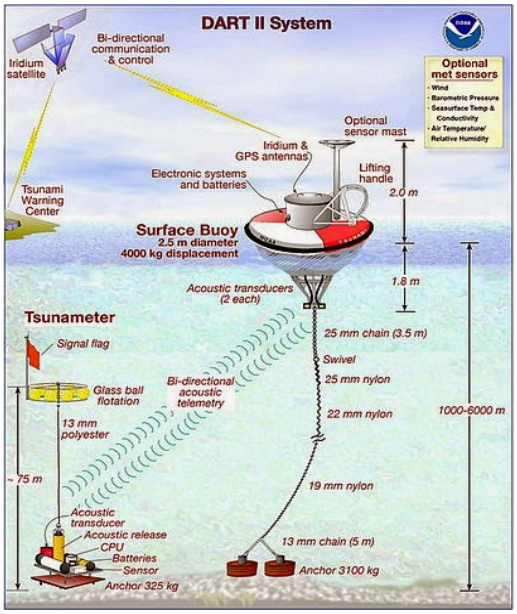

Figure 1.2: DART buoy tsunami early warning system. Image by Pacific Marine Environmental Laboratory, "DART II System Diagram", marked as public domain.

[4] https://www.oden.utexas.edu/news-and-events/news/Century-Old-Technology-Inspires-Tsunami-Earthquake-Detection/

Chapter 2

Foundations

2.1 Literature review

This chapter gives an outline of some of the key papers forming the foundations for my research efforts. The outline presented is not intended to be a comprehensive account of the historical development of acoustic–gravity wave and tsunami research - rather it is a summary of those papers that I feel made a contribution to my own work. Of course the contributions made by individual papers are not equal, with some having been pored over and studied intensely, whilst others may have revealed a single idea, equation or technique.

Only a brief discussion of the key papers will be presented, whilst attempting to build a coherent timeline leading from [18] through to [16] and [19]. The [16] paper then acts as a springboard for the research developed in Chapters 3, 4 and 5.

The timeline begins with [18]. This paper discusses the interaction of two opposing surface gravity waves in a heavy compressible fluid and finds that compression waves arise (acoustic–gravity waves). These in turn are able to generate microseisms - small oscillations of the seabed. This is possible because the acoustic–gravity waves can occupy the entire water column and so stress the seabed. This property also means they do not get trapped in the SOund Fixing And Ranging channel (SOFAR) [3] . In many fluid mechanics applications it is common to regard the water as incompressible since this simplifies some of the calculations. However in doing so a whole family of propagating waves is neglected, namely the acoustic–gravity waves [20, 15]. Longuet-Higgins [18], along with [21] sets the scene for much of the following research. In [21] the seabed rupture is modelled as a cylindrical elevation lifting the water column above it. The

seabed is taken to be rigid - this is a simplifying assumption common to many following papers. Also, as in [18] the water is regarded as compressible.

Advancing a few years [22] studies the 2D problem with the disturbance at the seabed now modelled as an infinite strip of constant width. The 1965 paper by Sells [22] distinguishes between acoustic–gravity waves derived from the edges of the strip, and those seen by an observer directly above the strip.

Advancing further [14] models the seabed rupture as an oscillating strip of infinite length, so again presenting a 2D scenario to solve. The importance of including compressibility of the water layer is reinforced, and the possibility of using the propagating acoustic–gravity waves as early tsunami warning signals far from the source is mentioned. Yamamoto [14] demonstrated that the (angular) frequency of the acoustic–gravity modes must be an integral multiple of $\pi c/2h$ where c is the speed of sound in water and h is the water depth. Also, the possibility of using the acoustic–gravity waves in order to determine characteristics of the rupture (size and magnitude) is discussed. Yamamoto [14] also clarifies the distinction between the propagating modes of the acoustic–gravity wave family and those that decay quickly and thus remain localised to the rupture zone - the evanescent modes.

In [15] we again find a 2D problem has been solved, but interestingly in the conclusion to his paper Nosov states that "the acoustic mode has a certain frequency spectrum which depends on bottom topography, sediment features and on the time history and spatial structure of the bottom displacement". Nosov refers to this as the tsunami's "voice". In other words information on the rupture timing and geometry is to be found within the acoustic–gravity wave signal.

The next item along the timeline is [12], in which the authors simulate tsunami propagation using a fully non-linear and dispersive model. They performed a comparison between their model and the results of an overflying satellite (Jason 1) which - by chance - happened to be measuring sea surface elevation in the Indian ocean at the time the Sumatra 2004 tsunami passed underneath it. The authors had succeeded in breaking up the giant rupture of 2004 into 10 segments, and conveniently provided details such as dimension, timing, location, strike angle etc. for each segment. This information proved invaluable in setting up my own models of this event later.

Stiassnie's paper [3] again works with the 2D problem and derives integral solutions as did earlier authors, but then applies the method of stationary phase to the propagating modes in order to achieve a fully analytic solution utilising only basic operations (sums,

products etc.) i.e. no integration necessary. The simplification afforded by the stationary phase method in computing the surface elevation and pressure field is considerable. However, there is a price to pay in that the stationary phase method fails at the front of the tsunami [3] and induces singularities into the equations. While working through this paper I discovered a small error in the calculation of the surface elevation and pressure due to the tsunami. The results given are missing a factor of 2, so that the surface wave amplitude and pressure due to the tsunami should be double that reported in the paper - see Appendix A. In the concluding remarks of [3] it is made clear that in seeking realistic predictions bottom elasticity would have to be considered.

The year 2013 marks the start of a period of heightened activity within the tsunami research community with three items listed on the timeline (and at least eight papers published that year). The first of these is by [23]. The paper derives a hyperbolic Mild-Slope Equation for Weakly Compressible fluids (MSEWC). The mild-slope condition places a restriction on the severity of the gradient encountered in the depth variation in that $|\nabla h(x,y,t)| \ll kh(x,y,t)$ where $h(x,y,t)$ is now local water depth and k the wave-number. This restriction means that changes in water depth should be gradual - no abrupt changes allowed. In practical terms the equation can be used for a bottom inclination up to 1:3 [24]. Their model based on depth-integrated equations can preserve all the physical features and yet avoid the computational costs associated with fully 3D models. The authors claim an order of magnitude improvement in computational time [23] over the full 3D model.

The first paper to tackle elasticity of the seabed in my timeline is [25]. The research leading to [25] was part of an MSc thesis which contained more detail than the standalone paper. The [25] paper formed the basis for much of Chapter 4. In [25] the 2D problem of acoustic–gravity waves in a compressible ocean overlying an elastic half-space is studied. The results are compared against those for a rigid seabed. When elasticity of the seabed is considered the shape of the phase velocity curves for the acoustic–gravity waves changes from those of the rigid case. The acoustic–gravity waves are able to propagate into shallower water before dissipating and the first acoustic mode travels all the way to shore as a Scholte wave. This is not seen when the seabed is rigid. The elasticity of the seabed also changes some of the surface wave properties as well. There is the possibility of a second surface wave when the seabed is elastic.

The third work in the timeline for the year 2013 is that of [4]. Here again we see the rupture modelled as a rising cylinder and the 3D problem is solved treating the regions lying inside and outside of the cylinder's circumference separately. A continuity condition

is applied at the circumference to derive the velocity potentials for the two regions in terms of Bessel and Hankel functions. The tsunami and acoustic–gravity waves can be calculated from this model, although at high computational cost. Also presented is a procedure for retrieving the rupture parameters (epicentre, start time, rupture duration, vertical velocity etc.) from measured bottom pressure records, i.e. a solution to the inverse problem. The work presented in [4] also became relevant in Chapter 5, where the effects of shifting perspective from Cartesian to spherical coordinates is presented.

Abdolali et al. [26] again develops depth-integrated equations building on the earlier work by [23], but now includes dissipation. The weakly compressible ocean overlies a weakly compressible sediment layer, which itself overlies a rigid seabed. Only acoustic–gravity waves are considered in this work, where it is found that the frequency spectrum and modal peaks are lowered in comparison to a rigid seabed. A change in the frequency spectrum is also encountered when the seabed is elastic - see Chapter 4 - where in this case the shift is upward. It would be interesting to combine the sediment layer of [26] with the elastic seabed of [2] and observe the resulting frequency shift in the acoustic–gravity waves.

Renzi, [27] working with a rigid seabed, derives an analytical solution of the mild slope equation based around a multiple scale perturbation technique. In the conclusions the authors remark "mathematical solutions of Hydro Acoustic (H.A.) waves generated by tsunamigenic disturbances over an elastic bottom in 3D appear not to be available in the literature, leaving this challenging issue as a topic for further research". This very topic is addressed and at least partially solved (for constant depth) in Chapter 4.

In the same year (2017) we find a discussion of complex multi-faults - [28] examines a multi-fault rupture which occurred in New Zealand 2016. The authors suggest that some re-evaluation of how rupture scenarios are defined may be important. The ability to model ruptures as multi-faults provides more flexibility in setting rupture parameters.

Next along the timeline [29] investigates the surface wave and acoustic–gravity wave fields generated by the Tohoku 2011 tsunamigenic event. Their model is based on the Mild Slope Equation for Dissipative Weakly Compressible fluids (MSEDWC), and utilised a dual tsunamigenic source consisting of a co-seismic source along with a Submarine Mass Failure (SMF). This way the authors obtained a better match with observations. Uplift and timing data from this paper contibuted to the Tohoku 2011 models set up in Chapters 3 and 4.

Arriving at 2018 we find the first paper on the timeline to treat the rupture geometry as

a slender, rectangular body - [16]. The rectangular shape is justified in many cases [16]. Also, more complex multi-fault scenarios can sometimes be approximated by taking two or more rectangular shapes and employing superposition. This facility is explored in Chapters 3 and 4. Taking advantage of the different length scales in the fault geometry the authors obtain analytical results by using the asymptotic technique of multiple scales. Modal envelopes of the 2D sound waves are governed by the Schrödinger equation and so a full 3D solution is obtained. However, [16] focuses on the acoustic side alone, so does not include gravity and therefore does not address the tsunami. The authors also extend the work of [4] to now apply to a rectangular geometry (previously cylindrical). Chapter 3 extends the results of [16] to include gravity for the "forward" problem of tsunami and acoustic–gravity wave propagation.

Next on the timeline is [20] which addresses the systematic discrepancies found when observed tsunami arrival times are compared with those predicted by models that assume incompressible water and a rigid seabed. Differences can run into tens of minutes. The relative contributions of gravity, compressibility and elasticity are quantified.

Completing the timeline is [19] which studies the Tonga volcanic eruption of 2022 and the global propagation of the resulting acoustic–gravity waves and tsunami. This event presented the authors with a unique opportunity to study resonance/energy transfer between air and water. Since this paper discussed tsunamis and acoustic–gravity waves on a global scale, it also provided a qualitative reference for the focusing/defocusing work developed in Chapter 5.

By 2018/19 the importance of including compressibility has been widely recognised. Of course if questions around tsunami behaviour are to be addressed then the restoring force of gravity must also be taken into account. Gaining in recognition, is the importance of elasticity, with its modifying effects on both surface waves and acoustic–gravity waves, particularly in phase velocity changes, but also other aspects. The geometry of the rupture zone has undergone its own evolution as well. Early papers used fixed width infinite strips (either transient or oscillatory motion) or cylindrical shapes. Arguably, a more realistic physical representation of a rupture would be the finite rectangular shape (slender fault) which is - at least approximately - found in nature [16]. More complex multi-fault scenarios can then be constructed by combining two (or more) slender faults into a multi-fault cluster. So as of 2018/19 the slender fault model exists, but is presented in "pure acoustic" form. There is no gravitation included in the model and so insights into tsunami behaviour are not possible. The realm of elasticity of the supporting seabed has been explored and found to induce significant modifications to both surface wave and

acoustic–gravity wave behaviour. However, the elasticity studies in [25] are devoid of fault motion. Also, a comprehensive study of tsunami and acoustic–gravity wave propagation on a global scale had to wait until 2022 and the massive Tonga eruption. This was the first event of its kind to be captured with arrays of modern instrumentation. So, at this point, some gaps in current tsunami research have been identified and this thesis aims to progress understanding in these areas as outlined in the next Section.

2.2 Thesis aims

The aims of this thesis are to advance current research by,

1. Adding gravitational effects to the slender fault model, thus enabling statements relating to the surface waves to be derived alongside those of the acoustic–gravity waves.

2. Developing the multi-fault aspect of rupture representation so as to handle more complex fault scenarios via superposition.

3. Combining the uplift of a slender fault [16, 1] with an elastic seabed [25] to study the effects of elasticity on the propagating acoustic–gravity waves and surface waves arising from the fault motion.

4. Shifting perspective from a Cartesian coordinate system to a spherical coordinate system, which better represents the actual geometry of the earth at large scales. Then study how the propagation of both the tsunami surface waves and the acoustic–gravity waves are affected by the change in geometry.

1950	**[18]** - Compressibility, acoustic–gravity waves.
1954	**[21]** - Cylindrical elevation of seabed, compressibility, rigid seabed.
1965	**[22]** - 2D problem, infinite, constant width strip.
1982	**[14]** - Oscillating infinite strip, early warning, rupture properties, propagating vs evanescent.
1999	**[15]** - 2D problem, tsunami voice.
2007	**[12]** - Sumatra 2004 source details.
2010	**[3]** - 2D, Stationary phase method.
2013	**[23]** - MSEWC.
	[25] - Phase velocity curves, Scholte wave, second surface wave mode.
	[30] - Extra details relating to earlier paper.
	[4] - 3D model, Bessel / Hankel functions, inverse model.
2015	**[26]** - Depth integrated, dissipation, frequency shift
2017	**[27]** - Rigid seabed,
	[28] - Complex multi-faults
	[29] - MSEDWC Tohoku 2011
2018	**[16]** - Slender fault, acoustic only, multiple scales, Schrödinger equation, inverse problem.
2019	**[20]** - Gravity, compressibility.
2022	**[19]** - Global extent, resonance.

TABLE 2.1 Timeline of key papers. Those papers regarded as forming the core of the research contained in this thesis are coloured teal.

2.3 Published / presented works

- Multiple scales analysis for sound signals from slender multi-faults, SIAM-IMA Student Chapter three minute thesis, 2018.
- Poster presented at 2018 South China Sea Tsunami Workshop 10 (SCSTW-10), 10^{th}, 11^{th} October in National University of Singapore.
- Virtual presentation for Underwater Acoustics Conference & Exhibition 05/08/2021.
- Virtual presentation American Geophysical Union (AGU) fall meeting 13^{th} to 17^{th} Dec 2021.
- [1], Williams, B., Kadri, U., and Abdolali, A. (2021). Acoustic–gravity waves from multi-fault rupture. Journal of Fluid Mechanics, 915:A108.
- [2], Williams, B., Kadri, U. (2023). On the propagation of acoustic–gravity waves due to a slender rupture in an elastic seabed. Journal of Fluid Mechanics, A6.
- Williams, B., Kadri, U. (2024). Propagation of acoustic–gravity waves on a sphere: focusing and defocusing.

Chapter 3

Slender faults with gravity and multi-fault extension[1]

3.1 Introduction.

As discussed in the introduction (Chapter 1), acoustic–gravity waves are compression waves that reside within the entire water column and can couple with the elastic seabed. They carry information about the source at relatively high speeds ranging from the speed of sound in water ($1500\,\mathrm{ms}^{-1}$), to Rayleigh wave speed in the solid ($3200\,\mathrm{ms}^{-1}$) that far exceeds the phase speed of the tsunami ($200\,\mathrm{ms}^{-1}$ at 4 km water depth), see [25]. In the solid layer, compression P (pressure) waves and S (shear) waves propagate at about $6800\,\mathrm{ms}^{-1}$ and $3900\,\mathrm{ms}^{-1}$, respectively [31]. A critical difference between analysing acoustic–gravity waves and P and S waves is that the former, being a compression wave in the liquid layer, is directly associated with the effective vertical uplift. Hence, acoustic–gravity waves can not only act as excellent precursors, but they could also provide vital information on the geometry and dynamics of the effective uplift, which eventually shapes the main characteristics of the tsunami. The next chapter contains more details on this possibility. Using the acoustic fore-runner as an early warning signal has long been established [15, 14, 3, 6, 32, 33, 34, 35, 36]. Finite fault models have also been investigated, providing a three dimensional theory of acoustic–gravity waves based on the classical method of the Green's function [4]. However, their utility in providing predictions for acoustic and surface wave behaviour in real time is limited due to the solution being in integral form. This requires partitioning of any shape considered into many

[1] [1]

small elements, calculating the contribution from each element, then performing a summation to arrive at the total contribution. In the absence of an explicit analytical solution, this proves to be computationally expensive [16] and, of course, the processing burden escalates with the addition of more complex multi-fault ruptures, as observed in nature [28]. An alternative approach was proposed by [16] who considered a slender fault and invoked multiple scale analysis to obtain a closed-form analytical solution for the propagating acoustic modes. Improvements in long-range modulation are provided by the introduction of envelope factors involving Fresnel integrals.

The aim of this chapter is to extend the results of [16] to include gravitational effects and multi-fault ruptures. The inclusion of gravitation involves a modification to the surface boundary condition. This modification gives rise to expressions for the gravity wave contribution to bottom pressure, along with the expected acoustic–gravity wave contributions. Evanescent modes are also derived, but later ignored, since their effects in the far field are negligible. Expressions for surface elevation are obtained - broken down into contributions from the surface wave and the acoustic–gravity waves. The form of the governing equations for the envelope factors involved in the long range modulations are found to be identical for both acoustic–gravity waves and the surface wave, i.e. they both obey the Schrödinger equation. The addition of gravitation to the current model may have a beneficial effect on the accuracy achievable in the inverse theory calculations originally discussed in [16]. One application of the multi-fault approach developed here is to tackle a long standing limitation which arises when applying a stationary phase approximation. The derived explicit solution for the gravity mode (tsunami) is singular at the arrival time [3] which results in overlooking the main peak of the tsunami. To overcome this difficulty, the fault is split into strips. Since each strip has a different spatio-temporal singularity, the main tsunami amplitude can be reconstructed by the superposition principle.

Extension to multi-fault ruptures arises naturally from the linear theory by application of the superposition principle enabling fault systems such as that discussed in [28] to be investigated. Two instances of multi-faults are considered here, one based upon the 2011 Tohoku event (detailed data can be found in [29]) and the second is based on the Sumatra 2004 event. We ignore terms of second order and higher (i.e. non-linear terms) since the free surface displacements are small in comparison with the water depth [37]. We also ignore viscous effects, capillary effects, surface tension and also assume constant atmospheric pressure.

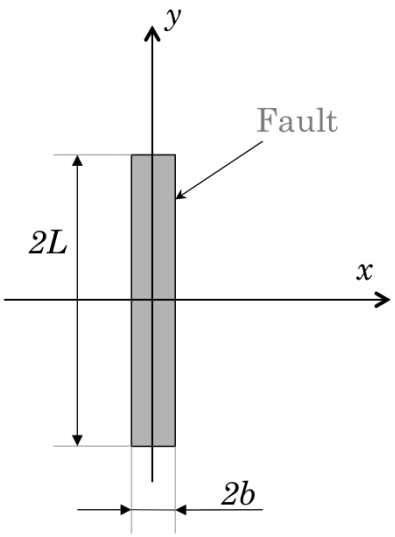

Figure 3.1: Sketch of slender fault.

Constant	Description	Value
g	Acceleration due to gravity	9.81 ms^{-2}
L	Fault half-length	400 km
b	Fault half-width	40 km
$2T$	Rupture duration	10 s
h	Water depth	4 km
ρ_l	Water density	1000 kgm^{-3}
C_l	Speed of sound in water	1500 ms^{-1}
W_0	Uplift velocity	0.1 ms^{-1}
N	Number of acoustic modes	10

Table 3.1: Constants and parameters used in validation of current model with gravity.

3.2 Governing equations

In addition to the assumptions above the water layer is assumed to be homogeneous and of constant depth h. The origin of the Cartesian co-ordinates is located at the seabed, at the centroid of the fault, with the vertical axis z directed vertically upward. Based on irrotational flow, the problem is formulated in terms of the velocity potential $\phi_l(x,y,z,t)$, where $\mathbf{u} = \nabla\phi_l$ is the velocity field. Considering the slight compressibility of the sea, the velocity potential obeys the standard three dimensional wave equation,

$$\frac{\partial^2\phi_l}{\partial x^2} + \frac{\partial^2\phi_l}{\partial y^2} + \frac{\partial^2\phi_l}{\partial z^2} - \frac{1}{C_l^2}\frac{\partial^2\phi_l}{\partial t^2} = 0, \tag{3.2.1}$$

where C_l is the speed of sound in water. For the boundary condition at the free surface, we follow the detailed derivation given in [8] Section (1.1.2). Beginning with the Bernoulli equation from page 8 of [8] and with ρ_l as the fluid density

$$-\frac{P}{\rho_l} = gz + \frac{\partial \phi_l}{\partial t} + \frac{1}{2}|\nabla \phi_l|^2 + C(t), \tag{3.2.2}$$

where $C(t)$ is an arbitrary function of t which can usually be omitted by redefining ϕ_l. The gz term is the hydro-static contribution. The other terms on the right-hand side of (3.2.2) are the hydrodynamic contributions to total pressure P. On the free surface assume the fluid moves only tangentially. Let the instantaneous equation of the boundary be

$$F(\mathbf{x}, t) = z - \zeta(x, y, t) = 0, \tag{3.2.3}$$

where ζ is the height from $z = 0$. Let the velocity of a point $\mathbf{x}$ on the free surface be $\mathbf{q}$ then after a time dt

$$F(\mathbf{x} + \mathbf{q}dt, t + dt) = 0 = F(\mathbf{x}, t) + \left(\frac{\partial F}{\partial t} + \mathbf{q} \cdot \nabla F\right) dt + O(dt)^2. \tag{3.2.4}$$

From equation (3.2.3) we have

$$\frac{\partial F}{\partial t} + \mathbf{q} \cdot \nabla F = 0 \tag{3.2.5}$$

for small dt. Tangential motion requires $\mathbf{u} \cdot \nabla F = \mathbf{q} \cdot \nabla F$ which implies

$$\frac{\partial F}{\partial t} + \mathbf{u} \cdot \nabla F = 0, \quad z = \zeta. \tag{3.2.6}$$

The pressure immediately below the free surface must equal the pressure P_a above. Applying (3.2.2) to the free surface we have

$$-\frac{P_a}{\rho_l} = g\zeta + \frac{\partial \phi_l}{\partial t} + \frac{1}{2}|\nabla \phi_l|^2 \qquad z = \zeta. \tag{3.2.7}$$

Taking the total derivative of (3.2.7)

$$\left(\frac{\partial}{\partial t} + \mathbf{u} \cdot \nabla\right) \frac{P_a}{\rho_l} + \left(\frac{\partial}{\partial t} + \mathbf{u} \cdot \nabla\right) \left(\frac{\partial \phi_l}{\partial t} + \frac{\mathbf{u}^2}{2} + g\zeta\right) = 0 \qquad z = \zeta \tag{3.2.8}$$

Then using (3.2.6) along with

$$\mathbf{u} \cdot \nabla \frac{\partial \phi_l}{\partial t} = \frac{\partial}{\partial t} \frac{1}{2} \mathbf{u}^2 \tag{3.2.9}$$

we have from (3.2.8)

$$\frac{D}{Dt}\frac{P_a}{\rho_l} + \left[\frac{\partial^2\phi_l}{\partial t^2} + g\frac{\partial\phi_l}{\partial z} + \frac{\partial \mathbf{u}^2}{\partial t} + \frac{1}{2}\mathbf{u}\cdot\nabla\mathbf{u}^2\right] = 0 \qquad z = \zeta. \tag{3.2.10}$$

Then with P_a considered constant and ignoring non-linear terms (3.2.10) becomes the linearised, combined dynamic and kinematic boundary condition

$$\frac{\partial^2\phi_l}{\partial t^2} + g\frac{\partial\phi_l}{\partial z} = 0. \tag{3.2.11}$$

Following [16], the fault's ground motion is confined to a rigid, slender rectangular stripe of width $2b$ and length $2L$, with a slenderness parameter $\varepsilon = b/L \ll 1$ (see Figure 3.1), such that

$$\frac{\partial\phi_l}{\partial z} = \mathrm{w}(x,y)\tau(t), \quad z = 0, \tag{3.2.12}$$

where

$$\mathrm{w}(x,y) = \begin{cases} W_0 = \text{const} & |x| < b, |y| < L \\ 0 & \text{elsewhere} \end{cases}, \quad \tau(t) = \begin{cases} 1 & -T < t < T \\ 0 & |t| > T \end{cases}, \quad z = 0. \tag{3.2.13}$$

where $\mathrm{w}(x,y)$ defines the spatial extent of the rupture, τ defines the time the rupture is active and W_0 is the uplift velocity. To study the long distance propagation of acoustic–gravity waves we introduce re-scaled co-ordinates (see [16])

$$X = \varepsilon^2 x, \qquad Y = \varepsilon y. \tag{3.2.14}$$

Letting $\phi_l = \phi_{l0}(x,X,Y,z,t) + \varepsilon^2\phi_{l2}(x,X,Y,z,t) + \cdots$, the potential reduces to the two-dimensional wave equation to leading order

$$\frac{\partial^2\phi_{l0}}{\partial x^2} + \frac{\partial^2\phi_{l0}}{\partial z^2} - \frac{1}{C_l^2}\frac{\partial^2\phi_{l0}}{\partial t^2} = 0, \tag{3.2.15}$$

with boundary conditions given by

$$\frac{\partial^2\phi_{l0}}{\partial t^2} + g\frac{\partial\phi_{l0}}{\partial z} = 0, \quad z = h \tag{3.2.16}$$

$$\frac{\partial\phi_{l0}}{\partial z} = \begin{cases} W_0\tau(t) & |x| < b, |y| < L \\ 0 & \text{elsewhere} \end{cases}, \quad \tau(t) = \begin{cases} 1 & -T < t < T \\ 0 & |t| > T \end{cases}, \quad z = 0. \tag{3.2.17}$$

The envelope of the radiated waves is governed by

$$\frac{\partial^2\phi_{l2}}{\partial x^2}+\frac{\partial^2\phi_{l2}}{\partial z^2}-\frac{1}{C_l^2}\frac{\partial^2\phi_{l2}}{\partial t^2}=-\left[\frac{\partial^2\phi_{l0}}{\partial Y^2}+2\frac{\partial^2\phi_{l0}}{\partial x\partial X}\right], \tag{3.2.18}$$

with the boundary conditions

$$\frac{\partial^2\phi_{l2}}{\partial t^2}+g\frac{\partial\phi_{l2}}{\partial z}=0, \quad z=h \tag{3.2.19}$$

$$\frac{\partial\phi_{l2}}{\partial z}=0, \quad z=0. \tag{3.2.20}$$

Note that the boundary conditions for ϕ_{l0} and ϕ_{l2} at $z=h$ here are different to those in the "no-gravity" case ($\phi_{l0}=\phi_{l2}=0$).

3.3 Solutions

3.3.1 Leading order

To derive the desired velocity potential first transform the wave equation and boundary conditions utilising the double Fourier transform $\Phi=\int_{-\infty}^{\infty}\int_{-\infty}^{\infty}\phi_{l0}\mathrm{e}^{-\mathrm{i}(kx-\omega t)}\mathrm{d}t\mathrm{d}x$, with ω representing angular velocity and k the wave number and solve. Once the transformed velocity potential has been obtained in the k,ω domain we can then transform back into the x,t domain using an inverse transform. Begin with (3.2.15) - after both transforms we arrive at

$$\frac{\partial^2\Phi}{\partial z^2}+\left(\frac{\omega^2}{C_l^2}-k^2\right)\Phi=0, \quad \mu=\sqrt{\frac{\omega^2}{C_l^2}-k^2}. \tag{3.3.21}$$

This is simple harmonic motion in the z direction and has solution of the form

$$\Phi=A\cos\left(\mu z\right)+B\sin\left(\mu z\right), \tag{3.3.22}$$

where A and B are integration constants to be determined. Next transform (3.2.16)

$$\begin{aligned}\int_{-\infty}^{\infty}\left(\frac{\partial^2\phi_{l0}}{\partial t^2}+g\frac{\partial\phi_{l0}}{\partial z}\right)\mathrm{e}^{\mathrm{i}\omega t}\mathrm{d}t&=\int_{-\infty}^{\infty}\frac{\partial^2\phi_{l0}}{\partial t^2}\mathrm{e}^{\mathrm{i}\omega t}\mathrm{d}t+g\frac{\partial}{\partial z}\int_{-\infty}^{\infty}\phi_{l0}\mathrm{e}^{\mathrm{i}\omega t}\mathrm{d}t,\\&=\left[\frac{\partial\phi_{l0}}{\partial t}\mathrm{e}^{\mathrm{i}\omega t}\right]_{-\infty}^{\infty}-\mathrm{i}\omega\int_{-\infty}^{\infty}\frac{\partial\phi_{l0}}{\partial t}\mathrm{e}^{\mathrm{i}\omega t}\mathrm{d}t+g\frac{\partial\bar{\phi}_{l0}}{\partial z}=0.\end{aligned} \tag{3.3.23}$$

Under the assumptions $\frac{\partial \phi_{l0}}{\partial t} \to 0$ and $\phi_{l0} \to 0$ as $|t| \to 0$ the term in square brackets drops out leaving

$$-\mathrm{i}\omega\left\{\left[\phi_{l0}\mathrm{e}^{\mathrm{i}\omega t}\right]_{-\infty}^{\infty} - \mathrm{i}\omega\int_{-\infty}^{\infty}\phi_{l0}\mathrm{e}^{\mathrm{i}\omega t}\mathrm{d}t\right\} + g\frac{\partial\bar{\phi}_{l0}}{\partial z} = -\omega^2\bar{\phi}_{l0} + g\frac{\partial\bar{\phi}_{l0}}{\partial z} = 0. \tag{3.3.24}$$

Similarly, after the second transform of (3.2.16) we have

$$-\omega^2\Phi + g\frac{\partial\Phi}{\partial z} = 0, \quad z = h. \tag{3.3.25}$$

The boundary condition at the seabed $z = 0$ transforms exactly as in [16] leading to

$$\frac{\partial\Phi}{\partial z} = W_0 G(k,\omega), \quad G(k,\omega) = \frac{4\sin(kb)\sin(\omega T}{k\omega}. \tag{3.3.26}$$

Evaluating the boundary condition at the surface $z = h$ gives

$$-A\left[\omega^2\cos(\mu h) + \mu g\sin(\mu h)\right] + B\left[\mu g\cos(\mu h) - \omega^2\sin(\mu h)\right] = 0. \tag{3.3.27}$$

which implies

$$B = A\frac{\left[\omega^2\cos(\mu h) + \mu g\sin(\mu h)\right]}{\left[\mu g\cos(\mu h) - \omega^2\sin(\mu h)\right]}. \tag{3.3.28}$$

Evaluating the boundary condition at $z = 0$ gives

$$\left[-\mu A\sin(\mu z) + \mu B\cos(\mu z)\right]_{z=0} = W_0 G \quad \Longrightarrow B = \frac{W_0 G}{\mu} \tag{3.3.29}$$

so that

$$A\frac{\left[\omega^2\cos(\mu h) + \mu g\sin(\mu h)\right]}{\left[\mu g\cos(\mu h) - \omega^2\sin(\mu h)\right]} = \frac{W_0 G}{\mu}, \tag{3.3.30}$$

and therefore

$$A = \frac{W_0 G\left[\mu g\cos(\mu h) - \omega^2\sin(\mu h)\right]}{\mu\left[\omega^2\cos(\mu h) + \mu g\sin(\mu h)\right]}. \tag{3.3.31}$$

From (3.3.22)

$$\Phi = \frac{W_0 G\left[\mu g\cos(\mu h) - \omega^2\sin(\mu h)\right]}{\mu\left[\omega^2\cos(\mu h) + \mu g\sin(\mu h)\right]}\cos(\mu z) + \frac{W_0 G}{\mu}\sin(\mu z). \tag{3.3.32}$$

After simplification this becomes

$$\Phi = \frac{4W_0\sin(kb)\sin(\omega T)}{\mu k\omega}\left\{\frac{\mu g\cos\left[\mu(h-z)\right] - \omega^2\sin\left[\mu(h-z)\right]}{\left[\omega^2\cos(\mu h) + \mu g\sin(\mu h)\right]}\right\}, \tag{3.3.33}$$

where $\mu^2 = (\omega^2/c^2) - k^2$. The only poles contributing to the contour integration derive from the dispersion relation $\omega^2 \cos(\mu h) + \mu g \sin(\mu h) = 0$ in the denominator of (3.3.33). The case $k = 0$ is a removable singularity, since $k \to 0 \implies \sin(kb)/k \to b$. The first eigenvalue μ_0 is imaginary - all the rest are real. The first wave number k_0 corresponding to a gravity wave is always real. The following $n \leq N$ wave numbers $[k_1 k_2 \dots k_N]$ are also real, and correspond to the acoustic–gravity waves where $N = \lfloor (\omega h/\pi C_l) + 1/2 \rfloor$. The gravity and acoustic–gravity modes are progressive waves. The next modes, $n > N$ with wave numbers λ_n correspond to decaying, evanescent modes [38]. Thus, all modes satisfy the dispersion relation where

$$k_0 = \sqrt{\frac{\omega^2}{C_l^2} + \mu_0^2}, \quad k_n = \sqrt{\frac{\omega^2}{C_l^2} - \mu_n^2}, \quad \lambda_n = \sqrt{\mu_n^2 - \frac{\omega^2}{C_l^2}}. \tag{3.3.34}$$

Inverting the transformation by contour integration we obtain the velocity potential

$$\begin{aligned}
\varphi_{l0} = &-\frac{W_0}{\pi} \mathrm{Re} \int_0^\infty \mathrm{i} \frac{8\mu_0 \sin(k_0 b) \sin(\omega T) \cosh\left(\mu_0 z\right)}{\omega k_0^2 \left[2\mu_0 h + \sinh(2\mu_0 h)\right]} \mathrm{e}^{\mathrm{i}(k_0|x| - \omega t)} \mathrm{d}\omega \\
&- \frac{W_0}{\pi} \mathrm{Re} \sum_{n=1}^{N} \int_{\omega_n}^\infty \mathrm{i} \frac{8\mu_n \sin(k_n b) \sin(\omega T) \cos\left(\mu_n z\right)}{\omega k_n^2 \left[2\mu_n h + \sin(2\mu_n h)\right]} \mathrm{e}^{\mathrm{i}(k_n|x| - \omega t)} \mathrm{d}\omega \\
&- \frac{W_0}{\pi} \sum_{n=N+1}^{\infty} \int_0^{\omega_n} \cos(\omega t) \frac{8\mu_n \sinh(k_n b) \sin(\omega T) \cos\left(\mu_n z\right)}{\omega \lambda_n^2 \left[2\mu_n h + \sin(2\mu_n h)\right]} \mathrm{e}^{-\lambda_n |x|} \mathrm{d}\omega,
\end{aligned} \tag{3.3.35}$$

where ω_n represents the cut-off frequency for mode n. Then picking out the real part for the propagating modes gives

$$\begin{aligned}
\varphi_{l0} = &\frac{8W_0}{\pi} \int_0^\infty \frac{\mu_0 \sin(k_0 b) \sin(\omega T) \cosh\left(\mu_0 z\right)}{\omega k_0^2 \left[2\mu_0 h + \sinh(2\mu_0 h)\right]} \sin\left(k_0 |x| - \omega t\right) \mathrm{d}\omega \\
&+ \frac{8W_0}{\pi} \sum_{n=1}^{N} \int_{\omega_n}^\infty \frac{\mu_n \sin(k_n b) \sin(\omega T) \cos\left(\mu_n z\right)}{\omega k_n^2 \left[2\mu_n h + \sin(2\mu_n h)\right]} \sin\left(k_n |x| - \omega t\right) \mathrm{d}\omega,
\end{aligned} \tag{3.3.36}$$

from which the pressure and surface elevation expressions can be obtained by differentiation using

$$P = -\rho_l \frac{\partial \varphi_{l0}}{\partial t}, \quad \eta = -\frac{1}{g} \frac{\partial \varphi_{l0}}{\partial t}. \tag{3.3.37}$$

Thus the pressure terms are now given by

$$\begin{aligned} P = &\frac{8\rho_l W_0}{\pi} \int_0^\infty \frac{\mu_0 \sin(k_0 b)\sin(\omega T)\cosh\left(\mu_0 z\right)}{k_0^2\left[2\mu_0 h + \sinh(2\mu_0 h)\right]} \cos(k_0|x| - \omega t)\,\mathrm{d}\omega \\ &+ \frac{8\rho_l W_0}{\pi} \sum_{n=1}^{N} \int_{\omega_n}^\infty \frac{\mu_n \sin(k_n b)\sin(\omega T)\cos\left(\mu_n z\right)}{k_n^2\left[2\mu_n h + \sin(2\mu_n h)\right]} \cos(k_n|x| - \omega t)\,\mathrm{d}\omega, \end{aligned} \tag{3.3.38}$$

with surface elevation terms given by

$$\begin{aligned} \eta = &\frac{8W_0}{g\pi} \int_0^\infty \frac{\mu_0 \sin(k_0 b)\sin(\omega T)\cosh\left(\mu_0 h\right)}{k_0^2\left[2\mu_0 h + \sinh(2\mu_0 h)\right]} \cos(k_0|x| - \omega t)\,\mathrm{d}\omega \\ &+ \frac{8W_0}{g\pi} \sum_{n=1}^{N} \int_{\omega_n}^\infty \frac{\mu_n \sin(k_n b)\sin(\omega T)\cos\left(\mu_n h\right)}{k_n^2\left[2\mu_n h + \sin(2\mu_n h)\right]} \cos(k_n|x| - \omega t)\,\mathrm{d}\omega. \end{aligned} \tag{3.3.39}$$

The expressions for pressure and surface elevation are in agreement with Stiassnie [3].

3.3.2 Long range modulation

Considering the region far from the fault, [16] showed that for pure acoustic modes the envelopes vary slowly, allowing the derivation of an analytical solution of the pressure. It is anticipated that the addition of gravity, would have a similar effect where the modal envelopes of both the acoustic–gravity modes (with the correction due to gravity), and the gravity mode (with correction due to compressibility) are all governed by the Schrödinger equation, which is derived as follows.

Introduce unknown envelope factors $A_n^{\pm}(X,Y)$ and $A_0^{\pm}(X,Y)$

$$A_n^{\pm} = \begin{cases} 1 & |Y| < l = \varepsilon L \\ 0 & |Y| > l = \varepsilon L \end{cases}, \quad A_0^{\pm} = \begin{cases} 1 & Y| < l = \varepsilon L \\ 0 & Y| > l = \varepsilon L \end{cases}, \quad X = \varepsilon^2 x, \tag{3.3.40}$$

then re-write the propagating parts of (3.3.35) as

$$\begin{aligned}\varphi_{l0} = &-\frac{W_0}{2\pi}\mathrm{Re}\int_0^{\infty}\mathrm{i}A_0^{+}\frac{8\mu_0\sin(k_0b)\sin(\omega T)\cosh\left(\mu_0 z\right)}{\omega k_0^2\left[2\mu_0 h+\sinh(2\mu_0 h)\right]}\mathrm{e}^{\mathrm{i}(k_0|x|-\omega t)}\mathrm{d}\omega\\ &-\frac{W_0}{2\pi}\mathrm{Re}\int_{-\infty}^{0}\mathrm{i}A_0^{-}\frac{8\mu_0\sin(k_0b)\sin(\omega T)\cosh\left(\mu_0 z\right)}{\omega k_0^2\left[2\mu_0 h+\sinh(2\mu_0 h)\right]}\mathrm{e}^{\mathrm{i}(k_0|x|-\omega t)}\mathrm{d}\omega\\ &-\frac{W_0}{2\pi}\mathrm{Re}\sum_{n=1}^{N}\int_{\omega_n}^{\infty}\mathrm{i}A_n^{+}\frac{8\mu_n\sin(k_nb)\sin(\omega T)\cos\left(\mu_n z\right)}{\omega k_n^2\left[2\mu_n h+\sin(2\mu_n h)\right]}\mathrm{e}^{\mathrm{i}(k_n|x|-\omega t)}\mathrm{d}\omega\\ &-\frac{W_0}{2\pi}\mathrm{Re}\sum_{n=1}^{N}\int_{-\infty}^{-\omega_n}\mathrm{i}A_n^{-}\frac{8\mu_n\sin(k_nb)\sin(\omega T)\cos\left(\mu_n z\right)}{\omega k_n^2\left[2\mu_n h+\sin(2\mu_n h)\right]}\mathrm{e}^{\mathrm{i}(k_n|x|-\omega t)}\mathrm{d}\omega,\end{aligned} \tag{3.3.41}$$

Consider the acoustic–gravity waves (the surface wave solution can be derived in a similar fashion). Take time Fourier transform of (3.2.18) and separate the resulting $\bar{\varphi}_{l2}$ into 3 ranges

$$\bar{\varphi}_{l2} = \begin{cases}\bar{\varphi}_{l2}^{+} & \omega_n < \omega < \infty\\ \bar{\varphi}_{l2}^{e} & -\omega_n < \omega < \omega_n\\ \bar{\varphi}_{l2}^{-} & -\infty < \omega < -\omega_n.\end{cases} \tag{3.3.42}$$

In the range $\omega_n < \omega < \infty$

$$\frac{\partial^2\bar{\varphi}_{l2}^{+}}{\partial x^2}+\frac{\partial^2\bar{\varphi}_{l2}^{+}}{\partial z^2}+\frac{\omega^2}{c^2}\bar{\varphi}_{l2}^{+} = -\frac{\partial^2\bar{\varphi}_{l0}^{+}}{\partial Y^2}-2\frac{\partial^2\bar{\varphi}_{l0}^{+}}{\partial x\partial X}, \tag{3.3.43}$$

with

$$\bar{\varphi}_{l0}^{+} = \int_{-\infty}^{\infty}\left\{-\frac{W_0}{2\pi}\mathrm{Re}\sum_{n=1}^{N}\int_{\omega_n}^{\infty}\mathrm{i}A_n^{+}\frac{8\mu_n\sin(k_nb)\sin(\omega T)\cos\left(\mu_n z\right)}{\omega k_n^2\left[2\mu_n h+\sin(2\mu_n h)\right]}\mathrm{e}^{\mathrm{i}(k_n|x|-\omega t)}\mathrm{d}\omega\right\}\mathrm{e}^{\mathrm{i}\omega t}\mathrm{d}t. \tag{3.3.44}$$

Therefore

$$\bar{\varphi}_{l0}^{+} = -\mathrm{i}W_0\sum_{n=1}^{N}A_n^{+}\frac{8\mu_n\sin(k_nb)\sin(\omega T)\cos\left(\mu_n z\right)}{\omega k_n^2\left[2\mu_n h+\sinh(2\mu_n h)\right]}\mathrm{e}^{\mathrm{i}k_n|x|}\int_{-\infty}^{\infty}\frac{1}{2\pi}\int_{\omega_n}^{\infty}\mathrm{e}^{\mathrm{i}\omega t}\mathrm{e}^{-\mathrm{i}\omega t}\mathrm{d}\omega\mathrm{d}t. \tag{3.3.45}$$

Note that in the range $\omega_n < \omega < \infty$ we have

$$\int_{-\infty}^{\infty}\frac{1}{2\pi}\int_{\omega_n}^{\infty}\mathrm{e}^{\mathrm{i}\omega t}\mathrm{e}^{-\mathrm{i}\omega t}\mathrm{d}\omega\mathrm{d}t = \int_{-\infty}^{\infty}\frac{1}{2\pi}\int_{-\infty}^{\infty}\mathrm{e}^{\mathrm{i}\omega t}\mathrm{e}^{-\mathrm{i}\omega t}\mathrm{d}\omega\mathrm{d}t = 1, \tag{3.3.46}$$

so that

$$\bar{\varphi}^{+}_{l0} = -\mathrm{i}W_0 \sum_{n=1}^{N} A^{+}_{n} \frac{8\mu_n \sin(k_n b)\sin(\omega T)\cos\left(\mu_n z\right)}{\omega k_n^2 \left[2\mu_n h + \sinh(2\mu_n h)\right]} \mathrm{e}^{\mathrm{i}k_n|x|}. \tag{3.3.47}$$

The first term on the RHS of (3.3.43) is

$$-\frac{\partial^2 \bar{\varphi}^{+}_{l0}}{\partial Y^2} = \mathrm{i}W_0 \sum_{n=1}^{N} \frac{\partial^2 A^{+}_{n}}{\partial Y^2} \frac{8\mu_n \sin(k_n b)\sin(\omega T)\cos\left(\mu_n z\right)}{\omega k_n^2 \left[2\mu_n h + \sinh(2\mu_n h)\right]} \mathrm{e}^{\mathrm{i}k_n|x|}. \tag{3.3.48}$$

The second term on the RHS of (3.3.43) is

$$-2\frac{\partial^2 \bar{\varphi}^{+}_{l0}}{\partial x \partial X} = \mathrm{i}W_0 \sum_{n=1}^{N} 2\mathrm{i}k_n \frac{\partial A^{+}_{n}}{\partial X} \frac{8\mu_n \sin(k_n b)\sin(\omega T)\cos\left(\mu_n z\right)}{\omega k_n^2 \left[2\mu_n h + \sinh(2\mu_n h)\right]} \mathrm{e}^{\mathrm{i}k_n|x|}. \tag{3.3.49}$$

Substitution into (3.3.43) gives

$$\begin{aligned}\frac{\partial^2 \bar{\varphi}^{+}_{l2}}{\partial x^2} + \frac{\partial^2 \bar{\varphi}^{+}_{l2}}{\partial z^2} + \frac{\omega^2}{c^2}\bar{\varphi}^{+}_{l2} =& \mathrm{i}W_0 \sum_{n=1}^{N} \frac{\partial^2 A^{+}_{n}}{\partial Y^2} \frac{8\mu_n \sin(k_n b)\sin(\omega T)\cos\left(\mu_n z\right)}{\omega k_n^2 \left[2\mu_n h + \sinh(2\mu_n h)\right]} \mathrm{e}^{\mathrm{i}k_n|x|} \\ &+ \mathrm{i}W_0 \sum_{n=1}^{N} 2\mathrm{i}k_n \frac{\partial A^{+}_{n}}{\partial X} \frac{8\mu_n \sin(k_n b)\sin(\omega T)\cos\left(\mu_n z\right)}{\omega k_n^2 \left[2\mu_n h + \sinh(2\mu_n h)\right]} \mathrm{e}^{\mathrm{i}k_n|x|}.\end{aligned} \tag{3.3.50}$$

Factoring

$$\frac{\partial^2 \bar{\varphi}^{+}_{l2}}{\partial x^2} + \frac{\partial^2 \bar{\varphi}^{+}_{l2}}{\partial z^2} + \frac{\omega^2}{c^2}\bar{\varphi}^{+}_{l2} = \mathrm{i}W_0 \sum_{n=1}^{N} \left[\frac{\partial^2 A^{+}_{n}}{\partial Y^2} + 2\mathrm{i}k_n \frac{\partial A^{+}_{n}}{\partial X}\right] \frac{8\mu_n \sin(k_n b)\sin(\omega T)\cos\left(\mu_n z\right)}{\omega k_n^2 \left[2\mu_n h + \sinh(2\mu_n h)\right]} \mathrm{e}^{\mathrm{i}k_n|x|}. \tag{3.3.51}$$

Assume $\bar{\varphi}^{+}_{l2}$ has a solution in the form $\bar{\varphi}^{+}_{l2} = \sum_{n=1}^{N} \psi^{+}_{n}(\omega, z)\mathrm{e}^{\mathrm{i}k_n x}$, then (3.3.50) becomes

$$\begin{aligned}&-\sum_{n=1}^{N} \psi^{+}_{n} k_n^2 \mathrm{e}^{\mathrm{i}k_n x} + \sum_{n=1}^{N} \frac{\partial^2 \psi^{+}_{n}}{\partial z^2} \mathrm{e}^{\mathrm{i}k_n x} + \frac{\omega^2}{c^2} \sum_{n=1}^{N} \psi^{+}_{n} \mathrm{e}^{\mathrm{i}k_n x} \\ &= \mathrm{i}W_0 \sum_{n=1}^{N} \left[\frac{\partial^2 A^{+}_{n}}{\partial Y^2} + 2\mathrm{i}k_n \frac{\partial A^{+}_{n}}{\partial X}\right] \frac{8\mu_n \sin(k_n b)\sin(\omega T)}{\omega k_n^2 \left[2\mu_n h + \sinh(2\mu_n h)\right]} \cos\left(\mu_n z\right) \mathrm{e}^{\mathrm{i}k_n|x|}.\end{aligned} \tag{3.3.52}$$

Let $F_n(z) = \cos\left(\mu_n z\right)$, then equating coefficients gives

$$\begin{aligned}&\frac{\partial^2 \psi^{+}_{n}}{\partial z^2} + \left(\frac{\omega^2}{c^2} - k_n^2\right)\psi^{+}_{n} = \\ &\mathrm{i}W_0 \sum_{n=1}^{N} \left[\frac{\partial^2 A^{+}_{n}}{\partial Y^2} + 2\mathrm{i}k_n \frac{\partial A^{+}_{n}}{\partial X}\right] \frac{8\mu_n \sin(k_n b)\sin(\omega T)}{\omega k_n^2 \left[2\mu_n h + \sinh(2\mu_n h)\right]} F_n(z).\end{aligned} \tag{3.3.53}$$

Where

$$\mu_n^2 = \frac{\omega^2}{c^2} - k_n^2, \tag{3.3.54}$$

then

$$\begin{aligned} &\frac{\partial^2 \psi_n^+}{\partial z^2} + \mu_n^2 \psi_n^+ = \\ &\mathrm{i}W_0 \sum_{n=1}^{N} \left[\frac{\partial^2 A_n^+}{\partial Y^2} + 2\mathrm{i}k_n \frac{\partial A_n^+}{\partial X} \right] \frac{8\mu_n \sin(k_n b)\sin(\omega T)}{\omega k_n^2 \left[2\mu_n h + \sinh(2\mu_n h)\right]} F_n(z). \end{aligned} \tag{3.3.55}$$

Where $F_n(z)$ is a solution of the homogeneous boundary value problem

$$\frac{\partial^2 F_n(z)}{\partial z^2} + \mu_n^2 F_n(z) = 0 \tag{3.3.56}$$

$$-\omega^2 F_n(z) + g\frac{\partial F_n(z)}{\partial z} = 0, \quad z = h \tag{3.3.57}$$

$$\frac{\partial F_n(z)}{\partial z} = 0, \quad z = 0 \tag{3.3.58}$$

Multiply (3.3.53) by $F_n(z)$ and (3.3.56) by ψ_n^+ then subtract

$$\begin{aligned} &F_n(z)\left(\frac{\partial^2 \psi_n^+}{\partial z^2} + \mu_n^2 \psi_n^+\right) - \psi_n^+ \left(\frac{\partial^2 F_n(z)}{\partial z^2} + \mu_n^2 F_n(z)\right) = \\ &\mathrm{i}W_0 \sum_{n=1}^{N} \left[\frac{\partial^2 A_n^+}{\partial Y^2} + 2\mathrm{i}k_n \frac{\partial A_n^+}{\partial X} \right] \frac{8\mu_n \sin(k_n b)\sin(\omega T)}{\omega k_n^2 \left[2\mu_n h + \sinh(2\mu_n h)\right]} F_n(z)^2. \end{aligned} \tag{3.3.59}$$

Following [16]

$$\int_0^h \left[F_n(z)\left(\frac{\partial^2 \psi_n^+}{\partial z^2} + \mu_n^2 \psi_n^+\right) - \psi_n^+ \left(\frac{\partial^2 F_n(z)}{\partial z^2} + \mu_n^2 F_n(z)\right) \right] \mathrm{d}z = \left[F_n(z)\frac{\partial^2 \psi_n^+}{\partial z^2} - \psi n^+ \frac{\partial^2 F_n(z)}{\partial z^2} \right]_0^h = 0. \tag{3.3.60}$$

Therefore

$$\frac{\partial^2 A_n^+}{\partial Y^2} + 2\mathrm{i}k_n \frac{\partial A_n^+}{\partial X} = 0, \tag{3.3.61}$$

As in [16] in addition to the initial condition (3.3.40), we require the waves to vanish far away from and be symmetric about the central axis

$$A_n^+ = 0, \quad |Y| \to \infty; \qquad \frac{\partial A_n^+}{\partial Y} = 0, \quad Y = 0. \tag{3.3.62}$$

The solvability requirement of ψ_n^- leads to the same result for A_n^- with solution due to

[16] given by

$$A_n = \frac{1-\mathrm{i}}{2}\left\{C\left(\sqrt{\frac{2}{\pi\chi_n}}\mathscr{Y}_+\right)+C\left(\sqrt{\frac{2}{\pi\chi_n}}\mathscr{Y}_-\right)\right\}+\frac{1+\mathrm{i}}{2}\left\{S\left(\sqrt{\frac{2}{\pi\chi_n}}\mathscr{Y}_+\right)+S\left(\sqrt{\frac{2}{\pi\chi_n}}\mathscr{Y}_-\right)\right\} \quad (3.3.63)$$

where $C(z)$ and $S(z)$ are Fresnel integrals and

$$\chi_n = X/2k_n, \quad \mathscr{Y}_\pm = (l \pm Y)/2. \quad (3.3.64)$$

This result (3.3.63) is identical in structure to that of [16], though here it is valid also for the gravity mode $n = 0$. With the inclusion of these results for $A_n(X,Y)$ the leading order term for the velocity potential in (3.3.35) is now valid in the ranges $x \le O(l\varepsilon^{-2}) = O(L\varepsilon^{-1})$, $y \le O(l\varepsilon^{-1})$.

3.3.3 Stationary phase approximation

We now apply the stationary phase approximation for different gravity phase speed conditions. We rewrite (3.3.38) as

$$\begin{aligned} P = {} & \frac{8\rho_l W_0}{\pi}\mathrm{Re}\int_0^\infty \frac{\mu_0 \sin(k_0 b)\sin(\omega T)\cosh\left(\mu_0 z\right)}{k_0^2\left[2\mu_0 h+\sinh(2\mu_0 h)\right]}\mathrm{e}^{\mathrm{i}(k_0|x|-\omega t)}\mathrm{d}\omega \\ & + \frac{8\rho_l W_0}{\pi}\mathrm{Re}\sum_{n=1}^{N}\int_{\omega_n}^\infty \frac{\mu_n \sin(k_n b)\sin(\omega T)\cos\left(\mu_n z\right)}{k_n^2\left[2\mu_n h+\sin(2\mu_n h)\right]}\mathrm{e}^{\mathrm{i}(k_n|x|-\omega t)}\mathrm{d}\omega. \end{aligned} \quad (3.3.65)$$

3.3.3.1 Acoustic–gravity modes

Consider the acoustic–gravity modes only - i.e. the second term in (3.3.65) - and let the phase of mode n be denoted by $\Gamma_n(\omega)$ with

$$\Gamma_n(\omega) = k_n(\omega)\frac{x}{t}-\omega, \quad \text{where} \quad k_n(\omega) = \frac{\sqrt{\omega^2-\omega_n^2}}{C_l}. \quad (3.3.66)$$

Take the first derivative of $\Gamma_n(\omega)$ with respect to ω and equate to zero to locate the stationary point

$$\Gamma_n'(\omega) = \frac{\omega}{\sqrt{\omega^2-\omega_n^2}}\frac{x}{C_l t}-1 = 0. \quad (3.3.67)$$

At the point of stationary phase $\omega = \Omega_n$

$$\Omega_n = \frac{\omega_n}{\sqrt{1-\left(\frac{x}{C_l t}\right)^2}}, \tag{3.3.68}$$

and a second derivative yields

$$\Gamma_n''(\omega) = -\frac{\omega_n^2 x}{C_l t\left(\Omega_n^2-\omega_n^2\right)^{\frac{3}{2}}} < 0, \tag{3.3.69}$$

$$k_n(\Omega_n) \equiv K_n = \frac{\sqrt{\Omega_n^2-\omega_n^2}}{C_l} = \frac{\omega_n}{C_l^2 t}\frac{x}{\sqrt{1-\left(\frac{x}{C_l t}\right)^2}}. \tag{3.3.70}$$

Knowledge of the sign of $\Gamma_n''(\omega)$ and also that $\Gamma_n''(\omega) \neq 0$ is required for the stationary phase calculations. Then, applying the known stationary phase, first approximation formula of [39], where $p_a(t)$ is the pressure contribution due to the acoustic–gravity waves and $f(\omega)$ is a general function of ω

$$p_a(t) = \int_0^\infty f(\omega)\mathrm{e}^{\mathrm{i}\Gamma(\omega)t}\mathrm{d}\omega, \tag{3.3.71}$$

$$p_a(t) = \sqrt{\frac{2\pi}{t}}\sum_{m=1}^{M}\frac{f(\omega_m)}{\sqrt{|\Gamma''(\omega_m)|}}\mathrm{e}^{\mathrm{i}\left(\Gamma(\omega_m)t+\frac{\pi}{4}\mathrm{sgn}[\Gamma''(\omega_m)]\right)}. \tag{3.3.72}$$

The index m counts the number of stationary points up to a maximum of M. In our case there is only one stationary point and so the summation over m drops out, leaving only the summation over the acoustic–gravity modes

$$f(\omega_n) = \frac{\rho_l W_0}{\pi}|A_n|\frac{8\mu_n \sin(K_n b)\sin(\Omega_n T)\cos(\mu_n z)}{K_n^2\left[2\mu_n h+\sin\left(2\mu_n h\right)\right]}. \tag{3.3.73}$$

Thus the contribution to the pressure arising from the acoustic–gravity waves becomes

$$p_a = \sum_{n=1}^{N}\frac{\rho_l W_0}{\pi}|A_n|\frac{8\mu_n \sin(K_n b)\sin(\Omega_n T)\cos(\mu_n z)}{K_n^2\left[2\mu_n h+\sin\left(2\mu_n h\right)\right]}\left[\frac{2\pi}{\frac{x}{C_l}\frac{\omega_n^2}{\left(\Omega_n^2-\omega_n^2\right)^{\frac{3}{2}}}}\right]^{\frac{1}{2}}\cos\left(K_n|x|-\Omega_n t-\frac{\pi}{4}+\Theta_{A_n}\right), \tag{3.3.74}$$

where Θ_{A_n} is the phase of A_n. The results for the acoustic–gravity modes are consistent with the results for the (pure) acoustic modes by [16] with the difference that the modes here have a correction due to gravity.

3.3.3.2 Gravity-acoustic mode

To obtain the stationary phase approximation for the contribution to bottom pressure arising from the surface-gravity wave - the first term in (3.3.65) - consider the phase term $\Gamma_0(\omega)$ for the general (compressible) case as

$$\Gamma_0(\omega) = k_0(\omega)\frac{x}{t} - \omega, \quad \Gamma_0'(\omega) = k_0'(\omega)\frac{x}{t} - 1 = 0, \quad \Gamma_0''(\omega) = k_0''(\omega)\frac{x}{t} \tag{3.3.75}$$

where single and doubles primes denote first and second derivatives with respect to ω. Noting that

$$k_0^2 = \frac{\omega^2}{C_l^2} + \mu_0^2, \quad k_0 = k_0(\omega) \quad \text{and} \quad \mu_0 = \mu_0(\omega), \tag{3.3.76}$$

differentiation with respect to ω yields

$$k_0' = \frac{1}{k_0}\left(\frac{\omega}{C_l^2} + \mu_0\mu_0'\right). \tag{3.3.77}$$

The stationary phase approximation requires a second derivative of k_0

$$k_0''(\omega) = \frac{1}{k_0}\left(\frac{1}{C_l^2} + (\mu_0')^2 + \mu_0\mu_0''\right) - \frac{1}{k_0^2}\left(\frac{\omega}{C_l^2} + \mu_0\mu_0'\right)k_0'. \tag{3.3.78}$$

Equation (3.3.78) contains terms in μ_0' and μ_0'', to obtain these we differentiate the general gravity dispersion relation

$$\omega^2 = g\mu_0 \tanh(\mu_0 h), \tag{3.3.79}$$

which gives,

$$\tilde{\mu}_0' = \frac{2\tilde{\omega}\tilde{\mu}_0}{\tilde{\omega}^2 + \tilde{\mu}_0^2 - \tilde{\omega}^4}, \qquad \tilde{\mu}_0'' = \frac{\tilde{\mu}_0'}{\tilde{\omega}} - \frac{(\tilde{\mu}_0')^3}{\tilde{\omega}}\left(1 - \tilde{\omega}^2 - \frac{\tilde{\omega}^4}{\tilde{\mu}_0} + \frac{\tilde{\omega}^6}{\tilde{\mu}_0^2}\right), \tag{3.3.80}$$

where, for simplicity, quantities with tilde were normalised with length scale h and timescale $\sqrt{h/g}$.

Following [39] and with $\omega = \Omega_0$ at the point of stationary phase, the pressure contribution arising from the surface gravity wave is given by

$$p_g = \frac{\rho_l W_0}{\pi}|A_0|\frac{8\mu_0 \sin(K_0 b)\sin(\Omega_0 T)\cosh(\mu_0 z)}{K_0^2\left[2\mu_0 h + \sinh(2\mu_0 h)\right]}\left[\frac{2\pi}{t\Gamma_0''(\Omega_0)}\right]^{\frac{1}{2}}\cos\left(K_0 x - \Omega_0 t + \frac{\pi}{4} + \Theta_{A_0}\right) \tag{3.3.81}$$

where Θ_{A_0} is the phase of A_0, and $\mu_0 \neq K_0$ in this case. For the total pressure contribution

from the propagating modes, we combine (3.3.74) with (3.3.81) to give

$$P(x,y,z,t) = \frac{\rho_l W_0}{\pi}|A_0|\frac{8\mu_0 \sin(K_0 b)\sin(\Omega_0 T)\cosh(\mu_0 z)}{K_0^2\left[2\mu_0 h + \sinh(2\mu_0 h)\right]}\left[\frac{2\pi}{t\Gamma_0''(\Omega_0)}\right]^{\frac{1}{2}}\cos\left(K_0 x - \Omega_0 t + \frac{\pi}{4} + \Theta_{A_0}\right)$$
$$+\sum_{n=1}^{N}\frac{\rho_l W_0}{\pi}|A_n|\frac{8\mu_n \sin(K_n b)\sin(\Omega_n T)\cos(\mu_n z)}{K_n^2\left[2\mu_n h + \sin\left(2\mu_n h\right)\right]}\left[\frac{2\pi}{\frac{x}{C_l}\frac{\omega_n^2}{(\Omega_n^2-\omega_n^2)^{\frac{3}{2}}}}\right]^{\frac{1}{2}}\cos\left(K_n|x| - \Omega_n t - \frac{\pi}{4} + \Theta_{A_n}\right) \tag{3.3.82}$$

Similarly the surface elevation terms add up to

$$\eta(x,y,t) = \frac{W_0}{g\pi}|A_0|\frac{8\mu_0 \sin(K_0 b)\sin(\Omega_0 T)\cosh\left(\mu_0 h\right)}{K_0^2\left[2\mu_0 h + \sinh(2\mu_0 h)\right]}\left[\frac{2\pi}{t\Gamma_0''(\Omega_0)}\right]^{\frac{1}{2}}\cos\left(K_0 x - \Omega_0 t + \frac{\pi}{4} + \Theta_{A_0}\right)$$
$$+\sum_{n=1}^{N}\frac{W_0}{g\pi}|A_n|\frac{8\mu_n \sin(K_n b)\sin(\Omega_n T)\cos\left(\mu_n h\right)}{K_n^2\left[2\mu_n h + \sin\left(2\mu_n h\right)\right]}\left[\frac{2\pi}{\frac{x}{C_l}\frac{\omega_n^2}{(\Omega_n^2-\omega_n^2)^{\frac{3}{2}}}}\right]^{\frac{1}{2}}\cos\left(K_n x - \Omega_n t - \frac{\pi}{4} + \Theta_{A_n}\right). \tag{3.3.83}$$

The forms of $\Gamma_0''(\Omega_0)$, Ω_0, and K_0 are dependent upon any assumptions made as detailed in the three cases considered below: (1) a general solution with the compressible dispersion relation (3.3.79); (2) an approximate high order dispersion relation; and (3) first order shallow water approximation. The latter two assume incompressibility. Note that for brevity cases 2 and 3 are presented in non-dimensional form.

Case 1: Compressible gravity dispersion relation

Evaluation of the surface-gravity wave contribution to surface elevation requires a method of calculation for μ_0, Ω_0, K_0 and Γ_0''. To obtain μ_0 we differentiate the general dispersion relation (3.3.79) with respect to k_0, and make use of $\Gamma_0'(\omega) = 0$ at stationary phase which gives

$$2\mu_0\frac{x}{t}\sqrt{g\mu_0\tanh(\mu_0 h)} - \left(g\mu_0\tanh(\mu_0 h) + g\mu_0^2 h - g\mu_0^2 h\tanh^2(\mu_0 h)\right)\frac{\mathrm{d}\mu_0}{\mathrm{d}k} = 0, \tag{3.3.84}$$

where

$$\frac{\mathrm{d}\mu_0}{\mathrm{d}k} = \sqrt{1 + \frac{g}{\mu_0 C_l^2}\tanh(\mu_0 h)} - \frac{x}{\mu_0 C_l^2 t}\sqrt{g\mu_0\tanh(\mu_0 h)}. \tag{3.3.85}$$

Equations (3.3.84) and (3.3.85) form an implicit relationship for μ_0, which can be solved numerically. Once μ_0 has been obtained, Ω_0 and K_0 can be derived directly from

$$\Omega_0 = \sqrt{g\mu_0 \tanh(\mu_0 h)}, \quad \text{and} \quad K_0 = \sqrt{\mu_0^2 + \frac{\Omega_0^2}{C_l^2}}, \tag{3.3.86}$$

and

$$\Gamma_0''(\Omega_0) = K_0''(\Omega_0)\frac{x}{t} = \frac{\mu_0}{K_0}\mu_0'' + \frac{1}{K_0^3 C_l^2}\left(\Omega_0\mu_0' - \mu_0\right)^2 \frac{x}{t}. \tag{3.3.87}$$

Equation (3.3.87) contains terms in μ_0' and μ_0'', these are obtained from (3.3.80).

Case 2: Third order incompressible dispersion relation

Neglecting the compressibility of the water we can set $\tilde{\mu}_0 = \tilde{k}_0$ in (3.3.79). Consideration of the first two terms in the Taylor expansion of $\tanh(\tilde{k}_0)$ results in explicit forms for $\tilde{\Omega}_0$, $\tilde{K}_0$ and $\tilde{\Gamma}_0''$ as

$$\tilde{\Omega}_0 = \frac{1}{8\tilde{t}^2}\left[6\tilde{t}^2 - \frac{3}{2}\tilde{x}\left(\tilde{x} + \sqrt{8\tilde{t}^2 + \tilde{x}^2}\right)\right]^{\frac{1}{2}}\left(\tilde{x} + \sqrt{8\tilde{t}^2 + \tilde{x}^2}\right), \tag{3.3.88}$$

$$\tilde{K}_0(\tilde{x}, \tilde{t}) = \sqrt{\frac{3}{2}}\left(1 - \sqrt{1 - \frac{4}{3}\tilde{\Omega}_0^2}\right)^{\frac{1}{2}}, \tag{3.3.89}$$

$$\tilde{\Gamma}_0''(\tilde{\Omega}_0) = \frac{\left(6\tilde{\Omega}_0^2 + 9\right)\left(3 - 2\tilde{K}_0^2\right) - 27}{\left(3\tilde{K}_0 - 2\tilde{K}_0^3\right)\left(3 - 4\tilde{\Omega}_0^2\right)\left(\sqrt{9 - 12\tilde{\Omega}_0^2} - 3\right)}\frac{\tilde{x}}{\tilde{t}}. \tag{3.3.90}$$

Case 3: Shallow water limit

In addition to the assumption of incompressibility ($\tilde{\mu}_0 = \tilde{k}_0$) we consider the case of shallow water, i.e. $\tanh(\tilde{k}_0) \approx \tilde{k}_0$, which leads to

$$\tilde{\Omega}_0 = \tilde{K}_0 = \sqrt{2}\left(\frac{\tilde{t}}{\tilde{x}} - 1\right)^{\frac{1}{2}}, \quad \tilde{\Gamma}_0'' = \tilde{K}_0''\frac{\tilde{x}}{\tilde{t}} \tag{3.3.91}$$

in agreement with Stiassnie [3]. To reduce to the 2D case of [3], the contribution from the envelope A_0 is removed (i.e. by setting $A_0 = 1$). Note that there is a factor of two magnification in the amplitude as compared to [3], which is believed to be due to a typographical error in [3] (see full derivation in Appendix A).

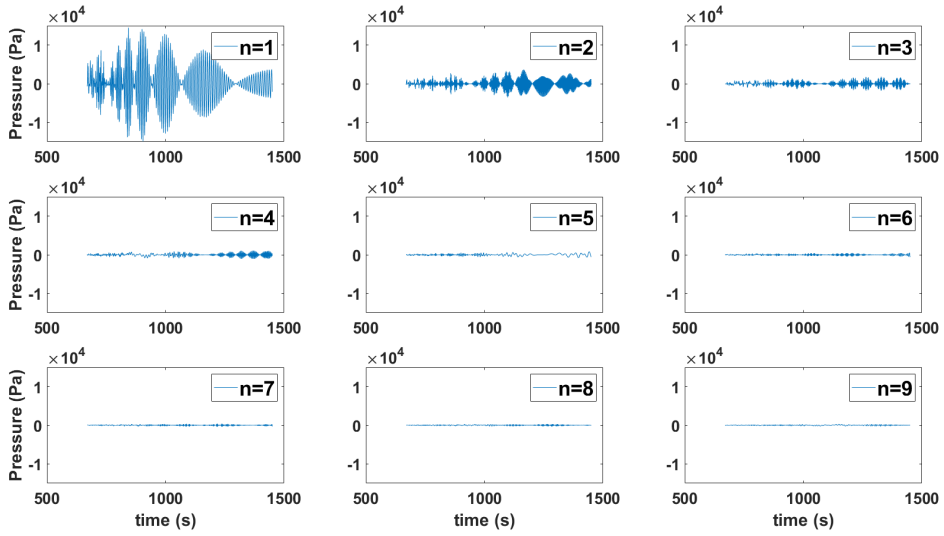

Figure 3.2: First nine acoustic–gravity modes for slender fault as in Table 3.1, $x = 1000$ km, $y = 0$ km. All nine modes are plotted with the same vertical scale which emphasises the rapid decrease in amplitude with increasing mode number.

3.4 Validation

For validation purposes we use input parameters similar to those found in [16] and [3], and that are listed in Table 3.1. The number of acoustic modes is set at $N = 10$. This was shown to be a "reasonable choice" in [3], wherein the convergence of the acoustic signal was demonstrated. A signal comprising 10 modes, is compared with a signal comprising 100 modes - very little difference is observed between the two. Thus 10 modes are enough to capture the overall behaviour. As a further illustration of the convergence with increasing mode number Figure 3.2 demonstrates the rapid decrease in amplitude with increasing mode number. Taking the peak amplitude found over the time interval 670 s to 1450 s for each mode $n = 1 \ldots 20$ and plotting against mode number results in Figure 3.3. The decay in amplitude is exponential and so rapid convergence can be achieved.

The uplift velocity of 0.1 ms^{-1}, along with rupture duration of 10 s, implies a fault displacement of 1 m. Aside from comparison with [3], further justification for using a duration of the order of tens of seconds can be found in [29] and [40].

The current model is first validated against the theoretical solution for infinitely distributed fault, proposed by [3] and a 3D numerical solver [23, 26]. The latter solves (3.2.1) with (3.2.11) at the surface, the movable bottom, representing the vertical uplift (3.2.12) and (3.2.13), and an outgoing Sommerfeld boundary condition at the end of the numeri-

cal domain. The Sommerfeld boundary condition essentially limits solutions to those that radiate outwards from the source i.e. no reflections at infinity. The undistributed fault length assumption for the first set of validations allows us to use the 3D numerical solver on a vertical transect, which is computationally affordable. It allows the presence of the surface gravity waves and all available acoustic modes to interact with each other. The only constraint is the minimum space-time resolution, required to resolve the range of dominant frequencies. In this simulation, proper values are used to ensure the first 10 modes exist in the domain.

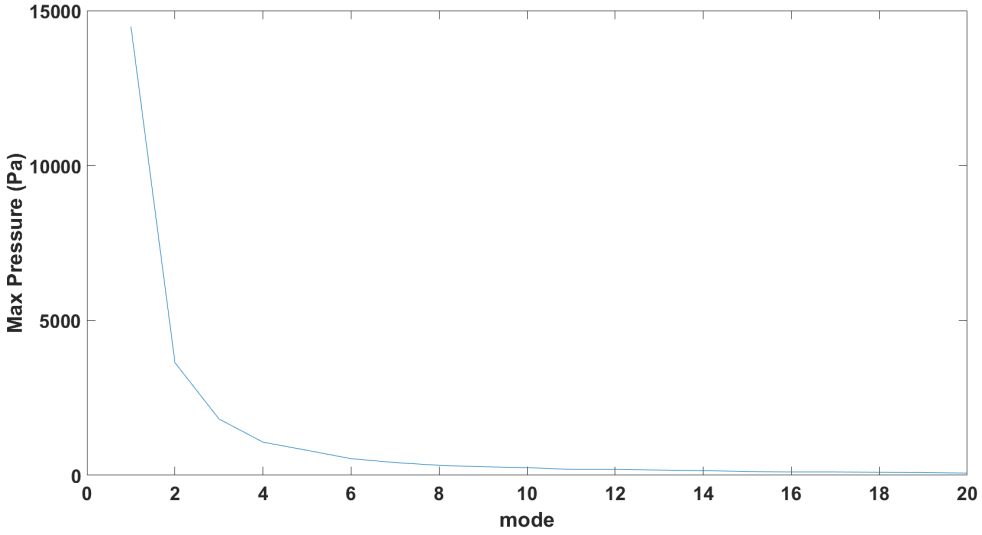

Figure 3.3: Peak amplitude attained during time interval (reference Figure 3.2) for first 20 modes. The decay in amplitude is exponential, facilitating rapid convergence.

For the second set of validations, a single finite fault case is considered over a large 2D domain. The validation is conducted between the current model and a 2D numerical solver based on the Mild Slope Equation (MSE) for weakly compressible fluid, rigid bottom [23].

In the third case, a real-world multifault scenario is considered over a large domain, where the theory and the depth integrated model are compared to prove the accuracy of the theory. Then simulation on a variable bed condition is conducted to highlight the missing processes (i.e. refraction and reflection) due to the presence of seamounts and trenches.

Note that the solution, proposed by [3] is fast, but has constant depth limit with an infinitely long fault assumption (2D model). The current theory provides a solution for the fault longitudinal extent to be finite and multi-fault condition. On the other hand, the

3D numerical solver is computationally expensive, but can take into account the entire problem without any assumption (i.e. variable depth profile). It is manageable to run it on transects, but requires massive computational resources for large 3D domains with the necessary resolution to resolve the acoustic–gravity wave field. The depth integrated model is faster than the 3D solver, but still much slower than the theoretical solution. In addition, it requires the forcing to be decomposed and solved on spectral bands. Here the validations are performed to prove the accuracy of each of the aforementioned models and theories, with proper overlaps. In other words, a coherent chain of cross-validation is performed to highlight the advantages of each method and the differences if assumptions are considered.

3.4.1 Bottom pressure

Consider a hydrophone station located at 1000 km along the positive x-axis. With the speed of sound fixed at 1500 ms^{-1}, the arrival time of the acoustic–gravity wave is approximately 670 s after the rupture. The tsunami arrives later at around 5000 s. Figure 3.4a compares the bottom pressure signature calculated by the current model (top trace), [3] (middle trace) and a 3D numerical solver, which solves (3.2.1) with proper boundary conditions at the surface and end of the numerical domain and movable seabed (bottom trace).

3.4.2 Surface elevation

With the inclusion of gravitational effects into the current model it is now possible to obtain surface elevation information in addition to the bottom pressure. Thus, the surface elevation results of Figure 3.4b constitute new findings for the current model. This is of consequence when considering the inverse problem, since it enables evaluation of the tsunami alongside the acoustic modes, thereby reducing computation time. A remarkable correction of the tsunami amplitude is obtained (black curve) by deserting the shallow water assumption suggested by [3], and instead solving the full compressible dispersion relation for μ_0, Ω_0 and K_0 numerically. To illustrate this improvement a comparison with a full numerical solution is presented (dashed red curve). Thus, an inclusion of compressibility in the tsunami calculations provides an important correction of the amplitude and frequency [41, 20]. It is also worth noting that an accurate gravitational constant g should be used.

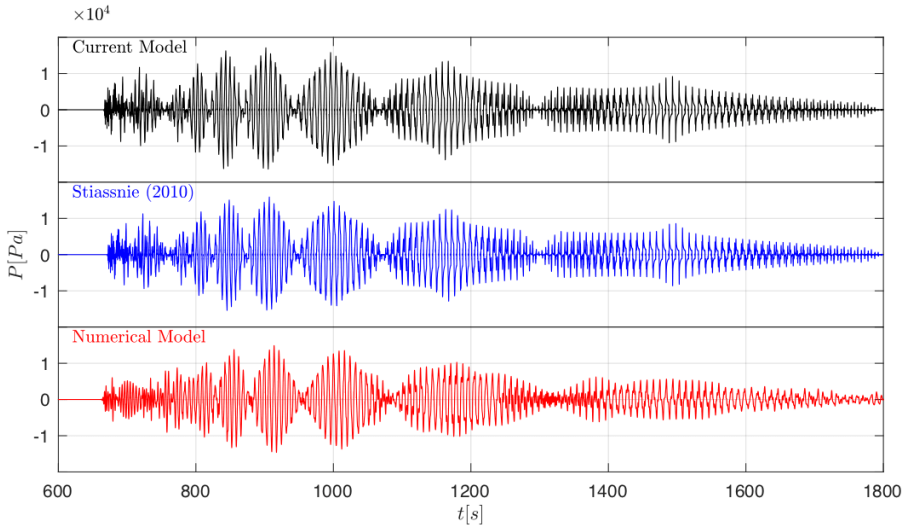

(a) Bottom pressure signals predicted by current model (top), [3] (middle) and numerical model (bottom). Co-ordinates are $x = 1000$ km, $y = 0$ km. Note the current model reduces to Stiassnie's 2D solution on the x axis.

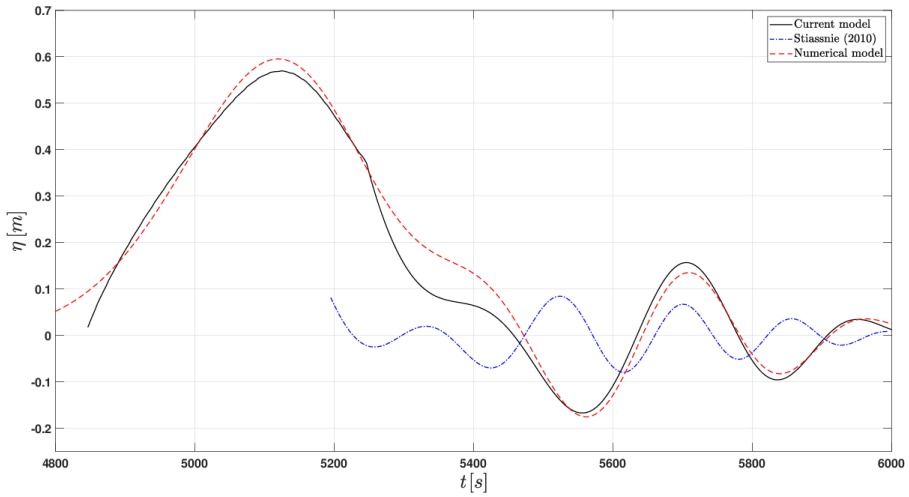

(b) Surface elevation plots generated by current model (stationary phase approximation inclusive of compressibility), [3] and the numerical model. Co-ordinates are $x = 1000$ km, $y = 0$ km.

Figure 3.4: Comparison of current model against numerical model and [3].

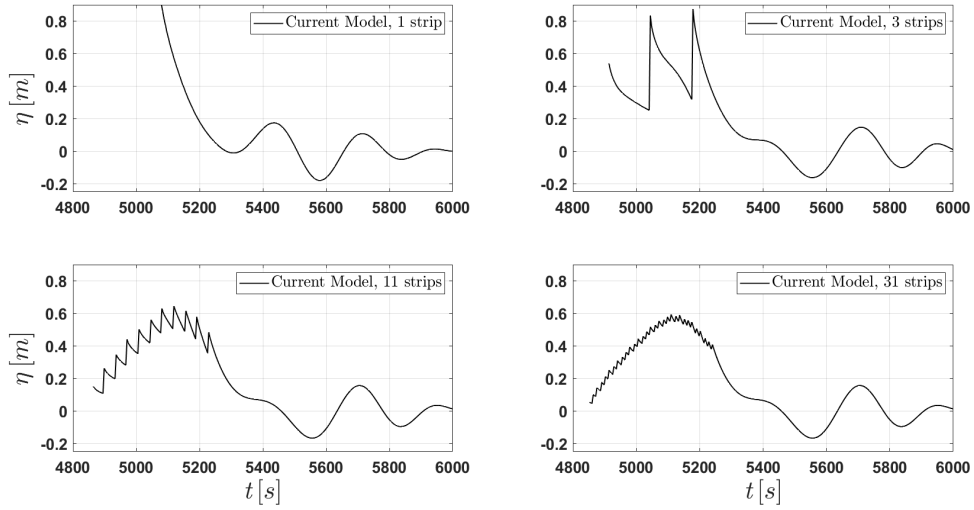

Figure 3.5: Surface elevation plots. Top left: one single fault, the singularity at the critical time is apparent. Top right: fault is now split into three parallel strips and the contributions from each added. Bottom left: At eleven strips the shape of the tsunami begins to form. Bottom right: At thirty-one strips the tsunami's shape is now apparent. The curve can be be further enhanced utilising a standard Matlab smoothing function.

At times approaching the critical time $\tilde{t}_c = \tilde{x}$ the solution is not valid, due to constraints arising from the limitations of the method of stationary phase and approximations made in calculating stationary points [3]. In this case the numerical model predicts a tsunami of peak amplitude approximately 0.6 m arriving at the critical time $\tilde{t}_c$. Unfortunately all of the analytic models have a singularity at times approaching the critical time. However, by splitting up the fault into a few parallel strips (say ≥ 10), each strip has a shift in the critical time which allows calculating the contribution of most of the fault at all times. To illustrate this process Figure 3.5 shows the surface elevation plot resulting from first a single fault, then breaking the original fault into three, eleven and finally thirty-one strips and adding their contributions. At thirty-one strips the outline of the tsunami can be seen. A further step making use of a standard Matlab smoothing function results in the plot displayed in Figure 3.4b. Thus, the general compressible solution can capture the main peak at $\tilde{t}_c$ - see Figure 3.4b which serves to further validate the linear multi-fault approach.

3.4.3 Theoretical solution vs. Mild Slope Equation

In the previous Section, the theoretical solutions for bottom pressure (3.3.82) have been validated against [3] where the solutions exist for an infinite fault problem ($y = 0$). Here,

the bottom pressure, calculated by the theory is validated against numerical simulations based on the Mild Slope Equation for weakly compressible fluids [23], not only for points lying on the x axis, but also for $y \neq 0$. The results are shown in Figure 3.6 for a fault with dimensions of L = 100 km, b = 10 km and rise time of $2T$ = 10 s, with residual displacement of ζ = 1 m. As y increases, especially for $y \gg L$, the signals become smaller as expected.

The statistics for the plots of Figure 3.6 are presented in Tables 3.2 and 3.3. Taking the dominant mode #1 and comparing the ranges we see agreement between theory and numerical model to better than 0.5%. The peaks occur in each plot before t = 1400 s. The trailing portion of each plot becomes less valid as time progresses due to elasticity of the seabed being neglected in this case - see Section 4.6.3.

Theory	**1**	**2**	**3**	**4**	**5**	**6**	**7**	**8**
Min	-18.0578	-3.4108	-1.8057	-1.2256	-16.6167	-2.7596	-1.5287	-1.0612
Max	17.9549	3.4286	1.7933	1.2101	16.6723	2.743	1.531	1.0619
Mean	0	0	0	0	0	0	0	0
Std	2.1253	1.0455	0.69	0.4281	2.0204	0.9	0.5678	0.3247
Range	36.0126	6.8394	3.5991	2.4357	33.289	5.5025	3.0597	2.1231

Table 3.2: Statistics for the eight pressure plots predicted by the Theory - see Figure 3.6.

Numerical	**1**	**2**	**3**	**4**	**5**	**6**	**7**	**8**
Min	-17.9845	-3.5659	-1.6258	-1.0183	-16.1535	-2.7429	-1.2852	-0.9312
Max	17.9132	3.5381	1.6208	1.0121	16.256	2.7447	1.2836	0.9212
Mean	0	0	0	0	0	0	0	0
Std	3.6434	0.8404	0.3453	0.2176	3.4524	0.6991	0.2919	0.1688
Range	35.8977	7.104	3.2466	2.0304	32.4095	5.4876	2.5688	1.8524

Table 3.3: Statistics for the eight pressure plots predicted by the Numerical Model - see Figure 3.6.

3.5 Multi-fault rupture

Hamling et al., [28] discussed a fault that occurred on 14^{th} November 2016 in Kaikōura New Zealand. This event was reported as a "complex multi-fault rupture" - complex in the sense that at least 12 major crustal faults and extensive uplift along much of the coastline were observed. The rupture jumped between faults located up to 15 km away from each other, and individual sub-faults showed both positive and negative displacements as well as translational slipping.

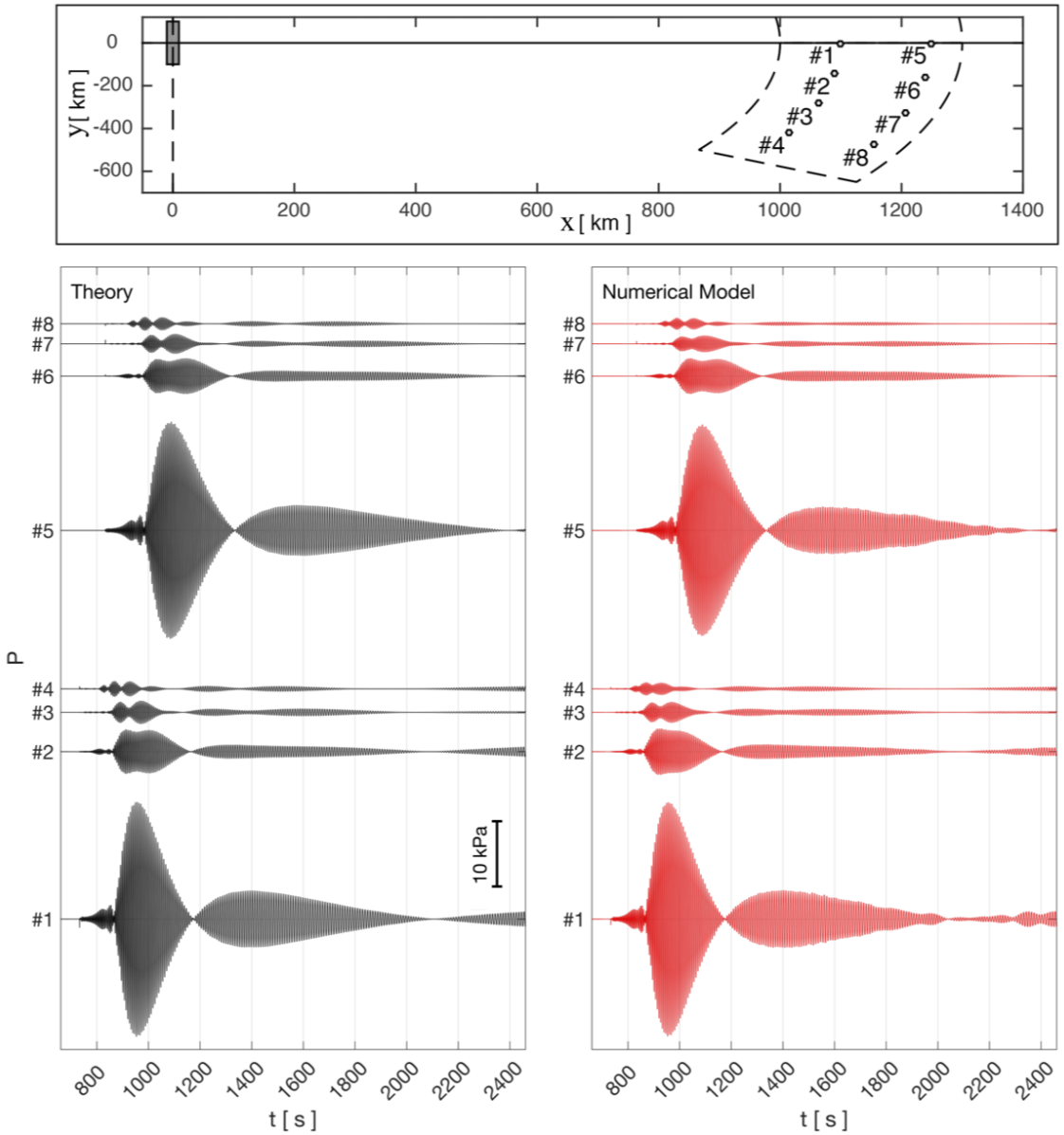

Figure 3.6: (Upper) indicates the fault dimensions (L = 100 km and b = 10 km), the numerical domain extent and the coordinates of the virtual point observations. The time series of bottom pressure calculated from the current model (black) and extracted from the numerical model (red). Only the first mode is considered in order to keep computation time manageable.

The theory developed in Section 3.3 is extended here to more complex situations, where two, or more, slender faults can be combined by linear superposition. Each fault may have its own uplift duration and velocity, as well as dimension and orientation. To take account of multiple faults relative to a reference time and location, the acoustic–gravity wave component of expression (3.3.82) is modified as

$$P = \sum_{i=1}^{M}\sum_{n=1}^{N} \frac{\rho_l W_{0,i}}{\pi}|A_{i,n}|\frac{8\mu_n \sin(K_{i,n}b_i)\sin(\Omega_{i,n}T_i)\cos(\mu_n z)}{K_{i,n}^2\left[2\mu_n h+\sin\left(2\mu_n h\right)\right]}\left[\frac{2\pi}{\frac{x_i}{C_l}\frac{\omega_n^2}{\left(\Omega_{i,n}^2-\omega_n^2\right)^{\frac{3}{2}}}}\right]^{\frac{1}{2}} \times \cos\left(K_{i,n}|x|-\Omega_{i,n}t(\bar{t})-\frac{\pi}{4}+\Theta_{A_{i,n}}\right), \tag{3.5.92}$$

where i indexes the faults up to a maximum of M faults and $t(\bar{t})$ is defined as

$$t(\bar{t}) = H(\bar{t}-\Delta_i)(\bar{t}-\Delta_i). \tag{3.5.93}$$

H is the Heaviside step function, $\bar{t}=0$ is the time of the first fault movement, and Δ_i is the time lag for each individual fault relative to that of the first moving fault.

Consider a hydrophone located on the seabed ($z=0$) and to the right of a cluster of faults as shown in Figure 3.7. Then the (x,y) location of the hydrophone in each fault's co-ordinate system is given by

$$x_i = -r_i\cos(\theta_i-\alpha_i), \qquad y_i = -r_i\sin(\theta_i-\alpha_i), \tag{3.5.94}$$

where r_i is the distance between the hydrophone and the centroid of the i^{th} fault, θ_i is the angle between the positive x axis at the hydrophone and the centroid of the i^{th} fault, α_i is the strike angle of the i^{th} fault.

3.5.1 Multi-fault examples

[28] does not contain information on multi-fault geometries and timings etc. that would facilitate a validation exercise, so to link the current model with real data we refer the reader to [12] and [29]. The first paper discusses the Sumatra 2004 tsunami, and we use this to investigate agreement between the developed theory and a numerical model for acoustic–gravity waves (constant and variable depth). Since the DART network was not available at that time, we could not reliably validate the surface wave using the Sumatra

event. Satellite records of surface displacement are available for Sumatra 2004 [42], but these vary in both time and space, as the satellite moves across the Indian ocean, and thus introduce unnecessarily delicate challenges. Instead, we opted to use the Tohoku 2011 event [29] as reference for the surface wave validation where reliable data via the DART network is available. The DART buoys benefit from being at fixed locations while recording their time series of surface elevations.

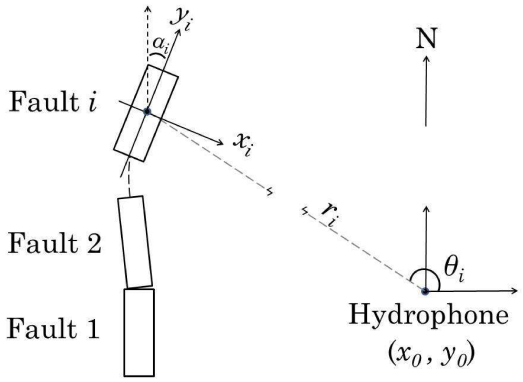

Figure 3.7: Location and orientation of a slender fault cluster relative to a hydrophone - axes and orientation of the i^{th} fault indicated.

3.5.1.1 Tohoku 2011 - surface elevation

[29] investigated the surface gravity and acoustic–gravity wave fields produced by the megathrust Tohoku 2011 tsunamigenic event. The surface deflections generated by this event were recorded by the DART network deployed by NOAA (National Oceanic and Atmospheric Administration). The event occurred at 14:46 local time (JST) [29], with the tsunami waves arriving at DART buoy 21418 located at 38.735 N, 148.655 E (NOAA web-site) approximately 30 minutes later [29]. This buoy lies at a distance of about 500 km east of the epicentre, and is a good candidate for testing the surface elevation predictions made by the current model. The parameters used in the model were derived from a variety of sources (see Table 3.4). The dimensions of the fault were obtained from Encyclopædia Britannica[27]

The coordinates of DART buoy 21418 referenced to the epicentre were calculated using the Haversine formula which calculates the geodesic distance between two points on a sphere given their longitudes and latitudes. The depth used for the calculation was

[27] `https://www.britannica.com/event/Japan-earthquake-and-tsunami-of-2011`

an average (constant) value derived from a Google Earth transect between the epicentre and the DART buoy location (Figure 3.8a). The strike angle α was taken from [43], and finally the uplift and rupture duration were estimated using Figure 3 of [29]. From this figure it can be seen that the majority of the uplift had already occurred by 90 seconds after t_0 - the start of the rupture. The maximum uplift was 11.35 m [29].

Constant	Description	Value
g	Acceleration due to gravity	$9.81\ \mathrm{ms}^{-2}$
L	Fault half-length	150 km
b	Fault half-width	75 km
$2T$	Rupture duration	90 s
h	Water depth	5277 m
C_l	Speed of sound in water	$1500\ \mathrm{ms}^{-1}$
ζ_0	Uplift	7 m
r	Distance from epicentre	496.6 km
θ	Angle to epicentre	$183.555°$
α	Strike angle of fault	$-13°$

Table 3.4: Constants and parameters used in the calculation of predicted surface elevation at DART buoy 21418 for Tohoku 2011 event.

By employing the multi-fault approach to this rupture, it was possible to capture both the amplitude and timing of the leading tsunami. A "kink" in the model waveform is visible located at approximately $t = 2400$ s, this is due to the singularities involved in the method as discussed in Section 3.4.3. The model over-predicts the trailing waveform ($t > 2500$ s).

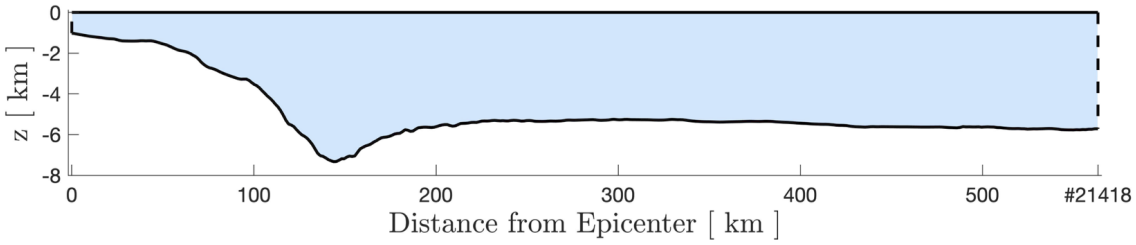

(a) Depth transect between Tohoku epicentre and DART buoy 21418

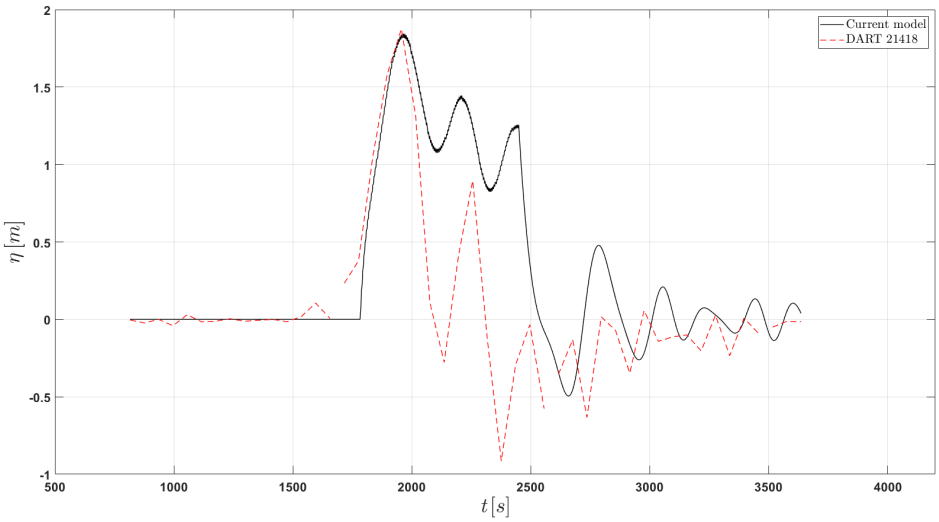

(b) Surface elevation comparison between current model (general compressible) and data recorded by DART buoy 21418 (red trace) for Tohoku 2011 event.

Figure 3.8: Comparison of current model against DART buoy data for Tohoku 2011.

3.5.1.2 Sumatra 2004 - acoustic–gravity waves

Figures 3.10 and 3.11 present results of a comparison made between the (linear) current model and a depth integrated numerical model applied to Sumatra 2004. Details of the parameters used in the model are summarised in Table 3.5.

Computation of the bottom pressure field is for the region to the left of the dashed line shown in Figure 3.9. Both the time series of Figure 3.10 and the pressure maps of Figure 3.11 demonstrate agreement between theory and numerics at constant depth. Introduction of variable depth leads to the expected discrepancies between theory and the numerical model. However, even in the variable depth case, most of the important physics can be captured using the model.

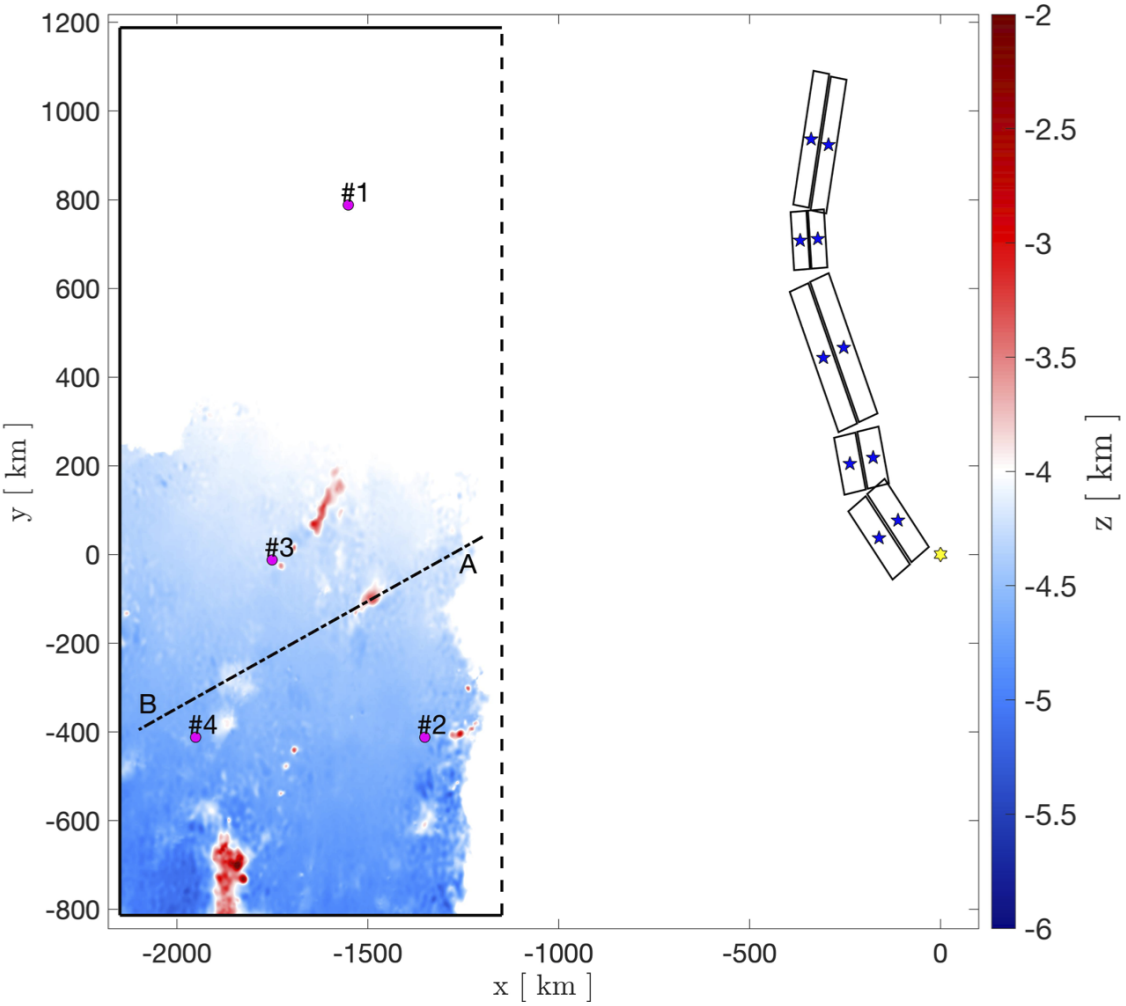

Figure 3.9: Overview of area considered for the bottom pressure map. The section to the left of the black dashed line is that used in the calculations for Figure 3.11. The origin of x, y co-ordinates is at the earthquake epicentre (yellow star). Fault centroids are shown by blue stars and the faults delineated by rectangles. Depth below sea-level is indicated by the colour bar with the white areas at 4 km depth. The four points used to construct the time series of Figure 3.10 are labelled #1, #2, #3 and #4. The transect AB is shown with dashed line.

Parameter	Fault 1,2	Fault 3,4	Fault 5,6	Fault 7,8	Fault 9,10
longitude	94.57°	93.90°	93.21°	92.60°	92.87°
latitude	3.83°	5.22°	7.41°	9.70°	11.70°
Δ	0 s	212 s	528 s	853 s	1213 s
L	110 km	75 km	195 km	75 km	175 km
b	65 km	65 km	60 km	47.5 km	47.5 km
$2T$	60 s	60 s	60 s	60 s	60 s
ζ odd	7.02 m	8.59 m	4.72 m	4.49 m	4.60 m
ζ even	-3.27 m	-3.84 m	-2.33 m	-2.08 m	-2.31 m
W_0 odd	0.1170 ms^{-1}	0.1432 ms^{-1}	0.0787 ms^{-1}	0.0748 ms^{-1}	0.0767 ms^{-1}
W_0 even	-0.0545 ms^{-1}	-0.0640 ms^{-1}	-0.0388 ms^{-1}	-0.0347 ms^{-1}	-0.0385 ms^{-1}
α	37°	12°	22°	4°	$-10°$

Table 3.5: Parameters used for Sumatra 2004 event - ten faults in total. Includes ζ - the vertical displacement.

In Figure 3.12 we can see the superposition of pressure signals emanating from multiple slender faults with differing orientations, resulting in areas of high pressure, and areas where the signal is weaker. The pressure contours of column three in Figure 3.11 and the third column of Figure 3.12 highlight the missing processes of refraction, diffraction and interference induced by the variable sea depth and areas of localised elevation (red coloured areas Figure 3.9), with refraction dominating all modes in deep water [27]. In Figure 3.9 there is a transect with a sea-mount located approximately one third of the way along AB. The depth profile for this transect is shown at the top of Figure 3.13. Also shown in Figure 3.13 are pressure signals along the transect for three different times. The variable depth case (red trace) shows attenuation of the signal for points along the transect past 400 km (i.e. just after the sea-mount). This shadowing effect is also apparent in Figure 3.12 where the sea-mount is to be found at approximately $x = -1500$ km, $y = -100$ km. More generally acoustic–gravity waves propagating into shallow sea depth experience frequency filtering by the water layer [33, 44]. Low order modes are associated with smaller critical depths and are therefore able to propagate further onshore [26, 27]. These results confirm that changing sea depth cannot be ignored when making these calculations, since it affects the timing and scale of the signals measurable at any particular point. For instance, in the placement of hydrophones the water should be of a depth so as to enable recording of a large frequency range [29, 44].

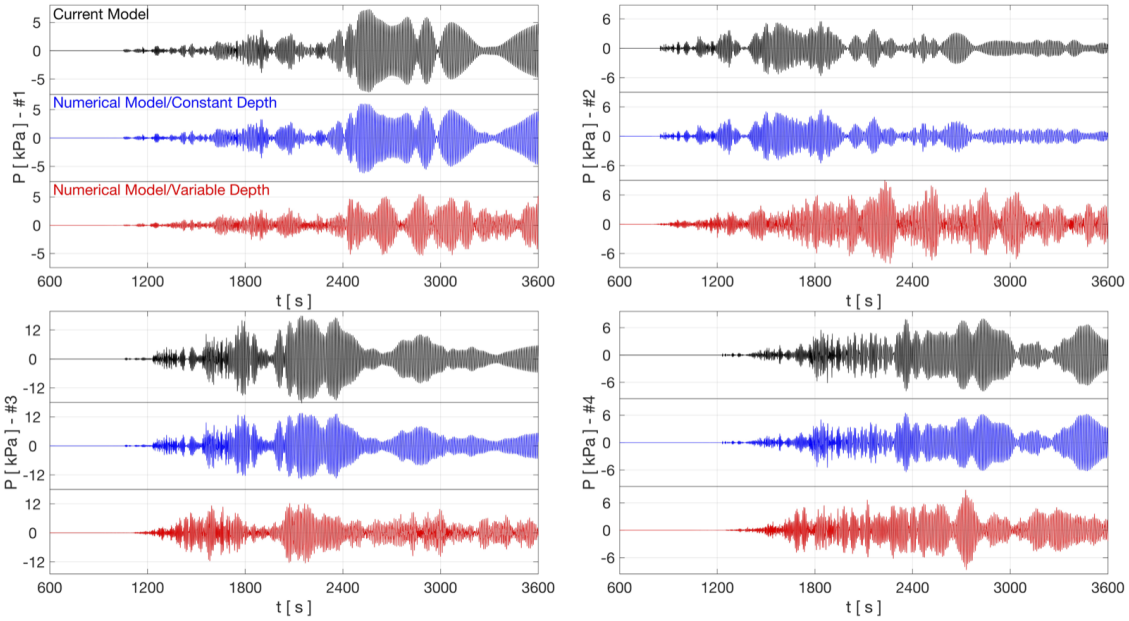

Figure 3.10: Dynamic pressure time series for points #1, #2, #3 and #4 (from Figure 3.9). The black trace is the current model (constant depth), the blue trace is a depth integrated numerical model (constant depth), the red trace is depth integrated numerical but with variable depth.

3.5.2 Displacement function

Aside from linear bottom displacement function (Eq. 3.2.13), the sensitivity of surface gravity and acoustic waves are investigated numerically for a half-sine (Eq. 3.5.95) and an exponential (Eq. 3.5.96) bottom displacement function as shown in the upper panel of Figure 3.14 [45]:

$$\zeta_s(x,y,t) = \zeta_0\left[\frac{1}{2}\left(1-\cos\frac{\pi t}{T}\right)H(T-t)+H(t-T)\right]H(b^2-x^2)H(L^2-y^2) \tag{3.5.95}$$

$$\zeta_e(x,y,t) = \zeta_0(1-\mathrm{e}^{-\alpha t})H(b^2-x^2)H(L^2-y^2) \tag{3.5.96}$$

where H is the Heaviside step function, ζ_0 is the residual displacement and α is a decay constant. For exponential displacement, $\zeta_e(t=T) = 2\zeta_0/3$ or $T = 1.11/\alpha$.

The linear and exponential displacement functions result in very similar surface elevation plots, whereas their associated acoustic–gravity wave plots show a difference in amplitude, with the exponential displacement function delivering a smaller amplitude. The surface elevation predicted by the current model (general compressible) for a linear displacement function is also shown.

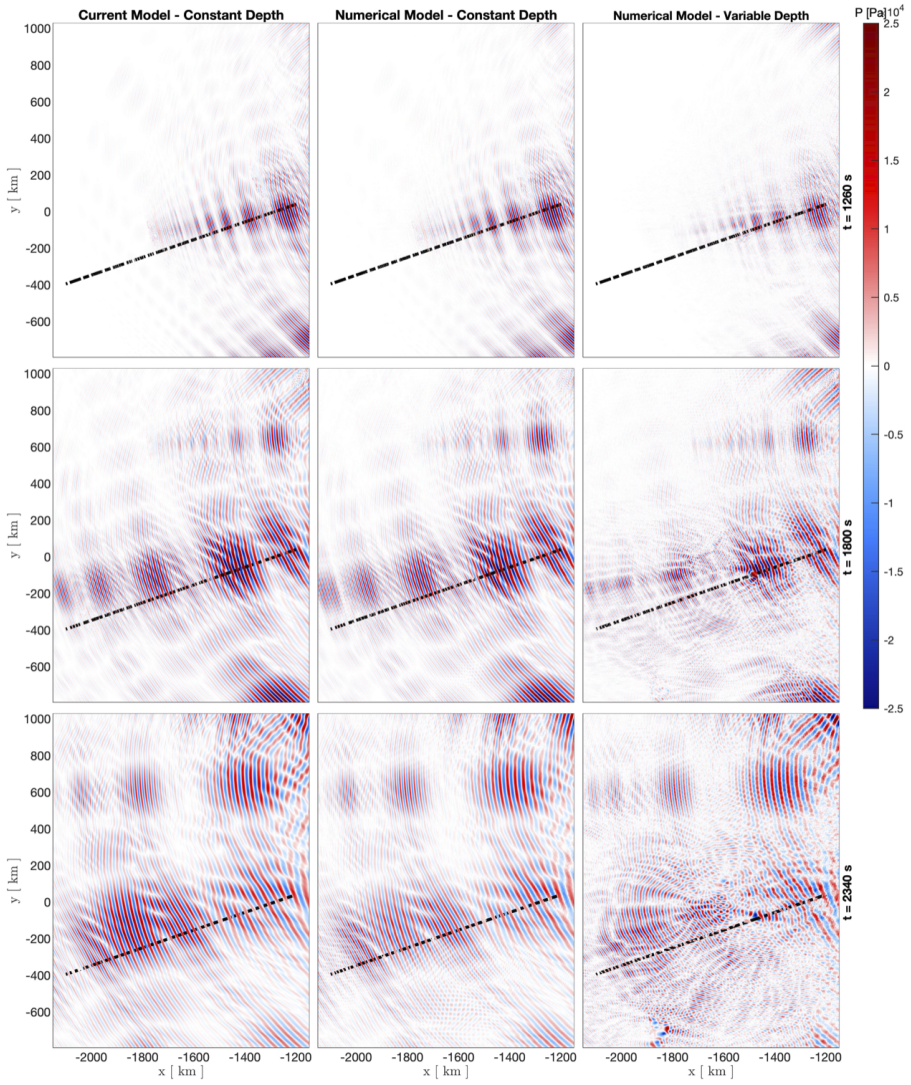

Figure 3.11: Snapshots of bottom pressure fields at t=1260 s (top row), t=1800 s (middle row) and t=2340 s (bottom row) from the current model, Eq. (3.5.92) (left column), numerical model for the case of constant depth of 4 km (middle column) and numerical model for the case of variable depth (right column). The domain extent is shown in Figure 3.9 and the boundary forcing is imposed along the dashed line - also Figure 3.9. The dynamic pressure variation is indicated with reference to the colour bar where white corresponds to 0 Pa. The transect AB is shown with dashed line in each subplot.

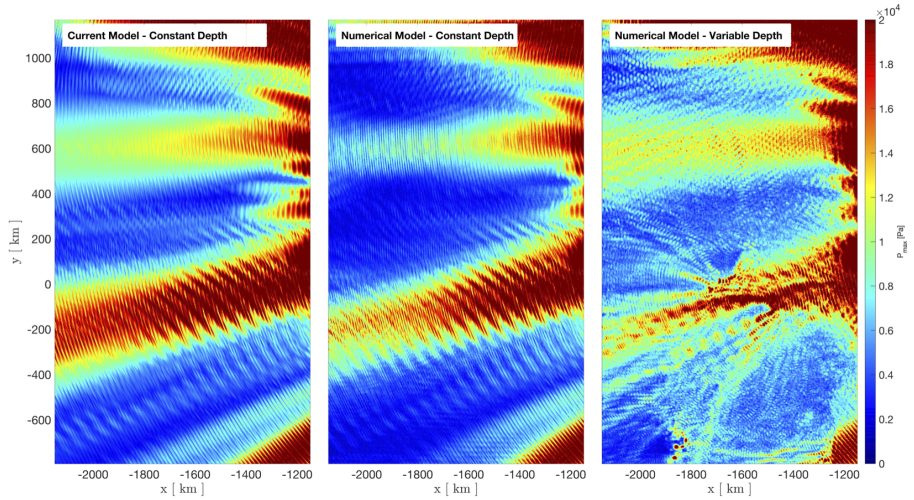

Figure 3.12: Maximum absolute values of the bottom pressure (P) of the acoustic wave generated by the Sumatra 2004 event during the first hour since rupture.

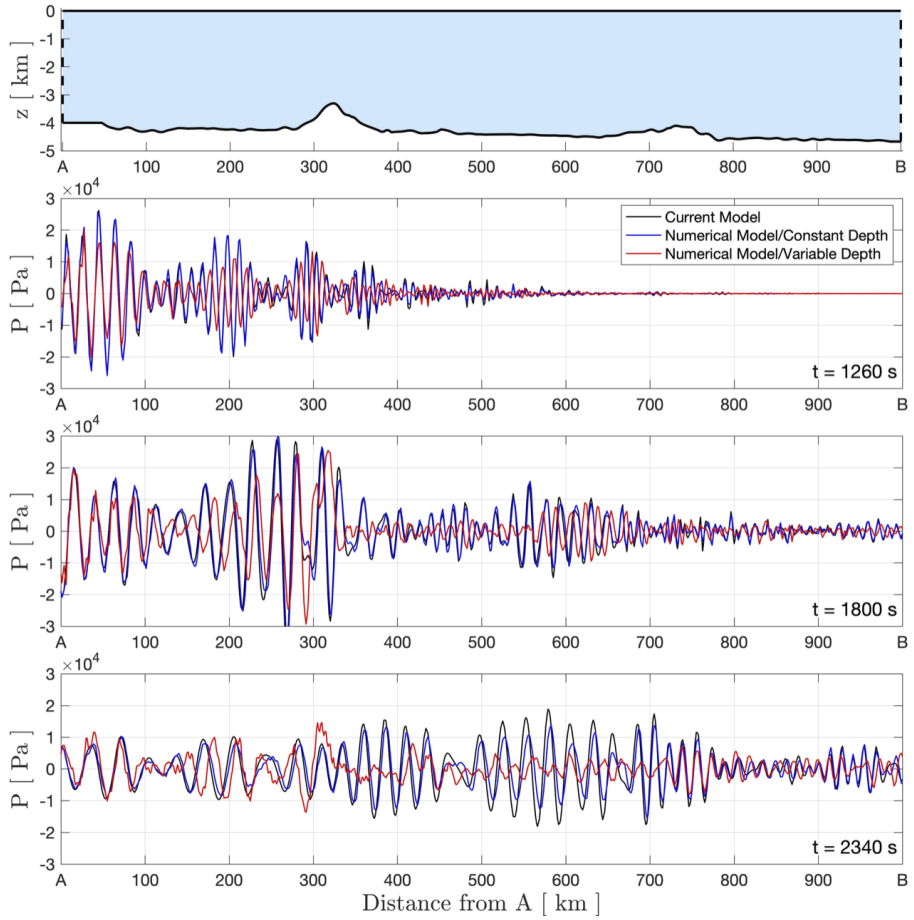

Figure 3.13: (Upper) The ocean profile along section AB (as shown in Figures 3.9 and 3.11). Bottom pressure anomalies along transect AB at t = 1260, 1800 and 2340 s from the current model (black), numerical model with constant depth (blue) and numerical model with variable depth (red).

The half-sine displacement function shows a marked difference in surface elevation amplitude when compared to either of the linear, or the exponential displacement functions - approximately 50%. Since energy is proportional to the square of the amplitude this would imply the energy content of the half-sine surface wave to be around one-quarter that of the other two. The half-sine displacement function is the only one of the three to have a smooth transition in velocity at $t = 0$, yet has the greatest acceleration - see Figure 3.15. The amplitude of the acoustic–gravity wave produced in this case ends up one order of magnitude larger (by $t = 1600$ s) than either of the linear or exponential cases (energy content 100 times greater), suggesting that energy is directed towards producing a larger acoustic–gravity wave at the expense of the surface wave. One could speculate that the acoustic–gravity waves are more sensitive to accelerations than the surface wave, but more work would be needed to establish this. Also. care is needed in interpreting these results since when the seabed is rigid the magnitude of the acoustic–gravity wave oscillations continue to increase with time in an unphysical way - see Section 4.6.3.

3.6 Discussion

The separation of scales between acoustic and gravity waves indeed suggests analysing each wave type separately, as reported in literature. Such separation allows a comprehensive, but simplified study compromising the accuracy only slightly. However, such compromise may lead to a two-fold negative impact on the implementation of a reliable TEWS. The first, is that reducing the uncertainties is critical in the inverse problem, which can be done, with the model without adversely affecting the calculation time. The second is that an inverse approach that employs pure acoustic theory only can initially provide properties of the fault, but then calculations of the rising tsunami need to be carried out. Our model enables simultaneous calculation of all acoustic–gravity modes, including the rising gravity mode (tsunami), thus minimising the calculation time.

The current model includes a constant water depth assumption, which has implications that cannot be ignored. While the model can estimate the tsunami in the deep water, it may not be effective in describing the propagation over varying bathymetry and the shelf break for two principal reasons. The first lies in the assumption of constant depth, and thus effective techniques that take into account changes due to topography without computing the whole 3D domain need to be developed. The second reason is seabed elasticity, which turns out to be important for both tsunami and acoustic–gravity wave arrival times [46].

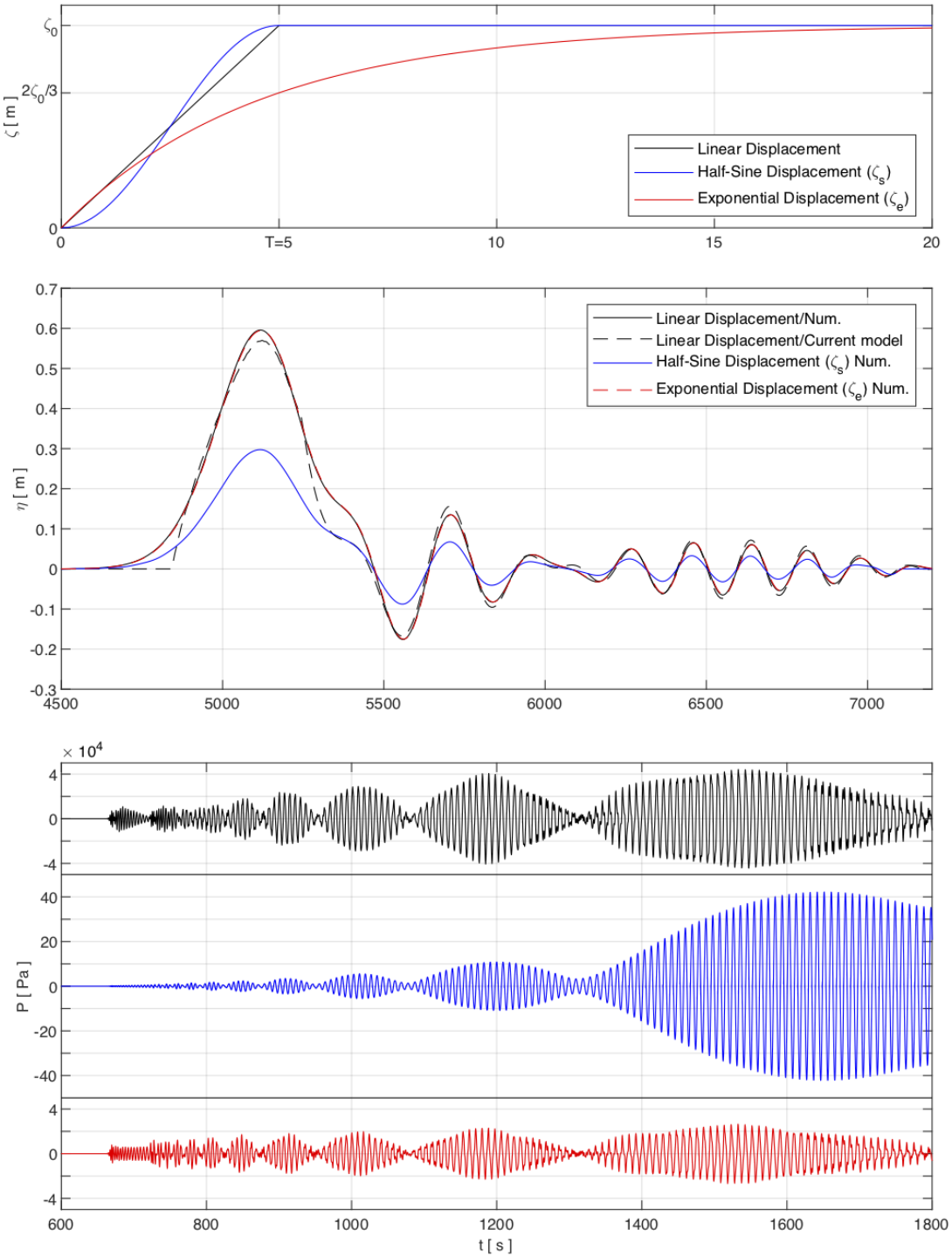

Figure 3.14: (Upper) The time series of bottom displacement for linear, half-sine (ζ_s) and exponential (ζ_e) functions. (Middle) The time series of surface elevation (η); and (Lower) Bottom Pressure signals. Coordinates are x= 1000 km, y = 0 km.

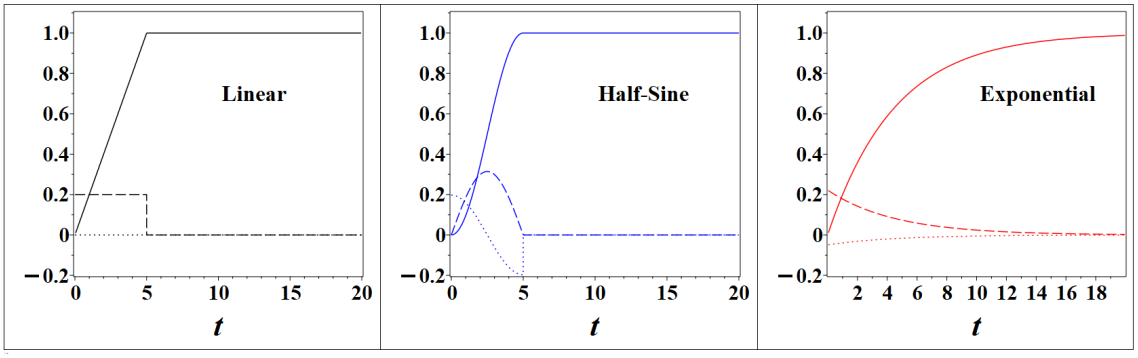

Figure 3.15: The left panel shows linear displacement function. The middle panel is the half-sine function and the right panel is the exponential function. Displacements are solid trace, velocities are dash trace and accelerations are dots. The half-sine function has the greatest acceleration of the three.

For the tsunami, neglecting elasticity results in overestimation of the phase speed [47, 26, 48, 49]. The effect is even more dramatic for acoustic–gravity waves as they can couple to the elastic seabed-floor and travel at speeds reaching $3900\,\mathrm{ms}^{-1}$ which significantly changes their arrival time [25]. The issue of how elasticity of the seabed modifies the behaviour of the propagating acoustic–gravity waves and surface waves is addressed in the next chapter.

Chapter 4

Acoustic–gravity & surface waves due to slender rupture in elastic seabed[1]

4.1 Introduction

Chapter 3 extended the work of [16] from a purely acoustic description of a slender fault rupture into one that now includes the surface wave components as well. Also developed was the idea of a multi-fault whereby more complex fault arrangements can be constructed from single slender faults by superposition. However, the seabed thus far has been regarded as rigid, although it is known that the elastic properties of the solid medium should not be ignored [46, 20]. Water compressibility and seabed elasticity affect the phase speed of surface waves, and thus the arrival times of trans-oceanic tsunamis [20].

A complementary work [25] investigated the consequences of imposing an elastic seabed as support for a liquid layer residing in a gravitational field upon the form of the dispersion relation. The inclusion of an elastic seabed, as opposed to a rigid one, results in modification of the boundary conditions at the seabed. In this setting the dispersion relation has a more complicated form, and the acoustic–gravity waves are able to enter shallower water before dissipating into the elastic medium. In stark contrast to the rigid-seabed case the first acoustic mode is able to propagate as a Scholte wave to the shore, where it then becomes a Rayleigh wave [25]. A Scholte wave (also known as a seismic interface wave) is a wave propagating along the interface between two media with different shear speeds, such as the interface between the seabed and the water. When propagating

[1] [2]

on the free surface of a solid the wave is referred to as a Rayleigh wave [50].

Note that no rupture was considered in [25]. The primary objective of this chapter is to combine the ground movement of rectangular slender faults with an elastic seabed, in order to study the contribution of elasticity to the propagation of both acoustic–gravity waves and surface waves. The results of this chapter should help fill a gap in the literature identified within [27] in which the authors claim solutions for acoustic–gravity waves produced by disturbances over an elastic seabed in 3D are missing from the literature.

Another difference encountered when studying the elastic case is that rather than the single surface gravity wave (found in rigid seabed analysis) there is now the possibility of two surface gravity waves [30]. There is the usual tsunami (referred here as mode 01), and another mode of negligible amplitude which does not propagate for all frequencies (referred here as mode 00 [30]). In the study of the acoustic–gravity waves propagating over an elastic seabed, we find that important information relating to the fault geometry and dynamics can be extracted from the acoustic signal. Also in this chapter we derive improved estimates for the acoustic–gravity wave critical frequencies, estimating the cut-off frequency for the second surface wave (mode 00), and presentation of a method for rapid calculation of approximate phase velocity curves which may be useful in developing a real time tsunami early warning system. We ignore terms of second order and higher (i.e. non-linear terms) since the free surface displacements are small in comparison with the water depth [37], and also small in comparison with the wavelengths considered [51]. In addition the gravity term that is present in the full wave equation is omitted because its contribution is small (see Figure 2 of [20]).

This chapter comprises seven main sections. The mathematical formulation combining ground movement with elasticity is found in Section 4.2, with its solution in Section 4.3. Section 4.4 presents improved approximations for the acoustic–gravity wave cutoff frequencies, and an estimate of the cutoff frequency for the mode 00 surface wave. Section 4.5 proposes a method for rapid calculation of approximate phase velocity curves which does not necessitate solution of the dispersion relation at each data point. Section 4.6 links the developed theory to numerical results obtained from both synthetic stimulus, and real data from hydrophone, seismograph and DART buoys. The chapter concludes with the discussion in Section 4.7.

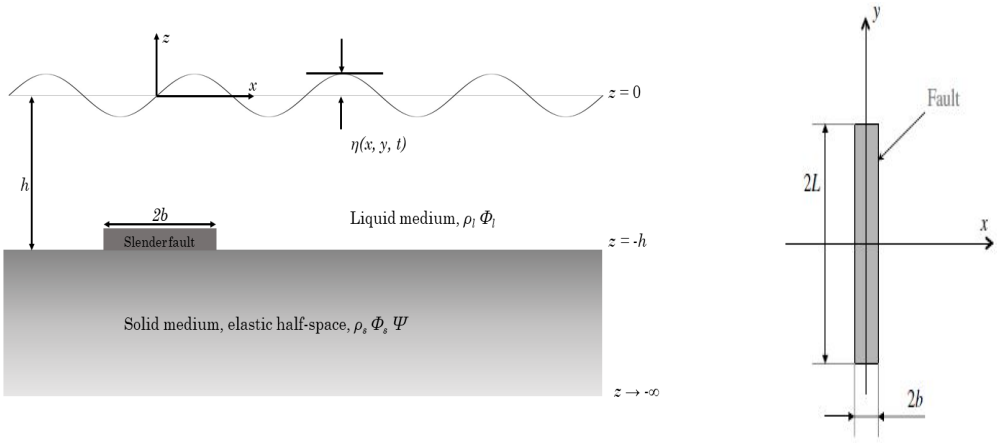

(a) Cross section through x, z plane. Water depth is h, surface elevation is $\eta(x, y, t)$, liquid velocity potential is ϕ_l, solid dilation potential is ϕ_s and solid rotation potential is Ψ. Densities in the liquid and solid medium are ρ_l and ρ_s respectively.

(b) Top view of slender fault

Figure 4.1: Representation of the flow domain.

4.2 Governing equations

The water layer is considered inviscid, homogeneous, of constant depth h, residing in a gravitational field of constant acceleration $9.81\,\mathrm{ms}^{-2}$. The water layer is assumed unbounded in x and y and is supported by an infinitely deep elastic half-space. The origin of coordinates is taken at the unperturbed free surface directly above the centroid of the slender fault, with the z axis pointing vertically upwards. Assuming irrotational flow the problem is expressed in terms of a velocity potential function for the liquid ϕ_l, along with a dilation potential ϕ_s and rotation potential Ψ for the solid layer (note that the subscript s was omitted from Ψ since it only exists in the solid.). As in [25] we make use of linearised, irrotational flow for the liquid and linear elasticity for the solid. A representation of the flow domain is given in Figure 4.1a with a top view of the slender fault in Figure 4.1b. With $\mathbf{i}, \mathbf{j}, \mathbf{k}$ as unit vectors the velocity in the liquid is given by,

$$\dot{\mathbf{U}}_l = -\nabla\phi_l = \dot{u}_l\mathbf{i} + \dot{v}_l\mathbf{j} + \dot{w}_l\mathbf{k} = -\frac{\partial\phi_l}{\partial x}\mathbf{i} - \frac{\partial\phi_l}{\partial y}\mathbf{j} - \frac{\partial\phi_l}{\partial z}\mathbf{k}, \tag{4.2.1}$$

which implies

$$\dot{u}_l = -\frac{\partial\phi_l}{\partial x}, \quad \dot{v}_l = -\frac{\partial\phi_l}{\partial y}, \quad \dot{w}_l = -\frac{\partial\phi_l}{\partial z}. \tag{4.2.2}$$

The solid displacements are then

$$\mathbf{U}_s = \nabla\phi_s + \nabla\times\Psi = u_s\mathbf{i} + v_s\mathbf{j} + w_s\mathbf{k}, \tag{4.2.3}$$

$$u_s = \frac{\partial\phi_s}{\partial x} + \left(\frac{\partial\psi_z}{\partial y} - \frac{\partial\psi_y}{\partial z}\right),\ v_s = \frac{\partial\phi_s}{\partial y} + \left(\frac{\partial\psi_x}{\partial z} - \frac{\partial\psi_z}{\partial x}\right),\ w_s = \frac{\partial\phi_s}{\partial z} + \left(\frac{\partial\psi_y}{\partial x} - \frac{\partial\psi_x}{\partial y}\right). \tag{4.2.4}$$

The potentials are governed by three wave equations. In the liquid region

$$\frac{\partial^2\phi_l}{\partial x^2} + \frac{\partial^2\phi_l}{\partial y^2} + \frac{\partial^2\phi_l}{\partial z^2} = \frac{1}{C_l^2}\frac{\partial^2\phi_l}{\partial t^2},\quad -h \le z \le 0, \tag{4.2.5}$$

where C_l is the speed of sound in water. In the solid region

$$\frac{\partial^2\phi_s}{\partial x^2} + \frac{\partial^2\phi_s}{\partial y^2} + \frac{\partial^2\phi_s}{\partial z^2} = \frac{1}{C_p^2}\frac{\partial^2\phi_s}{\partial t^2},\quad z \le -h, \tag{4.2.6}$$

$$\frac{\partial^2\Psi}{\partial x^2} + \frac{\partial^2\Psi}{\partial y^2} + \frac{\partial^2\Psi}{\partial z^2} = \frac{1}{C_s^2}\frac{\partial^2\Psi}{\partial t^2},\quad z \le -h, \tag{4.2.7}$$

where C_p and C_s are the pressure and shear wave velocities respectively

$$C_p = \sqrt{\frac{1}{\rho_s}\left(\lambda + 2\mu\right)},\quad C_s = \sqrt{\frac{\mu}{\rho_s}}, \tag{4.2.8}$$

λ, μ are Lamé constants and ρ_s is the density of the solid. At the free-surface we have the combined kinematic and dynamic boundary condition

$$\frac{\partial^2\phi_l}{\partial t^2} + g\frac{\partial\phi_l}{\partial z} = 0,\quad z = 0. \tag{4.2.9}$$

In addition, there are four boundary conditions for the seabed. The first of these ensures the vertical component of velocity in the liquid matches that of the solid. The component w_s is the vertical component of the seabed motion when there is no rupture (as studied in [25]) and is small, (however $\partial w_s/\partial t$ may not be). The magnitude of w_s ranges from 10^{-6} m for microseisms, to 10^{-2} m for severe earthquakes [25].

$$\dot{w}_l = \frac{\partial w_s}{\partial t} + W(x,y,t),\quad z = -h. \tag{4.2.10}$$

The definition of $W(x,y,t)$ closely follows that in [16] and describes the motion of the rupture

$$W(x,y,t) = R(x,y)\tau(t),\quad z = -h, \tag{4.2.11}$$

$$R(x,y)=\begin{cases} W_0=\text{const} & |x|<b,\ |Y|<\mathscr{L} \\ 0 & \text{elsewhere} \end{cases},\quad \tau(t)=\begin{cases} 1 & -T<t<T \\ 0 & |t|>T \end{cases},\quad \mathscr{L}=\epsilon L. \tag{4.2.12}$$

The duration of the rupture is $2T$, the slender fault half-width is b, and the slender fault half-length is L. The slenderness parameter is then $\epsilon = b/L \ll 1$ - see Figure 3.1. Note that if there is no rupture i.e. $W(x,y,t)=0$, then the boundary condition (4.2.10) reduces to that of 25, (8a), $\dot{w}_l = \partial w_s/\partial t$. On the other hand, when the seabed is rigid, $w_s = 0$, and we recover the bottom boundary condition 16, (2.3), $\dot{w}_l = W(x,y,t) = -\partial\phi_l/\partial z$, but this time with a minus sign due to this chapter following the sign choices in 25, (1a, 1b).

The next boundary condition states that the axial stress σ_{zz} is equal in magnitude, but of opposite direction to the liquid pressure at the seabed

$$\sigma_{zz}=\lambda\left(\frac{\partial u_s}{\partial x}+\frac{\partial v_s}{\partial y}+\frac{\partial w_s}{\partial z}\right)+2\mu\frac{\partial w_s}{\partial z}=-P_l,\quad z=-h. \tag{4.2.13}$$

The remaining two boundary conditions define no shear on the seabed

$$\sigma_{xz}=\mu\left(\frac{\partial u_s}{\partial z}+\frac{\partial w_s}{\partial x}\right)=0,\quad \sigma_{yz}=\mu\left(\frac{\partial v_s}{\partial z}+\frac{\partial w_s}{\partial y}\right)=0,\quad z=-h. \tag{4.2.14}$$

The dynamic pressure and surface elevation are obtained from

$$P_l=\rho_l\frac{\partial\phi_l}{\partial t},\quad \eta=\frac{1}{g}\frac{\partial\phi_l}{\partial t}. \tag{4.2.15}$$

We also require ϕ_l, ϕ_s, Ψ and all derivatives to decay to zero as $x,y,t\to\pm\infty$, $z\to-\infty$.

4.3 Solutions

We introduce multiple-scale co-ordinates following [16]

$$x,z,t;X=\epsilon^2 x, Y=\epsilon y. \tag{4.3.16}$$

The wave equations (4.2.5), (4.2.6), and (4.2.7) can then be re-written as

$$\frac{\partial^2\phi_l}{\partial x^2}+2\epsilon^2\frac{\partial^2\phi_l}{\partial x\partial X}+\epsilon^2\frac{\partial^2\phi_l}{\partial Y^2}+\frac{\partial^2\phi_l}{\partial z^2}=\frac{1}{C_l^2}\frac{\partial^2\phi_l}{\partial t^2},\quad -h\le z\le 0, \tag{4.3.17}$$

$$\frac{\partial^2\phi_s}{\partial x^2}+2\epsilon^2\frac{\partial^2\phi_s}{\partial x\partial X}+\epsilon^2\frac{\partial^2\phi_s}{\partial Y^2}+\frac{\partial^2\phi_s}{\partial z^2}=\frac{1}{C_p^2}\frac{\partial^2\phi_s}{\partial t^2},\quad -\infty\le z\le -h, \tag{4.3.18}$$

$$\frac{\partial^2\Psi}{\partial x^2}+2\epsilon^2\frac{\partial^2\Psi}{\partial x\partial X}+\epsilon^2\frac{\partial^2\Psi}{\partial Y^2}+\frac{\partial^2\Psi}{\partial z^2}=\frac{1}{C_s^2}\frac{\partial^2\Psi}{\partial t^2},\quad -\infty\le z\le -h. \tag{4.3.19}$$

Let $\phi_l=\phi_{l0}(x,X,Y,z,t)+\epsilon^2\phi_{l2}(x,X,Y,z,t)$, with similar expressions for ϕ_s and Ψ then the perturbation equations at $O(\epsilon^0)$ describe the two dimensional problem of an infinitely long slender fault

$$\frac{\partial^2\phi_{l0}}{\partial x^2}+\frac{\partial^2\phi_{l0}}{\partial z^2}-\frac{1}{C_l^2}\frac{\partial^2\phi_{l0}}{\partial t^2}=0,\quad -h\le z\le 0, \tag{4.3.20}$$

$$\frac{\partial^2\phi_{s0}}{\partial x^2}+\frac{\partial^2\phi_{s0}}{\partial z^2}-\frac{1}{C_p^2}\frac{\partial^2\phi_{s0}}{\partial t^2}=0,\quad -\infty< z\le -h, \tag{4.3.21}$$

$$\frac{\partial^2\Psi_0}{\partial x^2}+\frac{\partial^2\Psi_0}{\partial z^2}-\frac{1}{C_s^2}\frac{\partial^2\Psi_0}{\partial t^2}=0,\quad -\infty< z\le -h. \tag{4.3.22}$$

At $O(\epsilon^2)$,

$$\frac{\partial^2\phi_{l2}}{\partial x^2}+\frac{\partial^2\phi_{l2}}{\partial z^2}-\frac{1}{C_l^2}\frac{\partial^2\phi_{l2}}{\partial t^2}=-\left\{\frac{\partial^2\phi_{l0}}{\partial Y^2}+2\frac{\partial^2\phi_{l0}}{\partial x\partial X}\right\},\quad -h\le z\le 0, \tag{4.3.23}$$

$$\frac{\partial^2\phi_{s2}}{\partial x^2}+\frac{\partial^2\phi_{s2}}{\partial z^2}-\frac{1}{C_p^2}\frac{\partial^2\phi_{s2}}{\partial t^2}=-\left\{\frac{\partial^2\phi_{s0}}{\partial Y^2}+2\frac{\partial^2\phi_{s0}}{\partial x\partial X}\right\},\quad -\infty\le z\le -h, \tag{4.3.24}$$

$$\frac{\partial^2\Psi_2}{\partial x^2}+\frac{\partial^2\Psi_2}{\partial z^2}-\frac{1}{C_s^2}\frac{\partial^2\Psi_2}{\partial t^2}=-\left\{\frac{\partial^2\Psi_0}{\partial Y^2}+2\frac{\partial^2\Psi_0}{\partial x\partial X}\right\},\quad -\infty\le z\le -h. \tag{4.3.25}$$

The fault motion, elastic properties and elastic dispersion relation are all captured at $O(\epsilon^0)$. Thus, the $O(\epsilon^2)$ boundary conditions for the liquid layer are those for rigid seabed and no fault motion:

$$\frac{\partial^2\phi_{l2}}{\partial t^2}+g\frac{\partial\phi_{l2}}{\partial z}=0,\quad z=0, \tag{4.3.26}$$

$$\frac{\partial\phi_{l2}}{\partial z}=0,\quad z=-h. \tag{4.3.27}$$

4.3.1 Leading order potential

By the double Fourier transforms $\overline{\mathscr{F}}=\int_{-\infty}^{\infty}\mathscr{F}e^{i\omega t}dt$, $\overline{\overline{\mathscr{F}}}=\int_{-\infty}^{\infty}\overline{\mathscr{F}}e^{-ikx}dx$, with ω the angular velocity and k the wave-number, equations (4.3.20), (4.3.21), (4.3.22) become

$$\frac{\partial^2\overline{\overline{\phi}}_{l0}}{\partial z^2}+\left(\frac{\omega^2}{C_l^2}-k^2\right)\overline{\overline{\phi}}_{l0}=0, \tag{4.3.28}$$

$$\frac{\partial^2 \overline{\overline{\phi}}_{s0}}{\partial z^2} + \left(\frac{\omega^2}{C_p^2} - k^2\right)\overline{\overline{\phi}}_{s0} = 0, \tag{4.3.29}$$

$$\frac{\partial^2 \overline{\overline{\Psi}}_0}{\partial z^2} + \left(\frac{\omega^2}{C_s^2} - k^2\right)\overline{\overline{\Psi}}_0 = 0. \tag{4.3.30}$$

Let E_1, E_2, D_1, D_2 be unknowns to be solved for, then the choice exists to select either $r^2 = \left(\frac{\omega^2}{C_l^2} - k^2\right)$, with $r \in \mathbb{R}$, leading to a trial solution for $\overline{\overline{\phi}}_{l0}$ in (4.3.28) of the form $\overline{\overline{\phi}}_{l0}(z) = E_1\cos(rz) + E_2\sin(rz)$, or to select $r^2 = \left(k^2 - \frac{\omega^2}{C_l^2}\right)$, leading to a trial solution of the form $\overline{\overline{\phi}}_{l0}(z) = E_1\cos(\mathrm{i}rz) + E_2\sin(\mathrm{i}rz)$, as in [25]. To maintain compatibility with [25] we choose $r^2 = \left(k^2 - \frac{\omega^2}{C_l^2}\right)$. For equations (4.3.29) and (4.3.30) we take $q^2 = \left(k^2 - \frac{\omega^2}{C_p^2}\right)$ and $s^2 = \left(k^2 - \frac{\omega^2}{C_s^2}\right)$. As in [25] r, q, and s are wave-numbers.

To arrive at a trial solution for (4.3.29) choose $\overline{\overline{\phi}}_{s0}(z) = D_1 \mathrm{e}^{qz}$, because $\overline{\overline{\phi}}_{s0}(z) \to 0$ as $z \to -\infty$ implies no terms involving e^{-qz}.

In order to obtain physical solutions in which solid displacements decrease with depth we must also have $s, q \in \mathbb{R}_{\geq 0}$. If this were not the case, then displacements would oscillate or increase with depth - [30]. By a similar argument $\overline{\overline{\Psi}}_0(z) = D_2 \mathrm{e}^{sz}\mathbf{j}$.

The boundary condition at $z = 0$ (leading order term) is

$$\frac{\partial^2 \phi_{l0}}{\partial t^2} + g\frac{\partial \phi_{l0}}{\partial z} = 0, \quad z = 0. \tag{4.3.31}$$

Then applying first Fourier transform gives

$$\int_{-\infty}^{\infty}\left(\frac{\partial^2 \phi_{l0}}{\partial t^2} + g\frac{\partial \phi_{l0}}{\partial z}\right)\mathrm{e}^{\mathrm{i}\omega t}\mathrm{d}t = 0 \tag{4.3.32}$$

$$\int_{-\infty}^{\infty}\frac{\partial^2 \phi_{l0}}{\partial t^2}\mathrm{e}^{\mathrm{i}\omega t}\mathrm{d}t + g\frac{\partial}{\partial z}\int_{-\infty}^{\infty}\phi_{l0}\mathrm{e}^{\mathrm{i}\omega t}\mathrm{d}t = 0 \tag{4.3.33}$$

$$\left[\frac{\partial \phi_{l0}}{\partial t}\mathrm{e}^{\mathrm{i}\omega t}\right]_{-\infty}^{\infty} - \mathrm{i}\omega\int_{-\infty}^{\infty}\frac{\partial \phi_{l0}}{\partial t}\mathrm{e}^{\mathrm{i}\omega t}\mathrm{d}t + g\frac{\partial \bar{\phi}_{l0}}{\partial z} = 0. \tag{4.3.34}$$

Assume $\phi_{l0} \to 0$ as $|t| \to 0$ and $|x| \to 0$ along with all derivatives, then the boundary term in (4.3.34) becomes zero, leaving

$$-\mathrm{i}\omega\left\{\left[\phi_{l0}\mathrm{e}^{\mathrm{i}\omega t}\right]_{-\infty}^{\infty} - \mathrm{i}\omega\int_{-\infty}^{\infty}\phi_{l0}\mathrm{e}^{\mathrm{i}\omega t}\mathrm{d}t\right\} + g\frac{\partial \bar{\phi}_{l0}}{\partial z} = 0. \tag{4.3.35}$$

Which reduces to

$$-\omega^2\bar{\phi}_{l0}+g\frac{\partial\bar{\phi}_{l0}}{\partial z}=0. \tag{4.3.36}$$

Since (4.3.36) does not contain any terms involving x after both Fourier transforms (4.3.31) becomes

$$-\omega^2\overline{\overline{\phi}}_{l0}+g\frac{\partial\overline{\overline{\phi}}_{l0}}{\partial z}=0,\quad z=0. \tag{4.3.37}$$

Similarly applying Fourier transforms to the first boundary condition at $z=-h$

$$\dot{w}_l=\frac{\partial w_s}{\partial t}+W(x,y,t),\quad z=-h. \tag{4.3.38}$$

Using leading order terms

$$w_{s0}=\frac{\partial\phi_{s0}}{\partial z}+\frac{\partial\psi_{0y}}{\partial x},\quad\text{and}\quad \dot{w}_{l0}=-\frac{\partial\phi_{l0}}{\partial z}, \tag{4.3.39}$$

$$-\frac{\partial\phi_{l0}}{\partial z}=\frac{\partial^2\phi_{s0}}{\partial t\partial z}+\frac{\partial^2\psi_{0y}}{\partial t\partial x}+W(x,y,t). \tag{4.3.40}$$

It is only necessary to apply the relevant transforms to the first three terms of (4.3.40) - the required transforms for $W(x,y,t)$ are already known from [16]. Assembling terms gives

$$-\frac{\partial\overline{\overline{\phi}}_{l0}}{\partial z}=-\mathrm{i}\omega\frac{\partial\overline{\overline{\phi}}_{s0}}{\partial z}+\omega k\overline{\overline{\psi}}_{0y}+\frac{4W_0\sin(kb)\sin(\omega T)}{k\omega},\quad z=-h. \tag{4.3.41}$$

The second boundary condition at $z=-h$ is $\sigma_{zz}=-P_l$

$$\sigma_{zz}=\lambda\left(\frac{\partial u_{s0}}{\partial x}+\frac{\partial w_{s0}}{\partial z}\right)+2\mu\frac{\partial w_{s0}}{\partial z}=-P_{l0}=-\rho_l\frac{\partial\phi_{l0}}{\partial t}, \tag{4.3.42}$$

with

$$u_{s0}=\frac{\partial\phi_{s0}}{\partial x}-\frac{\partial\psi_{0y}}{\partial z},\quad w_{s0}=\frac{\partial\phi_{s0}}{\partial z}+\frac{\partial\psi_{0y}}{\partial x}. \tag{4.3.43}$$

After application of both Fourier transforms we have

$$\lambda\left(-k^2\overline{\overline{\phi}}_{s0}+\frac{\partial^2\overline{\overline{\phi}}_{s0}}{\partial z^2}\right)+2\mu\left(\frac{\partial^2\overline{\overline{\phi}}_{s0}}{\partial z^2}+\mathrm{i}k\frac{\partial\overline{\overline{\psi}}_{0y}}{\partial z}\right)=\mathrm{i}\rho_l\omega\overline{\overline{\phi}}_{l0},\quad z=-h. \tag{4.3.44}$$

The third boundary condition at $z=-h$ is $\sigma_{xz}=0$

$$\frac{\partial u_{s0}}{\partial z}+\frac{\partial w_{s0}}{\partial x}=0. \tag{4.3.45}$$

After application of both Fourier transforms we have

$$2\mathrm{i}k\frac{\partial\overline{\overline{\phi}}_{s0}}{\partial z}-k^2\overline{\overline{\psi}}_{0y}-\frac{\partial^2\overline{\overline{\psi}}_{0y}}{\partial z^2}=0,\quad z=-h. \tag{4.3.46}$$

Finally the fourth boundary condition at $z=-h$ is $\sigma_{yz}=0$

$$\frac{\partial v_{s0}}{\partial z}+\frac{\partial w_{s0}}{\partial y}=0, \tag{4.3.47}$$

with

$$v_{s0}=0,\quad \text{and}\quad w_{s0}=\frac{\partial\phi_{s0}}{\partial z}+\frac{\partial\psi_{0y}}{\partial x}. \tag{4.3.48}$$

Again, after application of both Fourier transforms to (4.3.47) we arrive at

$$\frac{\partial^2\overline{\overline{\phi}}_{s0}}{\partial z\partial y}+\mathrm{i}k\frac{\partial\overline{\overline{\psi}}_{0y}}{\partial y}=0,\quad z=-h. \tag{4.3.49}$$

4.3.2 Transformed governing equations

Re-name potentials in accordance with (4.3.50) for ease of notation.

$$\Phi_s=\overline{\overline{\phi}}_{s0},\quad \Phi_l=\overline{\overline{\phi}}_{l0},\quad \psi_y=\overline{\overline{\psi}}_{0y},\quad \Psi=\overline{\overline{\Psi}}, \tag{4.3.50}$$

$$\frac{\partial^2\Phi_l}{\partial z^2}+\left(\frac{\omega^2}{C_l^2}-k^2\right)\Phi_l=0,\quad \frac{\partial^2\Phi_s}{\partial z^2}+\left(\frac{\omega^2}{C_p^2}-k^2\right)\Phi_s=0,\quad \frac{\partial^2\Psi}{\partial z^2}+\left(\frac{\omega^2}{C_s^2}-k^2\right)\Psi=0. \tag{4.3.51}$$

At $z=0$ we have the (transformed) boundary condition for the liquid surface

$$-\omega^2\Phi_l+g\frac{\partial\Phi_l}{\partial z}=0. \tag{4.3.52}$$

Then, at $z=-h$ we have four (transformed) boundary conditions for the seabed

$$-\frac{\partial\Phi_l}{\partial z}=-\mathrm{i}\omega\frac{\partial\Phi_s}{\partial z}+\omega k\psi_y+\frac{4W_0\sin(kb)\sin(\omega T)}{k\omega}, \tag{4.3.53}$$

$$\lambda\left(-k^2\Phi_s+\frac{\partial^2\Phi_s}{\partial z^2}\right)+2\mu\left(\frac{\partial^2\Phi_s}{\partial z^2}+\mathrm{i}k\frac{\partial\psi_y}{\partial z}\right)=\mathrm{i}\rho_l\omega\Phi_l, \tag{4.3.54}$$

$$2\mathrm{i}k\frac{\partial\Phi_s}{\partial z}-k^2\psi_y-\frac{\partial^2\psi_y}{\partial z^2}=0, \tag{4.3.55}$$

$$\frac{\partial^2 \Phi_s}{\partial z \partial y} + \mathrm{i}k\frac{\partial \psi_y}{\partial y} = 0. \tag{4.3.56}$$

With the requirement that Φ_l, Φ_s and Ψ, along with all their derivatives, decay to zero as $y \to \pm\infty, z \to -\infty$.

4.3.3 Form for potentials

Substitute $\Phi_l(z) = E_1\cos(\mathrm{i}rz) + E_2\sin(\mathrm{i}rz)$, into boundary condition at $z = 0$ to arrive at

$$E_2 = -\frac{\mathrm{i}\omega^2}{gr}E_1, \tag{4.3.57}$$

in agreement with [25]. Also take $\Phi_s(z) = D_1\mathrm{e}^{qz} + \hat{D}_1\mathrm{e}^{-qz}$ and $\Psi(z) = \psi_y\mathbf{j}$ with $\psi_y = D_2\mathrm{e}^{sz} + \hat{D}_2\mathrm{e}^{-sz}$, but note; in order to obtain physical solutions in which solid displacements decrease with depth must have $\hat{D}_1 = \hat{D}_2 = 0$ and $s, q \in \mathbb{R}_{\geq 0}$. If this were not the case then displacements would oscillate or increase with depth - [30]. Applying boundary condition $\sigma_{xz} = 0$ (4.3.55) at $z = -h$

$$D_2 = \frac{2\mathrm{i}kq}{k^2+s^2}\mathrm{e}^{h(s-q)}D_1. \tag{4.3.58}$$

Applying boundary condition (4.3.53) at $z = -h$ we obtain

$$-E_1 r\sinh(rh) + \frac{\omega^2 E_1}{g}\cosh(rh) - \mathrm{i}\omega q D_1\mathrm{e}^{-qh} + \frac{2\mathrm{i}\omega k^2 q\mathrm{e}^{h(s-q)}D_1\mathrm{e}^{-sh}}{k^2+s^2} + \frac{4W_0\sin(kb)\sin(\omega T)}{\omega k} = 0. \tag{4.3.59}$$

Applying boundary condition (4.3.54) at $z = -h$

$$\lambda\left(-k^2 D_1\mathrm{e}^{-qh} + D_1 q^2\mathrm{e}^{-qh}\right) + 2\mu\left(D_1 q^2\mathrm{e}^{-qh} - \frac{2k^2 D_1 q\mathrm{e}^{-qh}s}{k^2+s^2}\right) - \mathrm{i}\rho_l\omega\left(E_1\cosh(rh) - \frac{\omega^2 E_1}{gr}\sinh(rh)\right) = 0. \tag{4.3.60}$$

Since (4.3.59) and (4.3.60) are essentially a pair of simultaneous equations in unknowns E_1 and D_1 they can be solved in this case resulting in

$$E_1 = -\frac{H_1}{\omega k H_2}, \quad D_1 = \frac{H_3}{kH_2}, \tag{4.3.61}$$

with

$$H_1 = 4grW_0 \sin(kb)\sin(\omega T)\mathrm{e}^{-qh}\left[-2k^2\mu qs + \left(k^2+s^2\right)\left[\left(\mu+\frac{\lambda}{2}\right)q^2 - \frac{\lambda k^2}{2}\right]\right], \quad (4.3.62)$$

and

$$H_2 = \left(-2qk^2\omega^2 r\left(\mu s + \frac{\rho_l g}{2}\right) + \left(k^2+s^2\right)\omega^2 r\left(q^2\left(\mu+\frac{\lambda}{2}\right) + \frac{\rho_l g q}{2} - \frac{k^2\lambda}{2}\right)\right)\mathrm{e}^{-qh}\cosh(rh)$$
$$+\left(2qk^2\left(\mu g r^2 s + \frac{\rho_l\omega^4}{2}\right) - \left(k^2+s^2\right)\left(gr^2\left(\mu+\frac{\lambda}{2}\right)q^2 + \frac{\rho_l\omega^4 q}{2} - \frac{gr^2k^2\lambda}{2}\right)\right)\mathrm{e}^{-qh}\sinh(rh), \quad (4.3.63)$$

$$H_3 = 2\mathrm{i}\rho_l W_0\left(k^2+s^2\right)\left(\omega^2\sinh(rh) - gr\cosh(rh)\right)\sin(kb)\sin(\omega T). \quad (4.3.64)$$

Setting $H_2 = 0$ and rearranging yields

$$\tanh(rh) = \frac{\frac{\omega^2}{r}\left\{\rho_l q\frac{(k^2-s^2)}{(k^2+s^2)} + \frac{1}{g}\left[\frac{4k^2qs\mu}{(k^2+s^2)} - \left(\left(\lambda+2\mu\right)q^2 - \lambda k^2\right)\right]\right\}}{\frac{\omega^4 q\rho_l}{gr^2}\frac{(k^2-s^2)}{(k^2+s^2)} + \left[\frac{4k^2qs\mu}{(k^2+s^2)} - \left(\left(\lambda+2\mu\right)q^2 - \lambda k^2\right)\right]}, \quad (4.3.65)$$

which is the dispersion relation of [25]. The zeros of H_2 (i.e. dispersion relation solutions) locate the poles for the residue calculations that come later. Therefore we have

$$\Phi_l(z,\omega,k) = -\frac{H_1}{\omega k H_2}\left(\cos(\mathrm{i}rz) - \frac{\mathrm{i}\omega^2}{gr}\sin(\mathrm{i}rz)\right), \quad (4.3.66)$$

$$\Phi_s(z,\omega,k) = \frac{H_3}{kH_2}\mathrm{e}^{qz}, \quad \Psi = \frac{2\mathrm{i}q}{k^2+s^2}\frac{H_3}{H_2}\mathrm{e}^{h(s-q)+sz}\mathbf{j}. \quad (4.3.67)$$

Setting $q = s = 0$ reduces to the rigid case where the velocity potential from [1] is recovered. H_1 and H_2 reduce to

$$H_1 = -2W_0 gr\lambda k^4\sin(kb)\sin(\omega T), \quad (4.3.68)$$

$$H_2 = -\frac{1}{2}r\lambda k^4\left(\omega^2\cosh(rh) - gr\sinh(rh)\right). \quad (4.3.69)$$

In this case, $\Phi_l(z,\omega,k)$ becomes

$$\Phi_l(z,\omega,k) = -\frac{4W_0\sin(kb)\sin(\omega T)}{\mu k\omega}\left\{\frac{\mu g\cos\left(\mu z\right) + \omega^2\sin\left(\mu z\right)}{\omega^2\cos\left(\mu h\right) + \mu g\sin\left(\mu h\right)}\right\}, \quad (4.3.70)$$

which is in agreement with [1] (note that the sign difference is due to the definition of the velocity potential).

4.3.4 Inverse Fourier transforms

The leading order potentials are retrieved by applying the inverse Fourier transforms as follows

$$\bar{\phi}_{l0}(z,\omega,x)=\frac{1}{2\pi}\int_{-\infty}^{\infty}\Phi_l(z,\omega,k)\mathrm{e}^{\mathrm{i}kx}\mathrm{d}k,\quad \phi_{l0}(z,t,x)=\frac{1}{2\pi}\int_{-\infty}^{\infty}\Phi_l(z,\omega,k)\mathrm{e}^{-\mathrm{i}\omega t}\mathrm{d}\omega. \tag{4.3.71}$$

From (4.3.66) we have

$$\phi_{l0}=\frac{1}{2\pi}\int_{-\infty}^{\infty}\left\{\frac{1}{2\pi}\int_{-\infty}^{\infty}\left\{-\frac{H_1}{\omega kH_2}\left[\cos(\mathrm{i}rz)-\frac{\mathrm{i}\omega^2}{gr}\sin(\mathrm{i}rz)\right]\right\}\mathrm{e}^{\mathrm{i}kx}\mathrm{d}k\right\}\mathrm{e}^{-\mathrm{i}\omega t}\mathrm{d}\omega, \tag{4.3.72}$$

$$\phi_{s0}=\frac{1}{2\pi}\int_{-\infty}^{\infty}\left\{\frac{1}{2\pi}\int_{-\infty}^{\infty}\left\{\frac{H_3}{kH_2}\mathrm{e}^{qz}\right\}\mathrm{e}^{\mathrm{i}kx}\mathrm{d}k\right\}\mathrm{e}^{-\mathrm{i}\omega t}\mathrm{d}\omega, \tag{4.3.73}$$

$$\psi_{0y}=\frac{1}{2\pi}\int_{-\infty}^{\infty}\left\{\frac{1}{2\pi}\int_{-\infty}^{\infty}\left\{\frac{2\mathrm{i}q}{k^2+s^2}\frac{H_3}{H_2}\mathrm{e}^{h(s-q)+sz}\right\}\mathrm{e}^{\mathrm{i}kx}\mathrm{d}k\right\}\mathrm{e}^{-\mathrm{i}\omega t}\mathrm{d}\omega. \tag{4.3.74}$$

Re-writing these expressions gives

$$\phi_{l0}=\frac{1}{2\pi}\int_{-\infty}^{\infty}\mathrm{i}\,\mathrm{e}^{-\mathrm{i}\omega t}I_1\mathrm{d}\omega,\quad \phi_{s0}=\frac{1}{2\pi}\int_{-\infty}^{\infty}\mathrm{i}\,\mathrm{e}^{-\mathrm{i}\omega t}I_2\mathrm{d}\omega,\quad \psi_{0y}=\frac{1}{2\pi}\int_{-\infty}^{\infty}\mathrm{i}\,\mathrm{e}^{-\mathrm{i}\omega t}I_3\mathrm{d}\omega, \tag{4.3.75}$$

where I_1, I_2, I_3 are the k integrals

$$I_1=\frac{1}{2\pi\mathrm{i}}\int_{-\infty}^{\infty}\mathrm{e}^{\mathrm{i}kx}\frac{-H_1}{\omega kH_2}\left[\cos(\mathrm{i}rz)-\frac{\mathrm{i}\omega^2}{gr}\sin(\mathrm{i}rz)\right]\mathrm{d}k,\quad I_2=\frac{1}{2\pi\mathrm{i}}\int_{-\infty}^{\infty}\mathrm{e}^{\mathrm{i}kx}\frac{H_3}{kH_2}\mathrm{e}^{qz}\mathrm{d}k, \tag{4.3.76}$$

$$I_3=\frac{1}{2\pi\mathrm{i}}\int_{-\infty}^{\infty}\mathrm{e}^{\mathrm{i}kx}\frac{2\mathrm{i}q}{k^2+s^2}\frac{H_3}{H_2}\mathrm{e}^{h(s-q)+sz}\mathrm{d}k. \tag{4.3.77}$$

In each case the integrand has poles at the zeros of H_2, i.e. whenever the dispersion relation (4.3.65) is satisfied. Substitute out r, q and s to make H_2 purely a function of k. Then values for I_1, I_2, I_3 can be calculated from the residues.

Figure 4.2 shows the various zones where r, q and s take on real and imaginary values. There are zones corresponding to surface waves and acoustic–gravity waves. The remaining zones close to $k = 0$ are not physical solutions, since imaginary values taken on by q and/or s would imply oscillations at infinite depth in the elastic medium.

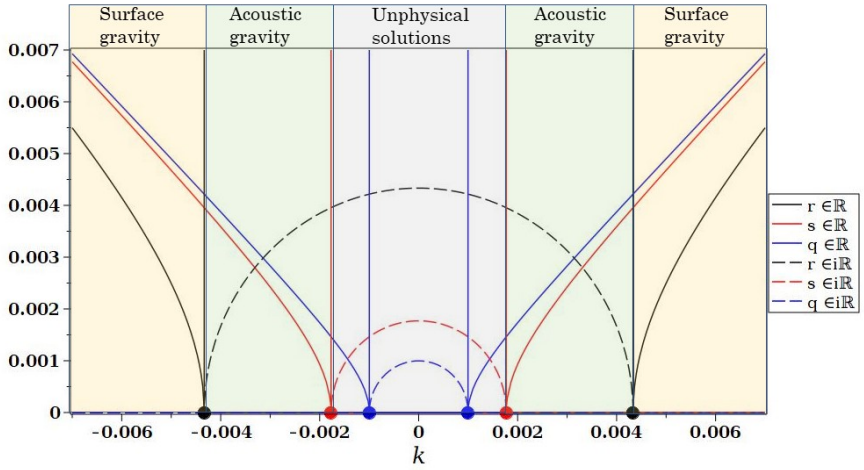

Figure 4.2: Zones possible according as r, q, s real or imaginary for the case $\omega = 2\pi$, $C_l = 1450\,\mathrm{ms}^{-1}$, $C_s = 3550\,\mathrm{ms}^{-1}$, $C_p = 6300\,\mathrm{ms}^{-1}$. Zone 1 (orange) has $r, q, s \in \mathbb{R}$ and corresponds to surface-gravity waves. Zone 2 (green) has $r \in \mathrm{i}\mathbb{R}$, with $q, s \in \mathbb{R}$ and corresponds to acoustic–gravity waves. The remaining zones near $k = 0$ (grey) are not physical solutions. The points where r, s, q transition real $\rightleftharpoons$ imaginary are designated $\pm k_r = \pm 0.00433$ (black dots) $\pm k_s = \pm 0.00177$ (red dots) and $\pm k_q = \pm 0.00099$ (blue dots) respectively.

Moreover, q and s have to be real and non-negative, otherwise oscillations would increase with increasing depth into the elastic medium. Examination of I_1, I_2, I_3 indicate possible poles might also exist at $k = 0$ and when $k^2 + s^2 = 0$. When $k = 0$ the $\sin(kb)$ term in the numerator (from H_1 and H_3) ensures a factor of b is reached in the limit $k \to 0$, so $k = 0$ is a removable singularity. For the case $k^2 + s^2 = 0$ there is a possible pole when $k = \omega/\sqrt{2}C_s$, but this pole lies in the unphysical zone of Figure 4.2. From [25] we have that $s = 0$ (at k_s) represents a point where the energy spreads out over the whole solid depth. At that point the wave amplitude vanishes and so ceases propagation.

When $r \Rightarrow r_{0m}$ with $m = 0, 1$

$$r = \sqrt{k^2 - \frac{\omega^2}{C_l^2}}, \qquad \Longrightarrow k_{0m} = \sqrt{\frac{\omega^2}{C_l^2} + r_{0m}^2}, \tag{4.3.78}$$

this corresponds to surface waves.

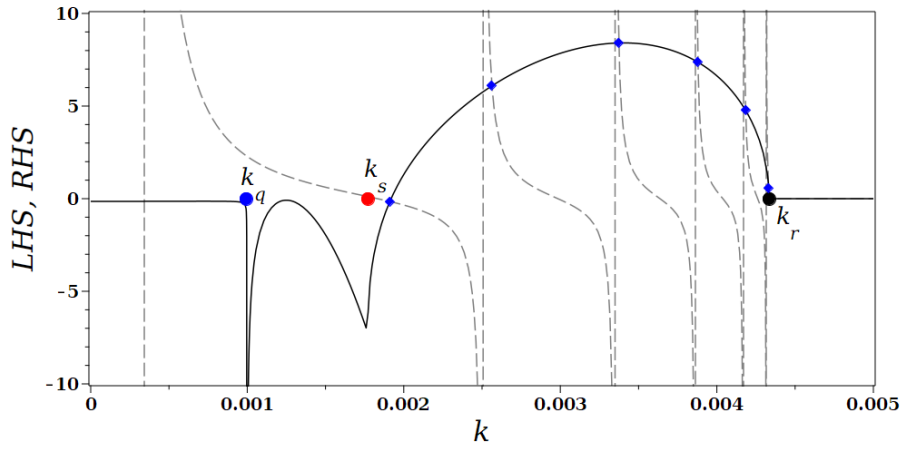

Figure 4.3: Acoustic–gravity wave solutions to dispersion relation are located at the intersections of dashed and solid curves (blue diamonds) for $\omega = 2\pi$ and depth $h = 4000$ m. Dash curve is LHS of (4.3.65), solid curve is RHS of (4.3.65) when $r \in \mathrm{i}\mathbb{R}$.

There are two possible modes for surface waves, mode 00 can propagate if $\omega > \omega_{00}$ - the cutoff frequency for this mode, and mode 01 is the usual tsunami. If instead $r \Rightarrow \mathrm{i}r_n$, then acoustic–gravity waves are possible and

$$k_n = \sqrt{\frac{\omega^2}{C_l^2} - r_n^2} \tag{4.3.79}$$

up to a maximum value of $n = N$, after which the evanescent waves exist with wavenumber Λ_n

$$k_n = \mathrm{i}\Lambda_n = \mathrm{i}\sqrt{r_n^2 - \frac{\omega^2}{C_l^2}} = \sqrt{\frac{\omega^2}{C_l^2} - r_n^2}. \tag{4.3.80}$$

Solutions to the dispersion relation involving acoustic–gravity waves for the case $\omega = 2\pi$ occur between $k_s = 0.00177$ and $k_r = 0.00433$. They are marked with blue diamonds in Figure 4.3.

Consider the liquid terms first, and break ϕ_{l0} into the different regions according to varying ω, for $r \in \mathrm{i}\mathbb{R}$:

$$\begin{aligned}\phi_{l0} = &\frac{1}{2\pi}\int_{-\infty}^{-\omega_n} \mathrm{i}\mathrm{e}^{-\mathrm{i}\omega t}\frac{1}{2\pi\mathrm{i}}\int_{-\infty}^{\infty}\mathrm{e}^{\mathrm{i}kx}\frac{-H_1}{\omega k H_2}\left[\cos(\mathrm{i}rz)-\frac{\mathrm{i}\omega^2}{gr}\sin(\mathrm{i}rz)\right]\mathrm{d}k\mathrm{d}\omega\\ &+\frac{1}{2\pi}\int_{-\omega_n}^{\omega_n} \mathrm{i}\mathrm{e}^{-\mathrm{i}\omega t}\frac{1}{2\pi\mathrm{i}}\int_{-\infty}^{\infty}\mathrm{e}^{\mathrm{i}kx}\frac{-H_1}{\omega k H_2}\left[\cos(\mathrm{i}rz)-\frac{\mathrm{i}\omega^2}{gr}\sin(\mathrm{i}rz)\right]\mathrm{d}k\mathrm{d}\omega\\ &+\frac{1}{2\pi}\int_{\omega_n}^{\infty} \mathrm{i}\mathrm{e}^{-\mathrm{i}\omega t}\frac{1}{2\pi\mathrm{i}}\int_{-\infty}^{\infty}\mathrm{e}^{\mathrm{i}kx}\frac{-H_1}{\omega k H_2}\left[\cos(\mathrm{i}rz)-\frac{\mathrm{i}\omega^2}{gr}\sin(\mathrm{i}rz)\right]\mathrm{d}k\mathrm{d}\omega,\end{aligned} \tag{4.3.81}$$

whereas for $r \in \mathbb{R}$:

$$\begin{aligned}\phi_{l0} = &\frac{1}{2\pi}\int_{-\infty}^{0} \mathrm{i}\mathrm{e}^{-\mathrm{i}\omega t}\frac{1}{2\pi\mathrm{i}}\int_{-\infty}^{\infty}\mathrm{e}^{\mathrm{i}kx}\frac{-H_1}{\omega k H_2}\left[\cos(\mathrm{i}rz)-\frac{\mathrm{i}\omega^2}{gr}\sin(\mathrm{i}rz)\right]\mathrm{d}k\mathrm{d}\omega\\ &+\frac{1}{2\pi}\int_{0}^{\infty} \mathrm{i}\mathrm{e}^{-\mathrm{i}\omega t}\frac{1}{2\pi\mathrm{i}}\int_{-\infty}^{\infty}\mathrm{e}^{\mathrm{i}kx}\frac{-H_1}{\omega k H_2}\left[\cos(\mathrm{i}rz)-\frac{\mathrm{i}\omega^2}{gr}\sin(\mathrm{i}rz)\right]\mathrm{d}k\mathrm{d}\omega\\ &+\frac{1}{2\pi}\int_{-\infty}^{-\omega_{00}} \mathrm{i}\mathrm{e}^{-\mathrm{i}\omega t}\frac{1}{2\pi\mathrm{i}}\int_{-\infty}^{\infty}\mathrm{e}^{\mathrm{i}kx}\frac{-H_1}{\omega k H_2}\left[\cos(\mathrm{i}rz)-\frac{\mathrm{i}\omega^2}{gr}\sin(\mathrm{i}rz)\right]\mathrm{d}k\mathrm{d}\omega\\ &+\frac{1}{2\pi}\int_{\omega_{00}}^{\infty} \mathrm{i}\mathrm{e}^{-\mathrm{i}\omega t}\frac{1}{2\pi\mathrm{i}}\int_{-\infty}^{\infty}\mathrm{e}^{\mathrm{i}kx}\frac{-H_1}{\omega k H_2}\left[\cos(\mathrm{i}rz)-\frac{\mathrm{i}\omega^2}{gr}\sin(\mathrm{i}rz)\right]\mathrm{d}k\mathrm{d}\omega.\end{aligned} \tag{4.3.82}$$

It might be noticed that in (4.3.82) the integration limits in the third and fourth terms do not encompass the entire real line. This is because there is no contribution to Mode 00 until $|\omega| > \omega_{00}$. At the cut-off frequency ω_{00} there is a bifurcation when one propagating mode becomes two - see Figure 4.4.

We demonstrate the application of Rayleigh damping and contour integration using residues for ϕ_{l0} from (4.3.75) along an integration path valid when $\omega_n < \omega < \infty$. The remaining paths when $-\infty < \omega < \omega_n$ and $-\omega_n < \omega < \omega_n$ are handled in a similar fashion.

Considering only the acoustic–gravity waves break the ω integral in (4.3.75)

$$\phi_{l0} = \frac{1}{2\pi}\int_{-\infty}^{\infty}\mathrm{i}\mathrm{e}^{-\mathrm{i}\omega t}I_1\mathrm{d}\omega = \frac{1}{2\pi}\int_{-\infty}^{-\omega_n}\mathrm{i}\mathrm{e}^{-\mathrm{i}\omega t}I^-\mathrm{d}\omega + \frac{1}{2\pi}\int_{-\omega_n}^{+\omega_n}\mathrm{i}\mathrm{e}^{-\mathrm{i}\omega t}I^e\mathrm{d}\omega + \frac{1}{2\pi}\int_{+\omega_n}^{\infty}\mathrm{i}\mathrm{e}^{-\mathrm{i}\omega t}I^+\mathrm{d}\omega. \tag{4.3.83}$$

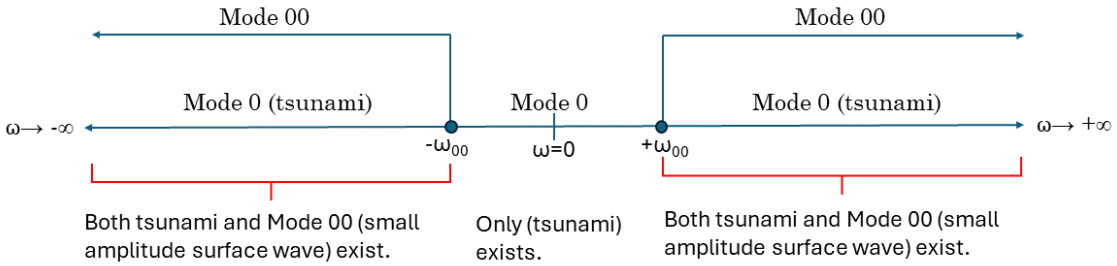

Figure 4.4: Activation of the surface wave modes with varying ω. For frequencies $|\omega| \leq \omega_{00}$ the only propagating mode is Mode 0 (tsunami). For frequencies $|\omega| \geq \omega_{00}$ two modes propagate, namely Mode 0 (tsunami) and Mode 00 (a small surface wave).

To enable the indentation of the path of integration in the complex k-plane follow [16] and apply the method of Rayleigh damping by replacing ω by $\omega' = \omega + \mathrm{i}\delta'$ where $\delta' > 0$ is a small positive number set to zero in the limit. Thus

$$\pm k_n' \approx \pm \frac{\sqrt{(\omega + \mathrm{i}\delta')^2 - \omega_n^2}}{C_l}, \quad n = 1, 2, 3, \ldots, N. \tag{4.3.84}$$

Expanding as a series in δ' and ignoring the very small terms of $O(\delta'^2)$ gives

$$k_n' \approx k_n + \mathrm{i}\frac{\delta'\omega}{C_l\sqrt{\omega^2 - \omega_n^2}}, \tag{4.3.85}$$

with $k_1 > k_2 > \cdots > k_N$. Due to Rayleigh damping $+k_n'$ is slightly above the k axis (the integration path) if $\omega > 0$ and slightly below the real axis if $\omega < 0$. Conversely $-k_n'$ is slightly below the real axis if $\omega > 0$ and slightly above the real axis if $\omega < 0$. Now, take the limit as $\delta' \to 0^+$. For the integral I^+ from (4.3.83) indent the path below the poles on the positive real side and above the poles on the negative real side of the k plane. The anticlockwise contour is closed by a large semi-circle in the upper k plane - see Figure 4.5. From [52] if

$$f(z) = \frac{P(z)}{Q(z)}, \tag{4.3.86}$$

and a is a simple root of Q, then

$$\mathrm{Res}[f(z), a] = \frac{P(a)}{Q'(a)}. \tag{4.3.87}$$

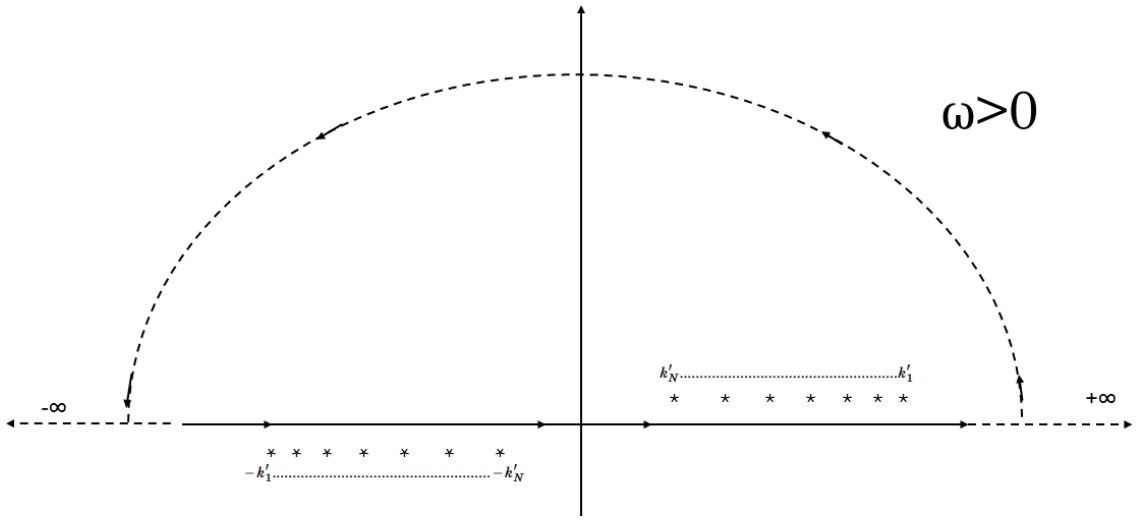

Figure 4.5: Integration path in the k plane for the case when $\omega > 0$.

Thus in our case

$$I^+ = \frac{-H_1|_{k=k_n}}{\omega k_n \partial_k H_2|_{k=k_n}} \left[\cos(\mathrm{i}rz) - \frac{\mathrm{i}\omega^2}{gr}\sin(\mathrm{i}rz)\right] \mathrm{e}^{\mathrm{i}k_n x} \tag{4.3.88}$$

Similar calculations determine I^- and I^e see [16] for more details. Therefore, after application of the Rayleigh damping method and contour integration using the residue theorem around a positively oriented simple closed curve, we have

$$\begin{aligned}
\phi_{l0} = {} & \frac{1}{2\pi}\sum_{n=1}^{N}\int_{-\infty}^{-\omega_n} \mathrm{i}\,\mathrm{e}^{-\mathrm{i}\omega t}\frac{-H_1|_{k=-k_n}}{-\omega k_n \partial_k H_2|_{k=-k_n}}\left[\cos(\mathrm{i}rz) - \frac{\mathrm{i}\omega^2}{gr}\sin(\mathrm{i}rz)\right]\mathrm{e}^{-\mathrm{i}k_n x}\mathrm{d}\omega \\
& + \frac{1}{2\pi}\sum_{n=N+1}^{\infty}\int_{-\omega_n}^{\omega_n} \mathrm{i}\,\mathrm{e}^{-\mathrm{i}\omega t}\frac{-H_1|_{k=\mathrm{i}\Lambda_n}}{\omega \mathrm{i}\Lambda_n \partial_k H_2|_{k=\mathrm{i}\Lambda_n}}\left[\cos(\mathrm{i}rz) - \frac{\mathrm{i}\omega^2}{gr}\sin(\mathrm{i}rz)\right]\mathrm{e}^{-\Lambda_n x}\mathrm{d}\omega \\
& + \frac{1}{2\pi}\sum_{n=1}^{N}\int_{\omega_n}^{\infty} \mathrm{i}\,\mathrm{e}^{-\mathrm{i}\omega t}\frac{-H_1|_{k=k_n}}{\omega k_n \partial_k H_2|_{k=k_n}}\left[\cos(\mathrm{i}rz) - \frac{\mathrm{i}\omega^2}{gr}\sin(\mathrm{i}rz)\right]\mathrm{e}^{\mathrm{i}k_n x}\mathrm{d}\omega,
\end{aligned} \tag{4.3.89}$$

with $r = \mathrm{i}r_n \in \mathrm{i}\mathbb{R}$, $\partial_k = \partial/\partial k$

$$H_1|_{k=k_n} = 4\mathrm{i}g r_n W_0 \sin(k_n b)\sin(\omega T)\mathrm{e}^{-q_n h}\left[-2k_n^2\mu q_n s_n + \left(k_n^2 + s_n^2\right)\left[\left(\mu + \frac{\lambda}{2}\right)q_n^2 - \frac{\lambda k_n^2}{2}\right]\right], \tag{4.3.90}$$

$$H_1|_{k=-k_n} = -H_1|_{k=k_n}, \tag{4.3.91}$$

$$H_1|_{k=\mathrm{i}\Lambda_n} = 4\mathrm{i}gr_nW_0\sin(\mathrm{i}\Lambda_n b)\sin(\omega T)\mathrm{e}^{-q_n h}\left[2\Lambda_n^2\mu q_n s_n + \left(s_n^2-\Lambda_n^2\right)\left[\left(\mu+\frac{\lambda}{2}\right)q_n^2+\frac{\lambda\Lambda_n^2}{2}\right]\right]. \tag{4.3.92}$$

The derivative terms are calculated by first making (4.3.63) for H_2 a function of k only using the following substitutions

$$q(k)=\sqrt{k^2-\frac{\omega^2}{C_p^2}},\quad s(k)=\sqrt{k^2-\frac{\omega^2}{C_s^2}},\quad r(k)=\sqrt{k^2-\frac{\omega^2}{C_l^2}}, \tag{4.3.93}$$

then differentiate with respect to k using Maple. The derivative terms so obtained are given in Appendix (B). The Maple code for these operations is available.

In support of the validity of the integration process Figure 4.6 shows a plot of $|H_2|^{-1}$ in the complex plane when $H_2 = H_2(k)$ and k is allowed to take on complex values. Cross-sections through the real and imaginary axes appear in Figures 4.7a and 4.7b respectively. The poles of the function lie on the real axis, whereas the zeroes lie on the imaginary axis. If the range of the plots were to be extended then the function decays to zero everywhere. As empirical evidence for the validity of the integration, when the calculations are complete, we find good agreement with existing synthetic and real data plots for both acoustic–gravity waves and surface waves (e.g. see Figures 4.20 and 4.24).

In the case where $r \Rightarrow r_{0m}, k \Rightarrow k_{0m}$ with r_{0m} a real number and $m = 0,1$ then there may exist two possibilities for surface waves

$$\begin{aligned}
\phi_{l0} = {} & \frac{1}{2\pi}\int_{-\infty}^{0}\mathrm{i}\mathrm{e}^{-\mathrm{i}\omega t}\frac{-H_1|_{k=-k_{01}}}{-\omega k_{01}\partial_k H_2|_{k=-k_{01}}}\left[\cos(\mathrm{i}rz)-\frac{\mathrm{i}\omega^2}{gr_{01}}\sin(\mathrm{i}rz)\right]\mathrm{e}^{-\mathrm{i}k_{01}x}\mathrm{d}\omega \\
& + \frac{1}{2\pi}\int_{0}^{\infty}\mathrm{i}\mathrm{e}^{-\mathrm{i}\omega t}\frac{-H_1|_{k=k_{01}}}{\omega k_{01}\partial_k H_2|_{k=k_{01}}}\left[\cos(\mathrm{i}rz)-\frac{\mathrm{i}\omega^2}{gr_{01}}\sin(\mathrm{i}rz)\right]\mathrm{e}^{\mathrm{i}k_{01}x}\mathrm{d}\omega \\
& + \frac{1}{2\pi}\int_{-\infty}^{-\omega_{00}}\mathrm{i}\mathrm{e}^{-\mathrm{i}\omega t}\frac{-H_1|_{k=-k_{00}}}{-\omega k_{00}\partial_k H_2|_{k=-k_{00}}}\left[\cos(\mathrm{i}rz)-\frac{\mathrm{i}\omega^2}{gr_{00}}\sin(\mathrm{i}rz)\right]\mathrm{e}^{-\mathrm{i}k_{00}x}\mathrm{d}\omega \\
& + \frac{1}{2\pi}\int_{\omega_{00}}^{\infty}\mathrm{i}\mathrm{e}^{-\mathrm{i}\omega t}\frac{-H_1|_{k=k_{00}}}{\omega k_{00}\partial_k H_2|_{k=k_{00}}}\left[\cos(\mathrm{i}rz)-\frac{\mathrm{i}\omega^2}{gr_{00}}\sin(\mathrm{i}rz)\right]\mathrm{e}^{\mathrm{i}k_{00}x}\mathrm{d}\omega.
\end{aligned} \tag{4.3.94}$$

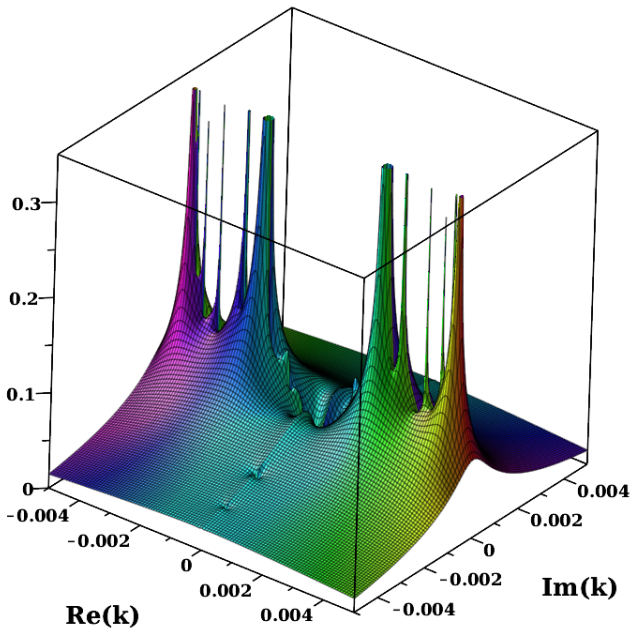

Figure 4.6: Plot of $\frac{1}{|H_2|}$ in the complex plane when $H_2 = H_2(k)$ and k is allowed to take on complex values. The angular frequency in this case is $\omega = 2\pi$ as in Figure 4.3.

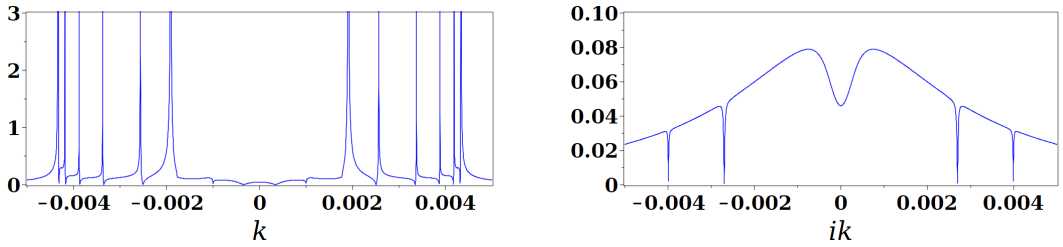

(a) (b)

Figure 4.7: (a) Cross-section of Figure 4.6 through real axis showing locations of the poles when $\omega = 2\pi$. (b) Cross-section of Figure 4.6 through imaginary axis showing locations of the zeroes when $\omega = 2\pi$

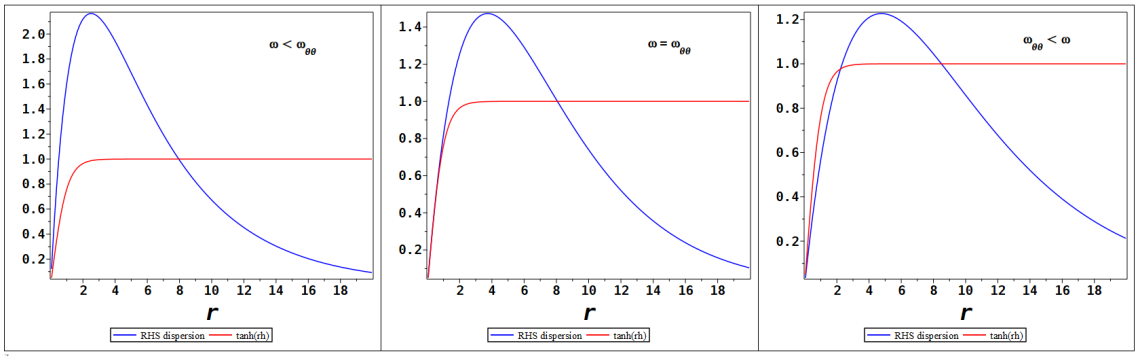

Figure 4.8: Left panel: $\omega < \omega_{00}$ in this case the dispersion relation has only one solution at the intersection of the red and blue curves - this is the usual tsunami mode. Middle panel: this is just at the point where the second mode becomes active. Right panel: for frequencies $\omega > \omega_{00}$ two intersections (solutions to the dispersion relation) are possible. The first being mode 00 and the second mode 0 (tsunami). Note in this figure the blue curve is not drawn to scale in order to give a better qualitative description of the behaviour.

In this case

$$H_1\Big|_{k=k_{0m}} = 4gr_{0m}W_0\sin(k_{0m}b)\sin(\omega T)\mathrm{e}^{-q_{0m}h} \times\left(-2k_{0m}^2\mu q_{0m}s_{0m}+\left(k_{0m}^2+s_{0m}^2\right)\left(q_{0m}^2\left(\mu+\frac{\lambda}{2}\right)-\frac{\lambda k_{0m}^2}{2}\right)\right), \quad (4.3.95)$$

$$H_1\Big|_{k=-k_{0m}} = -H_1\Big|_{k=k_{0m}}. \quad (4.3.96)$$

The derivative term is again to be found in Appendix (B).

Using the substitutions

$$k=\sqrt{r^2+\frac{\omega^2}{C_l^2}}, \quad q=\sqrt{r^2+\frac{\omega^2}{C_l^2}-\frac{\omega^2}{C_p^2}}, \quad s=\sqrt{r^2+\frac{\omega^2}{C_l^2}-\frac{\omega^2}{C_s^2}}, \quad (4.3.97)$$

the dispersion relation (4.3.65) can be written in terms of r and ω alone, and in this case the condition for the existence of the 00^{th} mode for a particular ω is

$$\frac{\mathrm{d}}{\mathrm{d}r}\tanh(rh) > \frac{\mathrm{d}}{\mathrm{d}r}[\text{RHS of (4.3.65)}]. \quad (4.3.98)$$

Also see Figure 4.8 for an illustration of the mode 00 cutoff frequency ω_{00}.

The expressions for the velocity potential in the liquid layer can be further reduced to

$$\begin{aligned}\phi_{l0} = \frac{1}{\pi}\sum_{n=1}^{N}\int_{\omega_n}^{\infty} \mathrm{i}\,\mathrm{e}^{-\mathrm{i}\omega t}\frac{-H_1|_{k=k_n}}{\omega k_n \partial_k H_2|_{k=k_n}}\left[\cos(\mathrm{i}rz) - \frac{\mathrm{i}\omega^2}{gr}\sin(\mathrm{i}rz)\right]\mathrm{e}^{\mathrm{i}k_n x}\mathrm{d}\omega \\ + \frac{1}{\pi}\int_{0}^{\infty} \mathrm{i}\,\mathrm{e}^{-\mathrm{i}\omega t}\frac{-H_1|_{k=k_{01}}}{\omega k_{01} \partial_k H_2|_{k=k_{01}}}\left[\cos(\mathrm{i}rz) - \frac{\mathrm{i}\omega^2}{gr}\sin(\mathrm{i}rz)\right]\mathrm{e}^{\mathrm{i}k_{01} x}\mathrm{d}\omega \\ + \frac{1}{\pi}\int_{\omega_{00}}^{\infty} \mathrm{i}\,\mathrm{e}^{-\mathrm{i}\omega t}\frac{-H_1|_{k=k_{00}}}{\omega k_{00} \partial_k H_2|_{k=k_{00}}}\left[\cos(\mathrm{i}rz) - \frac{\mathrm{i}\omega^2}{gr}\sin(\mathrm{i}rz)\right]\mathrm{e}^{\mathrm{i}k_{00} x}\mathrm{d}\omega \\ + \frac{1}{\pi}\sum_{n=N+1}^{\infty}\int_{0}^{\omega_n} \mathrm{i}\,\mathrm{e}^{-\mathrm{i}\omega t}\frac{-H_1|_{k=\mathrm{i}\Lambda_n}}{\omega \mathrm{i}\Lambda_n \partial_k H_2|_{k=\mathrm{i}\Lambda_n}}\left[\cos(\mathrm{i}rz) - \frac{\mathrm{i}\omega^2}{gr}\sin(\mathrm{i}rz)\right]\mathrm{e}^{-\Lambda_n x}\mathrm{d}\omega.\end{aligned} \tag{4.3.99}$$

Returning to the expression for the displacement potential in the solid given by

$$\phi_{s0} = \frac{1}{2\pi}\int_{-\infty}^{\infty} \mathrm{i}\,\mathrm{e}^{-\mathrm{i}\omega t}\frac{1}{2\pi\mathrm{i}}\int_{-\infty}^{\infty}\mathrm{e}^{\mathrm{i}kx}\frac{H_3}{kH_2}\mathrm{e}^{qz}\mathrm{d}k\mathrm{d}\omega, \tag{4.3.100}$$

and following a similar procedure to that of the liquid velocity potential case arrive at

$$\begin{aligned}\phi_{s0} = \frac{1}{\pi}\sum_{n=1}^{N}\int_{\omega_n}^{\infty} \mathrm{i}\,\mathrm{e}^{-\mathrm{i}\omega t}\frac{H_3|_{k=k_n}}{k_n \partial_k H_2|_{k=k_n}}\mathrm{e}^{q_n z}\mathrm{e}^{\mathrm{i}k_n x}\mathrm{d}\omega \\ + \frac{1}{\pi}\int_{0}^{\infty} \mathrm{i}\,\mathrm{e}^{-\mathrm{i}\omega t}\frac{H_3|_{k=k_{01}}}{k_{01} \partial_k H_2|_{k=k_{01}}}\mathrm{e}^{q_{01} z}\mathrm{e}^{\mathrm{i}k_{01} x}\mathrm{d}\omega \\ + \frac{1}{\pi}\int_{\omega_{00}}^{\infty} \mathrm{i}\,\mathrm{e}^{-\mathrm{i}\omega t}\frac{H_3|_{k=k_{00}}}{k_{00} \partial_k H_2|_{k=k_{00}}}\mathrm{e}^{q_{00} z}\mathrm{e}^{\mathrm{i}k_{00} x}\mathrm{d}\omega \\ + \frac{1}{\pi}\sum_{n=N+1}^{\infty}\int_{0}^{\omega_n} \mathrm{i}\,\mathrm{e}^{-\mathrm{i}\omega t}\frac{H_3|_{k=\mathrm{i}\Lambda_n}}{\mathrm{i}\Lambda_n \partial_k H_2|_{k=\mathrm{i}\Lambda_n}}\mathrm{e}^{q_n z - \Lambda_n x}\mathrm{d}\omega,\end{aligned} \tag{4.3.101}$$

with

$$\begin{aligned}H_3|_{k=k_n} &= -2\rho_l W_0\left(k_n^2 + s_n^2\right)\sin(k_n b)\sin(\omega T)\left(\omega^2\sin(r_n h) - g r_n\cos(r_n h)\right), \\ H_3|_{k=k_{0m}} &= 2i\rho_l W_0\left(k_{0m}^2 + s_{0m}^2\right)\sin(k_{0m} b)\sin(\omega T)\left(\omega^2\sinh(r_{0m} h) - g r_{0m}\cosh(r_{0m} h)\right), \\ H_3|_{k=\mathrm{i}\Lambda_n} &= 2\mathrm{i}\rho_l W_0\left(s_n^2 - \Lambda_n^2\right)\sinh(\Lambda_n b)\sin(\omega T)\left(\omega^2\sin(r_n h) - g r_n\cos(r_n h)\right).\end{aligned} \tag{4.3.102}$$

The derivative terms evaluated at $k = k_n$, $k = \mathrm{i}\Lambda_n$ and $k = k_{0m}$ remain as before. In a

similar way the rotation potential can be written as

$$\psi_{0y} = \frac{1}{2\pi}\int_{-\infty}^{\infty} \mathrm{i}\,\mathrm{e}^{-\mathrm{i}\omega t}\frac{1}{2\pi\mathrm{i}}\int_{-\infty}^{\infty}\mathrm{e}^{\mathrm{i}kx}\frac{2\mathrm{i}q}{k^2+s^2}\frac{H_3}{H_2}\mathrm{e}^{h(s-q)+sz}\mathrm{d}k\mathrm{d}\omega, \tag{4.3.103}$$

which becomes

$$\begin{aligned}\psi_{0y} = {} & \frac{1}{\pi}\sum_{n=1}^{N}\int_{\omega_n}^{\infty}\mathrm{i}\mathrm{e}^{-\mathrm{i}\omega t}\frac{2\mathrm{i}q_n}{k_n^2+s_n^2}\frac{H_3|_{k=k_n}}{\partial_k H_2|_{k=k_n}}\mathrm{e}^{h(s_n-q_n)+s_n z}\mathrm{e}^{\mathrm{i}k_n x}\mathrm{d}\omega \\ & + \frac{1}{\pi}\int_{0}^{\infty}\mathrm{i}\mathrm{e}^{-\mathrm{i}\omega t}\frac{2\mathrm{i}q_{01}}{k_{01}^2+s_{01}^2}\frac{H_3|_{k=k_{01}}}{\partial_k H_2|_{k=k_{01}}}\mathrm{e}^{h(s_{01}-q_{01})+s_{01}z}\mathrm{e}^{\mathrm{i}k_{01}x}\mathrm{d}\omega \\ & + \frac{1}{\pi}\int_{\omega_{00}}^{\infty}\mathrm{i}\mathrm{e}^{-\mathrm{i}\omega t}\frac{2\mathrm{i}q_{00}}{k_{00}^2+s_{00}^2}\frac{H_3|_{k=k_{00}}}{\partial_k H_2|_{k=k_{00}}}\mathrm{e}^{h(s_{00}-q_{00})+s_{00}z}\mathrm{e}^{\mathrm{i}k_{00}x}\mathrm{d}\omega \\ & + \frac{1}{\pi}\sum_{n=N+1}^{\infty}\int_{0}^{\omega_n}\mathrm{i}\mathrm{e}^{-\mathrm{i}\omega t}\frac{2\mathrm{i}q_n}{s_n^2-\Lambda_n^2}\frac{H_3|_{k=\mathrm{i}\Lambda_n}}{\partial_k H_2|_{k=\mathrm{i}\Lambda_n}}\mathrm{e}^{h(s_n-q_n)+s_n z-\Lambda_n x}\mathrm{d}\omega.\end{aligned} \tag{4.3.104}$$

4.3.5 Long range modulation - liquid layer

We introduce unknown envelope factors for the liquid layer $A_n^{\pm}(k_n,X,Y)$ and $A_{0m}^{\pm}(k_0 m,X,Y)$

$$\begin{aligned}
\phi_{l0} = &\frac{1}{2\pi}\sum_{n=1}^{N}\int_{\omega_n}^{\infty} \mathrm{i}\,\mathrm{e}^{-\mathrm{i}\omega t} A_n^{+} \frac{-H_1|_{k=k_n}}{\omega k_n \partial_k H_2|_{k=k_n}} \left[\cos(\mathrm{i}rz) - \frac{\mathrm{i}\omega^2}{gr_n}\sin(\mathrm{i}rz)\right] \mathrm{e}^{\mathrm{i}k_n x}\mathrm{d}\omega \\
&+ \frac{1}{2\pi}\int_{0}^{\infty} \mathrm{i}\,\mathrm{e}^{-\mathrm{i}\omega t} A_{01}^{+} \frac{-H_1|_{k=k_{01}}}{\omega k_{01} \partial_k H_2|_{k=k_{01}}} \left[\cos(\mathrm{i}rz) - \frac{\mathrm{i}\omega^2}{gr}\sin(\mathrm{i}rz)\right] \mathrm{e}^{\mathrm{i}k_{01} x}\mathrm{d}\omega \\
&+ \frac{1}{2\pi}\int_{\omega_{00}}^{\infty} \mathrm{i}\,\mathrm{e}^{-\mathrm{i}\omega t} A_{00}^{+} \frac{-H_1|_{k=k_{00}}}{\omega k_{00} \partial_k H_2|_{k=k_{00}}} \left[\cos(\mathrm{i}rz) - \frac{\mathrm{i}\omega^2}{gr}\sin(\mathrm{i}rz)\right] \mathrm{e}^{\mathrm{i}k_{00} x}\mathrm{d}\omega \\
&+ \frac{1}{2\pi}\sum_{n=1}^{N}\int_{-\infty}^{-\omega_n} \mathrm{i}\,\mathrm{e}^{-\mathrm{i}\omega t} A_n^{-} \frac{-H_1|_{k=-k_n}}{-\omega k_n \partial_k H_2|_{k=-k_n}} \left[\cos(\mathrm{i}rz) - \frac{\mathrm{i}\omega^2}{gr}\sin(\mathrm{i}rz)\right] \mathrm{e}^{-\mathrm{i}k_n x}\mathrm{d}\omega \\
&+ \frac{1}{2\pi}\int_{-\infty}^{0} \mathrm{i}\,\mathrm{e}^{-\mathrm{i}\omega t} A_{01}^{-} \frac{-H_1|_{k=-k_{01}}}{-\omega k_{01} \partial_k H_2|_{k=-k_{01}}} \left[\cos(\mathrm{i}rz) - \frac{\mathrm{i}\omega^2}{gr}\sin(\mathrm{i}rz)\right] \mathrm{e}^{-\mathrm{i}k_{01} x}\mathrm{d}\omega \\
&+ \frac{1}{2\pi}\int_{-\infty}^{-\omega_{00}} \mathrm{i}\,\mathrm{e}^{-\mathrm{i}\omega t} A_{00}^{-} \frac{-H_1|_{k=-k_{00}}}{-\omega k_{00} \partial_k H_2|_{k=-k_{00}}} \left[\cos(\mathrm{i}rz) - \frac{\mathrm{i}\omega^2}{gr}\sin(\mathrm{i}rz)\right] \mathrm{e}^{-\mathrm{i}k_{00} x}\mathrm{d}\omega \\
&+ \frac{1}{2\pi}\sum_{n=N+1}^{\infty}\left[\int_{-\omega_n}^{0} + \int_{0}^{\omega_n}\right] \mathrm{i}\,\mathrm{e}^{-\mathrm{i}\omega t} \frac{-H_1|_{k=\mathrm{i}\Lambda_n}}{\omega \mathrm{i}\Lambda_n \partial_k H_2|_{k=\mathrm{i}\Lambda_n}} \left[\cos(\mathrm{i}rz) - \frac{\mathrm{i}\omega^2}{gr}\sin(\mathrm{i}rz)\right] \mathrm{e}^{-\Lambda_n x}\mathrm{d}\omega.
\end{aligned} \tag{4.3.105}$$

The initial conditions are given by

$$A_n^{\pm} = \begin{cases} 1 & |Y| < \mathscr{L} = \epsilon L \\ 0 & |Y| > \mathscr{L} = \epsilon L \end{cases}, \quad A_{0m}^{\pm} = \begin{cases} 1 & Y| < \mathscr{L} = \epsilon L \\ 0 & Y| > \mathscr{L} = \epsilon L \end{cases}, \quad X = \epsilon^2 x \to 0. \tag{4.3.106}$$

Proceeding with acoustic modes, taking the time Fourier transform of (4.3.23) and separating $\bar{\phi}_{l2}$ into 3 ranges yields

$$\bar{\phi}_{l2} = \begin{cases} \bar{\phi}_{l2}^{+} & \omega_n < \omega < \infty \\ \bar{\phi}_{l2}^{e} & -\omega_n < \omega < \omega_n \\ \bar{\phi}_{l2}^{-} & -\infty < \omega < -\omega_n. \end{cases} \tag{4.3.107}$$

In the range $\omega_n < \omega < \infty$

$$\frac{\partial^2 \bar{\phi}_{l2}^+}{\partial x^2} + \frac{\partial^2 \bar{\phi}_{l2}^+}{\partial z^2} + \frac{\omega^2}{C_l^2}\bar{\phi}_{l2}^+ = -\frac{\partial^2 \bar{\phi}_{l0}}{\partial Y^2} - 2\frac{\partial^2 \bar{\phi}_{l0}}{\partial x \partial X}. \tag{4.3.108}$$

From this point the solution proceeds in an analogous way to that derived by [16],

$$\frac{\partial^2 \bar{\phi}_{l2}^+}{\partial x^2} + \frac{\partial^2 \bar{\phi}_{l2}^+}{\partial z^2} + \frac{\omega^2}{C_l^2}\bar{\phi}_{l2}^+ = -\mathrm{i}\sum_{n=1}^{N}\left[\frac{\partial^2 A_n^+}{\partial Y^2} + 2\mathrm{i}k_n\frac{\partial A_n^+}{\partial X}\right]\frac{-H_1|_{k=k_n}}{\omega k_n \partial_k H_2|_{k=k_n}} \times \left[\cos(\mathrm{i}rz) - \frac{\mathrm{i}\omega^2}{gr}\sin(\mathrm{i}rz)\right]\mathrm{e}^{\mathrm{i}k_n x}. \tag{4.3.109}$$

Assuming $\bar{\phi}_{l2}^+$ has solutions in the form $\sum_{n=1}^{N}\xi_n^+(\omega,z)\mathrm{e}^{\mathrm{i}k_n x}$, then substituting into (4.3.109) gives

$$-\sum_{n=1}^{N}\xi_n^+ k_n^2 \mathrm{e}^{\mathrm{i}k_n x} + \sum_{n=1}^{N}\frac{\partial^2 \xi_n^+}{\partial z^2}\mathrm{e}^{\mathrm{i}k_n x} + \frac{\omega^2}{C_l^2}\sum_{n=1}^{N}\xi_n^+ \mathrm{e}^{\mathrm{i}k_n x} = -\mathrm{i}\sum_{n=1}^{N}\left[\frac{\partial^2 A_n^+}{\partial Y^2} + 2\mathrm{i}k_n\frac{\partial A_n^+}{\partial X}\right] \times \frac{-H_1|_{k=k_n}}{\omega k_n \partial_k H_2|_{k=k_n}}F_n(z)\mathrm{e}^{\mathrm{i}k_n x}. \tag{4.3.110}$$

Equating coefficients gives

$$\frac{\partial^2 \xi_n^+}{\partial z^2} + \left(\frac{\omega^2}{C_l^2} - k_n^2\right)\xi_n^+ = -\mathrm{i}\left[\frac{\partial^2 A_n^+}{\partial Y^2} + 2\mathrm{i}k_n\frac{\partial A_n^+}{\partial X}\right]\frac{-H_1|_{k=k_n}}{\omega k_n \partial_k H_2|_{k=k_n}}F_n(z), \tag{4.3.111}$$

where

$$r^2 = k^2 - \frac{\omega^2}{C_l^2}\begin{cases} r = r_{0m}, & \frac{\omega^2}{C_l^2} - k_{0m}^2 = -r_{0m}^2, \quad \text{surface waves} \\ r = \mathrm{i}r_n, & \frac{\omega^2}{C_l^2} - k_n^2 = +r_n^2, \quad \text{acoustic–gravity waves} \end{cases} \tag{4.3.112}$$

resulting in

$$\frac{\partial^2 \xi_n^+}{\partial z^2} + r_n^2 \xi_n^+ = -\mathrm{i}\left[\frac{\partial^2 A_n^+}{\partial Y^2} + 2\mathrm{i}k_n\frac{\partial A_n^+}{\partial X}\right]\frac{-H_1|_{k=k_n}}{\omega k_n \partial_k H_2|_{k=k_n}}F_n(z), \tag{4.3.113}$$

where

$$F_n(z) = \cos(r_n z) + \frac{\omega^2}{g r_n}\sin(r_n z). \tag{4.3.114}$$

The ground motion is captured at $O(\epsilon^0)$, so the boundary conditions on $\bar{\phi}^+_{l2}$ (and therefore ξ^+_n) at O(ϵ^2) are

$$-\omega^2\bar{\phi}^+_{l2} + g\frac{\partial\bar{\phi}^+_{l2}}{\partial z} = 0, \quad z = 0, \tag{4.3.115}$$

$$\frac{\partial\bar{\phi}^+_{l2}}{\partial z} = 0, \quad z = -h. \tag{4.3.116}$$

$F_n(z)$ is a solution to the boundary value problem,

$$\frac{\partial^2 F_n}{\partial z^2} + r_n^2 F_n = 0, \tag{4.3.117}$$

$$F_n = 1, \quad \frac{\partial F_n}{\partial z} = \frac{\omega^2}{g}, \quad z = 0, \tag{4.3.118}$$

$$F_n = \cos(r_n h) - \frac{\omega^2}{g r_n}\sin(r_n h), \quad \frac{\partial F_n}{\partial z} = r_n \sin(r_n h) + \frac{\omega^2}{g}\cos(r_n h), \quad z = -h. \tag{4.3.119}$$

A similar process could be carried out for surface waves.

The next step is to extract the Schrödinger equation from (4.3.113). Multiply (4.3.113) by $F_n(z)$ and (4.3.117) by ξ^+_n then subtract

$$F_n\left(\frac{\partial^2\xi^+_n}{\partial z^2} + r_n^2\xi^+_n\right) - \xi^+_n\left(\frac{\partial^2 F_n}{\partial z^2} + r_n^2 F_n\right) = -\mathrm{i}\left[\frac{\partial^2 A^+_n}{\partial Y^2} + 2\mathrm{i}k_n\frac{\partial A^+_n}{\partial X}\right]\frac{-H_1|_{k=k_n}}{\omega k_n \partial_k H_2|_{k=k_n}}F_n^2(z). \tag{4.3.120}$$

Now integrate the LHS of (4.3.120) over the range $-h \le z \le 0$.

$$\int_{-h}^{0}\left[F_n\left(\frac{\partial^2\xi^+_n}{\partial z^2} + r_n^2\xi^+_n\right) - \xi^+_n\left(\frac{\partial^2 F_n}{\partial z^2} + r_n^2 F_n\right)\right]\mathrm{d}z = \left[F_n\frac{\partial\xi^+_n}{\partial z} - \xi^+_n\frac{\partial F_n}{\partial z}\right]_{-h}^{0}. \tag{4.3.121}$$

Evaluating the boundary term at $z = 0$ gives

$$\left[F_n\frac{\partial\xi^+_n}{\partial z} - \xi^+_n\frac{\partial F_n}{\partial z}\right]^0 = \frac{\omega^2}{g}\xi^+_n - \xi^+_n\frac{\omega^2}{g} = 0. \tag{4.3.122}$$

While the boundary term at $z = -h$ gives

$$\left[F_n\frac{\partial\xi^+_n}{\partial z} - \xi^+_n\frac{\partial F_n}{\partial z}\right]_{-h} = \left[\cos(r_n h) - \frac{\omega^2}{g r_n}\sin(r_n h)\right]\times 0 - \xi^+_n\left[r_n\sin(r_n h) + \frac{\omega^2}{g}\cos(r_n h)\right] = 0. \tag{4.3.123}$$

Note the term inside the square brackets of (4.3.123) is the rigid dispersion relation which

must be zero for valid solutions (no ground movement at $O(\epsilon^2)$). Therefore the integral (4.3.121) must be zero and for this to be true we must have

$$\frac{\partial^2 A_n^+}{\partial Y^2} + 2\mathrm{i}k_n \frac{\partial A_n^+}{\partial X} = 0, \quad r \in \mathrm{i}\mathbb{R}. \tag{4.3.124}$$

As in [16], the result is the Schrödinger equation for the 2D evolution of the envelope factors.

Having obtained the Schrödinger equation (4.3.124) for the acoustic–gravity wave case in the liquid layer the solution is analogous to that found in [16], but with mode properties now incorporating elasticity, via k_n. The envelope solution is derived following [16]. Consider the side $x > 0$ and re-name A_n^+ to A_n for brevity. Re-write (4.3.124) as

$$\frac{\partial A_n}{\partial X} = \frac{\mathrm{i}}{2k_n} \frac{\partial^2 A_n}{\partial Y^2}. \tag{4.3.125}$$

We make use of the following cosine transform/inverse transform

$$\hat{A}(X,\gamma) = \int_0^\infty A(X,Y)\cos\left(\gamma Y\right)\mathrm{d}Y, \quad A(X,Y) = \frac{2}{\pi}\int_0^\infty \hat{A}(X,\gamma)\cos\left(\gamma Y\right)\mathrm{d}\gamma. \tag{4.3.126}$$

Then transforming $\partial A_n/\partial X$ gives

$$\int_0^\infty \frac{\partial A_n}{\partial X}\cos\left(\gamma Y\right)\mathrm{d}Y = \frac{\partial}{\partial X}\int_0^\infty A_n\cos\left(\gamma Y\right)\mathrm{d}Y = \frac{\partial \hat{A}}{\partial X}. \tag{4.3.127}$$

Transforming $\partial^2 A_n/\partial Y^2$

$$\int_0^\infty \frac{\partial^2 A_n}{\partial Y^2}\cos\left(\gamma Y\right)\mathrm{d}Y = \left[\frac{\partial A_n}{\partial Y}\cos\left(\gamma Y\right)\right]_0^\infty + \gamma\int_0^\infty \frac{\partial A_n}{\partial Y}\sin\left(\gamma Y\right)\mathrm{d}Y. \tag{4.3.128}$$

Note we require the waves to vanish far away from and be symmetric about the central axis so that

$$A_n = 0, \quad |X|, |Y| \to \infty \quad \text{and} \quad \frac{\partial A_n}{\partial Y} = 0, \quad Y = 0, \tag{4.3.129}$$

and in this case, the boundary term vanishes

$$\gamma\int_0^\infty \frac{\partial A_n}{\partial Y}\sin\left(\gamma Y\right)\mathrm{d}Y = \gamma\left\{\left[A_n\sin\left(\gamma Y\right)\right]_0^\infty - \gamma\int_0^\infty A_n\cos\left(\gamma Y\right)\mathrm{d}Y\right\} = -\gamma^2\hat{A}_n. \tag{4.3.130}$$

From (4.3.125)

$$\frac{\partial \hat{A}_n}{\partial X} = \frac{\mathrm{i}}{2k_n}\left(-\gamma^2 \hat{A}_n\right) = \frac{-\mathrm{i}\gamma^2}{2k_n}\hat{A}_n. \tag{4.3.131}$$

Solving for $\hat{A}$ gives

$$\hat{A}_n(X,\gamma) = \hat{\beta}(\gamma)\mathrm{e}^{-\frac{\mathrm{i}\gamma}{2k_n}X}, \quad \hat{\beta}(\gamma) = \int_0^\infty \beta(\gamma)\cos\left(\gamma Y\right)\mathrm{d}Y. \tag{4.3.132}$$

Where $\hat{\beta}(\gamma)$ is a function of γ only. However $\hat{\beta}(\gamma) = \hat{A}(0,\gamma)$ so by the initial conditions on A_n (4.3.106)

$$\hat{\beta}(\gamma) = \int_0^\infty \beta(\gamma)\cos\left(\gamma Y\right)\mathrm{d}Y = \int_0^l \cos\left(\gamma Y\right)\mathrm{d}Y = \left[\frac{\sin(\gamma Y)}{\gamma}\right]_0^l = \frac{\sin(\gamma l)}{\gamma} \tag{4.3.133}$$

and therefore

$$\hat{A}_n(X,\gamma) = \frac{\sin(\gamma l)}{\gamma}\mathrm{e}^{\frac{-\mathrm{i}\gamma^2 X}{2k_n}} \tag{4.3.134}$$

Let $\nu = X/k_n$ then the inverse is

$$A_n(X,Y) = \frac{2}{\pi}\int_0^\infty \left\{\frac{\sin(\gamma l)}{\gamma}\mathrm{e}^{\frac{-\mathrm{i}\gamma^2\nu}{2}}\right\}\cos\left(\gamma Y\right)\mathrm{d}\gamma, \tag{4.3.135}$$

$$\begin{aligned} A_n(X,Y) = {} & \frac{1}{\pi}\int_0^\infty \frac{1}{\gamma}\left[\sin\left(\gamma(l+Y)\right)+\sin\left(\gamma(l-Y)\right)\right]\cos\left(\frac{\gamma^2\nu}{2}\right)\mathrm{d}\gamma \\ & -\frac{\mathrm{i}}{\pi}\int_0^\infty \frac{1}{\gamma}\left[\sin\left(\gamma(l+Y)\right)+\sin\left(\gamma(l-Y)\right)\right]\sin\left(\frac{\gamma^2\nu}{2}\right)\mathrm{d}\gamma. \end{aligned} \tag{4.3.136}$$

Again for brevity let $\chi = \nu/2$, $\quad 2\mathscr{Y}_+ = l+Y$, $\quad 2\mathscr{Y}_- = l-Y$ then since

$$\frac{1}{2}\frac{\mathrm{d}}{\mathrm{d}\gamma}\int_0^\infty \frac{1}{\gamma}\cos\left(\chi\gamma^2\right)\sin\left(2\gamma\mathscr{Y}\right)\mathrm{d}\gamma = \int_0^\infty \cos\left(\chi\gamma^2\right)\cos\left(2\gamma\mathscr{Y}\right)\mathrm{d}\gamma = \frac{1}{2}\sqrt{\frac{\pi}{2\chi}}\left\{\cos\left(\frac{\mathscr{Y}^2}{\chi}\right)+\sin\left(\frac{\mathscr{Y}^2}{\chi}\right)\right\} \tag{4.3.137}$$

$$\frac{1}{2}\frac{\mathrm{d}}{\mathrm{d}\gamma}\int_0^\infty \frac{1}{\gamma}\sin\left(\chi\gamma^2\right)\sin\left(2\gamma\mathscr{Y}\right)\mathrm{d}\gamma = \int_0^\infty \sin\left(\chi\gamma^2\right)\cos\left(2\gamma\mathscr{Y}\right)\mathrm{d}\gamma = \frac{1}{2}\sqrt{\frac{\pi}{2\chi}}\left\{\cos\left(\frac{\mathscr{Y}^2}{\chi}\right)-\sin\left(\frac{\mathscr{Y}^2}{\chi}\right)\right\} \tag{4.3.138}$$

After using the known integration formulas [53] it follows that

$$\begin{aligned}\int_0^\infty \frac{1}{\gamma}\cos\left(\chi\gamma^2\right)\sin\left(2\gamma\mathscr{Y}\right)\mathrm{d}\gamma &= \int_0^{\mathscr{Y}} \sqrt{\frac{\pi}{2\chi}}\left\{\cos\left(\frac{\mathscr{Y}^2}{\chi}\right)+\sin\left(\frac{\mathscr{Y}^2}{\chi}\right)\right\}\mathrm{d}\gamma \\ &= \frac{\pi}{2}\left\{C\left(\sqrt{\frac{2}{\pi\chi_n}}\mathscr{Y}_+\right)+S\left(\sqrt{\frac{2}{\pi\chi_n}}\mathscr{Y}_-\right)\right\},\end{aligned} \tag{4.3.139}$$

and

$$\begin{aligned}\int_0^\infty \frac{1}{\gamma}\sin\left(\chi\gamma^2\right)\sin\left(2\gamma\mathscr{Y}\right)\mathrm{d}\gamma &= \int_0^{\mathscr{Y}} \sqrt{\frac{\pi}{2\chi}}\left\{\cos\left(\frac{\mathscr{Y}^2}{\chi}\right)-\sin\left(\frac{\mathscr{Y}^2}{\chi}\right)\right\}\mathrm{d}\gamma \\ &= \frac{\pi}{2}\left\{C\left(\sqrt{\frac{2}{\pi\chi_n}}\mathscr{Y}_+\right)-S\left(\sqrt{\frac{2}{\pi\chi_n}}\mathscr{Y}_-\right)\right\},\end{aligned} \tag{4.3.140}$$

and so the envelope solution is obtained as

$$\begin{aligned}A_n &= \frac{1-\mathrm{i}}{2}\left\{C\left(\sqrt{\frac{2}{\pi\chi_n}}\mathscr{Y}_+\right)+C\left(\sqrt{\frac{2}{\pi\chi_n}}\mathscr{Y}_-\right)\right\}+\frac{1+\mathrm{i}}{2}\left\{S\left(\sqrt{\frac{2}{\pi\chi_n}}\mathscr{Y}_+\right)+S\left(\sqrt{\frac{2}{\pi\chi_n}}\mathscr{Y}_-\right)\right\} \\ \chi_n &= \frac{X}{2k_n} \quad \mathscr{Y}_\pm = \frac{\mathscr{L}\pm Y}{2},\end{aligned} \tag{4.3.141}$$

where $C(z)$ and $S(z)$ are Fresnel integrals. A similar process beginning at (4.3.107) can be applied to derive the expressions for the surface waves mode 01 and mode 00. Finally, the pressure obtained from the velocity potential (4.3.99) in the liquid (propagating parts) along with (4.2.15) inclusive of envelope factors is given by

$$\begin{aligned}P_l = &\frac{\rho_l}{\pi}\sum_{n=1}^{N}\int_{\omega_n}^{\infty}\frac{-H_1|_{k=k_n}A_n}{k_n\partial_k H_2|_{k=k_n}}\left[\cos(rz)+\frac{\omega^2}{gr}\sin(rz)\right]\mathrm{e}^{\mathrm{i}(k_n x-\omega t)}\mathrm{d}\omega \\ &+\frac{\rho_l}{\pi}\int_0^{\infty}\frac{-H_1|_{k=k_{01}}A_{01}}{k_{01}\partial_k H_2|_{k=k_{01}}}\left[\cosh(rz)+\frac{\omega^2}{gr}\sinh(rz)\right]\mathrm{e}^{\mathrm{i}(k_{01}x-\omega t)}\mathrm{d}\omega \\ &+\frac{\rho_l}{\pi}\int_{\omega_{00}}^{\infty}\frac{-H_1|_{k=k_{00}}A_{00}}{k_{00}\partial_k H_2|_{k=k_{00}}}\left[\cosh(rz)+\frac{\omega^2}{gr}\sinh(rz)\right]\mathrm{e}^{\mathrm{i}(k_{00}x-\omega t)}\mathrm{d}\omega.\end{aligned} \tag{4.3.142}$$

Similarly, the surface elevation is given by

$$\eta = \frac{1}{g\pi}\sum_{n=1}^{N}\int_{\omega_n}^{\infty}\frac{-H_1|_{k=k_n}A_n}{k_n\partial_k H_2|_{k=k_n}}e^{i(k_n x-\omega t)}d\omega + \frac{1}{g\pi}\int_{0}^{\infty}\frac{-H_1|_{k=k_{01}}A_{01}}{k_{01}\partial_k H_2|_{k=k_{01}}}e^{i(k_{01}x-\omega t)}d\omega + \frac{1}{g\pi}\int_{\omega_{00}}^{\infty}\frac{-H_1|_{k=k_{00}}A_{00}}{k_{00}\partial_k H_2|_{k=k_{00}}}e^{i(k_{00}x-\omega t)}d\omega. \tag{4.3.143}$$

4.4 Improved critical frequency approximations

In a practical application of (4.3.142) and (4.3.143) numerical solutions approximate the integrals over a finite range, and so knowledge of the critical frequencies ω_n, ω_{00} is essential. The critical frequencies ω_n represent the cutoff for acoustic–gravity wave mode numbers $n \geq 2$, and ω_{00} is the cutoff for the surface wave mode 00. The first acoustic–gravity wave mode does not have a cutoff frequency, see Figure 4.9b. An approximation for ω_n exists in the form of (4.4.144), [25], but this approximation is based upon the location of the vertical asymptotes found in the dispersion relation plots, an example of which is shown in Figure 4.9a. This approximation - although compact and easy to use - is not as accurate as it might be. The following subsections construct a more accurate approximation for ω_n (albeit more complicated), and an approximation to the surface wave mode 00 cutoff frequency based on the gradient condition (4.3.98).

4.4.1 Acoustic–gravity waves

When the acoustic–gravity wave propagating modes ($n = 2,3,...$) terminate, the phase velocity becomes equal to C_s and $s = \sqrt{k^2 - \frac{\omega^2}{C_s^2}} = 0$ [25]. The first progressive mode ($n = 1$) for an elastic seabed is a Scholte wave, which propagates all the way to the shore, where it turns into a Rayleigh wave. From 25, (30) the critical frequency for a particular depth is given by

$$\omega_{en} = \left(n - \frac{3}{2}\right)\pi\frac{C_l C_s}{h_{en}\sqrt{C_s^2 - C_l^2}} \quad n = 2,3,..., \tag{4.4.144}$$

which is a good approximation to the actual critical frequency, though it is based on the location of the vertical asymptotes in the dispersion relation plot - location of red dot in Figure 4.9a. For accuracy, we require a better approximation to the actual intersection of the two curves in the dispersion relation plot - blue dot in Figure 4.9a.

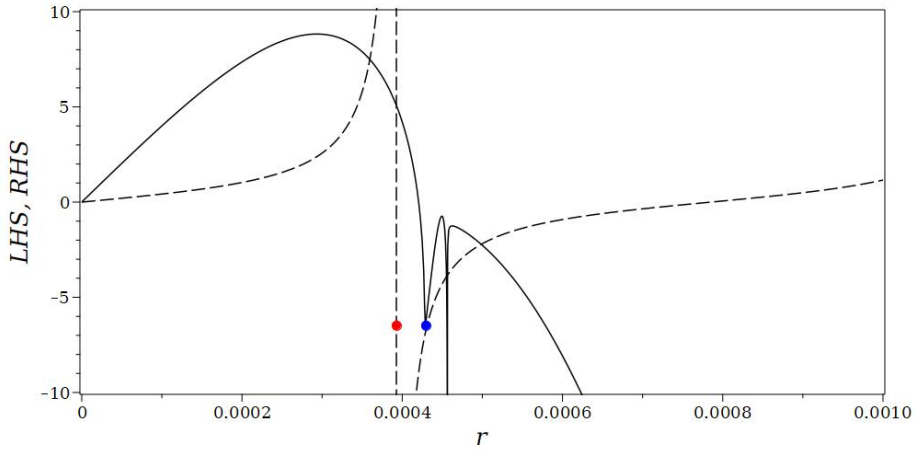

(a)

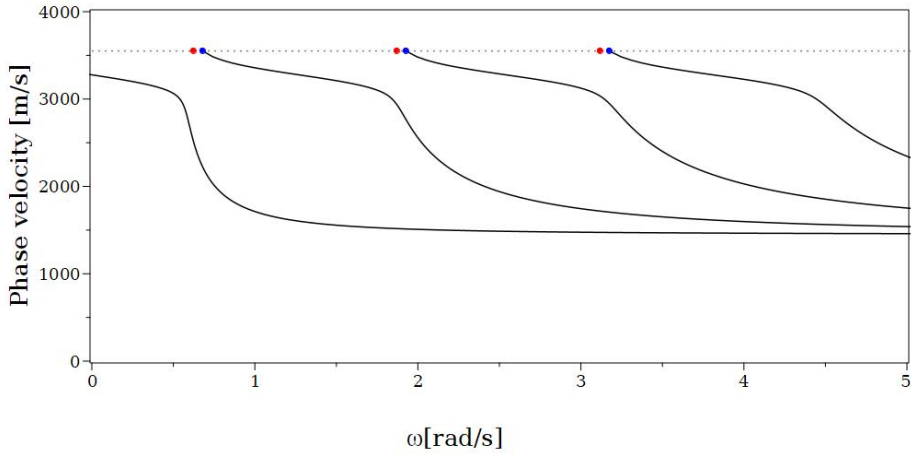

(b)

Figure 4.9: Approximate critical values from (4.4.144) - (red dots), actual critical values (blue dots). Fig 4.9a is the dispersion relation plot for $h = 4000$ m . Red dot marks vertical asymptote. Blue dot marks r_2 - the actual cutoff for mode 2. Dash trace LHS (4.3.65), solid trace RHS (4.3.65). Fig 4.9b Phase velocity curves for first four modes at constant depth of $h = 4000$ m. Dotted line is $C_s = 3550\,\mathrm{ms}^{-1}$

Begin with the dimensionless form of the dispersion relation (4.3.65)

$$\tanh(\tilde{r}) = \frac{\frac{\tilde{\omega}^2}{\tilde{r}}(\varepsilon_2+\varepsilon_1)}{\frac{\tilde{\omega}^4}{\tilde{r}^2}\varepsilon_2+\varepsilon_1}, \quad \varepsilon_1 = \frac{4\tilde{k}^2\tilde{q}\tilde{s}\tilde{\mu}}{\tilde{k}^2+\tilde{s}^2} + \tilde{\lambda}\tilde{k}^2 - \left(\tilde{\lambda}+2\tilde{\mu}\right)\tilde{q}^2, \quad \varepsilon_2 = \tilde{q}\left(\frac{\tilde{k}^2-\tilde{s}^2}{\tilde{k}^2+\tilde{s}^2}\right) \tag{4.4.145}$$

with $r, k, q, s, \omega, \lambda, \mu, C_l, C_s, C_p$ made dimensionless according to

$$\begin{aligned} &\tilde{r} = hr \quad \tilde{k} = hk \quad \tilde{q} = hq \quad \tilde{s} = hs \quad \tilde{\omega} = \sqrt{\frac{h}{g}}\omega \quad \tilde{\lambda} = \frac{\lambda}{\rho_l g h} \\ &\tilde{\mu} = \frac{\mu}{\rho_l g h} \quad \tilde{C}_l = \frac{C_l}{\sqrt{gh}} \quad \tilde{C}_s = \frac{C_s}{\sqrt{gh}} \quad \tilde{C}_p = \frac{C_p}{\sqrt{gh}}. \end{aligned} \tag{4.4.146}$$

Substitute (4.4.147) into (4.4.145) to obtain a function of $\tilde{r}$ alone, followed by the substitution $\tilde{r} \Rightarrow \mathrm{i}\tilde{r}$ to retrieve the acoustic–gravity wave solutions.

$$\tilde{k} = \sqrt{\tilde{r}^2 + \frac{\tilde{\omega}^2}{\tilde{C}_l{}^2}}, \quad \tilde{q} = \sqrt{\tilde{r}^2 + \frac{\tilde{\omega}^2}{\tilde{C}_l{}^2} - \frac{\tilde{\omega}^2}{\tilde{C}_p{}^2}}, \quad \tilde{s} = \sqrt{\tilde{r}^2 + \frac{\tilde{\omega}^2}{\tilde{C}_l{}^2} - \frac{\tilde{\omega}^2}{\tilde{C}_s{}^2}}, \tag{4.4.147}$$

Let $\tilde{\omega} = \frac{\tilde{r}\tilde{C}_s\tilde{C}_l}{\sqrt{\tilde{C}_s{}^2-\tilde{C}_l{}^2}}$, which is the $\tilde{s} = 0$ condition for the termination of progressive modes, and then let $\tilde{r} = \left(n-\frac{3}{2}\right)\pi + \delta(n)$, where $\delta(n)$ represents a small (mode dependent) positive offset away from the vertical asymptotes located at $\tilde{r} = \left(n-\frac{3}{2}\right)\pi$. With

$$R = \sqrt{-\frac{(2n\pi - 3\pi + 2\delta)^2\tilde{C}_l{}^2\left(\tilde{C}_p{}^2 - \tilde{C}_s{}^2\right)}{\tilde{C}_p{}^2\left(\tilde{C}_l{}^2 - \tilde{C}_s{}^2\right)}} \tag{4.4.148}$$

the dispersion relation now becomes

$$\begin{aligned} &\tan\left[\left(n-\frac{3}{2}\right)\pi+\delta\right] = \\ &\frac{-4\tilde{C}_s{}^2\left\{\frac{1}{4}\tilde{C}_p{}^2\left(\tilde{C}_l{}^2-\tilde{C}_s{}^2\right)R + \tilde{C}_l{}^2\left[\left(n-\frac{3}{2}\right)\pi+\delta\right]^2\left[\left(-\tilde{\mu}-\frac{\tilde{\lambda}}{2}\right)\tilde{C}_s{}^2 + \tilde{\mu}\tilde{C}_p{}^2\right]\right\}}{\left[\left(n-\frac{3}{2}\right)\pi+\delta\right]\left\{\tilde{C}_s{}^4\tilde{C}_l{}^2\tilde{C}_p{}^2R - 4\left(\tilde{C}_l{}^2-\tilde{C}_s{}^2\right)\left[\left(-\tilde{\mu}-\frac{\tilde{\lambda}}{2}\right)\tilde{C}_s{}^2 + \tilde{\mu}\tilde{C}_p{}^2\right]\right\}} \end{aligned} \tag{4.4.149}$$

The desired $\delta(n)$ is the $\tilde{r}$ separation between the blue and red dots in Figure 4.9a. Ignoring terms of $O(\delta(n)^2)$ in (4.4.149) an approximation of the dispersion relation can be written as

$$-\cot(\delta(n)) = \frac{a_n + b_n\delta(n)}{c_n + d_n\delta(n)}, \tag{4.4.150}$$

where the coefficients a_n, b_n, c_n, d_n are

$$a_n = -2\pi\tilde{C_s}^2\tilde{C_p}^2\left(\tilde{C_l}^2-\tilde{C_s}^2\right)\sqrt{\frac{(2n-3)^2\tilde{C_l}^2\left(\tilde{C_s}^2-\tilde{C_p}^2\right)}{\tilde{C_p}^2\left(\tilde{C_l}^2-\tilde{C_s}^2\right)}}+4\pi^2\tilde{C_s}^2\tilde{C_l}^2\left(n-\frac{3}{2}\right)^2\left[\left(\tilde{\lambda}+2\tilde{\mu}\right)\tilde{C_s}^2-2\tilde{\mu}\tilde{C_p}^2\right],$$

$$b_n = -2\tilde{C_s}^2\tilde{C_p}^2\frac{\left(\tilde{C_l}^2-\tilde{C_s}^2\right)}{\left(n-\frac{3}{2}\right)}\sqrt{\frac{(2n-3)^2\tilde{C_l}^2\left(\tilde{C_s}^2-\tilde{C_p}^2\right)}{\tilde{C_p}^2\left(\tilde{C_l}^2-\tilde{C_s}^2\right)}}+8\pi\tilde{C_s}^2\tilde{C_l}^2\left(n-\frac{3}{2}\right)\left[\left(\tilde{\lambda}+2\tilde{\mu}\right)\tilde{C_s}^2-2\tilde{\mu}\tilde{C_p}^2\right],$$

$$c_n = 2\left(n-\frac{3}{2}\right)\pi^2\tilde{C_s}^4\tilde{C_l}^2\tilde{C_p}^2\sqrt{\frac{(2n-3)^2\tilde{C_l}^2\left(\tilde{C_s}^2-\tilde{C_p}^2\right)}{\tilde{C_p}^2\left(\tilde{C_l}^2-\tilde{C_s}^2\right)}}+4\pi\left(n-\frac{3}{2}\right)\left(\tilde{C_l}^2-\tilde{C_s}^2\right)\left[\left(\tilde{\lambda}+2\tilde{\mu}\right)\tilde{C_s}^2-2\tilde{\mu}\tilde{C_p}^2\right],$$

$$d_n = 4\pi\tilde{C_s}^4\tilde{C_l}^2\tilde{C_p}^2\sqrt{\frac{(2n-3)^2\tilde{C_l}^2\left(\tilde{C_s}^2-\tilde{C_p}^2\right)}{\tilde{C_p}^2\left(\tilde{C_l}^2-\tilde{C_s}^2\right)}}+4\left(\tilde{C_l}^2-\tilde{C_s}^2\right)\left[\left(\tilde{\lambda}+2\tilde{\mu}\right)\tilde{C_s}^2-2\tilde{\mu}\tilde{C_p}^2\right]. \tag{4.4.151}$$

Then using the approximation $-\cot(\delta(n)) \simeq -\frac{1}{\delta(n)}$ for small $\delta(n)$, (4.4.150) can be put into quadratic form

$$b_n\delta(n)^2+(a_n+d_n)\delta(n)+c_n=0. \tag{4.4.152}$$

This can be solved for $\delta(n)$, and then the value of $\tilde{r}_n$ and the critical frequency ω_n can be obtained from

$$\tilde{r}_n=\left(n-\frac{3}{2}\right)\pi+\delta(n). \tag{4.4.153}$$

To determine how well the $\delta(n)$ predicts the offset a comparison was made between the approximate value of ω_n calculated using (4.4.153) and that found by using the dispersion relation

$$\text{error }[\%]=\left|\frac{\omega_n(\text{approx})-\omega_n(\text{dispersion})}{\omega_n(\text{dispersion})}\times 100\right|. \tag{4.4.154}$$

The comparison was carried out for depths ranging from 500 m to 8000 m and all available modes. The maximum error occurred in the second mode at a depth of 8000 m, but was still less than 0.1% - see Figure 4.10. In Section 4.5 the results for $\tilde{r}_n$ and $\delta(n)$ are used to construct approximate phase velocity curves.

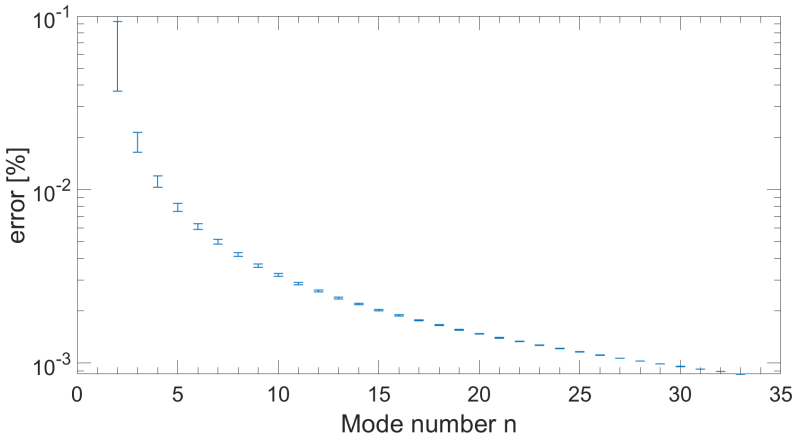

Figure 4.10: Percentage error for approximate critical frequencies ω_n from (4.4.153). Depths range between 500 m (lower error bound) and 8000 m (upper error bound) - all available modes.

4.4.2 Surface wave

The surface gravity mode 00 does not exist for all frequencies in the elastic seabed case and never exists for a rigid seabed. The cutoff condition for mode 00 is given by (4.3.98) which can be solved numerically to find the cutoff frequency at any particular depth. Alternatively a good approximation can be obtained by seeking the frequency at which the gradient of the left-hand-side of the dimensionless dispersion relation in (4.4.145) is equal to the right-hand side. This will occur for small (ultimately zero) $\tilde{r}$. In this case make the approximation $\tanh(\tilde{r}) \simeq \tilde{r}$. Now differentiate (4.4.145) with respect to $\tilde{r}$. Then express result as a series in $\tilde{r}^2$ to arrive at

$$1 = \frac{1}{\tilde{\omega}^2} + \frac{\mathscr{A}}{\tilde{\omega}} + O(\tilde{r}^2). \tag{4.4.155}$$

In the limit $\tilde{r} \to 0$ (4.4.155) can be written as the quadratic $\tilde{\omega}^2 - \mathscr{A}\tilde{\omega} - 1 = 0$ with

$$\mathscr{A} = 2\frac{\left[\left(\tilde{\mu} + \frac{\tilde{\lambda}}{2}\right)\tilde{C}_l^2 - \tilde{\mu}\tilde{C}_p^2\right]\left(2\tilde{C}_s^2 - \tilde{C}_l^2\right)\sqrt{\tilde{C}_s^2 - \tilde{C}_l^2} + 2\tilde{C}_p\tilde{C}_s\tilde{\mu}\sqrt{\tilde{C}_p^2 - \tilde{C}_l^2}\left(\tilde{C}_s^2 - \tilde{C}_l^2\right)}{\tilde{C}_l^3\tilde{C}_p\sqrt{\tilde{C}_p^2 - \tilde{C}_l^2}\sqrt{\tilde{C}_s^2 - \tilde{C}_l^2}}. \tag{4.4.156}$$

Taking the positive root of the quadratic gives the approximate cutoff frequency which we will name $\tilde{\Omega}_{00}$. The dimensional form can be recovered from $\Omega_{00} = \tilde{\Omega}_{00}\sqrt{g/h}$. A workable approximation to the cutoff frequency can be obtained by taking $\mathscr{A}$ - call this approximation $\mathscr{A}_{00}$. Table 4.1 gives values for ω_{00} found using a numeric solver and compares with the approximations Ω_{00} and $\mathscr{A}_{00}$ indicating errors for various depths. The

error values were calculated from

$$\text{error } [\%] = \left| \frac{\Omega_{00}(\text{ or} \mathscr{A}_{00}) - \omega_{00}}{\omega_{00}} \times 100 \right|. \tag{4.4.157}$$

h [m]	ω_{00} [rads^{-1}]	Ω_{00} [rads^{-1}]	error [%]	$\mathscr{A}_{00}$ [rads^{-1}]	error [%]
1000	27.79791617	27.79788874	9.86765E-05	27.79753583	0.001368232
2000	13.89917645	13.89912044	0.000402974	13.89876753	0.002942045
3000	9.266281835	9.266198102	0.000903631	9.265845209	0.00471198
4000	6.949848492	6.949736802	0.001607085	6.949383913	0.006684736
5000	5.559999661	5.559859937	0.002513022	5.559507051	0.008859893
6000	4.633443082	4.633275403	0.003618886	4.632922521	0.011234863
7000	3.971624933	3.971429412	0.004922947	3.971076536	0.013807875
8000	3.475268301	3.475044738	0.006432971	3.474691865	0.016586806
9000	3.089219349	3.088967935	0.008138431	3.088615067	0.019560994
10000	2.78038577	2.780106363	0.010049217	2.779753499	0.022740406
11000	2.527708826	2.52740152	0.012157492	2.527048661	0.02611713

Table 4.1: Comparison of cutoff frequencies obtained from numeric solver (ω_{00}) with approximations from quadratic solution (Ω_{00}) and coarse approximation $\mathscr{A}_{00}$ for various depths h.

4.5 Approximate phase velocity curves - shearing method

When plotting phase velocity curves it is typical to choose one or other of the following scenarios, either, (i) fix constant frequency ω and plot phase velocity vs depth h as in [25] Figure 2a or, (ii) fix a constant depth and plot phase velocity vs frequency (as in this chapter). In either case for each data point on every curve the dispersion relation has to be solved numerically which can be time consuming. Also, care has to be taken to ensure solutions are valid. The facility to quickly produce approximate phase velocity curves may help in reducing the computational burden in real-time analysis. In a side-by-side comparison of the shearing method against the dispersion solving method, the shearing method was found to be approximately twice as fast. The comparison was run on the same computer (Intel(R) i9 CPU, 3.60 GHz, 128GB RAM) and used the same software (Maple) to produce phase velocity curves for 16 modes with $\omega = 20\,\text{rads}^{-1}$ and depth of $h = 4000$ m.

Here we present an alternative method for quickly plotting an approximate version of the elastic seabed phase velocity curves. The rational behind the method is to first con-

struct a template curve for the phase velocity by manipulating the $\tanh^{-1}$ function, Then utilise the observation that the phase velocity curves for the rigid seabed case "encode" the degree of shearing required to produce the elastic phase velocity curves. However, before the rigid phase velocity curves can be used in this sense they have to be "inverted" - see Figure 4.17a and 4.17b.

In the following variables with a tilde are made dimensionless according to (4.4.146). The method is based around the $\tanh^{-1}$ function which is manipulated in the following ways:

1. Scale along the horizontal $\tilde{r}$ axis (the independent variable) so as to fit the range $\left(n-\frac{3}{2}\right)\pi \cdots \left(n-\frac{1}{2}\right)\pi$, with n being the mode number (Figure 4.11)

$$-\tanh^{-1}\left[\frac{2}{\pi}(\tilde{r}-(n-1)\pi)\right]. \tag{4.5.158}$$

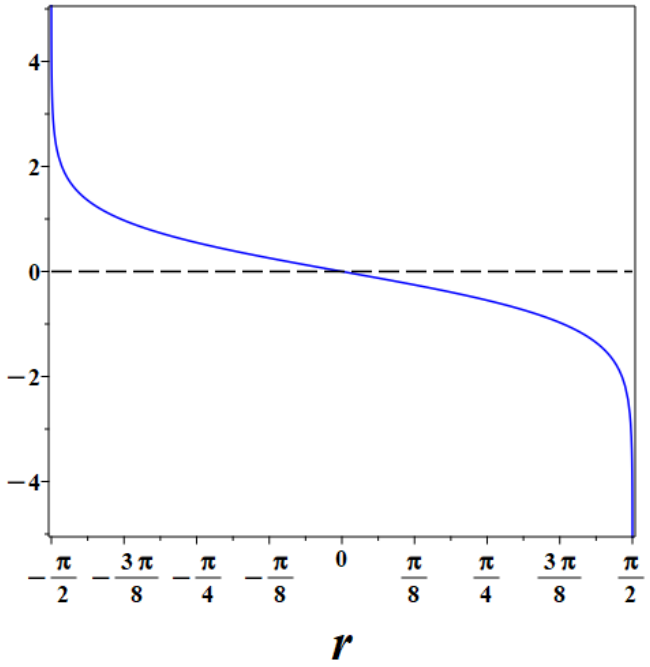

Figure 4.11: Plot of the function $-\tanh^{-1}\left[\frac{2}{\pi}(\tilde{r}-(n-1)\pi)\right]$ when $n=1$.

2. Shift up the vertical axis so that at centre range $\tilde{r}=(n-1)\pi$ the value is $\alpha\tilde{C}_s$ - the Rayleigh wave phase velocity where the first acoustic mode intersects the vertical axis, see Figure 4.9b and 4.12. The value of $\alpha = 0.922231$ is taken from [30].

$$\alpha\tilde{C}_s - \tanh^{-1}\left[\frac{2}{\pi}(\tilde{r}-(n-1)\pi)\right]. \tag{4.5.159}$$

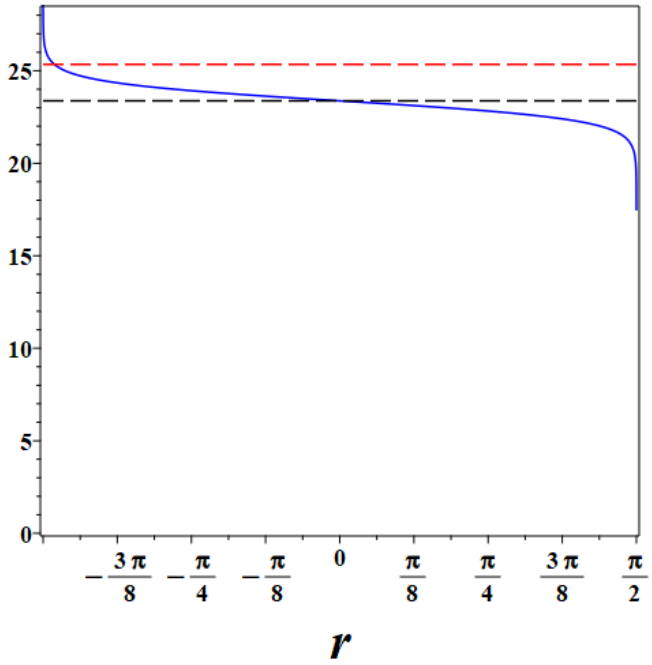

Figure 4.12: Plot of the function $\alpha\tilde{C}_s - \tanh^{-1}\left[\frac{2}{\pi}(\tilde{r}-(n-1)\pi)\right]$ when $n=1$.

3. Next, stretch the plot along the vertical axis by a factor $\tilde{\kappa}(n)$ so that the curve hits the shear velocity $\tilde{C}_s$ at the critical value $\tilde{r}_n$ determined from (4.4.153)

$$\alpha\tilde{C}_s - \tilde{\kappa}(n)\tanh^{-1}\left[\frac{2}{\pi}(\tilde{r}-(n-1)\pi)\right], \tag{4.5.160}$$

where

$$\tilde{\kappa}(n) = \frac{\tilde{C}_s(\alpha-1)}{\tanh^{-1}\left[\frac{2}{\pi}\left(-\frac{\pi}{2}+\delta(n)\right)\right]}, \tag{4.5.161}$$

and $\delta(n)$ is the critical offset calculated via the procedure described in Section 4.4 - see Figure 4.13.

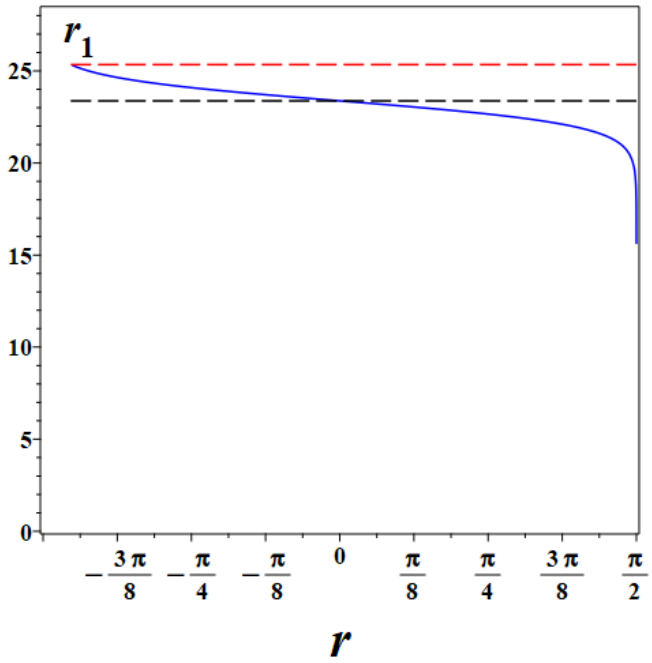

Figure 4.13: Plot of the function $\alpha\tilde{C}_s - \tilde{\kappa}(n)\tanh^{-1}\left[\frac{2}{\pi}(\tilde{r}-(n-1)\pi)\right]$ when $n=1$. In this example $\delta(1)=0.1464196273$, $\tilde{\kappa}(n)=1.306037799$ and $\tilde{r}_1=-1.4243767$

4. Include a multiplicative factor $\tilde{Y}(\tilde{r},n)$ to ensure that the curve has its region of rapid desent shifted away from the $\left(n-\frac{1}{2}\right)\pi$ asymptote to better align with the "reference" phase velocity curves derived from the dispersion relation, and so help minimise errors. The function $\tilde{v}(\tilde{r},n)$ so obtained is the generating function from which all the phase velocity curves are derived

$$\tilde{v}(\tilde{r},n)=\alpha\tilde{C}_s-\tilde{Y}(\tilde{r},n)\tilde{\kappa}(n)\tanh^{-1}\left[\frac{2}{\pi}(\tilde{r}-(n-1)\pi)\right], \tag{4.5.162}$$

where

$$\tilde{Y}(\tilde{r},n)=\frac{\left(n-\frac{1}{2}\right)\pi-\tilde{r}}{\sqrt{\left[\left(n-\frac{1}{2}\right)\pi-\tilde{r}\right]^2-\left(\frac{\pi}{18}\right)^2}}. \tag{4.5.163}$$

See Figure 4.14.

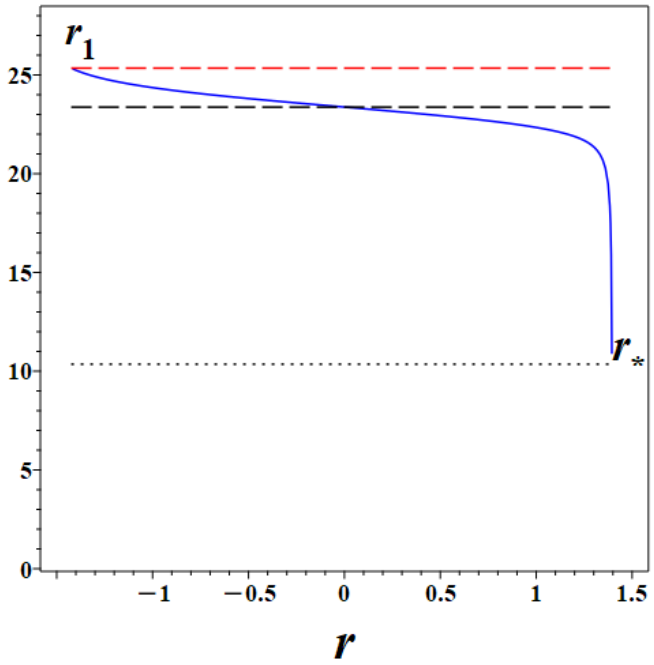

Figure 4.14: Plot of the function $\tilde{v}(\tilde{r},n)$ when $n=1$. In this example $\delta(1) = 0.1464196273$, $\tilde{\kappa}(n) = 1.306037799$, $\tilde{r}_1 = -1.4243767$ and $\tilde{r}_* \approx \frac{\pi}{2} - \frac{\pi}{18}$.

The resulting curve for the case $n=1$ is shown in Figure 4.15. Curves for higher modes are obtained by shifting the $n=1$ case by appropriate multiples of π along the positive $\tilde{r}$ axis. The variable $\tilde{r}$ ranges over the interval $\tilde{r}_n \le \tilde{r} \le (\tilde{r}_* - \epsilon)$ with $0 < \epsilon \ll 1$, defined by $\left(n-\frac{3}{2}\right)\pi < \tilde{r}_n \le \tilde{r} \le (\tilde{r}_* - \epsilon) < \left(n-\frac{1}{2}\right)\pi$ and $\tilde{r}_*$ is such that $\tilde{v}(\tilde{r}_*,n) = \tilde{C}_l$. This represents the phase velocity asymptotically approaching C_l with increasing frequency (all modes).

5. Take the generating function for each mode and translate, so that the known point $(\tilde{\omega}_n, \tilde{C}_s) \to (0,0)$. This is the black curve $\tilde{t}(\tilde{r},n)$ in Figure 4.16

$$\tilde{t}(\tilde{r},n) = \tilde{r}\frac{\tilde{C}_s\tilde{C}_l}{\sqrt{\tilde{C}_s^2 - \tilde{C}_l^2}} + \mathrm{i}\tilde{v} - \tilde{z}_n, \quad \tilde{z}_n = \tilde{r}_n\frac{\tilde{C}_s\tilde{C}_l}{\sqrt{\tilde{C}_s^2 - \tilde{C}_l^2}} + \mathrm{i}\tilde{C}_s, \quad \tilde{r}_n = \left(n - \frac{3}{2}\right)\pi + \delta(n). \tag{4.5.164}$$

Where $\tilde{z}_n$ is a fixed complex number representing the known cutoff point $(\tilde{\omega}_n, \tilde{C}_s)$. In this example $\tilde{z}_1 = -16.15388791 + 25.34421543\mathrm{i}$ and $\tilde{r}_1 = -1.424376700$.

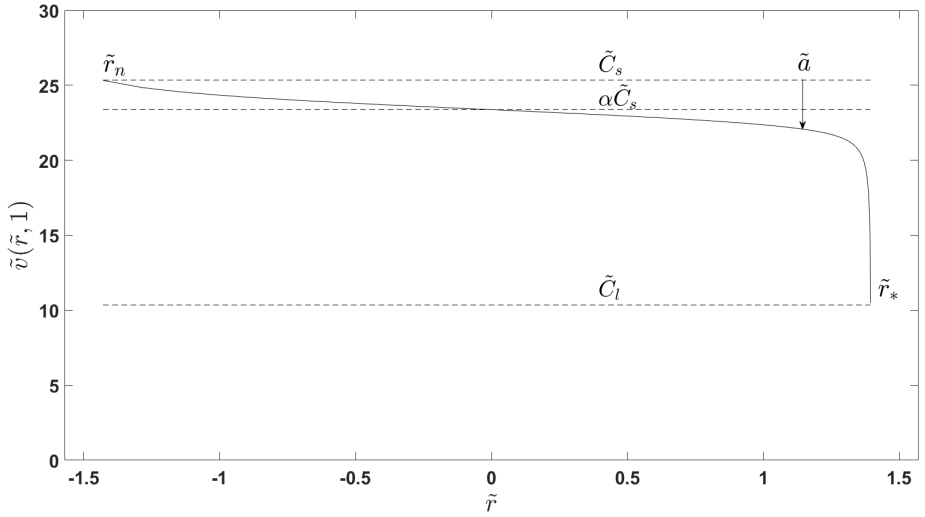

Figure 4.15: Generating function $\tilde{v}(\tilde{r},n)$ for first acoustic–gravity mode ($n=1$) with depth $h=2000$ m. Other modes are derived by shifting the horizontal axis through $(n-1)\pi$ and using the appropriate values for $\tilde{r}_n$ and $\tilde{r}_*$

6. Apply the shearing function $\tilde{S}(\tilde{a},n)$ to distort the black curve into the appropriate shape for the mode considered - the coloured curves $\tilde{z}_t$ in Figure 4.16

$$\tilde{z}_t = \left[\Re\left(\tilde{t}\right) - \tilde{S}\,\Im\left(\tilde{t}\right)\right] + \mathrm{i}\,\Im\left(\tilde{t}\right), \tag{4.5.165}$$

$$\tilde{S}(\tilde{a},n) = \frac{1}{\tilde{a}}\left[\tilde{w}(\tilde{a},n) - \tilde{w}(0,n)\right]. \tag{4.5.166}$$

The function $\tilde{w}(\tilde{a},n)$ is derived from the phase velocity curves for the rigid seabed case (Figure 4.17a) by inverting (4.5.167) to give $\tilde{\omega}$ in terms of rigid seabed phase velocity $\tilde{v}_r$

$$\tilde{v}_r = \frac{\tilde{\omega}}{\tilde{k}_n}, \quad \tilde{k}_n = \sqrt{\frac{\tilde{\omega}^2}{\tilde{C}_l^2} - \frac{\tilde{\omega}_{rn}^2}{\tilde{C}_l^2}}, \quad \tilde{\omega}_{rn} = \left(n-\frac{1}{2}\right)\pi\tilde{C}_l. \tag{4.5.167}$$

The expressions for $\tilde{k}_n$ and $\tilde{\omega}_{rn}$ appearing in (4.5.167) are from 16, (3.9), (3.10) here made dimensionless. After performing the inversion

$$\tilde{\omega} = \frac{\tilde{v}_r\tilde{\omega}_{rn}}{\sqrt{\tilde{v}_r^2 - \tilde{C}_l^2}} = \frac{\tilde{v}_r}{\sqrt{\tilde{v}_r{}^2 - \tilde{C}_l^2}}\left(n-\frac{1}{2}\right)\pi\tilde{C}_l. \tag{4.5.168}$$

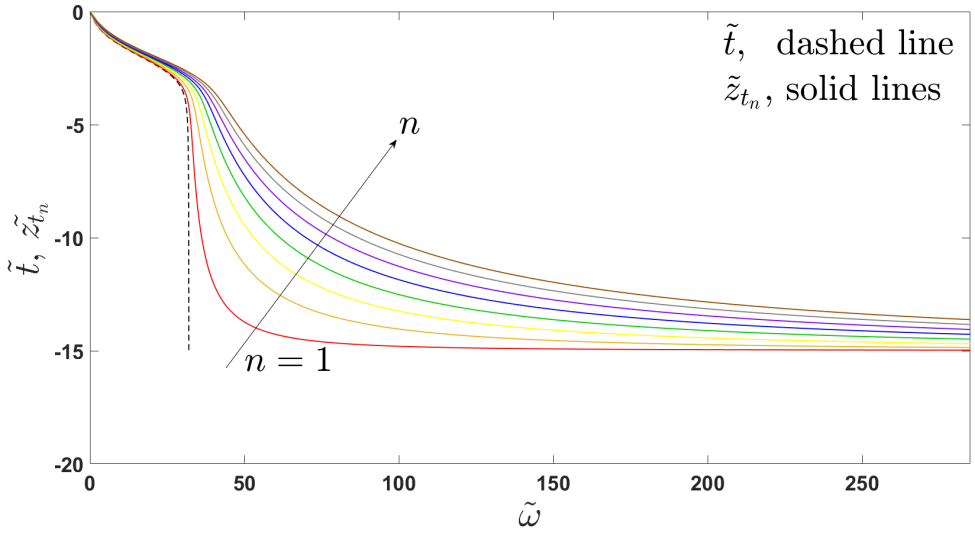

Figure 4.16: The black trace $\tilde{t}$ is sheared by the action of $\tilde{S}$ into each of the coloured curves for each mode. Depth in this case is 2000 m, first eight modes shown. Then the result is translated and scaled to give the final phase velocity curves.

Substitute $\tilde{v}_r = \tilde{C}_s - \tilde{a}$ into (4.5.168) then re-name $\tilde{\omega}$ to $\tilde{w}$ to arrive at

$$\tilde{w}(\tilde{a},n) = \frac{\tilde{C}_s - \tilde{a}}{\sqrt{\left(\tilde{C}_s - \tilde{a}\right)^2 - \tilde{C}_l^2}}\left(n - \frac{1}{2}\right)\pi\tilde{C}_l. \tag{4.5.169}$$

The function $\tilde{a}$ is a measure of the vertical drop from the constant line $\tilde{C}_s$ down to the phase velocity curves $\tilde{v}_r$, see Figure 4.17a. In order to apply $\tilde{S}(\tilde{a},n)$ to the generating function define $\tilde{a} = C_s - \tilde{v}(\tilde{r},n)$ so now $\tilde{a}$ represents the vertical drop from the constant line $\tilde{C}_s$ down to the phase velocity curves $\tilde{v}(\tilde{r},n)$ (see Figure 4.15).

7. Add $\tilde{z}_n$ to undo the translation from step 5

$$\tilde{z} = \tilde{z}_{t_n} + \tilde{z}_n = \left[\Re\left(\tilde{t}\right) - \tilde{S}\Im\left(\tilde{t}\right)\right] + \mathrm{i}\Im\left(\tilde{t}\right) + \tilde{z}_n. \tag{4.5.170}$$

8. Finally re-scale to obtain the desired phase velocity curves - solid black trace Figure 4.18

$$\omega + \mathrm{i}v_e = \tilde{\omega}\sqrt{\frac{g}{h}} + \mathrm{i}\tilde{v}_e\sqrt{gh} = \Re(\tilde{z})\sqrt{\frac{g}{h}} + \mathrm{i}\Im(\tilde{z})\sqrt{gh}. \tag{4.5.171}$$

The solid black trace of Figure 4.18 is a complex plot with real part representing the

angular frequency ω, and imaginary part representing the elastic seabed phase velocity v_e. The dashed curves of Figure 4.18 are those obtained by numerically solving the dispersion relation (4.3.65). To quantify the errors between the phase velocity obtained using the shearing method and that obtained by solving the dispersion relation use

$$\text{error } [\%] = \left| \frac{v_e(\text{shear}) - v_e(\text{dispersion})}{v_e(\text{dispersion})} \times 100 \right|. \tag{4.5.172}$$

The resulting error plot - Figure 4.19 - indicates that the maximum error occurs for the first mode and that errors decrease with increasing frequency and increasing mode number. There is some freedom in the expression for $\tilde{Y}(\tilde{r}, n)$ which could potentially reduce the errors a little by carefully replacing the $\pi/18$ term with an alternative value derived from some error minimisation technique (e.g. minimax approximation [54]), which we did not pursue further here.

4.6 Numerical results

4.6.1 Acoustic–gravity waves

Figure 4.20 compares the first acoustic mode for the elastic case (4.3.142) and the rigid case 1, (3.22). As in [25] the values used for ρ_l, ρ_s, C_l, C_s and C_p are average values taken from [31]. One obvious difference, is that the signal terminates after some time in the elastic case, whereas the signal continues indefinitely in the rigid case. Another difference is the presence of signal at times earlier than the main pulse in the elastic case, but no signal at all in the rigid stationary phase model. The phase velocity curves for the elastic case Figure 4.18 indicate that frequencies close to the critical frequency for each mode receive a boost in phase velocity enabling signals to propagate faster. For these frequencies speeds close to C_s are achievable. The rigid seabed stationary phase model produces complex numbers for times earlier than x/C_l due to a singularity induced by the stationary phase method [3]. The pressure amplitudes are similar.

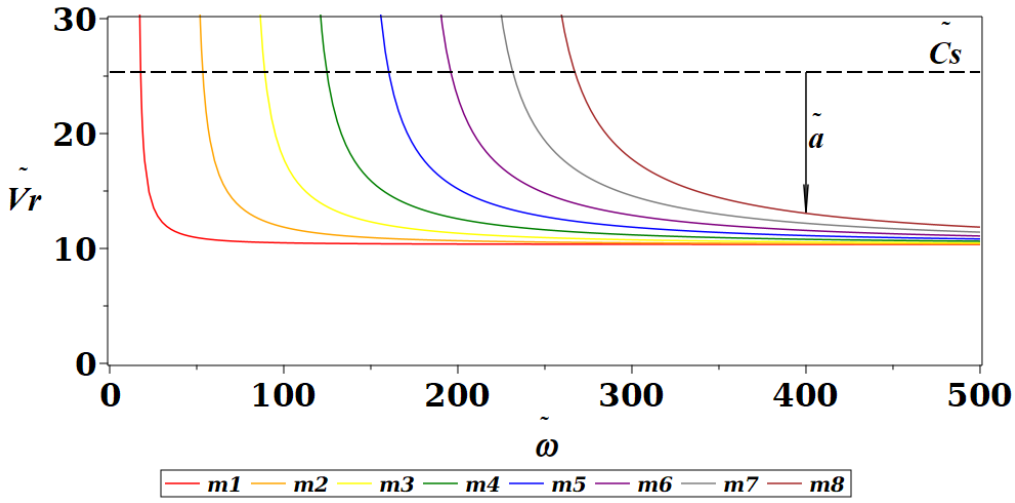

(a)

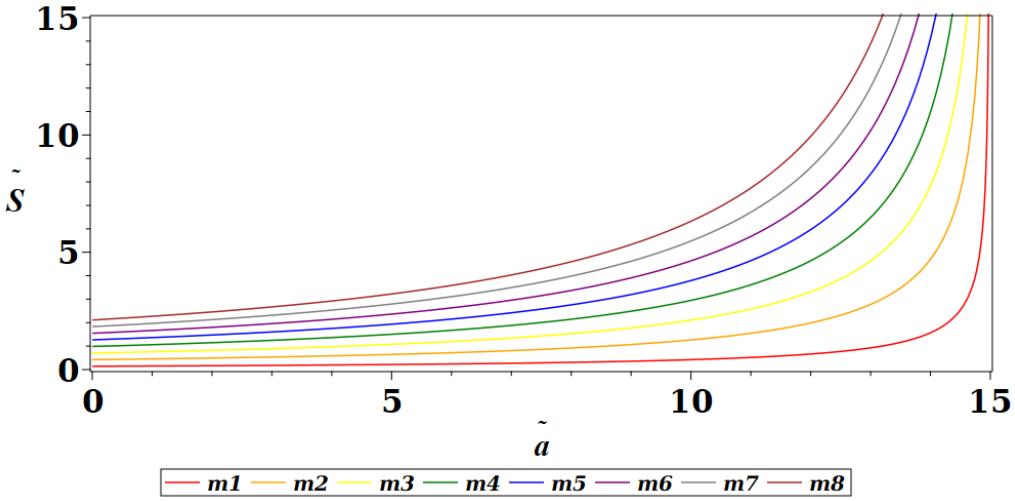

(b)

Figure 4.17: Rigid seabed phase velocity curves along with shearing function. Figure 4.17a shows rigid seabed phase velocity $\tilde{V}_r$ vs $\tilde{\omega}$. Depth $h = 2000$ m. First eight modes. Figure 4.17b is plot of shear function $\tilde{S}$ vs $\tilde{a}$. Depth $h = 2000$ m. First eight modes.

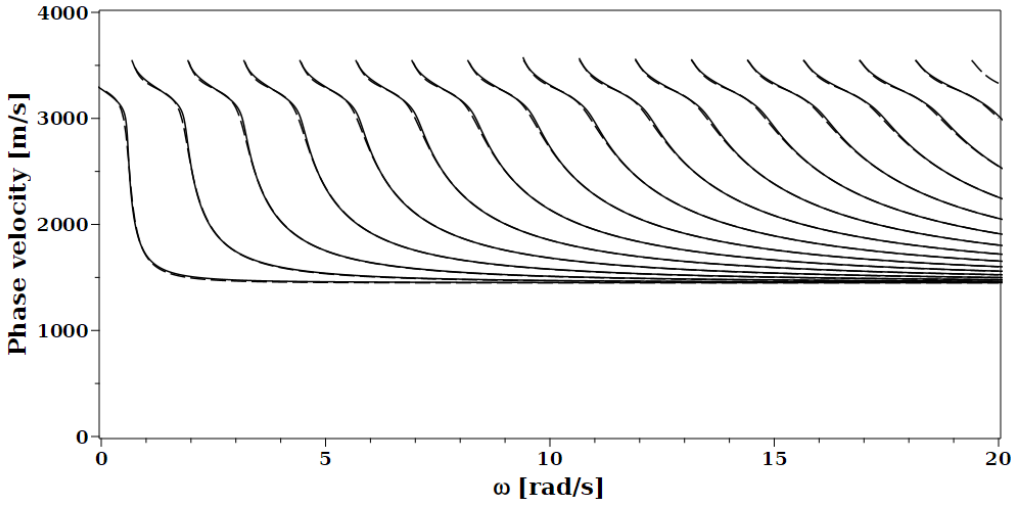

Figure 4.18: Overlay of phase velocity curves for depth of $h = 4000$ m. Solid black are the approximate curves, dashed are those obtained from solving the dispersion relation. First 16 modes shown.

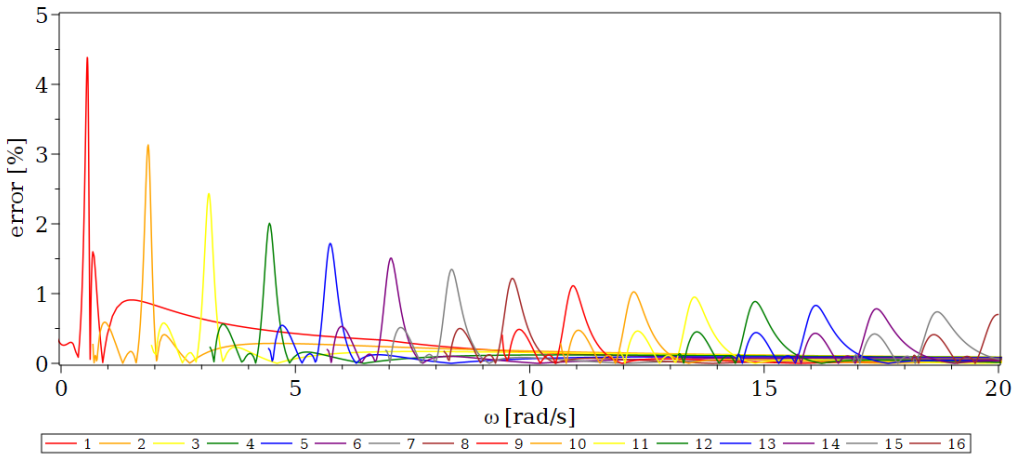

Figure 4.19: Percentage error for first 16 modes from Fig 4.18. The maximum error occurs at the knee of each phase velocity curve ($\approx 3000\,\mathrm{ms}^{-1}$). Depth $h = 4000$ m

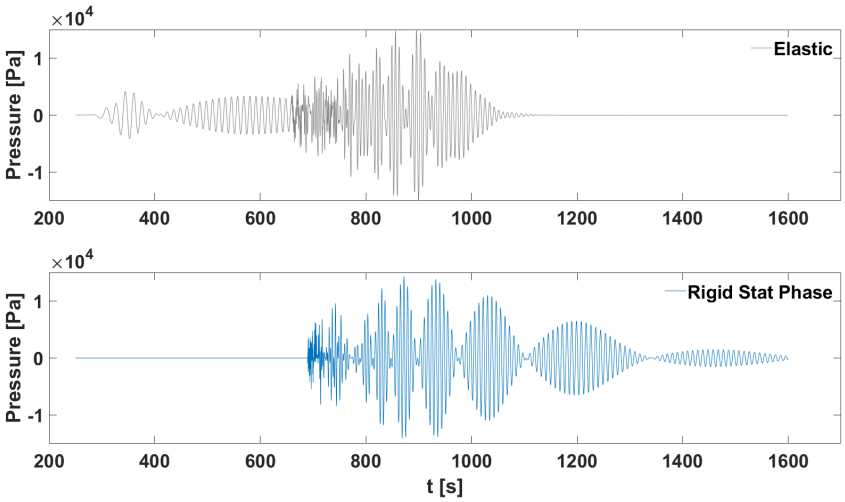

Figure 4.20: Top plot, first acoustic mode with elastic seabed, bottom plot with rigid seabed

Parameter	Description	Elastic	Rigid
g	Acceleration due to gravity	$9.81\ \mathrm{ms}^{-2}$	$9.81\ \mathrm{ms}^{-2}$
L	Fault half-length	400 km	400 km
b	Fault half-width	40 km	40 km
$2T$	Rupture duration	10 s	10 s
h	Water depth	4 km	4 km
ρ_l	Water density	$1020\ \mathrm{kgm}^{-3}$	$1020\ \mathrm{kgm}^{-3}$
ρ_s	Solid density	$2750\ \mathrm{kgm}^{-3}$	$\cdots$
C_l	Speed of sound in water	$1450\ \mathrm{ms}^{-1}$	$1450\ \mathrm{ms}^{-1}$
C_s	Speed of shear waves in solid	$3550\ \mathrm{ms}^{-1}$	$\cdots$
C_p	Speed of compression waves in solid	$6300\ \mathrm{ms}^{-1}$	$\cdots$
λ	Lamé first parameter	3.9833750×10^{10} Pa	$\cdots$
μ	Lamé second parameter	3.4656875×10^{10} Pa	$\cdots$
W_0	Uplift velocity	$0.1\ \mathrm{ms}^{-1}$	$0.1\ \mathrm{ms}^{-1}$

Table 4.2: Constants and parameters used in comparison of elastic seabed with rigid seabed.

A sensitivity analysis was carried out looking at the effects of six parameters on the signal duration - see Figure 4.21. Each parameter was varied individually away from its reference value, Table 4.2, while holding all other parameters at reference. Then the percentage change in pulse duration was divided by the percentage change in the parameter to arrive at the sensitivity value. It was found that the rigidity of the seabed most affected the signal duration. Increasing the Lamé parameters increases C_s and C_p in accordance with (4.2.8), the ratio C_p/C_s was kept constant.

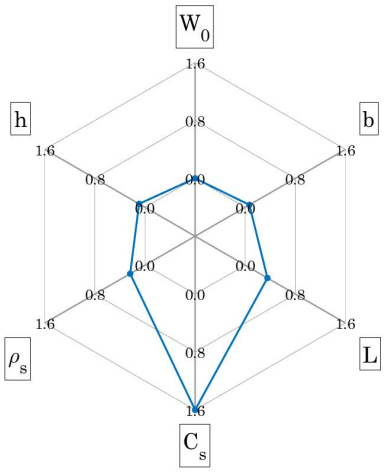

Figure 4.21: Response of signal duration when changing parameters.

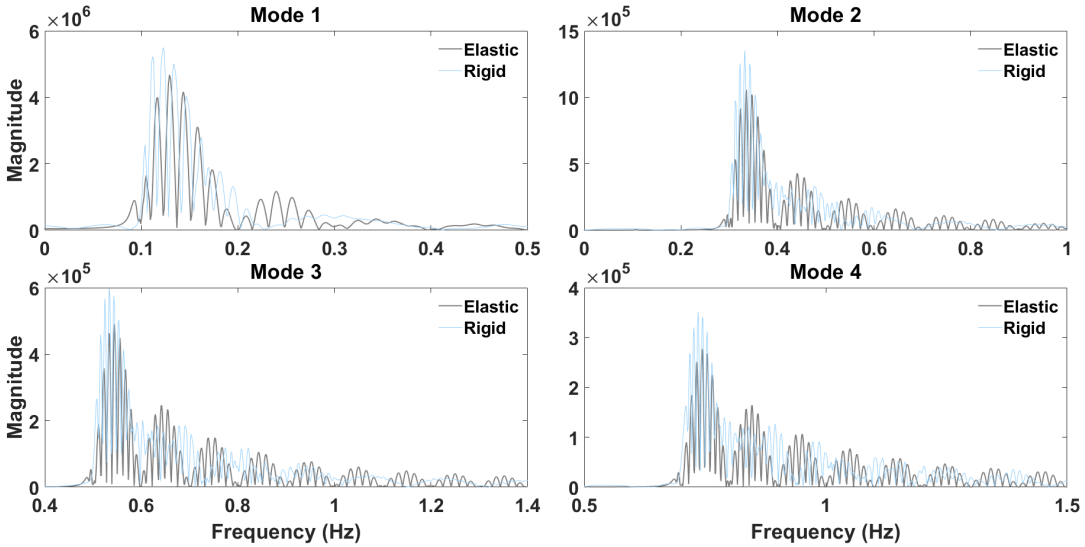

Figure 4.22: FFT of First four available modes $h = 4000$ m.

Another difference between the elastic seabed case and the rigid seabed case appears when a Fast Fourier Transform (FFT) of the signals is examined. The elastic case shows a slight upward shift in the frequency peak, see Figure 4.22. This is in contrast to the slight downward shift found when a viscous compressible sediment layer is overlying the seabed as in [26]. Whilst investigating the synthetic acoustic–gravity waves, we found that band-pass filtering applied to the signal generated by combining the first 10 modes (Figure 4.23a), revealed some interesting peaks located close to the expected arrival time for a phase velocity of C_l (Figure 4.23b). There are four peaks of particular interest labelled 1,2,3,4. The presence of the peaks is a consequence of the fault's geometry and motion, and is not related to the rigidity of the seabed, since the peaks are also present under rigid seabed conditions, and even when the signal considered was purely acoustic, as in [16]. The time spacing between pairs of peaks respond to changes in either fault half-width b, or rupture duration $\tau = 2T$ in a linear fashion, so that details of the fault's geometry and dynamics are encoded in the acoustic–gravity waves. Time Δt_1 between peak numbers 1 and 2 (or 3 and 4) is exactly the rupture duration, and Δt_2 between peaks 1 and 3 (or 2 and 4) is linearly related to the fault half-width through $\Delta t_2 = 2b/C_l$. When the slender fault begins to move peaks 1 and 3 are generated at the edges of the slender fault and begin to propagate. The time separation between these peaks is explained as the time required for a wave travelling at speed C_l to cross the fault width of $2b$. At the end of the fault's motion, after τ seconds, the second pair of peaks (2 and 4) is generated and propagates away - also separated in time by Δt_2. The resultant waveform as would be seen in the far-field is a collection of four peaks. The amplitude of the peaks depends linearly on the uplift velocity W_0. The timings between peaks agree well with the figures given in Table 4.3. Let the subscripts $1,2,3,4$ represent the peaks denoted by the numbers 1,2,3,4 respectively. Then, $\Delta t_{12} = 10.97\,s \quad \Delta t_{34} = 8.9\,s \quad \Delta t_{13} = 57.67\,s \quad \Delta t_{24} = 55.46\,s$. The times Δt_{12} and Δt_{34} represent τ - the uplift time - which (from Table 4.2) is actually 10 s. The times Δt_{13} and Δt_{24} are the transit times for an acoustic signal to cross the fault width $2b$, which again, from Table 4.2 is actually 55.17 s. The information that could be extracted from the timings embedded in the acoustic modes would be of interest to the inverse process that reconstructs fault parameters from received signals [17]. In Section 4.6.3 an actual hydrophone recording made during the Samoa 2009 event is filtered to reveal the four peaks encoded within it. [15] concludes that the acoustic modes have a frequency spectrum which depends on the time history and spatial structure of the bottom displacement - which is referred to as the tsunami's voice. This is exactly what we find encoded into the characteristic (four) peaks.

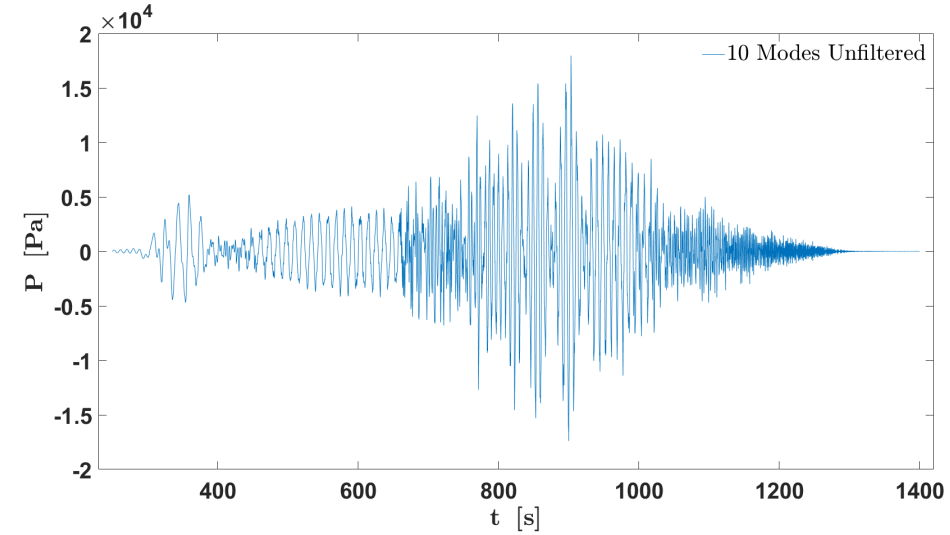

(a)

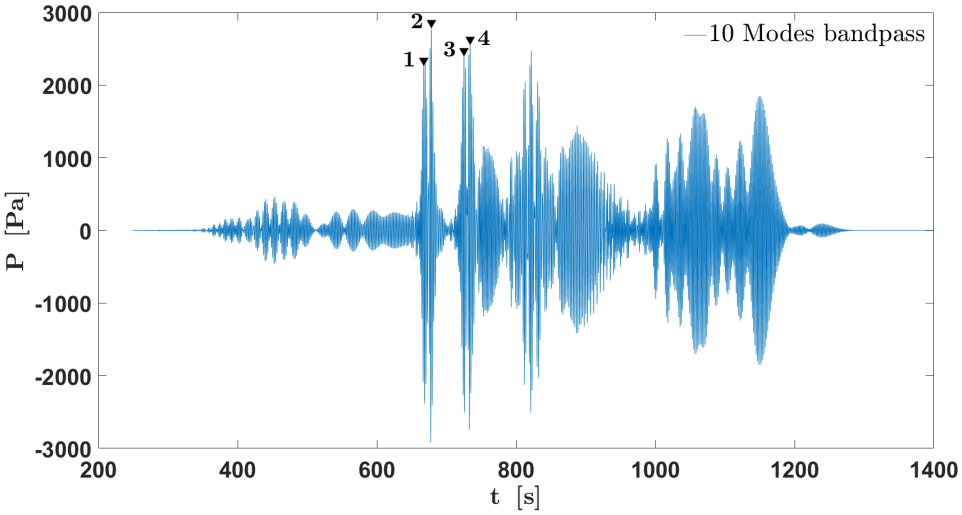

(b)

Figure 4.23: Band-pass filtering applied to the 10 combined modes of the synthetic acoustic–gravity wave generated by a single slender fault. The data in Figure 4.23a shows the first 10 modes combined and is sampled at a rate of 100 Hz. Figure 4.23b shows the resulting signal after application of band-pass filtering with passband 0.45 Hz to 0.6 Hz. The characteristic peaks are numbered 1,2,3,4. The passband was chosen to eliminate low/high frequencies.

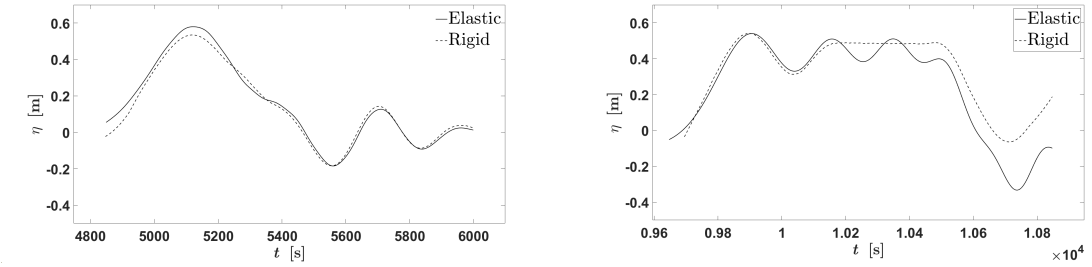

(a) (b)

Figure 4.24: Surface elevation comparison (elastic vs rigid). Co-ordinates are $x = 1000$ km, $y = 0$ km Co-ordinate origin at fault centroid. Figure 4.24a $h = 4000$ m. Figure 4.24b $h = 1000$ m

4.6.2 Surface wave

Consider now the surface waves generated by the single slender fault with parameters as per Table 4.2. The equations generating the surface waves are (4.3.143) for the elastic case, and 1, (3.23) for the rigid case. At a depth of $h = 4000$ m there is little difference between elastic and rigid cases (Figure 4.24a), but at the depth of $h = 1000$ m differences are more apparent (Figure 4.24b). In deeper water the surface wave is almost unaffected by the elasticity of the seabed [30]. This surface wave is the main tsunami, i.e. mode 01.

When the seabed is elastic the possibility of a second surface wave arises. This wave does not exist for all frequencies and never exists in the rigid case [30]. The gradient condition (4.3.98) has to be satisfied before mode 00 can propagate, see Figure 4.25. The mode 00 surface wave has a phase velocity C_l, and a negligible amplitude, in the order of μm. A plot of mode 00 under the conditions of Table 4.2 can be found in Figure 4.26. In the plot there are four distinct peaks numbered 1 to 4. These peaks in the mode 00 surface wave correspond to the peaks numbered 1,2,3,4 found in the acoustic signal. The assumption of a rectangular fault moving at a uniform speed results in symmetric peaks, whereas in reality the motion is much more complicated thus upsetting the symmetry of the peaks seen in Figure 4.26.

4.6.3 Hydrophone recordings

The theory developed in this chapter leading to the equations for pressure (4.3.142) and surface elevation (4.3.143) is linear. Therefore, as in [1], more complicated multi-fault scenarios can be constructed from single slender fault solutions by linear superposition, given that the parameters for each individual fault are known.

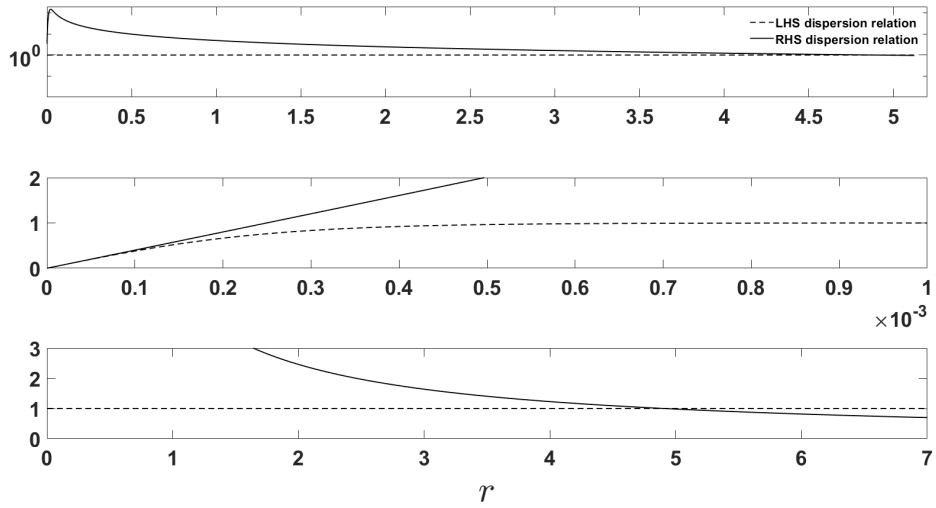

Figure 4.25: LHS of dispersion relation (4.3.65) - dash trace - and RHS of dispersion relation - solid trace - when $r \in \mathbb{R}$. The frequency is at the point where mode 00 becomes active $\omega \simeq 6.95\,\mathrm{rad\,s^{-1}}$, $h = 4000$ m (see Table 4.1). The top log-plot indicates overall behaviour. The next two plots provide an expanded view. The mode 00 solution in the middle plot where the solid curve touches the dashed curve $0 \leq r \leq 0.0001$, and the mode 01 solution (the usual tsunami) in the bottom plot where the solid curve again makes contact with the dashed curve in the descending phase $4 \leq r \leq 6$.

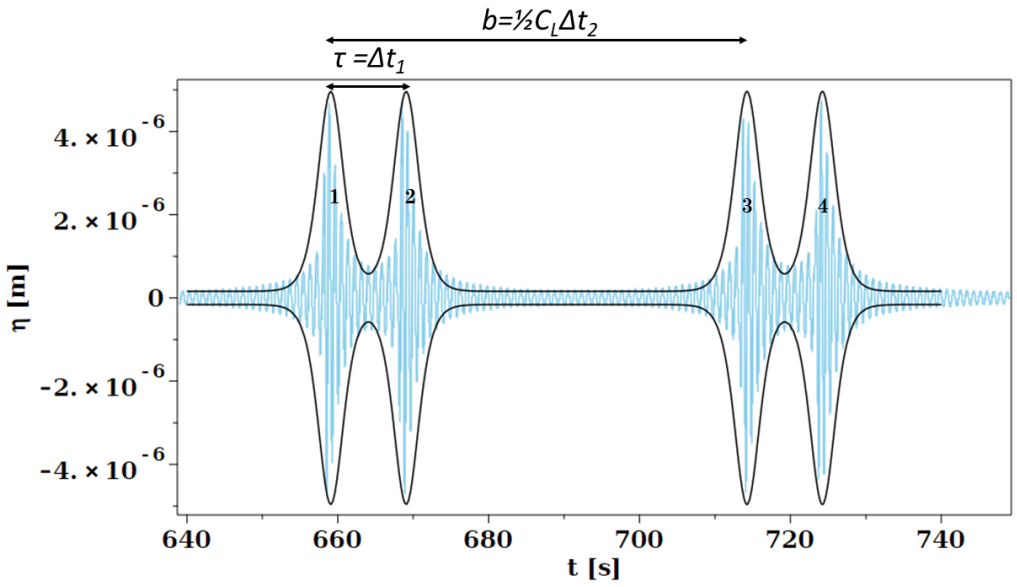

Figure 4.26: Mode 00 surface-gravity wave with envelope.

To contrast the case of elastic seabed with that of a rigid seabed we revisit the Sumatra 2004 earthquake discussed in Section 5.1.2 of [1]. The geographical area considered here ranges over $[70^\circ \ldots, 100^\circ]$E longitude and $[-15^\circ \ldots, 20^\circ]$N latitude. This curved patch on the (idealised) spherical earth is mapped to flat x, y coordinates. The conversion factor of meters per degree is fixed for the latitude (y) direction, but the meters per degree in the longitudinal (x) direction varies with latitude, being maximum at the equator and decreasing as the poles are approached. To simplify the calculations an average value for meters per degree longitude was used, and the area considered kept reasonably small.

The fault centroids are marked by black stars in Figures 4.27a and 4.27b and all faults are contained within the masked off "earthquake zone". The purpose of the earthquake zone was to avoid pressure calculations too close to the faults. The location of hydrophone H08N is marked with a red star. Figure 4.27 indicates the time evolution of the bottom pressure signal for both rigid and elastic seabeds. The elastic seabed has pressure signals already close to the hydrophone at $t = 1000$ s, whereas the rigid seabed only has pressure signals local to the earthquake zone at this time. This is due to the twin effects of a boost in phase velocity for frequencies close to critical in the elastic case, and the absence of signal ahead of the main pulse in the rigid stationary phase model. As time proceeds the pressure signals for the elastic case can be seen to traverse the area considered, so that by $t = 3625$ s the area is largely clear of pressure oscillations. In contrast, the rigid stationary phase model shows persistent and ever-increasing pressure oscillations around the earthquake zone. The elastic seabed could therefore be considered more physically realistic.

Figure 4.28 compares the predictions made by the elastic seabed model, against data for the Sumatra event derived from the southern (H08S1) hydrophone and the seismograph at nearby Diego Garcia. The signals recorded by the three hydrophones at station H08S were very similar to each other, and so only H08S1 is displayed in the plots (similarly for station H08N). The amplitude of the main acoustic–gravity wave signal for the northern triad is much smaller than that of the southern triad - possibly due to the shielding effect of the Chagos Archipelago (see Figure 4.29a and Figure 4.30). However, the leading pulses (P-waves) are of similar amplitude. This suggests that the detection of the P-waves by the hydrophones is largely unaffected by the presence of the island - unlike signals that travel only through the water. The hydrophone data was obtained from the Comprehensive nuclear-Test-Ban Treaty Organisation (CTBTO), and the seismic data from the Incorporated Research Institutions for Seismology (IRIS). The fault configuration is that of [1] and the start time given by the USGS (United States Geological Survey)

website is UTC 2004-12-26 00:58:53, which corresponds to $t = 0$. In the plots the blue vertical lines correspond to the expected arrival time of acoustic–gravity waves travelling at phase speed of $1450\,\mathrm{ms}^{-1}$. The green vertical lines for acoustic–gravity waves travelling at a phase speed of $C_s = 3550\,\mathrm{ms}^{-1}$, and the red vertical lines correspond to a phase speed of $\simeq 8000\,\mathrm{ms}^{-1}$. The Diego Garcia (DGAR) seismometer records small amplitude P-waves arriving at the red vertical line, which then transition to larger amplitude S-waves at the green line. The hydrophone H08S weakly detects the P-wave activity. The seismic S-waves do not exist in the liquid (no shear). The main acoustic–gravity wave signal then arrives and is detected by the hydrophone at the blue line. The re-scaled plot of the hydrophone signal shows this behaviour more clearly. Since C_s is the speed limit for the acoustic–gravity waves in the elastic model, the model is unable to predict the P-wave portion of the hydrophone signal. Modifications to the existing model, or maybe a new model would be needed to capture this behaviour. Between the green and blue lines the elastic model predicts acoustic–gravity waves that can travel at phase speeds close to C_s for some frequencies. The hydrophones show weak signal in this region, possibly due to the filtering effect of the hydrophone's response. After the blue line the elastic model predicts a signal that is close in amplitude to the hydrophone recordings, but decays more slowly - possibly due to a lack of dissipation included in the model. However, the signal duration is at least finite in the elastic case. There are processes missing from the elastic model, (varying bathymetry, reflection, refraction, dissipation etc.) so an exact match is not expected. Examination of Figure 4.28 shows the arrival times for P-waves, S-waves and the main acoustic–gravity wave pulse (travelling at a phase speed of C_l) are consistent with our assumptions of constant water density, constant speed of sound in liquid and constant speed of propagation in the solid. The leading pulse seen in the hydrophone recordings is primarily made up of lower frequency components. To show this, a band-pass filter was applied to the hydrophone recording at H08S. The filter eliminates most of the frequency components below 3 Hz and has largely flattened the leading pulse of the H08S signal (Figure 4.31). In order to enhance the detection of acoustic signal between the red and blue lines ultra low frequency hydrophones (ULF) should be used.

To demonstrate the extraction of fault timing and geometry from acoustic–gravity wave signals a band-pass filter was applied to the data obtained from hydrophone H11 located at Wake Island during the Samoa 2009 event (data supplied by CTBTO). The timings for the peaks are $\Delta t_{12} = 15.46\,\mathrm{s}$, $\Delta t_{34} = 27.75\,\mathrm{s}$, $\Delta t_{13} = 29.89\,\mathrm{s}$, $\Delta t_{24} = 42.18\,\mathrm{s}$, (Figure 4.32). Note that the time axis in Figure 4.32 does not begin from the start of the rupture. The time axis in this case represents an 1800 s window around the main hydrophone signal.

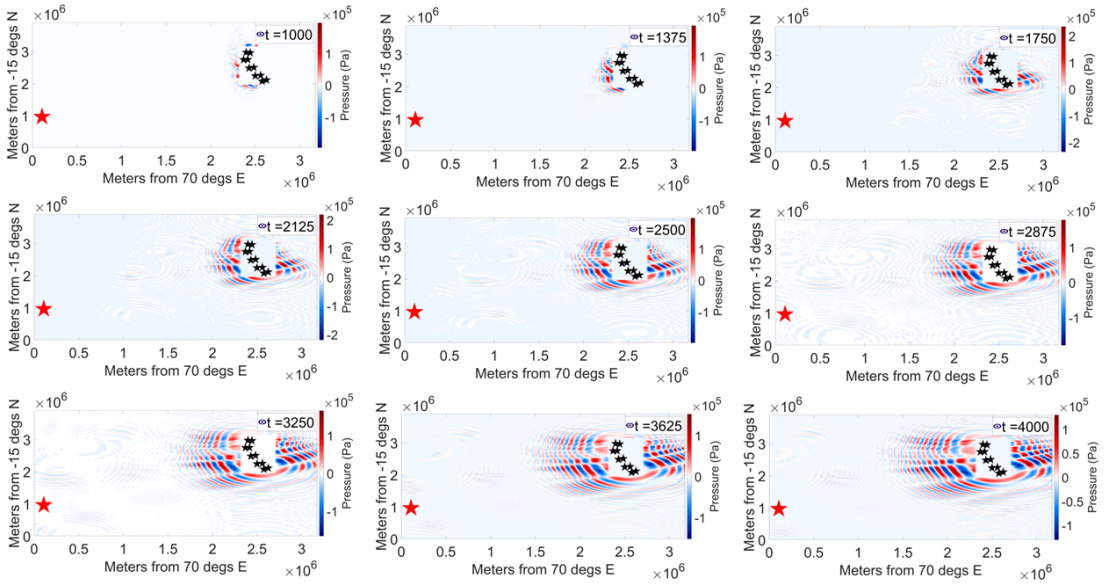

(a) Rigid seabed, bottom pressure map calculated at 9 time intervals after first fault movement.

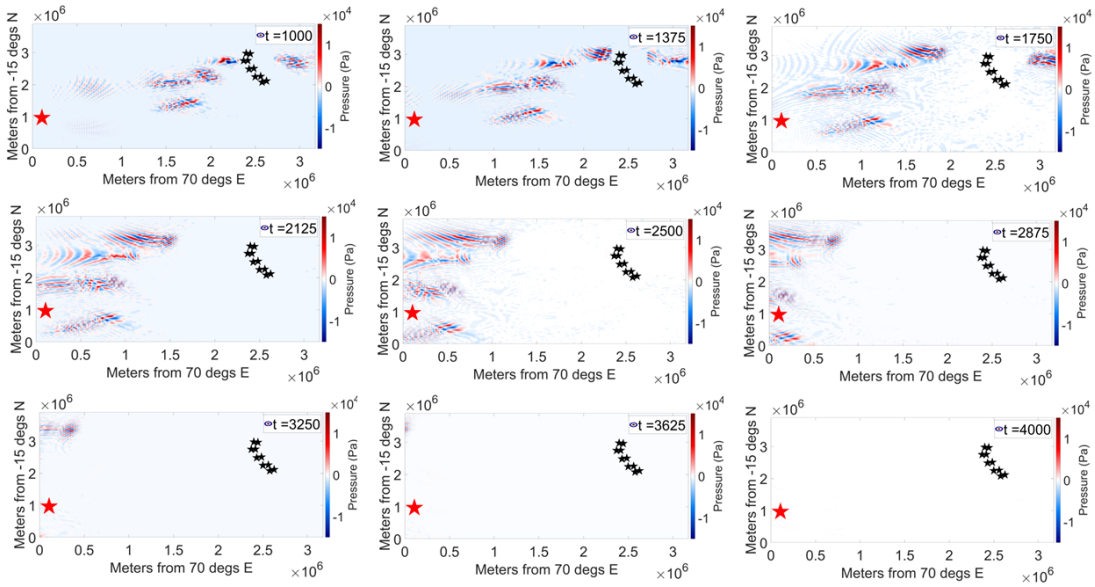

(b) Elastic seabed, bottom pressure map calculated at the same time intervals.

Figure 4.27: Bottom pressure comparison between rigid and elastic seabed. The location of H08N hydrophone is indicated by a red star bottom left. By 3625 s the elastic model has largely cleared of acoustic–gravity waves whereas the rigid model still has strong oscillations around the earthquake zone.

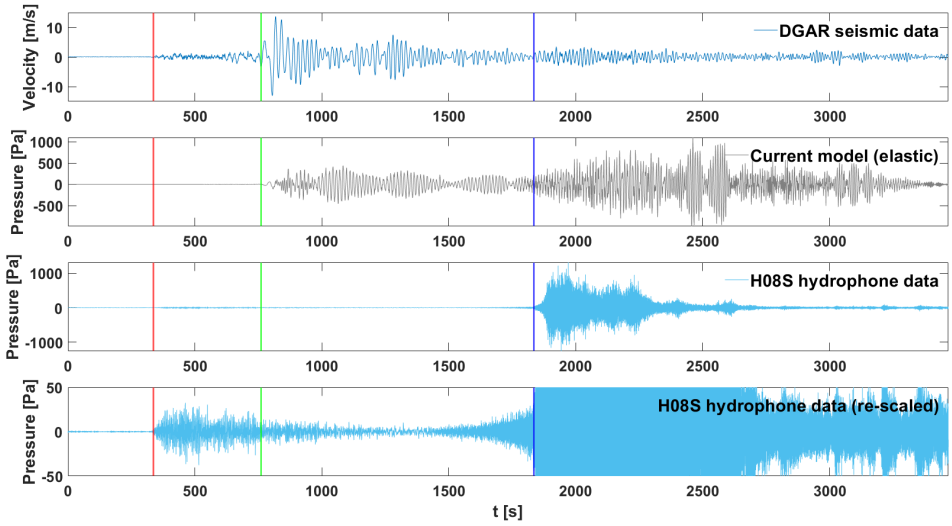

Figure 4.28: Comparison of the current elastic model with both hydrophone and seismic data for the Sumatra 2004 event. The time axis begins at UTC 2004-12-26 00:58:53 ($t = 0$). The vertical red line represents the arrival time for a propagation speed $8000\,\mathrm{ms}^{-1}$, the vertical green line represents the arrival time for a propagation speed $C_s = 3550\,\mathrm{ms}^{-1}$ and the vertical blue line represents the arrival time for a propagation speed $C_l = 1450\,\mathrm{ms}^{-1}$.

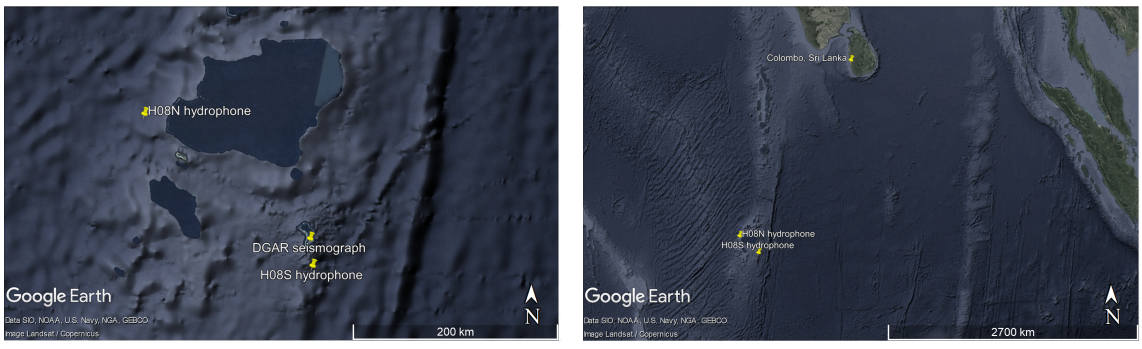

(a) (b)

Figure 4.29: (a) Locations for the H08N and H08S hydrophone triads, along with the Diego Garcia seismograph (yellow markers). The northern triad is shielded by the Chagos Archipelago. (b) Expanded view of island, and west coast of Sumatra. Images from Google Earth

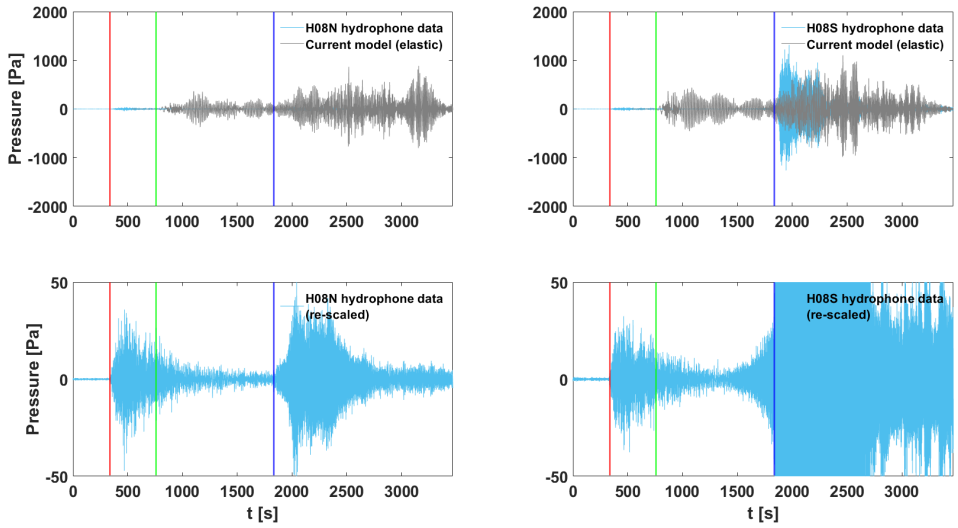

Figure 4.30: Top left and right: Overlay of elastic model prediction onto hydrophone data north and south locations. Bottom left and right: North and south hydrophone data with re-scaled vertical axis. Red vertical line = arrival time for phase speed $8000\,\mathrm{ms}^{-1}$, green vertical line = arrival time for phase speed $C_s = 3550\,\mathrm{ms}^{-1}$, blue vertical line = arrival time for phase speed $C_l = 1450\,\mathrm{ms}^{-1}$

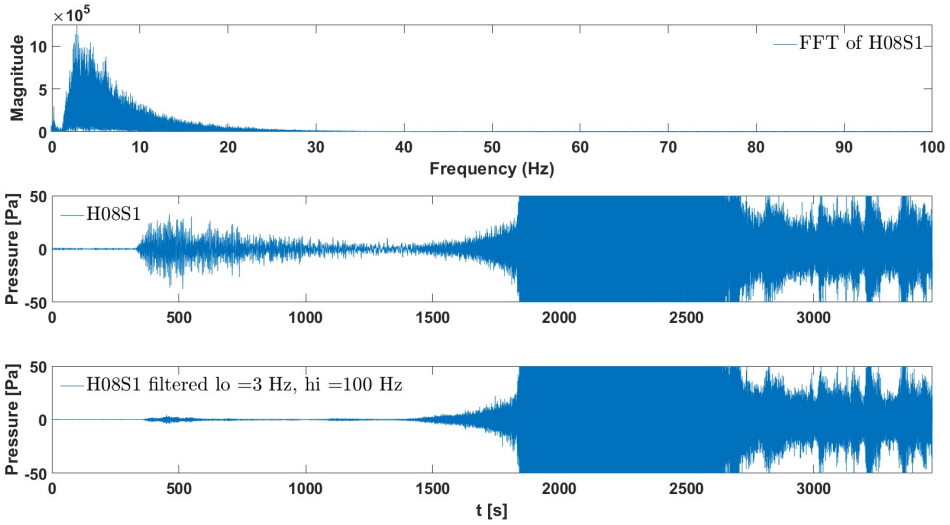

Figure 4.31: Leading pulse of hydrophone signal is largely made up of low frequency components which filtering is able to suppress.

This is not a concern here since only time differences (Δt's) are required. Unlike in the synthetic case this event is asymmetric in the sense that the timings suggest either a trapezoidal rupture geometry, or non-uniform uplift velocity (or both). The time $\Delta t_{12} = 15.46$ s represents the uplift time for the leading edge of the fault. Assuming that the front and back edges of the fault begin moving together, then $\Delta t_{13} = 29.89$ s represents the time for the acoustic signal to travel from the back of the fault, across the fault width, to the front and thus indicates a fault width of $2b = C_l \Delta t_{13} \equiv 43.3$ km. the time $\Delta t_{34} = 27.75$ s represents the total time for the fault movement (the back end continues moving after the front has stopped). These figures compare quite well with those retrieved via inverse modelling in [5]. Also, the fault width and timing is approximately that found in the USGS finite fault model (see Figure 4.33[56]) .

Parameter	$\Delta t_{1,2,3,4}$	Gomez 2022	USGS
$\tau = 2T$	27.75 s	25.46 s s	$\simeq 25 \rightarrow 35$ s
$2b$	43.3 km	22.6 km	$\simeq 30$ km

Table 4.3: Comparison of two key fault parameters (rupture duration and width) obtained by different methods. The first column ($\Delta t_{1,2,3,4}$) reports figures obtained by filtering the H11 hydrophone signal and measuring timings between peaks. The second column reports figures obtained by the methods described within [5]. The data in the third column are estimates derived from USGS website figures.

4.6.4 DART buoy data

For the validation of the surface wave calculations against real data we consider the Tohoku event of March 2011 as covered in [1]. The parameters used in the elastic model of this chapter were changed slightly from those found in [1] and are listed in Table 4.4. In [1] the event was treated as a multi-fault, so as to capture the main tsunami. However, this chapter uses the elastic model and the middle term of (4.3.143), integrated directly to describe the tsunami (mode 01). It was not necessary to split the fault into a number of faults. By integrating directly the tsunami could be modelled by a single fault. The main peak of the tsunami is described quite well by the elastic model, both in terms of timing and amplitude, see Figure 4.34.

[56] `https://earthquake.usgs.gov/earthquakes/eventpage/usp000h1ys/executive`

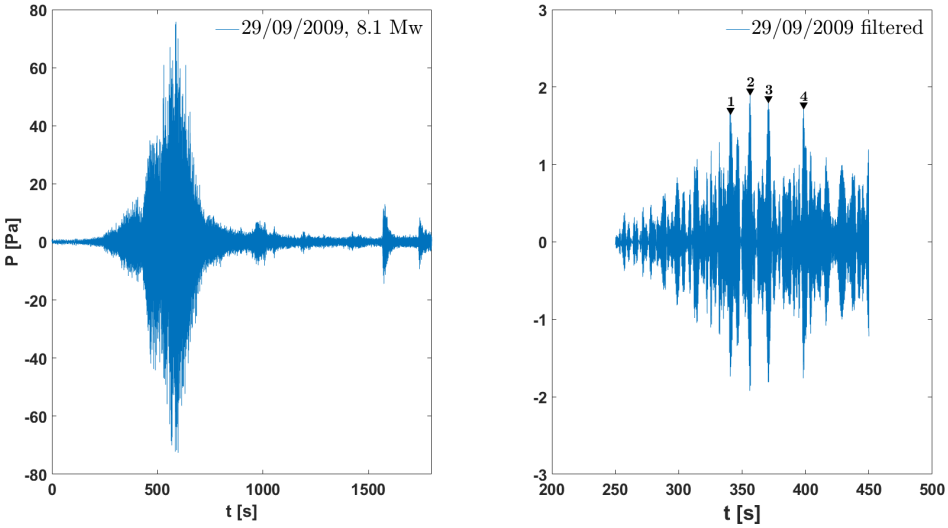

Figure 4.32: Left frame: recorded hydrophone data from H11 at Wake Island for Samoa 2009 event. Note $t = 0$ does not correspond to the rupture start time. Right frame: Signal after application of band-pass filtering, focusing on the time interval containing the initiation of the main pulse. Data sampling occurs at 250 Hz (1 sample every 4 ms).

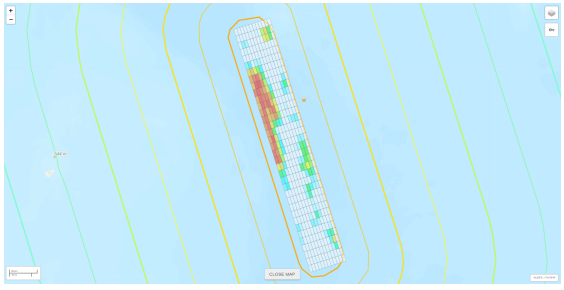

(a) USGS Finite fault model for Samoa 2009 event with scale bottom left corner. Rectangular region shown is approximately 30km x 180km

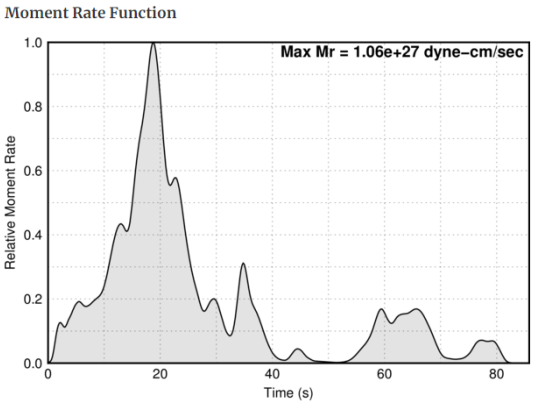

(b) USGS moment rate function for Samoa 2009 event. The main peak ends between 25 and 35 seconds.

Figure 4.33: USGS finite fault model dimensions and timings

Parameter	Description	Value
g	Acceleration due to gravity	$9.81\ \mathrm{ms}^{-2}$
L	Fault half-length	150 km
b	Fault half-width	80 km
$2T$	Rupture duration	90 s
h	Water depth	5277 m
C_l	Speed of sound in water	$1500\,\mathrm{ms}^{-1}$
C_s	Shear speed in solid	$3550\,\mathrm{ms}^{-1}$
C_p	Compression speed in solid	$6300\,\mathrm{ms}^{-1}$
ζ_0	Uplift	6 m
r	Distance from epicentre	496.6 km
θ	Angle to epicentre	$183.555°$
α	Strike angle of fault	$-13°$

Table 4.4: Constants and parameters used in the calculation of surface elevation at DART buoy 21418 for Tohoku 2011 event - elastic model. Also refer to [1]

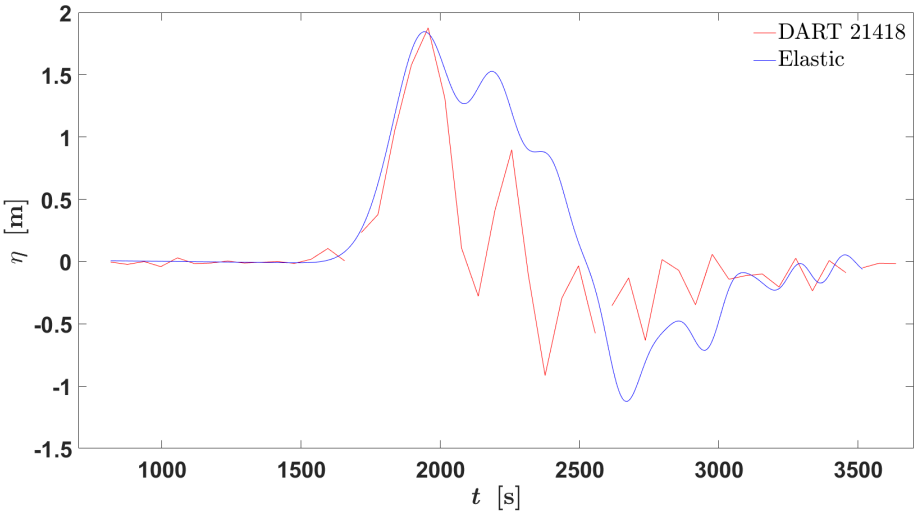

Figure 4.34: Surface elevations compared for Tohoku 2011 event at DART buoy 21418

4.7 Discussion / summary

We have developed a new mathematical model which combines ground movement of a rectangular slender fault with the properties of an elastic seabed. The model derives expressions for the velocity potential in the liquid, along with dilation potential and rotation potential for the solid. From the liquid velocity potential, we derived expressions for the dynamic pressure (acoustic–gravity waves), and the surface elevation. Far-field behaviour is described by envelope functions containing Fresnel integrals. Elasticity has been shown to be an important consideration when calculating tsunami and acoustic–gravity wave arrival times [26, 20, 46]. The model developed in this chapter demonstrates the capacity for the acoustic–gravity waves to travel at speeds near the shear wave velocity for frequencies close to critical. Examination of hydrophone data for the Sumatra 2004 event at H08N and H08S locations revealed a leading acoustic signal travelling ahead of the main acoustic–gravity waves at phase speeds in excess of the shear wave velocity C_s. The elastic model developed in [25] and applied in this chapter has C_s as the speed limit for acoustic–gravity waves, and so does not describe the leading signal in its entirety. Future work could involve modification to the present model, or development of a new elastic model to remedy this.

The tsunami profile is affected by seabed elasticity in shallower water. The inclusion of elasticity induces a decay into the acoustic–gravity wave signals so that the signals terminate after some finite time, unlike the rigid, stationary phase model. From the parameters studied, we find that the signal duration is most affected by the seabed rigidity, with duration increasing alongside rigidity until the totally rigid condition is achieved, at which point the signals persist indefinitely. Thus the inclusion of elasticity helps facilitate a more realistic representation of the pressure field. When the seabed is elastic there exists the possibility of two surface waves. The first (mode 01) is the usual tsunami, but the second (mode 00) is an interesting mode which does not propagate for all frequencies in the elastic case, and never exists in the rigid case. Linear relationships between mode 00 timing of signal peaks and the fault parameters b (half-width) and τ (rupture duration) are found and explained. There is also a linear relationship between uplift velocity and mode 00 amplitude. Information on the fault geometry and timing is encoded into the mode 00 surface wave, and is also found to be imprinted into the acoustic–gravity wave signals as well. With appropriate filtering it is possible to extract this information from the acoustic–gravity wave signal (at least in some instances), which would be helpful in solving the inverse problem of deriving fault properties from acoustic/seismic information. Additionally, an improved estimate of the critical cutoff frequency for acoustic

modes $n \geq 2$ is presented, which is then used in a new method for calculating approximate phase velocity curves which does not rely on solving the dispersion relation (4.3.65) at each point.

An approximation for the mode 00 surface wave cutoff frequency is also derived. As in many previous studies, the model developed here has a constant water depth assumption, so while the model can determine the tsunami properties for deep water, it may fail for varying bathymetry. It remains to develop techniques that can account for changes in bathymetry without computation of the entire 3D domain. For slowly varying bathymetry (i.e. mild slopes where $|\nabla h(x,y,t)| \ll kh$) there already exist techniques in the form of the depth-integrated equations [26, 55, 27]. In the conclusion to [27] the authors remark that models of tsunamigenic events over an elastic seabed do not appear in the literature to date. This topic is addressed and solved (at least for constant depth) in Section 3.3 of this chapter.

In the study of the bottom pressure field for the Sumatra 2004 event covered in Section 4.6 a curved patch of the earth's surface was mapped to a flat x, y plane. An interesting extension to this work could be to move the perspective of the study into a more global viewpoint by use of spherical co-ordinates. In that way far-field predictions may become more accurate. The extension into spherical co-ordinates is the topic of the next chapter.

Chapter 5

Propagation of acoustic–gravity waves on a sphere: focusing and defocusing

5.1 Introduction

For oceanic studies involving acoustic–gravity waves on a global scale, the curvature of the earth can have a measurable effect on propagation. For local, near-field, calculations it is common practice to make use of Cartesian or cylindrical coordinates systems. However, these coordinate systems are only valid locally, where a tangent plane to the earth's surface can be taken as an approximation to the actual curved surface. At large distances rectilinear coordinate systems fail to describe the intrinsic curvature, and the spherical coordinate system becomes a better representation of the earth's geometry. This chapter investigates the effects upon tsunami and acoustic–gravity wave propagation of shifting from a local cylindrical coordinate system, to a global spherical coordinate system. The investigation is carried out in two different length scale regimes. The first normalises lengths to the (constant) water depth. The second regime normalises lengths to the earth's radius, and thus provides a global perspective. It is found that the amplitude of the tsunami and acoustic–gravity waves undergo a defocusing effect as the waves propagate from their source (the North pole) to the equator. Then continuing past the equator the waves focus again approaching the antipodal point (the South pole). A qualitative comparison with the 2022 Hunga Tonga–Hunga Ha'apai eruption in the South Pacific is made in the case of acoustic–gravity wave propagation through the atmosphere by treating the air layer as a low density fluid.

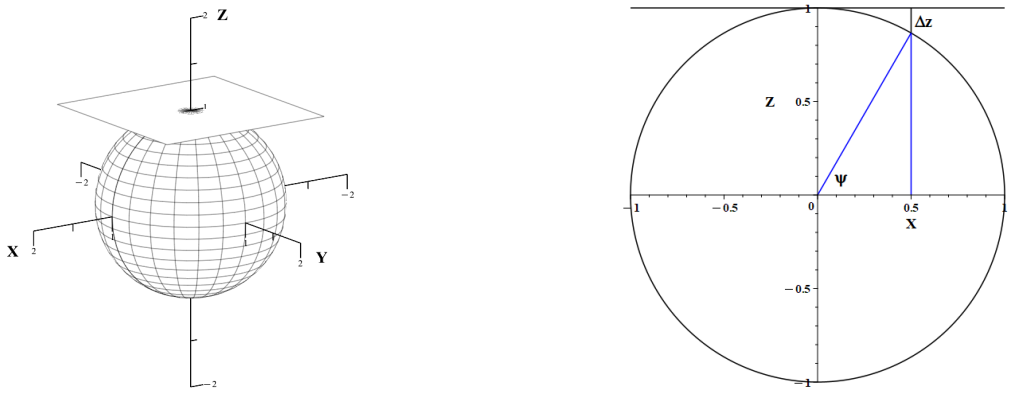

(a) (b)

Figure 5.1: A tangent plane can approximate spherical geometry locally over a limited range. (a) Unit sphere with tangent plane incident at $(x,y,z) = (0,0,1)$. (b) Cross-section through x/z plane. The Δz represents the difference between the tangent approximation and the actual curved surface.

In many calculations involving propagation of either surface–gravity waves or acoustic–gravity waves in the earth's oceans a Cartesian coordinate system is employed [14, 3, 25, 16]. The axes are unbounded, and the origin is typically located either at the seabed, or at the unperturbed liquid surface. In setting up such a Cartesian coordinate system one assumption made is that a tangent plane to the sphere will remain a close approximation over the area of interest - see Figure 5.1a. If Δz in Figure 5.1b is taken as a measure of error between the tangent plane approximation and the actual curved surface, then it is possible to derive a coarse value for how far along a geodesic on the surface of the sphere can be travelled before the error exceeds some specified limit, e.g., 1% (which corresponds to $\Delta Z = 0.01$ in Figure 5.1b). Since the circle in Figure 5.1b is of unit radius the angle ψ is given by

$$\psi = \tan^{-1}\left(\frac{1-\Delta Z}{\sqrt{1-(1-\Delta Z))^2}}\right). \tag{5.1.1}$$

Taking the earth's radius $r_e = 6371$ km ([31]) the arc length from the point of tangency [$(0,1)$ in the x/z plane] to the 1% error point is given by

$$L = r_e\left[\frac{\pi}{2} - \psi\right] = r_e\left[\frac{\pi}{2} - \tan^{-1}\left(\frac{1-\Delta Z}{\sqrt{1-(1-\Delta Z))^2}}\right)\right] = 901.7\,\text{km}. \tag{5.1.2}$$

Thus in the study of long-range propagation of tsunamis, and their accompanying acoustic–gravity waves, a 1% deviation from Cartesian is apparent after travelling approximately 900 km from the source. In addition, the error does not increase linearly with distance

travelled. For propagation in large bodies of water, such as the Pacific ocean, these errors may be significant. To examine some of the consequences of moving to a global framework, where the earth is modelled as a rigid sphere supporting a thin, constant depth ocean, we employ spherical coordinates and solve the wave equation in these coordinates.

The method employed in the solution normalises lengths to two different scales, corresponding to two regimes, in the near and far fields. In the near-field we take the water depth h as the reference length scale. In this regime, the earth's curvature is neglected, and we consider the generation of acoustic–gravity waves and the tsunami due to an uplifting cylinder. For the near-field view we can use axisymmetric cylindrical coordinates as studied in [4]. In the far-field we normalise length scales to that of earth's radius r_e. At the interface between the near-field and far-field regions, both the value, and first derivative, of the velocity functions either side of the interface must match. These matching conditions are enough to establish the unknowns of the equations and admit a full solution.

The outcome reveals that the amplitude of the tsunami and acoustic–gravity waves undergo a modulation governed by the envelope of the theta function $\Theta(\theta)$. This function determines the degree of defocusing (i.e., attenuation) dependent upon how far around the spherical body the wave has travelled. For example, for a wave originating at the north pole, maximum defocusing occurs in the vicinity of the equator. Continued travel beyond the equator towards the south pole would then see a focusing effect as evidenced in [19]. Reflections, at or near, the poles have not been considered in this work. The envelope itself can be described by a modified form of Bernstein's equation , which is discussed in Section 5.4.

It should be noted that although we are working at a global scale in these studies, we have not taken into account any tidal effects. For acoustic–gravity waves this should not pose a problem since their speeds are much greater than those of tides. However, for completeness, tidal effects should be part of any future work.

5.2 Formulation

The water layer is considered inviscid, homogeneous, of constant depth h, residing in a gravitational field of constant magnitude $g = 9.81\,\mathrm{ms}^{-2}$. The water layer is supported by a rigid, solid, homogeneous and isotropic sphere of fixed radius r_e.

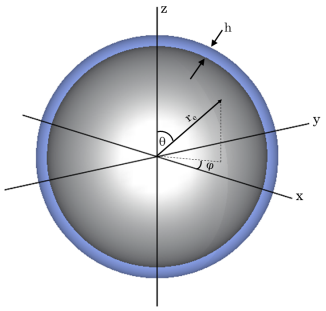

Figure 5.2: Water layer of constant depth h covering a rigid, solid non-rotating sphere of radius r_e.

Spherical coordinates (r,θ,ϕ) are employed, with the origin of coordinates taken to be the centre of the sphere (see Figure 5.2). The radial coordinate is denoted by r, the polar coordinate by θ and the azimuthal coordinate by ϕ. Assuming irrotational flow the problem is expressed in terms of a velocity potential function for the liquid φ. We make use of linearised, irrotational flow for the liquid. A representation of the flow domain is given in Figure 5.2. Taking into account the small compressibility of the sea, and neglecting the gravitational potential term, $g\varphi_z$, the velocity potential is governed by the wave equation [20]

$$\nabla^2\varphi - \frac{1}{c^2}\frac{\partial^2\varphi}{\partial t^2} = 0, \quad r_e \le r \le r_e + h, \quad 0 \le \theta \le \pi, \quad 0 \le \phi \le 2\pi, \quad t \ge 0, \tag{5.2.3}$$

where $h = 4000$ m is the (constant) depth of the water layer and $c = 1500\,\mathrm{ms}^{-1}$ is the speed of sound in water. When the Laplacian for spherical coordinates is applied the wave equation becomes

$$\frac{\partial^2\varphi}{\partial r^2} + \frac{2}{r}\frac{\partial\varphi}{\partial r} + \frac{1}{r^2\sin(\theta)}\frac{\partial}{\partial\theta}\left(\sin(\theta)\frac{\partial\varphi}{\partial\theta}\right) + \frac{1}{r^2\sin^2(\theta)}\frac{\partial^2\varphi}{\partial\phi^2} - \frac{1}{c^2}\frac{\partial^2\varphi}{\partial t^2} = 0, \tag{5.2.4}$$

subject to boundary conditions. Following the derivations given in [8], at the free-surface we have the combined kinematic and dynamic boundary condition

$$\frac{\partial^2\varphi}{\partial t^2} + g\frac{\partial\varphi}{\partial r} = 0, \quad r = r_e + h. \tag{5.2.5}$$

At the rigid seabed (inner and outer regions) the radial component of velocity in the liquid is zero

$$\frac{\partial}{\partial r}\varphi\left(r,\theta,\phi,t\right)\Big|_{r=r_e} = 0. \tag{5.2.6}$$

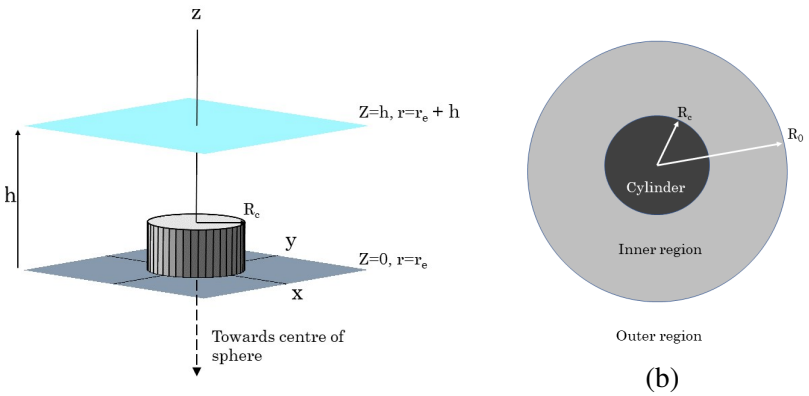

Figure 5.3: Representation of the seabed rupture as an uplifting cylinder of radius R_c. Surrounding the cylinder is an annulus of outer radius R_0. Solutions involve matching function values and first derivatives of the velocity potential at R_0. (a) Uniform cylindrical uplift at the seabed of compressible ocean of constant depth h. (b) Top view of rupture regions. The black disc is the uplifting cylinder, the surrounding grey annulus is the inner region and everything at distance $> R_0$ is referred to as the outer region.

Since ϕ is an angular coordinate, solutions should be single-valued, i.e., unchanged as $\phi \to \phi + 2\pi$

$$\varphi\left(r,\theta,\phi,t\right) = \varphi\left(r,\theta,\phi+2\pi,t\right). \tag{5.2.7}$$

The rupture in the seabed is modelled in the same way as in [4]. The model consists of a transient, uniform vertical uplift with circular cross-section located at the seabed where the spherical coordinate $\theta = 0$ (i.e., the north pole of the sphere) - see Figures 5.3a and 5.3b. There is no loss of generality in choosing the North pole as the origin of the rupture, since any other location on the sphere can be reached with a single rotation. Located immediately outside of the rising cylinder we have an annulus between radii R_c (the wall of the cylinder) and R_0. This annulus is designated the inner region, and is made large enough to ensure the evanescent waves arising from the rupture have decayed away, but not so large as to introduce curvature errors.

5.3 Solutions

5.3.1 Short-range inner region

The tsunami will travel at speed $\sqrt{gh}$, with timescale $\sqrt{h/g}$ and length-scale h. The acoustic–gravity waves will propagate with velocity c, timescale h/c, and length-scale

h. Let $\xi = \sqrt{gh}/c$ be a non-dimensional parameter. Then with ω as the frequency and variables made non-dimensional and denoted with a hat circumflex as follows

$$\hat{r} = \frac{r}{h}, \quad \hat{t} = \frac{t}{\sqrt{(h/g)}} = \sqrt{\frac{g}{h}}t, \quad \hat{\omega} = \sqrt{\frac{h}{g}}\omega, \tag{5.3.8}$$

the wave equation becomes

$$\frac{\partial^2\varphi}{\partial\hat{r}^2} + \frac{2}{\hat{r}}\frac{\partial\varphi}{\partial\hat{r}} + \frac{1}{\hat{r}^2\sin(\theta)}\frac{\partial}{\partial\theta}\left(\sin(\theta)\frac{\partial\varphi}{\partial\theta}\right) + \frac{1}{\hat{r}^2\sin^2(\theta)}\frac{\partial^2\varphi}{\partial\phi^2} - \xi^2\frac{\partial^2\varphi}{\partial\hat{t}^2} = 0. \tag{5.3.9}$$

Let $h/r_e = \epsilon \ll 1$, and with Z the height above the seabed $r = r_e + Z$, $0 \le Z \le h$, then the non-dimensional forms become

$$\hat{r} = \frac{1}{\epsilon} + \hat{Z}, \quad \hat{Z} = \frac{Z}{h}. \tag{5.3.10}$$

Substituting in the wave equation gives

$$\frac{\partial^2\varphi}{\partial\hat{Z}^2} + 2\epsilon\frac{\partial\varphi}{\partial\hat{Z}} + \frac{\epsilon^2}{\sin(\theta)}\frac{\partial}{\partial\theta}\left(\sin(\theta)\frac{\partial\varphi}{\partial\theta}\right) + \frac{\epsilon^2}{\sin^2(\theta)}\frac{\partial^2\varphi}{\partial\phi^2} - \xi^2\frac{\partial^2\varphi}{\partial\hat{t}^2} = 0. \tag{5.3.11}$$

For small θ (near-field solution), we have

$$\frac{\partial^2\varphi}{\partial\hat{Z}^2} + 2\epsilon\frac{\partial\varphi}{\partial\hat{Z}} + \frac{\epsilon^2}{\theta}\frac{\partial\varphi}{\partial\theta} + \epsilon^2\frac{\partial^2\varphi}{\partial\theta^2} + \frac{\epsilon^2}{\theta^2}\frac{\partial^2\varphi}{\partial\phi^2} - \xi^2\frac{\partial^2\varphi}{\partial\hat{t}^2} = 0. \tag{5.3.12}$$

Note that $\theta \ll 1$, but not ϕ. From Figure 5.4 we see that the arc length from the north pole is given by $R = \theta r_e$. For small θ we have $\sin(\theta) \approx \theta$, $\theta = \frac{R}{r_e} = \frac{h}{r_e}\frac{R}{h} = \epsilon\hat{R}$ with $\hat{R} = \frac{R}{h}$ being the arc length scaled to the water depth h. Thus

$$\frac{\partial^2\varphi}{\partial\hat{Z}^2} + 2\epsilon\frac{\partial\varphi}{\partial\hat{Z}} + \frac{1}{\hat{R}}\frac{\partial\varphi}{\partial\hat{R}} + \frac{\partial^2\varphi}{\partial\hat{R}^2} + \frac{1}{\hat{R}^2}\frac{\partial^2\varphi}{\partial\phi^2} - \xi^2\frac{\partial^2\varphi}{\partial\hat{t}^2} = 0. \tag{5.3.13}$$

Also note $\xi = O(\epsilon^{\frac{1}{2}})$. Assuming axisymmetric propagation, $\partial_\phi = 0$. Then for the near-field solution, to leading order, we reduce to symmetric cylindrical coordinates

$$\frac{\partial^2\varphi}{\partial\hat{Z}^2} + \frac{1}{\hat{R}}\frac{\partial\varphi}{\partial\hat{R}} + \frac{\partial^2\varphi}{\partial\hat{R}^2} - \xi^2\frac{\partial^2\varphi}{\partial\hat{t}^2} = 0, \tag{5.3.14}$$

along with the boundary conditions.

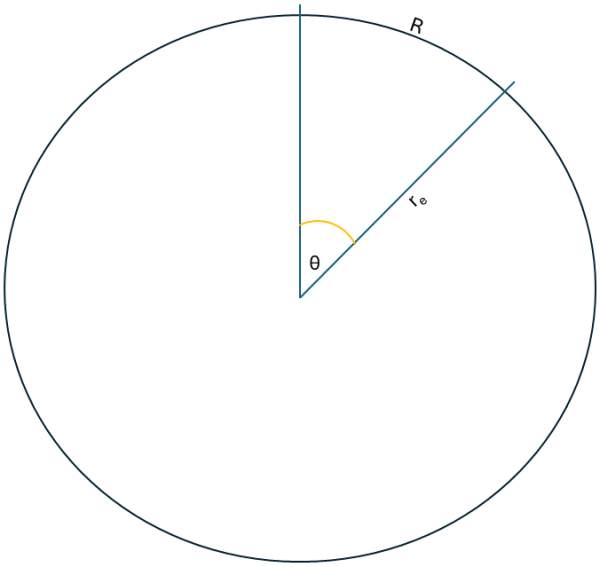

Figure 5.4: Arc length $R = r_e\theta$. In practice θ is small for the inner region i.e $\theta < \frac{L}{r_e} \approx 0.14$ - see (5.1.2).

At the surface

$$\frac{\partial^2\varphi}{\partial\hat{t}^2} + \frac{\partial\varphi}{\partial\hat{Z}} = 0. \tag{5.3.15}$$

At the seabed

$$\frac{\partial\varphi}{\partial\hat{Z}} = 0, \tag{5.3.16}$$

with continuity conditions given by

$$\varphi_{\text{in}}|_{\hat{R}_0} = \varphi_{\text{out}}|_{\theta_0=\epsilon\hat{R}_0}, \tag{5.3.17}$$

$$\frac{\partial}{\partial\hat{R}}\varphi_{\text{in}}\Big|_{\hat{R}_0} = \frac{\partial\theta}{\partial\hat{R}}\frac{\partial}{\partial\theta}\varphi_{\text{out}} = \epsilon\frac{\partial}{\partial\theta}\varphi_{\text{out}}\Big|_{\theta_0=\epsilon\hat{R}_0}. \tag{5.3.18}$$

The point at which the matching takes place in the continuity equations is R_0 on the LHS of the continuity equations where $\varphi = \varphi_{in}(R,Z,t)$ and its equivalent $\theta_0 = \epsilon R_0$ on the RHS where $\varphi_{out} = \varphi_{out}(t,\theta)$.

The velocity potential φ_{in} appearing in the continuity conditions is already known in integral form from [4] and will be referenced in the following text as the Cylindrical

Solution (CS):

$$\begin{aligned}\varphi_{in}(R,Z,t) = 4R_c W_0 \int_0^\infty \frac{\mu_0 \cosh(\mu_0 Z)\sin\left(\frac{\omega\tau}{2}\right)}{\omega q_0\left[\sinh(2\mu_0 h)+2\mu_0 h\right]}\Big[Y_0(q_0R)\cos\Big(\omega t-\frac{\omega\tau}{2}\Big)\\ -J_0(q_0R)\sin\Big(\omega t-\frac{\omega\tau}{2}\Big)\Big]J_1(q_0R_c)\mathrm{d}\omega\\ +4R_c W_0\sum_{n=1}^{\infty}\int_{\omega_n}^\infty \frac{\mu_n\cos(\mu_n Z)\sin\left(\frac{\omega\tau}{2}\right)}{\omega q_n\left[\sin(2\mu_n h)+2\mu_n h\right]}\Big[Y_0(q_0R)\cos\Big(\omega t-\frac{\omega\tau}{2}\Big)\\ -J_0(q_nR)\sin\Big(\omega t-\frac{\omega\tau}{2}\Big)\Big]J_1(q_nR_c)\mathrm{d}\omega\end{aligned} \tag{5.3.19}$$

In (5.3.19) W_0 is the cylinder uplift velocity, μ and q are wave numbers, τ is the rupture duration, R is distance from the cylinder centre, and J, Y are Bessel functions. Assume $\varphi(\hat{Z},\hat{R},\hat{t}) = \zeta(\hat{Z})\rho(\hat{R})\Upsilon(\hat{t})$ and substitute into (5.3.14) to give

$$\frac{1}{\zeta}\frac{\mathrm{d}^2\zeta}{\mathrm{d}\hat{Z}^2}+\frac{1}{\rho\hat{R}}\frac{\mathrm{d}\rho}{\mathrm{d}\hat{R}}+\frac{1}{\rho}\frac{\mathrm{d}^2\rho}{\mathrm{d}\hat{R}^2}-\frac{\xi^2}{\Upsilon}\frac{\mathrm{d}^2\Upsilon}{\mathrm{d}\hat{t}^2}=0. \tag{5.3.20}$$

Re-arranging (5.3.20) gives

$$\frac{1}{\zeta}\frac{\mathrm{d}^2\zeta}{\mathrm{d}\hat{Z}^2}+\frac{1}{\rho\hat{R}}\frac{\mathrm{d}\rho}{\mathrm{d}\hat{R}}+\frac{1}{\rho}\frac{\mathrm{d}^2\rho}{\mathrm{d}\hat{R}^2}=\frac{\xi^2}{\Upsilon}\frac{\mathrm{d}^2\Upsilon}{\mathrm{d}\hat{t}^2}=\text{constant}=-\hat{k}_s^2, \tag{5.3.21}$$

$$\implies \Upsilon(\hat{t}) = A_1\cos\left(\frac{\hat{k}_s}{\xi}\hat{t}\right)+A_2\sin\left(\frac{\hat{k}_s}{\xi}\hat{t}\right), \tag{5.3.22}$$

with k_s a wave-number. From (5.3.21), and following [4] we have

$$\frac{1}{\rho\hat{R}}\frac{\mathrm{d}\rho}{\mathrm{d}\hat{R}}+\frac{1}{\rho}\frac{\mathrm{d}^2\rho}{\mathrm{d}\hat{R}^2}=-\left(\frac{1}{\zeta}\frac{\mathrm{d}^2\zeta}{\mathrm{d}\hat{Z}^2}+\hat{k}_s^2\right)=\hat{q}^2, \tag{5.3.23}$$

where $\hat{q}^2$ is the separation constant between $\hat{R}$ and $\hat{Z}$. The separation produces a set of two ODE's,

$$\frac{\mathrm{d}^2\zeta}{\mathrm{d}\hat{Z}^2}+\left(\hat{k}_s^2+\hat{q}^2\right)\zeta=0,\qquad \frac{\mathrm{d}^2\rho}{\mathrm{d}\hat{R}^2}+\frac{1}{\hat{R}}\frac{\mathrm{d}\rho}{\mathrm{d}\hat{R}}-\hat{q}^2\rho=0. \tag{5.3.24}$$

The solution in the $\hat{Z}$ direction is

$$\zeta(\hat{Z}) = B_1\cos\left(\hat{\mu}\hat{Z}\right)+B_2\sin\left(\hat{\mu}\hat{Z}\right),\qquad \hat{\mu}=\sqrt{\hat{k}_s^2+\hat{q}^2}, \tag{5.3.25}$$

which is in agreement with [4].

5.3.2 Dispersion relation

At this point it is possible to derive the dispersion relation even without knowledge of the function $\rho(\hat{R})$. The method shown here utilises (5.3.22) and (5.3.25), along with $\varphi(\hat{Z},\hat{R},\hat{t}) = \zeta(\hat{Z})\rho(\hat{R})\Upsilon(\hat{t})$, and reverts back to dimensional quantities for the calculation. Let $A_1, A_2, B_1, B_2, C_1, C_2$ be constants then

$$\Upsilon(\hat{t}) = A_1\cos\left(\frac{\hat{k}_s}{\xi}\hat{t}\right) + A_2\sin\left(\frac{\hat{k}_s}{\xi}\hat{t}\right) \implies \Upsilon(t) = A_1\cos(\omega t) + A_2\sin(\omega t), \quad \frac{\hat{k}_s}{\xi}\hat{t} = k_s c t = \omega t, \tag{5.3.26}$$

$$\zeta(\hat{Z}) = B_1\cos\left(\hat{\mu}\hat{Z}\right) + B_2\sin\left(\hat{\mu}\hat{Z}\right) \implies \zeta(Z) = B_1\cos\left(\mu Z\right) + B_2\sin\left(\mu Z\right). \tag{5.3.27}$$

Application of the boundary conditions for the surface ($Z = h$) and the seabed ($Z = 0$)

$$\frac{\partial^2\varphi}{\partial t^2} + g\frac{\partial\varphi}{\partial Z} = 0\Big|_{Z=h}, \qquad \frac{\partial\varphi}{\partial z} = 0\Big|_{Z=0}, \quad \implies \tan(\mu h) = -\frac{\omega^2}{g\mu}. \tag{5.3.28}$$

Re-arrangement of the expression for μ from (5.3.25), and examination of the roots of the dispersion relation - (5.3.28), produces three categories

$$\text{(i) Single imaginary root} \quad \mu = \mathrm{i}\mu_0, \implies q_0 = \mathrm{i}|q_0| = \mathrm{i}\sqrt{k_s^2 + \mu_0^2} = \mathrm{i}\sqrt{\frac{\omega^2}{c^2} + \mu_0^2}, \tag{5.3.29}$$

$$\text{(ii) Finite number of real roots } \mu_n, \text{ when } \mu_n^2 < \frac{\omega^2}{c^2}, \implies q_n = \mathrm{i}|q_n| = \mathrm{i}\sqrt{\frac{\omega^2}{c^2} - \mu_n^2}, \tag{5.3.30}$$

$$\text{(iii) Infinite number of real roots } \mu_n, \text{ when } \mu_n^2 > \frac{\omega^2}{c^2} \implies q_n = \sqrt{\mu_n^2 - \frac{\omega^2}{c^2}}. \tag{5.3.31}$$

The general solution for the radial ODE - (5.3.32) - is a linear combination of the Bessel functions J_0 and Y_0 ([56])

$$\frac{\mathrm{d}^2}{\mathrm{d}\hat{R}^2}\rho(\hat{R}) + \frac{1}{\hat{R}}\frac{\mathrm{d}}{\mathrm{d}\hat{R}}\rho(\hat{R}) - \hat{q}^2\rho(\hat{R}) = 0, \quad \rho(\hat{R}) = C_1 J_0(\mathrm{i}\hat{q}\hat{R}) + C_2 Y_0(\mathrm{i}\hat{q}\hat{R}). \tag{5.3.32}$$

For the tsunami and acoustic–gravity modes $n = 0,\ldots,N$ and q_n is purely imaginary and so the argument of the Bessel functions becomes real indicating oscillating, progressive modes. When $n = N+1,\ldots\infty$, q_n is real and in that case we have the modified Bessel functions representing non-progressive modes. Thus the situation for the near-field region is exactly that found in [4] with solution given by (5.3.19).

5.3.3 Long range outer region

To tackle the far-field solution re-scale r to length scale r_e and to time-scale $\sqrt{r_e/g}$. The non-dimensional parameter is now $\chi = \sqrt{gr_e}/c$

$$\bar{r} = \frac{r}{r_e}, \quad \bar{r}_e = 1, \quad \bar{Z} = O(\epsilon), \quad \bar{t} = \frac{t}{\sqrt{(r_e/g)}} = \sqrt{\frac{g}{r_e}}t. \tag{5.3.33}$$

So now $r = r_e + Z$ becomes $\bar{r} = 1 + O(\epsilon)$ and $\partial_{\bar{r}} = 0$. The small angle approximation is no longer valid in the far-field (the outer region). Substitute into the wave equation, whilst maintaining the axial symmetry from the inner region. Then take the leading term and remove the remaining dimensionless $\bar{t}$, to arrive at

$$\frac{1}{\sin(\theta)}\frac{\partial}{\partial\theta}\left(\sin(\theta)\frac{\partial\varphi}{\partial\theta}\right) - \frac{r_e^2}{c^2}\frac{\partial^2\varphi}{\partial t^2} = 0. \tag{5.3.34}$$

5.3.4 Constructing the outer solution

Take the function $\varphi = A\left(T,\beta\right)\Theta(\theta)\mathrm{e}^{-\mathrm{i}\omega t}$ where $T = \sigma_1\left(t - \frac{\tau}{2}\right)$, $\beta = \sigma_2\theta$ with $\sigma_i^2 \ll \sigma_i$, $\sigma_1 \approx \sigma_2, \sigma_i \ll 1, i = 1,2$. We seek to demonstrate that the function $A(T,\beta)$ appearing in the ansatz solution ϕ to (5.3.34) is equivalent to the long range version of the solution for the inner region CS which is already known from [4] and appears in (5.3.19). Take only the tsunami ($Z = h$) contribution from the propagating parts of (5.3.19), i.e., the first line

$$\varphi_{in}(R,t) = 4R_c W_0 \int_0^\infty \frac{\mu_0\cosh(\mu_0 h)\sin\left(\frac{\omega\tau}{2}\right)}{\omega q_0\left[\sinh(2\mu_0 h) + 2\mu_0 h\right]}\left[Y_0(q_0R)\cos\left(\omega t - \frac{\omega\tau}{2}\right)\right.$$
$$\left. - J_0(q_0R)\sin\left(\omega t - \frac{\omega\tau}{2}\right)\right]J_1(q_0R_c)\mathrm{d}\omega. \tag{5.3.35}$$

The long range approximations for the Bessel functions 57, e.q. (10.7.8) are

$$J_0(q_0R) = \sqrt{\frac{2}{\pi q_0 R}}\cos\left(q_0R - \frac{\pi}{4}\right), \quad Y_0(q_0R) = \sqrt{\frac{2}{\pi q_0 R}}\sin\left(q_0R - \frac{\pi}{4}\right). \tag{5.3.36}$$

With these approximations substituted into (5.3.35) along with the trigonometric identity $\sin(A-B) = \sin(A)\cos(B) - \cos(A)\sin(B)$ we have

$$\varphi_{in}(R,t) = 4W_0R_c\int_0^\infty \frac{\mu_0\cosh(\mu_0 h)\sin\left(\frac{\omega\tau}{2}\right)}{\omega q_0\left[\sinh(2\mu_0 h) + 2\mu_0 h\right]}\sqrt{\frac{2}{\pi q_0 R}}\sin\left[-\omega\left(t - \frac{\tau}{2}\right) + q_0R - \frac{\pi}{4}\right]J_1(q_0R_c)\mathrm{d}\omega. \tag{5.3.37}$$

Substitute $\varphi = A\left(T,\beta\right)\Theta(\theta)\mathrm{e}^{-\mathrm{i}\omega t}$ into (5.3.34) to give

$$\cot(\theta)\frac{\partial A}{\partial \beta}\sigma_2\Theta + A\cot(\theta)\frac{d\Theta}{d\theta} + \sigma_2^2\Theta\frac{\partial^2 A}{\partial \beta^2} + 2\sigma_2\frac{\partial A}{\partial \beta}\frac{d\Theta}{d\theta} + A\frac{d^2\Theta}{d\theta^2} - \frac{r_e^2}{c^2}\left[\sigma_1^2\Theta\frac{\partial^2 A}{\partial T^2} - 2\mathrm{i}\sigma_1\Theta\omega\frac{\partial A}{\partial T} - \omega^2\Theta A\right] = 0. \quad (5.3.38)$$

Collecting leading order terms, and applying the change of variable $w = \cos(\theta)$, (5.3.38) can be re-written as

$$(1-w^2)\frac{\mathrm{d}^2\Theta}{\mathrm{d}w^2} - 2w\frac{\mathrm{d}\Theta}{\mathrm{d}w} + \frac{r_e^2}{c^2}\omega^2\Theta = 0. \quad (5.3.39)$$

This is a Legendre equation which has solutions that are a linear combination of the Legendre functions $P_\lambda(w)$ and $Q_\lambda(w)$, where λ is the degree of the Legendre function. Thus with E_1, E_2 as integration constants to be determined we have

$$\Theta(w) = E_1 P_\lambda(w) + E_2 Q_\lambda(w), \quad \lambda = \frac{1}{2}\sqrt{4\frac{r_e^2}{c^2}\omega^2 + 1} - \frac{1}{2}, \quad w = \cos(\theta). \quad (5.3.40)$$

Then ignoring the small terms containing σ_i^2 we arrive at the order $O(\sigma)$ equation from which, after some re-arrangement, we find $\partial A/\partial T$ can be written in terms of $\partial A/\partial \beta$ as follows

$$\frac{\partial A}{\partial T} = \frac{\mathrm{i}c^2\left[\Theta\cot(\theta) + 2\Theta_\theta\right]}{2r_e^2\Theta\omega}\frac{\partial A}{\partial \beta}. \quad (5.3.41)$$

The equation $\partial A/\partial T = \mathrm{i}\partial A/\partial\beta$ has solutions of the form $A(T,\beta) = f(\mathrm{i}T + \beta)$, where f is some arbitrary function. The solution of (5.3.41) is of the form

$$A(T,\beta) = f\left(\left[\frac{\Theta\cot(\theta) + 2\Theta_\theta}{2r_e^2\Theta\omega}\right]\mathrm{i}c^2T + \beta\right). \quad (5.3.42)$$

Where again f is some arbitrary function. Let

$$\begin{aligned} &P_{\lambda_0} = P_\lambda(\cos\theta_0), \quad Q_{\lambda_0} = Q_\lambda(\cos\theta_0), \quad P_{\lambda_0+1} = P_{\lambda+1}(\cos\theta_0), \quad Q_{\lambda_0+1} = Q_{\lambda+1}(\cos\theta_0),\\ &P_\lambda = P_\lambda(\cos\theta), \quad Q_\lambda = Q_\lambda(\cos\theta), \quad P_{\lambda+1} = P_{\lambda+1}(\cos\theta), \quad Q_{\lambda+1} = Q_{\lambda+1}(\cos\theta),\\ &x = \left[\frac{\Theta\cot(\theta) + 2\Theta_\theta}{2\Theta r_e^2\omega}\right]\mathrm{i}c^2T + \beta, \end{aligned} \quad (5.3.43)$$

with

$$\Theta_\theta = \frac{(\lambda+1)\sin(\theta)}{\cos^2(\theta)-1}\left[E_1\left(\cos(\theta)P_\lambda - P_{\lambda+1}\right) + E_2\left(\cos(\theta)Q_\lambda - Q_{\lambda+1}\right)\right]. \quad (5.3.44)$$

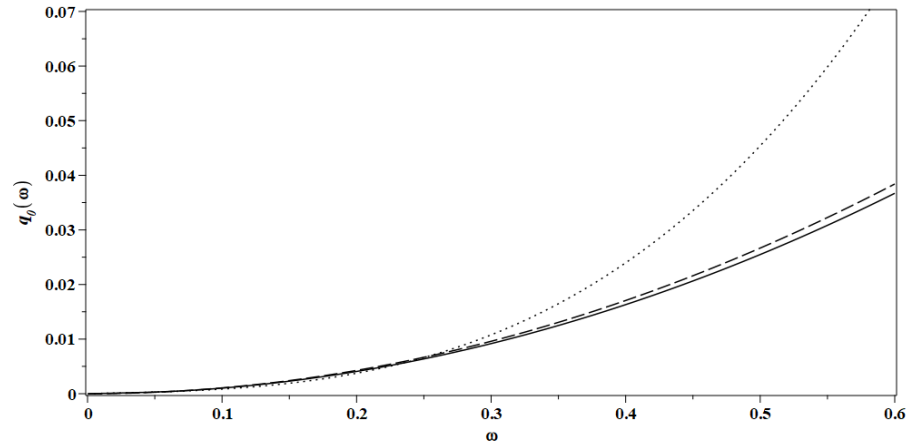

Figure 5.5: Plot of $q_0(\omega)$. Solid trace is dispersion relation, dash trace is (5.3.46), dot trace (5.3.47), is an approximate expression derived in [4].

Then the sine term with square brackets in (5.3.37) can be written in the form $f(x) = \sin[ax+b]$ with $a = \frac{q_0 r_e}{\sigma_2}$ and $b = -\frac{\pi}{4}$. This implies

$$\frac{q_0 r_e}{\sigma_2}\left[\frac{\Theta\cot(\theta)+2\Theta_\theta}{2\Theta r_e^2\omega}\right]\mathrm{i}c^2 = -\frac{\omega}{\sigma_1}, \qquad \frac{q_0 r_e}{\sigma_2}\beta = q_0 R. \tag{5.3.45}$$

From (5.3.29), ($\sigma_1, \sigma_2 \neq 0$), and with q_0 numerically positive (so we are able to drop the magnitude bars) we have

$$q_0(\omega) = \frac{2\Theta r_e}{c^2(\Theta\cot(\theta)+2\Theta_\theta)}\omega^2, \qquad \frac{q_0 r_e}{\sigma_2}\beta = q_0 R. \tag{5.3.46}$$

As numerical verification of the relationship between q_0 and ω in (5.3.46), Figure 5.5 compares values for q_0 obtained from solving the dispersion relation at the matching point θ_0, against values given by (5.3.46) and an approximate expression derived in [4] - (5.3.47)

$$q_0 = \frac{\omega}{\sqrt{gh}}\left(1+\frac{\omega^2 h}{6g}\right). \tag{5.3.47}$$

The values for q_0 obtained from (5.3.46) remain close to the dispersion relation solution as far as $\omega = 0.6\,\mathrm{rads}^{-1}$. Thus $A(T,\beta)$ can be written as (5.3.37) since we require equality at the interface between inner and outer regions, hence φ_{out} can now be written as

$$\varphi_{out}(t,\theta) = A(t,R)[E_1 P_\lambda + E_2 Q_\lambda]\mathrm{e}^{-\mathrm{i}\omega t}, \quad R = \theta r_e \tag{5.3.48}$$

5.3.5 Continuity at interface between inner and outer regions

The initial conditions are determined by the particular rupture conditions studied. The near-field solution is given by (5.3.19), so we can take this as our given velocity potential. Matching at R_0 then ensures a smooth transition between the CS of the inner region, and the long range spherical coordinates of the outer region. The velocity potential functions either side of R_0 must match in value and first derivative at R_0

$$\varphi_{in}(t,R)|_{R_0} = \varphi_{out}(t,\theta)|_{\theta_0=\frac{R_0}{r_e}} \tag{5.3.49}$$

$$\frac{\partial}{\partial R}\varphi_{in}(t,R)\Big|_{R_0} = \frac{1}{r_e}\frac{\partial}{\partial\theta}\varphi_{out}(t,\theta)\Big|_{\theta_0=\frac{R_0}{r_e}} \tag{5.3.50}$$

(5.3.50) is obtained via the chain rule as follows

$$\frac{\partial\varphi}{\partial R} = \frac{\partial\theta}{\partial R}\frac{\partial\varphi}{\partial\theta}, \quad \text{where} \quad \frac{\partial\theta}{\partial R} = \frac{1}{r_e}. \tag{5.3.51}$$

5.3.6 Determine unknown constants

The known velocity potential $\varphi_{in}(R,t)$ for the inner region now has to satisfy the continuity conditions (5.3.49) and (5.3.50) with the outer region. Choose $R_0 = 120$ km and $t = t_0 = R_0/\sqrt{gh}$ (the arrival time of the tsunami at the distance R_0) to carry out the matching. The value of 120 km for R_0 is a compromise between being far enough away from the rising cylinder in order for the evanescent waves to decay away, while not being so far as to introduce curvature issues - see (5.1.2) for upper limit. Allowing $5h = 20$ km for evanescent wave decay in addition to the cylinder radius of $R_c = 40$ km gives a lower limit of 60 km. So choose $R_0 = 120$ km to be safely within these constraints. Increasing this radius up to the upper limit of (5.1.2) would retain the inner solution for longer before the defocusing effects begin. Conversely decreasing the radius would begin the defocusing earlier. Given the radius of the earth the overall effect of relocating R_0 on defocusing/focusing would be negligible.

The first continuity condition gives

$$\Phi = \varphi_{in}(R_0,t_0) = A(t_0,R_0)\left[E_1 P_{\lambda_0} + E_2 Q_{\lambda_0}\right]\mathrm{e}^{-\mathrm{i}\omega t_0}, \quad \theta_0 = \frac{R_0}{r_e}. \tag{5.3.52}$$

The second continuity condition then gives

$$\Phi_R = \frac{\partial}{\partial R}\varphi_{in}\Big|_{t_0,R_0} = \frac{\partial\theta}{\partial R}\frac{\partial}{\partial\theta}\varphi_{out}\Big|_{t_0,\theta_0}, \quad \frac{\partial\theta}{\partial R} = \frac{1}{r_e}, \tag{5.3.53}$$

To obtain the left-hand side of (5.3.53) differentiate (5.3.35) with respect to R to give

$$\Phi_R = 4R_c W_0 \int_0^\infty \frac{\mu_0 \cosh(\mu_0 h)\sin\left(\frac{\omega\tau}{2}\right)}{\omega\left[\sinh(2\mu_0 h)+2\mu_0 h\right]}\left[-Y_1(q_0R_0)\cos\left(\omega t_0 - \frac{\omega\tau}{2}\right) + J_1(q_0R_0)\sin\left(\omega t_0 - \frac{\omega\tau}{2}\right)\right] J_1(q_0R_c)\mathrm{d}\omega. \tag{5.3.54}$$

To obtain the right-hand side of (5.3.53) use

$$\frac{1}{r_e}\frac{\partial}{\partial\theta}\varphi_{out}\Big|_{t_0,\theta_0} = \frac{1}{r_e}\frac{\partial}{\partial\theta}\left\{\sigma_2\frac{\partial}{\partial\beta}A\left(T,\beta\right)\left[E_1P_{\lambda_0}+E_2Q_{\lambda_0}\right] + A\left(T,\beta\right)\frac{(\lambda+1)\sin(\theta_0)}{\cos^2(\theta_0-1)}\left[E_1\cos(\theta_0)P_{\lambda_0}+E_2\cos(\theta_0)Q_{\lambda_0}-E_1P_{\lambda_0+1}-E_2Q_{\lambda_0+1}\right]\right\}\mathrm{e}^{-\mathrm{i}\omega t} \tag{5.3.55}$$

Equations (5.3.52), (5.3.53) form a set of simultaneous equations in unknowns E_1 and E_2 which can be solved to give

$$E_1 = -\frac{\left(\left(-\Phi(\lambda+1)Q_{\lambda_0+1}+Q_{\lambda_0}\left(\Phi(\lambda+1)\cos(\theta_0)+\sin(\theta_0)r_e\Phi_R\right)\right)-\sin(\theta_0)r_e\Phi_RQ_{\lambda_0}\right)\mathrm{e}^{\mathrm{i}\omega t_0}}{\Phi(\lambda+1)\left(P_{\lambda_0}Q_{\lambda_0+1}-Q_{\lambda_0}P_{\lambda_0+1}\right)}, \tag{5.3.56}$$

$$E_2 = \frac{\left(\left(-\Phi(\lambda+1)P_{\lambda_0+1}+P_{\lambda_0}\left(\Phi(\lambda+1)\cos(\theta_0)+\sin(\theta_0)r_e\Phi_R\right)\right)-\sin(\theta_0)r_e\Phi_RP_{\lambda_0}\right)\mathrm{e}^{\mathrm{i}\omega t_0}}{\Phi(\lambda+1)\left(P_{\lambda_0}Q_{\lambda_0+1}-Q_{\lambda_0}P_{\lambda_0+1}\right)}, \tag{5.3.57}$$

With E_1 and E_2 now determined (5.3.48) can be reduced by cancellation of the $\mathrm{e}^{\pm\mathrm{i}\omega t_0}$ terms to

$$\varphi_{out}(t,\theta) = A(t,R)[E_1P_\lambda + E_2Q_\lambda], \quad R = \theta r_e. \tag{5.3.58}$$

Note that it is not necessary to assign numerical values to σ_i since the terms cancel out during the derivations. Taking the water density to be ρ_l, the surface elevation and dynamic pressure can be derived from

$$\eta = -\frac{1}{g}\frac{\partial}{\partial t}\varphi_{out}(t,\theta), \qquad P = -\rho_l\frac{\partial}{\partial t}\varphi_{out}(t,\theta). \tag{5.3.59}$$

Constant	Description	Value
g	Acceleration due to gravity	$9.81\ \mathrm{ms}^{-2}$
r_e	Radius of earth	6371 km
R_c	Radius of cylindrical rupture	40 km
R_0	Radius of inner region	120 km
c	Speed of sound in water	$1500\ \mathrm{ms}^{-1}$
W_0	Uplift velocity	$0.1\ \mathrm{ms}^{-1}$

Table 5.1: Constants and parameters used in surface elevation comparison of Figure 5.7.

5.4 Results and discussion

Many studies of acoustic–gravity wave propagation use Cartesian or cylindrical coordinates. However, the curvature of the earth unavoidably introduces errors for points far removed from the source. In this chapter we have considered an axially symmetric rupture occurring at the north pole and studied the propagation over the surface of the sphere. The earth system being modelled as a thin water layer of constant depth overlying a rigid sphere.

To achieve this goal we split our studies into two regions (inner and outer) with different scales in each. By employing a suitable scaling for the inner region (the near-field), we were able to show that the situation is exactly analogous to that studied in an earlier work [4]. This correspondence allowed us to take an established integral solution (5.3.19) as our desired initial velocity potential, valid for the region outside of the uplifting cylinder, but within some arbitrary radius R_0. The radius R_0 being chosen so as to be far enough away from the rupture for the evanescent waves to decay, but not so far as to suffer from curvature effects. A value of 120 km was taken to satisfy these requirements.

For the outer region ($R > R_0$) the scaling was changed to reflect the reference length scale switching from h to r_e thus providing a far-field perspective. We found that the amplitude derived in the CS is multiplied by $\Theta(\theta)$ when moving to the spherical case. $\Theta(\theta)$ governs the defocusing/focusing behaviour of the wave-forms due to the spherical geometry involved. The action of $\Theta(\theta)$ is as follows: $\Theta(\theta)$ begins with a value of 1 at θ_0 since the amplitudes of the CS and the spherical solution must match at this radius. Then, as θ increases, we see a decrease in amplitude (defocusing) as θ approaches $\pi/2$. From this point $\Theta(\theta)$ begins to increase in magnitude (focusing effect) until the value of 1 is again attained at $\theta = \pi - \theta_0$.

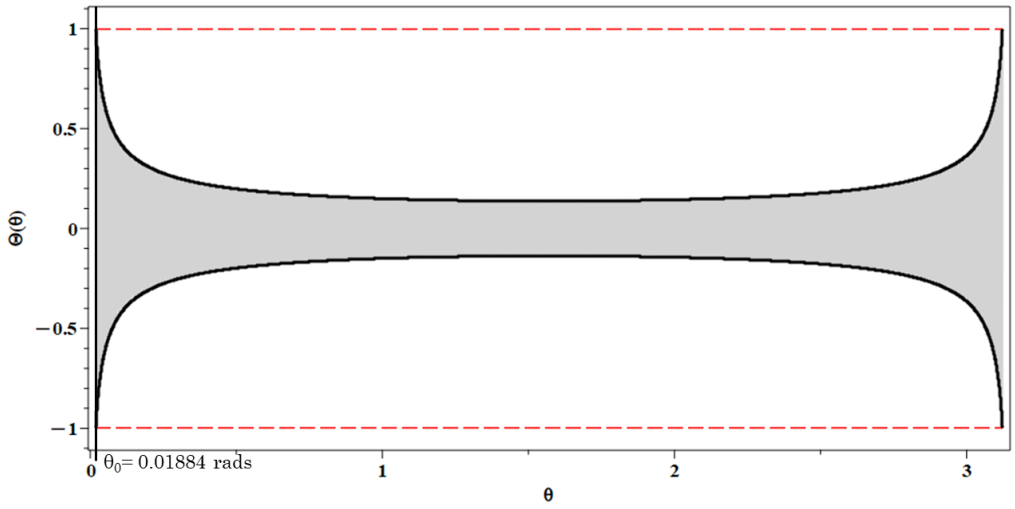

Figure 5.6: Plot of theta function (5.3.40) (grey), upper and lower limits ± 1 (red), and approximate envelope function (5.4.60) (black). North pole (rupture origin) is located at $\theta = 0$, matching point at $\theta = \theta_0 = R_0/R_e = 0.01884$, maximum defocusing occurs at $\theta = \pi/2$, antipodal matching point is at $\theta = \pi - \theta_0$, and the South pole is at $\theta = \pi$.

Since $\Theta(\theta)$ multiplies the CS then the amplitude of the CS is modulated by $\Theta(\theta)$ as the waves propagate over the surface of the sphere, first defocusing as they approach the equator $\theta = \pi/2$, and then focusing again as they near the South pole $\theta = \pi$. The acoustic–gravity waves resulting from the second term in (5.3.19), would undergo similar defocusing/focusing. A plot of $\Theta(\theta)$ is shown in Figure 5.6. Note that $\Theta(\theta)$ is only valid in the range $\theta_0 \leq \theta \leq (\pi - \theta_0)$. If calculations are carried out using the outer velocity potential for distances not falling within this range, then amplification of the surface elevation can be reported. However, this is not valid (see Figure 5.7d).

The envelope governing the changing magnitude of $\Theta(\theta)$ can be closely approximated by a modified form of a result found in [58] and attributed to Bernstein. The modification involves a re-scaling of Bernstein's original result by a constant K:

$$|\Theta(\theta)| \leq K\sqrt{\frac{2}{\pi\lambda}}\left(1-\cos^2(\theta)\right)^{-\frac{1}{4}}, \qquad K = \frac{1}{\sqrt{\frac{2}{\pi\lambda}}\left(1-\cos^2(\theta_0)\right)^{-\frac{1}{4}}}. \tag{5.4.60}$$

The black traces in Figure 5.6 were obtained with ($K = 8.68$). As a numerical example we take those parameters listed in Table 5.1 which reproduce Figure 5.2 from [4]. The aim is to compile a side-by-side comparison of the tsunami contribution of the CS, against the solution for η generated by (5.3.59), which utilises spherical coordinates. Comparisons

are made at four distances from the source, namely 120 km (the matching point), 1000 km (as in Figure 5.2 [4]), 10000 km (which corresponds to $\theta \approx \pi/2$) and 20000 km (which corresponds to $\theta \approx \pi$). The resulting surface elevation wave-forms are found in Figure 5.7.

Having described the spherical solution, (5.3.58), some of the underlying assumptions and limitations of the model can be discussed. The model consists of a constant depth water layer covering a rigid sphere with no protruding land masses - "a water world". In practice the water depth is not constant, with many deep trenches, sea-mounts and land masses dispersed over the surface of the approximately spherical earth. The land masses in particular would break up the uniform film of water covering the sphere into distinct oceans. This alone is enough to introduce reflection/refraction effects unaccounted for in the model. The model does not take into account any dissipative mechanisms such as friction, and with the sphere being considered rigid, no elastic effects of the seabed are considered either. It is known that elasticity can be important [20, 46]. Also, a more realistic model of the earth system would require the rotation of the planet to be taken in account along with the tidal forces generated by the moon and (to a lesser extent) the sun.

Constant	Description	Value
g	Acceleration due to gravity	$9.81\ \mathrm{ms}^{-2}$
r_e	Radius of earth	6371 km
R_c	Radius of cylindrical rupture	1100 m
R_0	Radius of inner region	120000 m
ρ_a	Air density	$1.2\ \mathrm{kgm}^{-3}$
c	Speed of sound in air	$343\ \mathrm{ms}^{-1}$
W_0	Uplift velocity	$400\ \mathrm{ms}^{-1}$
n	Acoustic mode	1
τ	Uplift duration	0.2 s

Table 5.2: Constants and parameters used in Tonga qualitative model.

5.4.1 Hunga Tonga–Hunga Ha'apai eruption

The axially symmetric, cylindrical rupture model developed in [4], coupled with the global extent of the results obtained in this chapter suggest a qualitative comparison may be made with the Hunga Tonga–Hunga Ha'apai eruption studied in [19]. The Tonga volcanic eruption of 15th January 2022 was one of the largest of the last 30 years, and generated concentric, propagating atmospheric acoustic–gravity waves which radiated outwards globally from the source.

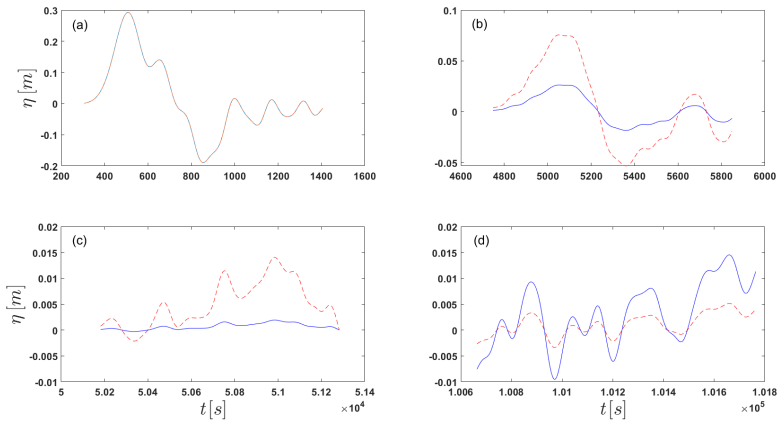

Figure 5.7: Comparison between the surface elevation from (5.3.19), against (5.3.59) which uses spherical coordinates. CS is red dash trace, spherical solution is blue solid trace. (a) Distance from source 120 km. This is the matching point. (b) Distance from source 1000 km as in [4] (c) Distance from source 10000 km. Near the maximum defocusing point. (d) Distance from source 20000 km. As this distance is slightly further away than the antipodal matching point ($\theta = \pi - \theta_0$) some amplification is seen. However, this is not a valid result because the calculation was carried out beyond the range of applicability of $\Theta(\theta)$.

The Tonga eruption was modelled in [19] as a moving atmospheric source, coupled to the ocean surface, able to transfer energy into the ocean via a triad resonance mechanism [19]. For comparison purposes we regard the volcanic eruption as an uplifting cylinder moving in a low density fluid (the atmosphere). The parameters used for the comparison are those found in Figure 7 of [19], and reproduced in Table 5.2. The explosive nature of the event is reflected in the supersonic uplift velocity and short duration. Our model is that of a point source, rather than a moving source, as in [19], and no coupling (resonance) with the liquid layer is considered. These constraints limit our comparison to be qualitative only. Figure 5.8 shows the progression of the acoustic–gravity wave front at four distinct times. Figure 5.8(a) is just after the eruption, and shows the circular wave-front of the acoustic–gravity waves as pictured in the satellite imagery of Figure 1 [19]. Figure 5.8(b) and (c) represent the acoustic–gravity wave's progression just before, and just after, the point of maximum defocusing respectively. Figure 5.8(d) has the acoustic–gravity wave focusing at its antipodal point lying over north Africa. The defocusing is apparent in the less intense acoustic–gravity wave in Figures 5.8(b) and (c) when compared to Figures 5.8(a) and 5.8(d) - see supplementary video.

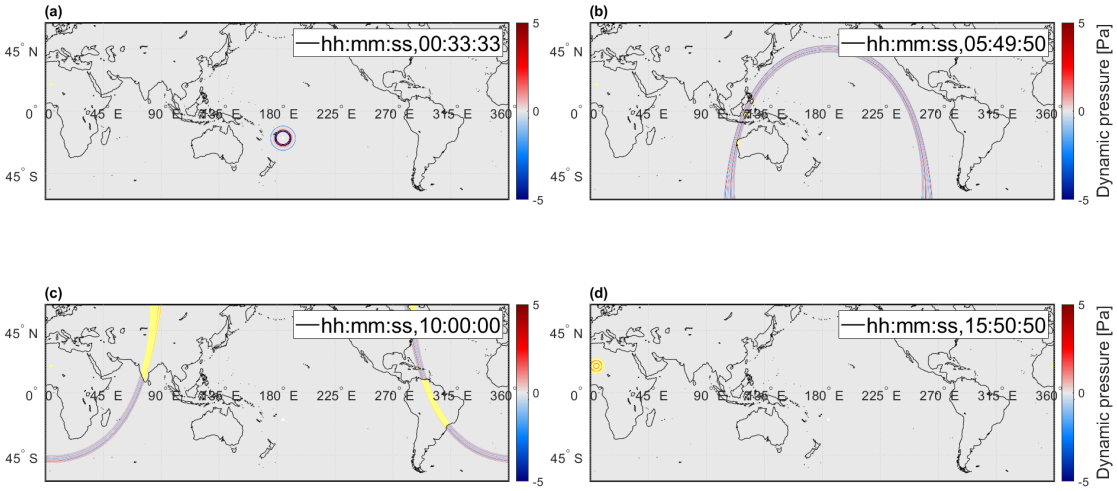

Figure 5.8: Progression of acoustic–gravity waves generated by point source model of the Tonga 2022 eruption. (a) Circular wavefront shortly after eruption, (b) Wavefront has now travelled almost half way around the world. This is just before maximum defocusing is achieved. (c) Just after maximum defocusing, the wavefront is now past the half-way point and is beginning to focus again. (d) The wavefront has reached its antipodal point over north Africa and has focused here.

5.4.2 Future work

The work presented in this chapter could be extended in a number of ways. One of which could be the development of a computational fluid dynamics (CFD) validation model. The assumptions of constant depth, solid and rigid sphere, no tides and no rotation discussed earlier could make validation using recorded data difficult. Experiments using water tanks are also of no help due to the global scale and curvature involved. Once the CFD model had been set up, and the focusing/defocusing effects verified, then other assumptions could be investigated. Elasticity, tides, rotation (Coriolis) and dissipation would all be candidates for further study. Also, the small correction due to earth's geometry being closer to an oblate spheroid rather than a perfect sphere could be included.

Chapter 6

Concluding remarks

This concluding chapter to the thesis will be composed of a general discussion around the contents of Chapters 2 to 5, and highlight how the aims of the thesis proposed in Section (2.2) have been met. Finally, some ideas for ways in which the work could be extended in future will be proposed.

Fluid flow in its most general sense is a difficult phenomenon to study. For flow velocities that are small when compared to the speed of light, the governing equations for Newtonian fluids are the Navier–Stokes (NS) equations. These are a collection of coupled nonlinear differential equations that are notoriously difficult to solve. The equations in their purest form do not have a closed form solution. In this guise they are principally found in Computational Fluid Dynamics (CFD). The study of tsunami and acoustic–gravity wave propagation in the oceans would ideally make use of the full NS equations, taking into account varying bathymetry, the elastic properties of the seabed, varying sound speed, tidal effects, Coriolis forces, dissipation and the possibility of many more variables. In practice, with current technology, the NS equations are too difficult to solve this way, and simplifying assumptions are made in order to make the problem more tractable. A functional mathematical model is always a balance between simplicity, accuracy and speed of computation, and modelling of tsunamis is no exception. In the construction of any mathematical model it is necessary to identify those parameters that are essential for the mathematical description of the underlying physics. Then there are those that can be regarded as optional - in the sense that their inclusion provides a fine-tuning effect - and those that can be ignored. For example, in the study of tsunamis and acoustic–gravity waves, essential parameters might include the fault's geometry and dynamics along with the compressibility of water. Optional parameters could include elasticity and the varying

depth of the ocean, while parameters that can be ignored might include the movements of marine life. Over the course of the timeline in Chapter 2 there has been an evolution in terms of adding/refining essential and optional parameters and adding/refining mathematical techniques. The fault geometry has been represented by infinite strips (both oscillating and transient) [14, 3], cylinders [4] and, more recently, by rectangular blocks [16, 1, 2]. The inclusion of water compressibility is essential if acoustic–gravity waves are to be studied [18, 21]. The development of stationary phase techniques has helped reduce computational burden where they can be applied [3, 4]. Progress has been made on the issue of varying bathymetry by depth-integrated/mild-slope equations [55, 26] and the effects of elasticity have been studied in the absence of ground motion [25].

Chapter 3 extends the results of [16] by adding gravitational effects to the existing pure acoustic analysis. The motion of the seabed was modelled in [16] as the transient uplift of a rectangular block. Gravity would enter the equations through the surface boundary condition, and once the analysis was completed, we would have equations describing both the acoustic–gravity waves (with slight correction due to gravity) and the tsunami. The tsunami equations were a new result. Also, the finite extent of the rectangular block representing the fault, and the linear nature of the model, meant that more complex fault clusters could be addressed via superposition. This completed thesis aims 1 and 2 Section 2.2.

Chapter 4 added fault motion to the elastic seabed analysis of [25] and yielded some interesting results. Considering the acoustic-gravity wave signals first, a new result that emerged was that the signals terminate after some finite time. In contrast, the signals derived using a rigid seabed analysis persist indefinitely. The determining factor in the longevity of the signals turned out to be the seabed rigidity. Another new result found that the fault's geometry and dynamics were encoded into the acoustic–gravity wave signals in such a way that - in some cases - the uplift duration and fault width could be retrieved by careful filtering of the signals received in the far-field. In the highly symmetric case of a rectangular block playing the part of a fault the information could be easily retrieved. However, when examining real data, the interpretation became more difficult. The elastic solutions involve integrals whereas the solutions for a rigid seabed could be obtained through application of the stationary phase method, eliminating the integrals. A consequence of the integral method was that solutions could be obtained for times preceding the critical arrival time and thus the timing relationships buried in the acoustic–gravity wave signals were noticed. Although the stationary phase method is much faster to calculate, it does introduce a singularity at the critical time [3] and so information before the critical

time is lost.

In addition, more accurate estimates for the cut-off frequencies for acoustic–gravity wave modes $n \geq 2$ were obtained.

Turning to the surface waves, it was found that the main tsunami was almost unaffected by the elastic seabed when travelling over deep water - the wave did not "feel" the seabed. In shallower water the elasticity of the seabed does make a difference to the tsunami amplitude and wave shape. Also when the seabed is elastic there is a possibility of second - very small - surface wave which propagates with the speed of sound. The shape of this small wave also encodes the fault's geometry and dynamics within it. An estimate for the cut-off frequency for this surface wave was derived. This completes thesis aim 3 Section 2.2.

Finally, in Chapter 5, the perspective was broadened to a global scale. In this chapter the influence of the (approximately) spherical geometry of the earth upon tsunami and acoustic–gravity wave propagation was studied. Our studies found that the near-field solution given in cylindrical coordinates, and valid for regions close to the rupture (located at the north pole), underwent a modulation when moving to the far-field. Firstly, the modulation resulted in a defocusing effect as the waves spread away from the north pole towards the equator. Then, once propagation had passed the equator, the modulation produced a focusing effect until the antipodal point (south pole) was approached. The end of Chapter 5 completes thesis aim 5 Section 2.2.

6.1 Future work

Extensions to the model developed in Chapter 3 could be developed in many ways, one of which would be to address the assumption of constant sound speed. The work of [51] highlighted the importance of including variable sound speed profiles into practical applications such as tsunami early warning. Another area in which the model may be improved lies in the assumption of an idealised rectangular geometry for the faults. Although [16] shows the rectangular fault assumption to be valid in many cases, it is obviously not valid for all. Future work could include the addition of dip and rake angles as parameters and also provision for the fault to rise with different velocities along its length, rather than the whole fault moving together with one set velocity. It remains to develop techniques that can account for changes in bathymetry without computation of the entire 3D domain. For slowly varying bathymetry (i.e. mild slopes where $|\nabla h(x,y,t)| \ll kh$) there already exist

techniques in the form of the depth-integrated equations [26, 55, 27].

For Chapter 4, the possibility of capturing the behaviour of acoustic–gravity waves propagating at speeds higher than C_s could be investigated. Modifications to the model developed in Chapter 4 might be possible, or maybe a new model would be required to capture the leading pulse of hydrophone H08S (Figure 4.28).

The work presented in Chapter 5 could be extended in a number of ways. One of which could be the development of a computational fluid dynamics (CFD) validation model. The assumptions of constant depth, solid and rigid sphere, no tides and no rotation discussed earlier could make validation using recorded data difficult. Experiments using water tanks are also of no help due to the global scale and curvature involved. Once the C.F.D. model had been set up, and the focusing/defocusing effects verified, then other assumptions could be investigated. Elasticity, tides, rotation (Coriolis) and dissipation would all be candidates for further study. Also, the small correction due to earth's geometry being closer to an oblate spheroid rather than a perfect sphere could be included.

Appendices

Appendix A

Derivation of first term in equation (4.2) [3]

While analysing the equations and plot data for Chapter three 3.4b it was noticed that the amplitude of the tsunami waveform derived from Stiassnie's equations [3] was approximately half that predicted by the equations of [1] and the numerical model. Further investigation revealed a possible typo in the derivations appearing in [3]. These investigations showed the equations for tsunami amplitude and the pressure contribution resulting from the tsunami wave to be missing a factor of two. The calculations in this appendix illustrate this discrepancy.

Starting with the contribution to bottom pressure arising from the surface wave i.e. the first integral in [3] (3.14).

$$\frac{8\rho\tilde{\zeta}_0}{\pi\tau}\int_0^\infty \frac{\mu_0 \sin(\omega\tau/2)\sin(k_0 b)}{k_0^2\left[2\mu_0 h + \sinh(2\mu_0 h)\right]} \cos\left(k_0 x - \omega t + \frac{\omega\tau}{2}\right) \mathrm{d}\omega \tag{1.0.1}$$

- $\hat{x} = \frac{x}{h},\ \Rightarrow x = \hat{x}h$
- $\hat{b} = \frac{b}{h},\ \Rightarrow b = \hat{b}h$
- $\hat{t} = \tilde{t} - \frac{\hat{\tau}}{2} = \sqrt{\frac{g}{h}}t - \frac{1}{2}\sqrt{\frac{g}{h}}\tau = \sqrt{\frac{g}{h}}\left(t - \frac{\tau}{2}\right),\ \Rightarrow t - \frac{\tau}{2} = \sqrt{\frac{h}{g}}\hat{t}$
- $\hat{\tau} = \sqrt{\frac{g}{h}}\tau,\ \Rightarrow \tau = \sqrt{\frac{h}{g}}\hat{\tau}$
- $\hat{k}_0 = k_0 h,\ \Rightarrow k_0 = \frac{\hat{k}_0}{h}$
- $\hat{\omega} = \sqrt{\frac{h}{g}}\omega,\ \Rightarrow \omega = \sqrt{\frac{g}{h}}\hat{\omega}$ also $\mathrm{d}\omega = \sqrt{\frac{g}{h}}\mathrm{d}\hat{\omega}$

- $k_0 = \sqrt{\mu_0^2 + \frac{\omega^2}{c^2}}$, [3] (3.7a) & (3.8)

$\frac{\omega^2}{c^2} \ll 1$, so that $\mu_0 \approx k_0$ (incompressible).

$$\frac{8\rho\tilde{\zeta}_0}{\pi\sqrt{\frac{h}{g}}\hat{t}}\mathrm{Re}\int_0^\infty \frac{\sin\left(\sqrt{\frac{g}{h}}\hat{\omega}\sqrt{\frac{h}{g}}\frac{\hat{t}}{2}\right)\sin\left(\frac{\hat{k}_0}{h}\hat{b}h\right)}{\frac{\hat{k}_0}{h}\left[2\frac{\hat{k}_0}{h}h + \sinh(2\frac{\hat{k}_0}{h}h)\right]} e^{i\left(\frac{\hat{k}_0}{h}\hat{x}h - \sqrt{\frac{g}{h}}\hat{\omega}\sqrt{\frac{h}{g}}\hat{t}\right)}\sqrt{\frac{g}{h}}\mathrm{d}\hat{\omega} \tag{1.0.2}$$

$$\frac{8\rho g\tilde{\zeta}_0}{\pi\hat{\tau}}\mathrm{Re}\int_0^\infty \frac{\sin(\hat{\omega}\hat{\tau}/2)\sin(\hat{k}_0\hat{b})}{\hat{k}_0\left[2\hat{k}_0 + \sinh(2\hat{k}_0)\right]} e^{i(\hat{k}_0\hat{x} - \hat{\omega}\hat{t})}\mathrm{d}\hat{\omega} \tag{1.0.3}$$

The phase is given by,

$$g_0(\hat{\omega}) = \hat{k}_0(\hat{\omega})\frac{x}{t} - \hat{\omega}. \tag{1.0.4}$$

Differentiation of the phase term leads to,

$$\frac{\partial g_0(\hat{\omega})}{\partial\hat{\omega}} = \frac{d\hat{k}_0(\hat{\omega})}{d\hat{\omega}}\frac{x}{t} - 1 = 0 \quad \text{at stationary point,} \tag{1.0.5}$$

with $\frac{\mathrm{d}\hat{k}_0(\hat{\omega})}{\mathrm{d}\hat{\omega}}$ obtained by differentiation of the dispersion relation $\hat{\omega}^2 = \hat{k}_0\tanh\hat{k}_0$,

$$\frac{\mathrm{d}\hat{k}_0(\hat{\omega})}{\mathrm{d}\hat{\omega}} = \frac{-2\hat{\omega}}{k_0(\hat{\omega})\tanh^2 k_0(\hat{\omega}) - \tanh k_0(\hat{\omega}) - k_0(\hat{\omega})}. \tag{1.0.6}$$

The stationary phase calculation requires the second derivative of $g_0(\hat{\omega})$ so differentiate 1.0.6 again to give,

$$\begin{aligned}\frac{\mathrm{d}^2\hat{k}_0(\hat{\omega})}{\mathrm{d}\hat{\omega}^2} = &\frac{-2}{\hat{k}_0(\hat{\omega})\tanh^2\hat{k}_0(\hat{\omega}) - \tanh\hat{k}_0(\hat{\omega}) - \hat{k}_0(\hat{\omega})} \\ &+ \frac{\left(4\hat{\omega}\hat{k}_0\tanh\hat{k}_0(\hat{\omega})\frac{\mathrm{d}\hat{k}_0(\hat{\omega})}{\mathrm{d}\hat{\omega}}\right)\left(1-\tanh^2\hat{k}_0(\hat{\omega})\right) + 2\hat{\omega}\tanh^2\hat{k}_0(\hat{\omega})\frac{\mathrm{d}\hat{k}_0(\hat{\omega})}{\mathrm{d}\hat{\omega}}}{\left(k_0(\hat{\omega})\tanh^2 k_0(\hat{\omega}) - \tanh k_0(\hat{\omega}) - k_0(\hat{\omega})\right)^2} \\ &- \frac{2\hat{\omega}\frac{\mathrm{d}\hat{k}_0(\hat{\omega})}{\mathrm{d}\hat{\omega}}\left(1-\tanh^2\hat{k}_0(\hat{\omega})\right) + 2\hat{\omega}\frac{\mathrm{d}\hat{k}_0(\hat{\omega})}{\mathrm{d}\hat{\omega}}}{\left(k_0(\hat{\omega})\tanh^2 k_0(\hat{\omega}) - \tanh k_0(\hat{\omega}) - k_0(\hat{\omega})\right)^2}.\end{aligned} \tag{1.0.7}$$

The expression 1.0.7 contains $\frac{\mathrm{d}\hat{k}_0(\hat{\omega})}{\mathrm{d}\hat{\omega}}$ terms, so to eliminate them substitute 1.0.6 to give,

$$\begin{aligned}\frac{\mathrm{d}^2\hat{k}_0(\hat{\omega})}{\mathrm{d}\hat{\omega}^2} &= \frac{8\hat{\omega}^2\left(\hat{k}_0(\hat{\omega})\tanh^3\hat{k}_0(\hat{\omega})\right)-\tanh^2\hat{k}_0(\hat{\omega})-\hat{k}_0(\hat{\omega})\tanh\hat{k}_0(\hat{\omega})+1}{\left(\hat{k}_0(\hat{\omega})\tanh^2\hat{k}_0(\hat{\omega})-\tanh\hat{k}_0(\hat{\omega})-\hat{k}_0(\hat{\omega})\right)^3} \\ &\quad - \frac{2}{\hat{k}_0(\hat{\omega})\tanh^2\hat{k}_0(\hat{\omega})-\tanh\hat{k}_0(\hat{\omega})-\hat{k}_0(\hat{\omega})}.\end{aligned} \tag{1.0.8}$$

Further remove the tanh terms by substituting from the dispersion relation $\tanh\left(\hat{k}_0(\hat{\omega})\right) = \frac{\hat{\omega}^2}{\hat{k}_0(\hat{\omega})}$ to arrive at,

$$\begin{aligned}\frac{\mathrm{d}^2\hat{k}_0(\hat{\omega})}{\mathrm{d}\hat{\omega}^2} &= \frac{8\hat{\omega}^2\hat{k}_0(\hat{\omega})\left(-\hat{\omega}^6+\hat{\omega}^2\hat{k}_0(\hat{\omega})^2+\hat{\omega}^4-\hat{k}_0(\hat{\omega})^2\right)}{\left(-\hat{\omega}^4+\hat{k}_0(\hat{\omega})^2+\hat{\omega}^2\right)^3} \\ &\quad + \frac{2\hat{k}_0(\hat{\omega})}{-\hat{\omega}^4+\hat{k}_0(\hat{\omega})^2+\hat{\omega}^2}.\end{aligned} \tag{1.0.9}$$

Finally making use of the shallow water approximation $\hat{k}_0(\hat{\omega}) = \hat{\omega}$ [3] reduces the expression for the second derivative to,

$$\frac{\mathrm{d}^2\hat{k}_0(\hat{\omega})}{\mathrm{d}\hat{\omega}^2} = \frac{6\hat{\omega}^3-8\hat{\omega}}{\left(\hat{\omega}^2-2\right)^3} = \hat{\omega}+\frac{3}{4}\hat{\omega}^3+\frac{3}{8}\hat{\omega}^5+O(\hat{\omega}^7). \tag{1.0.10}$$

Which to leading order becomes,

$$\frac{\mathrm{d}^2\hat{k}_0(\hat{\omega})}{\mathrm{d}\hat{\omega}^2} = \hat{\omega} = \hat{\Omega}_0 \quad \text{at point of stationary phase.} \tag{1.0.11}$$

Therefore,

$$\frac{\partial^2 g_0(\hat{\omega})}{\partial\hat{\omega}^2} = \hat{\Omega}_0\frac{\hat{x}}{\hat{t}}$$

Stationary phase approximation now gives,

$$\frac{8\rho g\tilde{\zeta}_0}{\pi\hat{\tau}}\frac{\sin\left(\hat{\Omega}_0\hat{\tau}/2\right)\sin\left(\hat{K}_0\hat{b}\right)}{\hat{K}_0\left[2\hat{K}_0+\sinh\left(2\hat{K}_0\right)\right]}\sqrt{\frac{2\pi}{\hat{t}}}\frac{1}{\left[\hat{\Omega}_0\frac{\hat{x}}{\hat{t}}\right]^{\frac{1}{2}}}\cos\left(\hat{K}_0\hat{x}-\hat{\Omega}_0\hat{t}+\frac{\pi}{4}\right)$$

$$\frac{8\rho g\tilde{\zeta}_0}{\sqrt{\pi}\hat{\tau}\hat{x}^{\frac{1}{2}}}\frac{2^{\frac{1}{2}}\sin\left(\hat{\Omega}_0\hat{\tau}/2\right)\sin\left(\hat{K}_0\hat{b}\right)}{\hat{K}_0\hat{\Omega}_0^{\frac{1}{2}}\left[2\hat{K}_0+\sinh\left(2\hat{K}_0\right)\right]}\cos\left(\hat{K}_0\hat{x}-\hat{\Omega}_0\hat{t}+\frac{\pi}{4}\right) \tag{1.0.12}$$

Note that,

$$\hat{K}_0\hat{\Omega}_0^{\frac{1}{2}} = \sqrt{2}\left(\frac{\hat{t}}{\hat{x}}-1\right)^{\frac{1}{2}}\left[\sqrt{2}\left(\frac{\hat{t}}{\hat{x}}-1\right)^{\frac{1}{2}}\right]^{\frac{1}{2}} = 2^{\frac{1}{2}}2^{\frac{1}{4}}\left(\frac{\hat{t}}{\hat{x}}-1\right)^{\frac{3}{4}}$$

substituting and re-arranging 1.0.12 gives,

$$\frac{8\sqrt{2}\rho g\tilde{\zeta}_0}{2^{\frac{1}{2}}2^{\frac{1}{4}}\sqrt{\pi}\hat{\tau}\hat{x}^{\frac{1}{2}}}\frac{\sin\left(\hat{\Omega}_0\hat{\tau}/2\right)\sin\left(\hat{K}_0\hat{b}\right)}{\left(\frac{\hat{t}}{\hat{x}}-1\right)^{\frac{3}{4}}\left[2\hat{K}_0+\sinh\left(2\hat{K}_0\right)\right]}\cos\left(\hat{K}_0\hat{x}-\hat{\Omega}_0\hat{t}+\frac{\pi}{4}\right)$$

$$\frac{2^{\frac{11}{4}}\rho g\tilde{\zeta}_0}{\sqrt{\pi}\hat{\tau}\hat{x}^{\frac{1}{2}}}\frac{\sin\left(\hat{\Omega}_0\hat{\tau}/2\right)\sin\left(\hat{K}_0\hat{b}\right)}{\left(\frac{\hat{t}}{\hat{x}}-1\right)^{\frac{3}{4}}\left[2\hat{K}_0+\sinh\left(2\hat{K}_0\right)\right]}\cos\left(\hat{K}_0\hat{x}-\hat{\Omega}_0\hat{t}+\frac{\pi}{4}\right) \tag{1.0.13}$$

Since we also have,

$$\sin\left(\hat{\Omega}_0\hat{\tau}/2\right) = \sin\left[\sqrt{2}\hat{\tau}\left(\frac{\hat{t}}{\hat{x}}-1\right)^{\frac{1}{2}}/2\right]$$

$$\sin\left(\hat{K}_0\hat{b}\right) = \sin\left[\sqrt{2}\hat{b}\left(\frac{\hat{t}}{\hat{x}}-1\right)^{\frac{1}{2}}\right]$$

$$2\hat{K}_0 = 2\sqrt{2}\left(\frac{\hat{t}}{\hat{x}}-1\right)^{\frac{1}{2}} = 2^{\frac{3}{2}}\left(\frac{\hat{t}}{\hat{x}}-1\right)^{\frac{1}{2}}$$

Using $\cos(-\theta)=\cos(\theta)$,

$$\cos\left[\hat{K}_0\hat{x}-\hat{\Omega}_0\hat{t}+\frac{\pi}{4}\right] = \cos\left[-\left(\hat{K}_0\hat{x}-\hat{\Omega}_0\hat{t}+\frac{\pi}{4}\right)\right]$$

$$\cos\left[\hat{\Omega}_0\hat{t}-\hat{K}_0\hat{x}-\frac{\pi}{4}\right] = \cos\left[\sqrt{2}\left(\frac{\hat{t}}{\hat{x}}-1\right)^{\frac{1}{2}}\hat{t}-\sqrt{2}\left(\frac{\hat{t}}{\hat{x}}-1\right)^{\frac{1}{2}}\hat{x}-\frac{\pi}{4}\right]$$

$$= \cos\left[\sqrt{2}\left(\frac{\hat{t}}{\hat{x}}-1\right)^{\frac{1}{2}}\left(\hat{t}-\hat{x}\right)-\frac{\pi}{4}\right]$$

but,

$$\left(\hat{t}-\hat{x}\right) = \hat{x}\left(\frac{\hat{t}}{\hat{x}}-1\right)$$

so that,

$$\cos\left[\sqrt{2}\left(\frac{\hat{t}}{\hat{x}}-1\right)^{\frac{1}{2}}\left(\hat{t}-\hat{x}\right)-\frac{\pi}{4}\right] = \cos\left[\sqrt{2}\hat{x}\left(\frac{\hat{t}}{\hat{x}}-1\right)^{\frac{3}{2}}-\frac{\pi}{4}\right]$$

so the final result is identical with the first line of equation (4.2) in [3] with the exception

of an extra factor of 2 in the numerator.

$$2^{\frac{7}{4}}.2 = 2^{\frac{7}{4}}.2^{\frac{4}{4}} = 2^{\frac{11}{4}}$$

In summary the first line of equation (4.2) in [3] is given as,

$$\frac{2^{\frac{7}{4}}\rho g\tilde{\zeta}_0 \sin\left[\sqrt{2}\hat{\tau}\left(\frac{\hat{t}}{\hat{x}}-1\right)^{\frac{1}{2}}/2\right]\sin\left[\sqrt{2}\hat{b}\left(\frac{\hat{t}}{\hat{x}}-1\right)^{\frac{1}{2}}\right]\cos\left[\sqrt{2}\hat{x}\left(\frac{\hat{t}}{\hat{x}}-1\right)^{\frac{3}{2}}-\frac{\pi}{4}\right]}{\sqrt{\pi}\hat{\tau}\hat{x}^{\frac{1}{2}}\left(\frac{\hat{t}}{\hat{x}}-1\right)^{\frac{3}{4}}\left[2^{\frac{3}{2}}\left(\frac{\hat{t}}{\hat{x}}-1\right)^{\frac{1}{2}}+\sinh\left(2^{\frac{3}{2}}\left(\frac{\hat{t}}{\hat{x}}-1\right)^{\frac{1}{2}}\right)\right]}, \tag{1.0.14}$$

but should read,

$$\frac{2^{\frac{11}{4}}\rho g\tilde{\zeta}_0 \sin\left[\sqrt{2}\hat{\tau}\left(\frac{\hat{t}}{\hat{x}}-1\right)^{\frac{1}{2}}/2\right]\sin\left[\sqrt{2}\hat{b}\left(\frac{\hat{t}}{\hat{x}}-1\right)^{\frac{1}{2}}\right]\cos\left[\sqrt{2}\hat{x}\left(\frac{\hat{t}}{\hat{x}}-1\right)^{\frac{3}{2}}-\frac{\pi}{4}\right]}{\sqrt{\pi}\hat{\tau}\hat{x}^{\frac{1}{2}}\left(\frac{\hat{t}}{\hat{x}}-1\right)^{\frac{3}{4}}\left[2^{\frac{3}{2}}\left(\frac{\hat{t}}{\hat{x}}-1\right)^{\frac{1}{2}}+\sinh\left(2^{\frac{3}{2}}\left(\frac{\hat{t}}{\hat{x}}-1\right)^{\frac{1}{2}}\right)\right]}. \tag{1.0.15}$$

A similar derivation applies to the first term in equation (4.1) of [3] relating to the surface elevation.

Appendix B

Derivative terms from section 4.3.4

$$\frac{\partial H_2}{\partial k}\Big|_{k=k_n} = \Bigg[\Bigg[-\frac{2\mathrm{i}k_n^3\omega^2 r_n}{q_n}\left(\mu s_n+\frac{\rho_l g}{2}\right)-4\mathrm{i}q_n k_n\omega^2 r_n\left(\mu s_n+\frac{\rho_l g}{2}\right)+\frac{2\mathrm{i}q_n k_n^3\omega^2}{r_n}\left(\mu s_n+\frac{\rho_l g}{2}\right)$$
$$-\frac{2\mathrm{i}q_n k_n^3\omega^2 r_n\mu}{s_n}+4\mathrm{i}k_n\omega^2 r_n\left(\left(\mu+\frac{\lambda}{2}\right)q_n^2+\frac{\rho_l g q_n}{2}-\frac{\lambda k_n^2}{2}\right)-\mathrm{i}k_n\left(k_n^2+s_n^2\right)\frac{\omega^2}{r_n}\left(\left(\mu+\frac{\lambda}{2}\right)q_n^2+\frac{\rho_l g q_n}{2}-\frac{\lambda k_n^2}{2}\right)$$
$$+\mathrm{i}\left(k_n^2+s_n^2\right)\omega^2 r_n\left(2k_n\left(\mu+\frac{\lambda}{2}\right)+\frac{\rho_l g k_n}{2q_n}-\lambda k_n\right)\Bigg]\mathrm{e}^{-q_n}$$
$$-\left(-2\mathrm{i}q_n k_n^2\omega^2 r_n\left(\mu s_n+\frac{\rho_l g}{2}\right)+\mathrm{i}\left(k_n^2+s_n^2\right)\omega^2 r_n\left(\left(\mu+\frac{\lambda}{2}\right)q_n^2+\frac{\rho_l g q_n}{2}-\frac{\lambda k_n^2}{2}\right)\right)\frac{hk_n\mathrm{e}^{-q_n h}}{q_n}$$
$$-\mathrm{i}\left(2q_n k_n^2\left(-\mu g r_n^2 s_n+\frac{\rho_l\omega^4}{2}\right)-\left(k_n^2+s_n^2\right)\left(-g r_n^2\left(\mu+\frac{\lambda}{2}\right)q_n^2+\frac{\rho_l\omega^4 q_n}{2}+\frac{g r_n^2\lambda k_n^2}{2}\right)\right)\frac{\mathrm{e}^{-q_n h}hk_n}{r_n}\Bigg]\cos(r_n h)$$

$$+\Bigg[\mathrm{i}\Bigg[\frac{2k_n^3}{q_n}\left(-\mu g r_n^2 s_n+\frac{\rho_l\omega^4}{2}\right)+4q_n k_n\left(-\mu g r_n^2 s_n+\frac{\rho_l\omega^4}{2}\right)+2q_n k_n^2\left(2\mu g k_n s_n-\frac{\mu g r_n^2 k_n}{s_n}\right)$$
$$-4k_n\left(-g r_n^2\left(\mu+\frac{\lambda}{2}\right)q_n^2+\frac{\rho_l\omega^4 q_n}{2}+\frac{g r_n^2\lambda k_n^2}{2}\right)$$
$$-\left(k_n^2+s_n^2\right)\left(2gk_n\left(\mu+\frac{\lambda}{2}\right)q_n^2-2g r_n^2\left(\mu+\frac{\lambda}{2}\right)k_n+\frac{\rho_l\omega^4 k_n}{2q_n}-gk_n^3\lambda+g r_n^2\lambda k_n\right)\Bigg]\mathrm{e}^{-q_n}$$
$$+\left(-2\mathrm{i}q_n k_n^2\omega^2 r_n\left(\mu s_n+\frac{\rho_l g}{2}\right)+\mathrm{i}\left(k_n^2+s_n^2\right)\omega^2 r_n\left(\left(\mu+\frac{\lambda}{2}\right)q_n^2+\frac{\rho_l g q_n}{2}-\frac{\lambda k_n^2}{2}\right)\right)\frac{\mathrm{e}^{-q_n h}hk_n}{r_n}$$
$$-\mathrm{i}\left(2q_n k_n^2\left(-\mu g r_n^2 s_n+\frac{\rho_l\omega^4}{2}\right)-\left(k_n^2+s_n^2\right)\left(-g r_n^2\left(\mu+\frac{\lambda}{2}\right)q_n^2+\frac{\rho_l\omega^4 q_n}{2}+\frac{g r_n^2\lambda k_n^2}{2}\right)\right)\frac{hk_n\mathrm{e}^{-q_n h}}{q_n}\Bigg]\sin(r_n h)$$

$$\frac{\partial H_2}{\partial k}\Big|_{k=-k_n} = \frac{\partial H_2}{\partial k}\Big|_{k=k_n} \tag{2.0.1}$$

$$\left.\frac{\partial H_2}{\partial k}\right|_{k=\mathrm{i}\Lambda_n} = \left[\left[-\frac{2\Lambda_n^3\omega^2 r_n}{q_n}\left(\mu s_n+\frac{\rho_l g}{2}\right)+4q_n\Lambda_n\omega^2 r_n\left(\mu s_n+\frac{\rho_l g}{2}\right)+\frac{2q_n\Lambda_n^3\omega^2}{r_n}\left(\mu s_n+\frac{\rho_l g}{2}\right)\right.\right.$$
$$-\frac{2q_n\Lambda_n^3\omega^2 r_n\mu}{s_n}-4\Lambda_n\omega^2 r_n\left(\left(\mu+\frac{\lambda}{2}\right)q_n^2+\frac{\rho_l g q_n}{2}+\frac{\lambda\Lambda_n^2}{2}\right)+\left(-\Lambda_n^2+s_n^2\right)\frac{\omega^2}{r_n}\left(\left(\mu+\frac{\lambda}{2}\right)q_n^2+\frac{\rho_l g q_n}{2}+\frac{\lambda\Lambda_n^2}{2}\right)\Lambda_n$$
$$+\mathrm{i}\left(-\Lambda_n^2+s_n^2\right)\omega^2 r_n\left(2\mathrm{i}\Lambda_n\left(\mu+\frac{\lambda}{2}\right)+\frac{\mathrm{i}\rho_l g\Lambda_n}{2q_n}-\mathrm{i}\lambda\Lambda_n\right)\Bigg]\mathrm{e}^{-q_n h}$$
$$-\mathrm{i}\left(2\mathrm{i}q_n\Lambda_n^2\omega^2 r_n\left(\mu s_n+\frac{\rho_l g}{2}\right)+\mathrm{i}\left(-\Lambda_n^2+s_n^2\right)\omega^2 r_n\left(\left(\mu+\frac{\lambda}{2}\right)q_n^2+\frac{\rho_l g q_n}{2}+\frac{\lambda\Lambda_n^2}{2}\right)\right)\frac{h\Lambda_n\mathrm{e}^{-q_n h}}{q_n}$$
$$\left.+\left(-2q_n\Lambda_n^2\left(-\mu g r_n^2 s_n+\frac{\rho_l\omega^4}{2}\right)-\left(-\Lambda_n^2+s_n^2\right)\left(-g r_n^2\left(\mu+\frac{\lambda}{2}\right)q_n^2+\frac{\rho_l\omega^4 q_n}{2}-\frac{g r_n^2\lambda\Lambda_n^2}{2}\right)\right)\frac{h\Lambda_n\mathrm{e}^{-q_n h}}{r_n}\right]\cos(r_n h)$$

$$+\left[\mathrm{i}\left[-\frac{2\mathrm{i}\Lambda_n^3}{q_n}\left(-\mu g r_n^2 s_n+\frac{\rho_l\omega^4}{2}\right)+4\mathrm{i}q_n\Lambda_n\left(-\mu g r_n^2 s_n+\frac{\rho_l\omega^4}{2}\right)-2q_n\Lambda_n^2\left(2\mathrm{i}\mu g\Lambda_n s_n-\frac{\mathrm{i}\mu g r_n^2\Lambda_n}{s_n}\right)\right.\right.$$
$$-4\mathrm{i}\Lambda_n\left(-g r_n^2\left(\mu+\frac{\lambda}{2}\right)q_n^2+\frac{\rho_l\omega^4 q_n}{2}-\frac{g r_n^2\lambda\Lambda_n^2}{2}\right)$$
$$\left.-\left(-\Lambda_n^2+s_n^2\right)\left(2\mathrm{i}g\Lambda_n\left(\mu+\frac{\lambda}{2}\right)q_n^2-2\mathrm{i}g r_n^2\left(\mu+\frac{\lambda}{2}\right)\Lambda_n+\frac{\mathrm{i}\rho_l\omega^4\Lambda_n}{2q_n}+g\Lambda_n^3\lambda\mathrm{i}+g r_n^2\lambda\Lambda_n\mathrm{i}\right)\right]\mathrm{e}^{-q_n h}$$
$$+\mathrm{i}\left(2\mathrm{i}q_n\Lambda_n^2\omega^2 r_n\left(\mu s_n+\frac{\rho_l g}{2}\right)+\mathrm{i}\left(-\Lambda_n^2+s_n^2\right)\omega^2 r_n\left(\left(\mu+\frac{\lambda}{2}\right)q_n^2+\frac{\rho_l g q_n}{2}+\frac{\lambda\Lambda_n^2}{2}\right)\right)\frac{h\Lambda_n\mathrm{e}^{-q_n h}}{r_n}$$
$$\left.+\left(-2q_n\Lambda_n^2\left(-\mu g r_n^2 s_n+\frac{\rho_l\omega^4}{2}\right)-\left(-\Lambda_n^2+s_n^2\right)\left(-g r_n^2\left(\mu+\frac{\lambda}{2}\right)q_n^2+\frac{\rho_l\omega^4 q_n}{2}-\frac{g r_n^2\lambda\Lambda_n^2}{2}\right)\right)\frac{h\Lambda_n\mathrm{e}^{-q_n h}}{q_n}\right]\sin(r_n h)$$

$$\left.\frac{\partial H_2}{\partial k}\right|_{k=k_{0m}} = \left[\left[-\frac{2k_{0m}^3\omega^2 r_{0m}}{q_{0m}}\left(\mu s_{0m}+\frac{\rho_l g}{2}\right)-4q_{0m}k_{0m}\omega^2 r_{0m}\left(\mu s_{0m}+\frac{\rho_l g}{2}\right)-\frac{2q_{0m}k_{0m}^3\omega^2}{r_{0m}}\left(\mu s_{0m}+\frac{\rho_l g}{2}\right)\right.\right.$$
$$-\frac{2q_{0m}k_{0m}^3\omega^2 r_{0m}\mu}{s_{0m}}+4k_{0m}\omega^2 r_{0m}\left(\left(\mu+\frac{\lambda}{2}\right)q_{0m}^2+\frac{\rho_l g q_{0m}}{2}-\frac{\lambda k_{0m}^2}{2}\right)$$
$$+\left(k_{0m}^2+s_{0m}^2\right)\frac{\omega^2 k_{0m}}{r_{0m}}\left(\left(\mu+\frac{\lambda}{2}\right)q_{0m}^2+\frac{\rho_l g q_{0m}}{2}-\frac{\lambda k_{0m}^2}{2}\right)$$
$$\left.+\left(k_{0m}^2+s_{0m}^2\right)\omega^2 r_{0m}\left(2k_{0m}\left(\mu+\frac{\lambda}{2}\right)+\frac{\rho_l g k_{0m}}{2q_{0m}}-\lambda k_{0m}\right)\right]e^{-q_{0m}h}$$
$$-\left(-2q_{0m}k_{0m}^2\omega^2 r_{0m}\left(\mu s_{0m}+\frac{\rho_l g}{2}\right)+\left(k_{0m}^2+s_{0m}^2\right)\omega^2 r_{0m}\left(\left(\mu+\frac{\lambda}{2}\right)q_{0m}^2+\frac{\rho_l g q_{0m}}{2}-\frac{\lambda k_{0m}^2}{2}\right)\right)\frac{hk_{0m}e^{-q_{0m}h}}{q_{0m}}$$
$$\left.+\left(2q_{0m}k_{0m}^2\left(\mu g r_{0m}^2 s_{0m}+\frac{\rho_l\omega^4}{2}\right)-\left(k_{0m}^2+s_{0m}^2\right)\left(g r_{0m}^2\left(\mu+\frac{\lambda}{2}\right)q_{0m}^2+\frac{\rho_l\omega^4 q_{0m}}{2}-\frac{g r_{0m}^2\lambda k_{0m}^2}{2}\right)\right)\frac{hk_{0m}e^{-q_{0m}h}}{r_{0m}}\right]\cosh(r_{0m}h)$$

$$+\left[\left(-2q_{0m}k_{0m}^2\omega^2 r_{0m}\left(\mu s_{0m}+\frac{\rho_l g}{2}\right)+\left(k_{0m}^2+s_{0m}^2\right)\omega^2 r_{0m}\left(\left(\mu+\frac{\lambda}{2}\right)q_{0m}^2+\frac{\rho_l g q_{0m}}{2}-\frac{\lambda k_{0m}^2}{2}\right)\right)\frac{hk_{0m}e^{-q_{0m}h}}{r_{0m}}\right.$$
$$-\left(2q_{0m}k_{0m}^2\left(\mu g r_{0m}^2 s_{0m}+\frac{\rho_l\omega^4}{2}\right)-\left(k_{0m}^2+s_{0m}^2\right)\left(g r_{0m}^2\left(\mu+\frac{\lambda}{2}\right)q_{0m}^2+\frac{\rho_l\omega^4 q_{0m}}{2}-\frac{g r_{0m}^2\lambda k_{0m}^2}{2}\right)\right)\frac{hk_{0m}e^{-q_{0m}h}}{q_{0m}}$$
$$+\left[\frac{2k_{0m}^3}{q_{0m}}\left(\mu g r_{0m}^2 s_{0m}+\frac{\rho_l\omega^4}{2}\right)+4q_{0m}k_{0m}\left(\mu g r_{0m}^2 s_{0m}+\frac{\rho_l\omega^4}{2}\right)+2q_{0m}k_{0m}^2\left(2\mu g k_{0m}s_{0m}+\frac{\mu g r_{0m}^2 k_{0m}}{s_{0m}}\right)\right.$$
$$-4k_{0m}\left(g r_{0m}^2\left(\mu+\frac{\lambda}{2}\right)q_{0m}^2+\frac{\rho_l\omega^4 q_{0m}}{2}-\frac{g r_{0m}^2\lambda k_{0m}^2}{2}\right)$$
$$\left.\left.-\left(k_{0m}^2+s_{0m}^2\right)\left(2gk_{0m}\left(\mu+\frac{\lambda}{2}\right)q_{0m}^2+2g r_{0m}^2 k_{0m}\left(\mu+\frac{\lambda}{2}\right)+\frac{\rho_l\omega^4 k_{0m}}{2q_{0m}}-gk_{0m}^3\lambda-g r_{0m}^2\lambda k_{0m}\right)\right]e^{-q_{0m}h}\right]\sinh(r_{0m}))$$

$$\left.\frac{\partial H_2}{\partial k}\right|_{k=-k_{0m}} = -\left.\frac{\partial H_2}{\partial k}\right|_{k=k_{0m}} \tag{2.0.2}$$

Bibliography

[1] Byron Williams, Usama Kadri, and Ali Abdolali. Acoustic–gravity waves from multi-fault rupture. *Journal of Fluid Mechanics*, 915:A108, 2021.

[2] Byron Williams and Usama Kadri. On the propagation of acoustic–gravity waves due to a slender rupture in an elastic seabed. *Journal of Fluid Mechanics*, 956:A6, February 2023.

[3] Michael Stiassnie. Tsunamis and acoustic-gravity waves from underwater earthquakes. *Journal of Engineering Mathematics*, 67(1-2):23–32, June 2010.

[4] Gali Hendin and Michael Stiassnie. Tsunami and acoustic-gravity waves in water of constant depth. *Physics of Fluids*, 25(8):086103, August 2013.

[5] Bernabe Gomez. *Underwater Earthquake Characterization by Acoustic Radiation Analysis*. *Cardiff University*, Thesis (PhD):1 – 149, 2022. Cardiff University.

[6] Usama Kadri and Michael Stiassnie. Generation of an acoustic-gravity wave by two gravity waves, and their subsequent mutual interaction. *Journal of Fluid Mechanics*, 735:R6, November 2013.

[7] Usama Kadri. Tsunami mitigation by resonant triad interaction with acoustic–gravity waves. *Heliyon*, 3(1):e00234, January 2017.

[8] Chiang C. Mei, Michael. Stiassnie, and Dick K.-P. Yue. *Theory and applications of ocean surface waves*. World Scientific, New Jersey, 2009.

[9] Kenji Satake, Mohammad Heidarzadeh, Marco Quiroz, and Rodrigo Cienfuegos. History and features of trans-oceanic tsunamis and implications for paleo-tsunami studies. *Earth-Science Reviews*, 202:103112, March 2020.

[10] A. B. Rabinovich, V. V. Titov, C. W. Moore, and M. C. Eblé. The 2004 Sumatra tsunami in the Southeastern Pacific Ocean: New Global Insight from Observations

and Modeling. *Journal of Geophysical Research: Oceans*, 122(10):7992–8019, October 2017.

[11] Walter H F Smith, Remko Scharroo, Vasily V Titov, Diego Arcas, and Brian K Arbic. Satellite Altimeters Measure Tsunami. *Oceanography, Vol.18, No.2*, pages 11–13, 2005.

[12] S. T. Grilli, M. Ioualalen, J. Asavanant, F. Shi, J. T. Kirby, and P. Watts. Source Constraints and Model Simulation of the December 26, 2004, Indian Ocean Tsunami. *Journal of Waterway, Port, Coastal, and Ocean Engineering*, 133(6):414–428, November 2007.

[13] Bernabe Gomez and Usama Kadri. Earthquake source characterization by machine learning algorithms applied to acoustic signals. *Scientific Reports*, 11(1):23062, November 2021.

[14] Tokuo Yamamoto. Gravity waves and acoustic waves generated by submarine earthquakes. *International Journal of Soil Dynamics and Earthquake Engineering*, 1(2):75–82, April 1982.

[15] M.A. Nosov. Tsunami generation in compressible ocean. *Physics and Chemistry of the Earth, Part B: Hydrology, Oceans and Atmosphere*, 24(5):437–441, January 1999.

[16] Chiang C. Mei and Usama Kadri. Sound signals of tsunamis from a slender fault. *Journal of Fluid Mechanics*, 836:352–373, February 2018.

[17] Bernabe Gomez and Usama Kadri. Near real-time calculation of submarine fault properties using an inverse model of acoustic signals. *Applied Ocean Research*, 109:102557, 2021.

[18] M. S. Longuet-Higgins. A Theory of the Origin of Microseisms. *Philosophical Transactions of the Royal Society of London. Series A, Mathematical and Physical Sciences*, 243(857):1–35, 1950. Publisher: The Royal Society.

[19] R. Omira, R. S. Ramalho, J. Kim, P. J. González, U. Kadri, J. M. Miranda, F. Carrilho, and M. A. Baptista. Global Tonga tsunami explained by a fast-moving atmospheric source. *Nature*, 609(7928):734–740, September 2022.

[20] Ali Abdolali, Usama Kadri, and James T. Kirby. Effect of Water Compressibility, Sea-floor Elasticity, and Field Gravitational Potential on Tsunami Phase Speed. *Scientific Reports*, 9(1):16874, December 2019.

[21] H. Miyoshi. Generation of the Tsunami in Compressible Water (Part I). *Journal of the Oceanographical Society of Japan*, 10(1):1–9, 1954.

[22] C. C. L. Sells. The Effect of a Sudden Change of Shape of the Bottom of a Slightly Compressible Ocean. *Philosophical Transactions of the Royal Society A: Mathematical, Physical and Engineering Sciences*, 258(1092):495–528, December 1965.

[23] P Sammarco, C Cecioni, G Bellotti, and A Abdolali. Depth-integrated equation for large-scale modelling of low-frequency hydroacoustic waves. *Journal of Fluid Mechanics*, 722:R6, 2013.

[24] N. Booij. A note on the accuracy of the mild-slope equation. *Coastal Engineering*, 7(3):191–203, 1983.

[25] Erez Eyov, Assaf Klar, Usama Kadri, and Michael Stiassnie. Progressive waves in a compressible-ocean with an elastic bottom. *Wave Motion*, 50(5):929–939, July 2013.

[26] Ali Abdolali, James T. Kirby, and Giorgio Bellotti. Depth-integrated equation for hydro-acoustic waves with bottom damping. *Journal of Fluid Mechanics*, 766:R1, March 2015.

[27] Emiliano Renzi. Hydro-acoustic frequencies of the weakly compressible mild-slope equation. *Journal of Fluid Mechanics*, 812:5–25, February 2017.

[28] Ian J. Hamling et al. Complex multifault rupture during the 2016 M_{w} 7.8 Kaikōura earthquake, New Zealand. *Science*, 356(6334):eaam7194, April 2017.

[29] A. Abdolali, James T. Kirby, Giorgio Bellotti, S. Grilli, and J. C. Harris. Hydro-Acoustic Wave Generation during the Tohoku-Oki 2011 Earthquake. In *Coastal Structures and Solutions to Coastal Disasters 2015*, pages 24–34, Boston, Massachusetts, July 2017. American Society of Civil Engineers.

[30] Erez Eyov. *Progressive Acoustic–Gravity Waves on Top of an Elastic Seabed. Technion - Israel Institute of Technology*, Research Thesis:1 –124, 2013. Technion - Israel Institute of Technology, Adar, 5773 Haifa.

[31] Adam M. Dziewonski and Don L. Anderson. Preliminary earth reference model. *Physics of the Earth and Planetary Interiors*, 25(4):297–356, 1981.

[32] Usama Kadri. Acoustic-Gravity Waves Interacting with a Rectangular Trench. *International Journal of Geophysics*, 2015:1–9, 2015.

[33] A. Abdolali, C. Cecioni, G. Bellotti, and J. T. Kirby. Hydro-acoustic and tsunami waves generated by the 2012 haida gwaii earthquake: Modeling and in situ measurements. *Journal of Geophysical Research: Oceans*, 120(2):958–971, 2015.

[34] Usama Kadri. Generation of Hydroacoustic Waves by an Oscillating Ice Block in Arctic Zones. *Advances in Acoustics and Vibration*, 2016:1–7, 2016.

[35] Usama Kadri and T. R. Akylas. On resonant triad interactions of acoustic–gravity waves. *Journal of Fluid Mechanics*, 788:R1, February 2016.

[36] Emiliano Renzi and F. Dias. Hydro-acoustic precursors of gravity waves generated by surface pressure disturbances localised in space and time. *Journal of Fluid Mechanics*, 754:250–262, September 2014.

[37] Sung B. Yoon. Propagation of distant tsunamis over slowly varying topography. *Journal of Geophysical Research: Oceans*, 107(C10):4–1–4–11, 2002. https://agupubs.onlinelibrary.wiley.com/doi/pdf/10.1029/2001JC000791.

[38] U. Kadri and M. Stiassnie. Acoustic-gravity waves interacting with the shelf break: Interaction Of Acoustic-Gravity Waves. *Journal of Geophysical Research: Oceans*, 117(C3), March 2012.

[39] D. Richards. *Advanced Mathematical Methods with Maple 2 Part Set: Advanced Mathematical Methods with Maple 2 Part Paperback Set*. Cambridge University Press, Cambridge, June 2009.

[40] Stephan T. Grilli, Jeffrey C. Harris, Tayebeh S. Tajalli Bakhsh, Timothy L. Masterlark, Christodoulos Kyriakopoulos, James T. Kirby, and Fengyan Shi. Numerical Simulation of the 2011 Tohoku Tsunami Based on a New Transient FEM Co-seismic Source: Comparison to Far- and Near-Field Observations. *Pure and Applied Geophysics*, 170(6-8):1333–1359, June 2013.

[41] A. Abdolali and J. T. Kirby. Role of compressibility on tsunami propagation. *Journal of Geophysical Research: Oceans*, 122(12):9780–9794, 2017.

[42] J. Gower. Jason 1 detects the 26 December 2004 tsunami. *Eos, Transactions American Geophysical Union*, 86(4):37, 2005.

[43] Emile A. Okal, Dominique Reymond, and Hélène Hébert. From earthquake size to far-field tsunami amplitude: development of a simple formula and application

to DART buoy data. *Geophysical Journal International*, 196(1):340–356, January 2014.

[44] C. Cecioni, A. Abdolali, G. Bellotti, and P. Sammarco. Large-scale numerical modeling of hydro-acoustic waves generated by tsunamigenic earthquakes. *Natural Hazards and Earth System Sciences*, 15(3):627–636, March 2015.

[45] Joseph L. Hammack. A note on tsunamis: their generation and propagation in an ocean of uniform depth. *Journal of Fluid Mechanics*, 60(4):769–799, 1973.

[46] Usama Kadri. Effect of sea-bottom elasticity on the propagation of acoustic–gravity waves from impacting objects. *Scientific Reports*, 9(1):912, December 2019.

[47] A. Abdolali, U. Kadri, W. Parsons, and J. T. Kirby. On the propagation of acoustic–gravity waves under elastic ice sheets. *Journal of Fluid Mechanics*, 837:640–656, February 2018.

[48] S. Watada. Tsunami speed variations in density-stratified compressible global oceans: Tsunami Speed In Layered Ocean. *Geophysical Research Letters*, 40(15):4001–4006, August 2013.

[49] S. Watada, S. Kusumoto, and K. Satake. Traveltime delay and initial phase reversal of distant tsunamis coupled with the self-gravitating elastic Earth: Delay And Precursor Of Distant Tsunami. *Journal of Geophysical Research: Solid Earth*, 119(5):4287–4310, May 2014.

[50] Finn B. Jensen. *Computational Ocean Acoustics. Jensen, Jensen,*. Springer Science+Business Media, LLC, New York, NY, 2011.

[51] S. Michele and E. Renzi. Effects of the sound speed vertical profile on the evolution of hydroacoustic waves. *Journal of Fluid Mechanics*, 883:A28, January 2020.

[52] Tristan Needham and Roger Penrose. *Visual Complex Analysis: 25th Anniversary Edition*. Oxford University Press, February 2023. _eprint: https://academic.oup.com/book/45765/book-pdf/51126812/9780192695451_web.pdf.

[53] Izrail S. Gradštejn, Josif M. Ryžik, Alan Jeffrey, Daniel Zwillinger, and Izrail S. Gradštejn. *Table of integrals, series and products*. Elsevier Acad. Press, Amsterdam, 7. ed., [3. nachdr.] edition, 2009.

[54] M.J.D. Powell. Approximation Theory and Methods, 1996.

[55] P. Sammarco, C. Cecioni, G. Bellotti, and A. Abdolali. Depth-integrated equation for large-scale modelling of low-frequency hydroacoustic waves. *Journal of Fluid Mechanics*, 722:R6, May 2013.

[56] P. Moon and D. E. Spencer. *Field Theory Handbook: Including Coordinate Systems, Differential Equations and Their Solutions*. Springer Science & Business Media, December 1961.

[57] Frank W. J. Olver and National Institute of Standards and Technology (U.S.), editors. *NIST handbook of mathematical functions*. Cambridge University Press : NIST, Cambridge ; New York, 2010. OCLC: ocn502037224.

[58] G. Szegö. *Orthogonal Polynomials*. Number v. 23 in American Mathematical Society colloquium publications. American Mathematical Society, 1959.